PLASMA PRODUCTION AND TRANSPORT IN A SIMPLE MAGNETISED TOROIDAL PLASMA

THÈSE N^{O} 3765 (2007)

PRÉSENTÉE LE 27 AVRIL 2007

À LA FACULTÉ DES SCIENCES DE BASE

CRPP Association Euratom

SECTION DE PHYSIQUE

ÉCOLE POLYTECHNIQUE FÉDÉRALE DE LAUSANNE

POUR L'OBTENTION DU GRADE DE DOCTEUR ÈS SCIENCES

PAR

Mario PODESTÀ

Laurea in Ingegneria Nucleare, Politecnico di Milano, Italie
et de nationalité italienne

acceptée sur proposition du jury:

Prof. A. Fasoli , directeur de thèse
Dr S. Alberti, rapporteur
Dr C. Hidalgo, rapporteur
Prof. M. Porkolab, rapporteu

ÉCOLE POLYTECHNIQUE
FÉDÉRALE DE LAUSANNE

Lausanne, EPFL
2007

Contents

Abstract

This Thesis addresses questions related to transport phenomena and the plasma production mechanisms by injection of microwaves in the electron-cyclotron frequency range in the simple magnetised toroidal plasma TORPEX.
The second subject is investigated in detail in Part II. The mechanisms of the interaction between the injected microwaves and the plasma are identified. The experimental results highlight the different roles played by the electron-cyclotron and upper-hybrid plasma resonances in the absoprtion of the microwave power by the plasma. The effects of the plasma-wave interaction on the electron distribution function are investigated, confirming that the high-energy electrons that are able to ionise the neutral gas mainly come from interactions at the upper-hybrid resonance. Based on the experimental results, an expression is derived for the particle source term, which can be used in numerical codes simulating the plasma dynamics on TORPEX. The plasma production mechanisms are then related to the properties of the time-averaged plasma profiles. A set of control parameters, including the injected microwave power and the vertical magnetic field, are identified. These allow one to vary in a systematic way the plasma profiles, as needed for a detailed study of plasma instabilities and related transport.
The study of particle and heat transport is undertaken in Part III. A number of experimental and analysis techniques, including a method based on the combination of 'conditional-average sampling' and 'boxcar-averaging', are applied to identify and quantify specific contributions to the total fluxes. The two-dimensional temporal behaviour of density, electron temperature and plasma potential is simultaneously reconstructed, thus contributing significantly to the characterisation of transport mechanisms at play in TORPEX plasmas. Two clearly distinct mechanisms are mainly responsible for the transport across the magnetic field. They are respectively associated to unstable low-frequency electrostatic modes, identified as drift waves and interchange modes, and to intermittent high-density plasma structures (or *blobs*). It is shown that the blobs originate from the intermittent radial expansion of the unstable modes in a region of strongly sheared $E \times B$ flow.

Keywords: TORPEX, experiment, plasma, toroidal, transport, anomalous, instabilities, blob, flux, ECH, production, microwaves

Version abrégée

Cette thèse est dédiée à l'étude expérimentale des phénomènes de transport dans les plasmas magnétisés de la machine toroïdale de base TORPEX (TORoidal Plasma EXperiment), ainsi qu'à l'étude expérimentale des mécanismes de production du plasma par injection de micro-ondes dans le domaine de fréquence électron-cyclotron. La production du plasma est décrite en détail dans la partie II. Les différents mécanismes d'interaction entre le plasma et les micro-ondes sont d'abord identifiés. En particulier, le rôle essentiel joué par les résonances électron-cyclotron et hybride supérieure dans le couplage de la puissance micro-onde au plasma est mis en évidence. L'effet de l'interaction entre le plasma et les micro-ondes sur le fonction de distribution des électrons est ensuite étudié, confirmant que les électrons de haute énergie, responsable de l'ionisation du gaz neutre servant à produire le plasma, sont principalement produits à la résonance hybride supérieure. A partir des ces résultats expérimentaux, une expression semi-empirique est établie afin de modéliser les sources de particules dans les simulations numériques de la dynamique des plasmas de TORPEX. L'influence des mécanismes de production du plasma sur ses caractéristiques est également étudiée et conduit à l'identification d'un ensemble de paramètres de contrôle, tels que la puissance injectée des micro-ondes et le champ magnétique vertical. La variation de ces paramètres de contrôle permet de changer systématiquement les profils du plasma et rend ainsi possible l'étude systématique des instabilités du plasma et du transport qui y est associé.
Le transport de particules et de chaleur est étudié dans la partie III. Les diverses contributions aux flux de particules et de chaleur sont identifiées et évaluées à l'aide de plusieurs techniques expérimentales et méthodes d'analyses, incluant notamment une méthode basée sur l'utilisation combinée d'une moyenne par échantillonnage conditionné et d'une moyenne 'boxcar'. Une contribution significative à la caractérisation du transport dans les plasmas de TORPEX est apportée en reconstruisant, simultanément et sur toute la section poloïdale, les variations temporelles de la densité, de la température électronique et du potentiel électrostatique du plasma. Il est établi que deux mécanismes distincts sont principalement responsables du transport dans la direction perpendiculaire aux lignes de champ magnétique. Le premier est associé à des modes instables électrostatiques de basse fréquence, identifiés comme étant des ondes de dérive et des modes de type 'interchange'. Le deuxième est associé à l'apparition intermittente de structure de haute densité (*blobs*) résultant de l'extension radiale et intermittente des modes instables dans une région où le flux $E \times B$ est fortement cisaillé.

Mots-clés: TORPEX, expérience, plasma, toroïdal, transport, anormal, instabilité, blob, flux, ECH, production, micro-ondes

Chapter 1

Introduction

It is commonly recognised that the transport of plasma particles and heat across the magnetic field is *anomalous*, i.e. faster than the classical transport induced by collisional processes. The close similarity, at least in a statistical sense, of transport phenomena observed in devices with different magnetic field configurations suggests that the mechanisms responsible for the anomalous cross-field transport have a common fundamental character. Explanations based on the physics of drift waves and instabilities represent the most promising avenue [45]. Drift instabilities are universal, in the sense that, being destabilised by pressure gradients, they are potentially present in almost all magnetically confined plasmas. Correlated fluctuations of density and potential due to unstable modes can drive a *fluctuation-induced* flux [83], to which an 'anomalous' diffusion coefficient is sometimes associated [45][20].
According to theory, the non-linear evolution of unstable drift modes leads to small-scale turbulence [45]. The subsequent wave-wave interactions over a broad spectrum of wave-numbers may give rise to macroscopic, long-living 'structures' of density and potential [45]. The interest for these structures resides in the fact that they can be elongated both across (*zonal flows* [59]) and along (*streamers* [52]) the direction of the pressure gradient. The first case is generally associated with the presence of a strong shear layer of the background plasma velocity and a reduction of transport ([73][44] and references therein). In the second case, hot and dense plasma regions are connected to the cold and rarefied peripheral plasma, leading to the formation of an efficient channel for cross-field transport from the core into the edge plasma. From the edge, the plasma is partly lost along the open magnetic field lines. However, a considerable fraction of non-diffusive cross-field particle and heat fluxes is observed [12]. Experiments suggest that this is associated with the intermittent ejection of high-density plasma structures, or *blobs*, poloidally localised and stretched along the magnetic field lines. Understanding the relationship between plasma instabilities, turbulence, structures and blobs, and the related transport across the magnetic field lines has, therefore, deserved considerable attention in the past years.

Progress in the characterisation of anomalous transport has been achieved in fusion-oriented devices through a synergy between theoretical work and numerical codes [24]. Simulations of the core plasma based on gyro-kinetic [59] and gyro-fluid [41] models have pointed out the role of the turbulent flux associated with particular classes of drift modes, destabilised by the ion and/or electron temperature gradient, which may account for a considerable fraction of plasma losses from the core to the edge of fusion devices. At the same time, fluid simulations of the edge region propose mechanisms leading to the formation and propagation of blobs, which transport plasma from the last closed flux surface out into the scrape-off layer (SOL) [95][35], and from here to the walls.

Theoretical and numerical work has progressed in parallel with experiments aimed at unfolding the nature of the transport mechanisms, and their relationship with turbulence and instabilities. Though limited by the diagnostics accessibility, experimental information has become available from the core of fusion devices, supporting the theoretical picture of large-scale structures generated by drift wave turbulence [19][66][40][21].

Measurements are easier in the SOL region, which is accessible, for example, to electrostatic probes and optical imaging techniques ([12][103][109] and references therein). In the SOL region, the generally intermittent character of fluctuations and transport has been established [12], and associated with blobs detaching (or ejected) from regions across the last closed flux surface. An extensive characterisation of the spatio-temporal and statistical properties of fluctuations in the SOL has been carried out. Striking similarities appear among different devices [13], for example in terms of probability distribution functions and their higher order moments, suggesting the existence of a sort of *universality* [1][38], i.e. a common behaviour for different physical systems and experimental conditions. Additional experimental observations from basic magnetised plasmas, conducted both in linear [75][15] and toroidal [115][69][31] devices, have reinforced the idea of universality, whose possible relation with the development of electrostatic drift and interchange modes has recently been suggested [56].

Similarly to fusion-oriented devices, a significant cross-field flux associated with the propagation of blobs has been reported in these basic devices. Blobs form at the transition between core and edge regions [12][103][6], from which they propagate outward to the walls [35][55]. At present, only little is known about the mechanisms behind the blob formation, and a better understanding of the physical phenomena occurring at the transition between the main plasma and the edge region is needed. Moreover, although the intrinsically non-diffusive nature of the flux related to blobs has been recognised [12], the dynamics behind the blob motion is not clear yet, and radial as well as poloidal patterns are observed [103].

More generally, several open issues, a resolution of which may lead to a deeper understanding of the basic mechanisms behind the anomalous transport, can be

identified:

1. What is the relative contribution to the cross-field flux from correlated density and potential fluctuations, associated to unstable modes, and from isolated intermittent events (blobs)?

2. Which modes are most relevant for transport, and how are they related to the specific configuration and plasma parameters of different devices?

3. How do blobs originate, and which mechanisms determine their dynamics?

4. Is there a direct link between linearly unstable modes and blobs?

A TORoidal Plasma EXperiment, TORPEX, has been constructed at CRPP/EPFL to address these issues [28][27]. It is characterised by a high flexibility of the magnetic field configuration. Aiming at low density and low temperature plasmas, local measurements with high spatial resolution are possible via electrostatic probes, that can be inserted into the plasma throughout the whole cross-section. The diagnostics setup, completed by a number of non-intrusive optical diagnostics, is intended to produce the needed data to benchmark the many physical and numerical models being developed at the moment.
This Thesis work presents the development of the TORPEX experimental facility and the results from the first experimental investigations of the transport mechanisms at play in TORPEX plasmas. A detailed characterisation of the plasma production mechanisms and of the properties of the resulting plasma profiles is also undertaken to provide the necessary background for transport studies. The rest of the Thesis is divided into four main parts:

- Part I: The TORPEX experiment.
- Part II: Plasma production and properties of the time-averaged profiles.
- Part III: Particle and heat transport in TORPEX.
- Part IV: Summary, discussion and outlook.

Part I describes the TORPEX experiment, including its development and the guidelines, in terms of physics and engineering, that have led us to specific choices of the magnetic field configuration and plasma production scheme (Chap. 2). The diagnostics setup is presented separately in Chap. 3. The technical details on the microwave system and on the analysis of electrostatic probes data are given in Appendix A and Appendix B.
In Part II the plasma production mechanisms and the properties of the resulting plasma profiles are investigated. The mechanisms leading to ionisation of the neutral gas by injection of microwaves in the electron-cyclotron range of frequency

are discussed in Chap. 4. The spatial profile of the particle source term and its dependence upon the experimental parameters are described in Chap. 5. A model, partially based on a simple numerical code (Appendix C), is developed to summarise the information on the source profile into a semi-empirical expression. The study of the plasma production mechanisms is concluded in Chap. 6 with an experimental characterisation of the electron distribution function and of its link with the particle source profile. Chapter 7 presents an overview of the properties of TORPEX plasmas, in terms of time-averaged profiles, unstable modes developing on top of them and intermediate time-scales of the macroscopic plasma dynamics.
The issue of particle and heat transport is addressed in Part. III. The experimental and analysis techniques applied for transport studies on TORPEX are reviewed in Chap. 8. The results for the total particle flux, estimated from the plasma dynamical response to a modulation of the microwave power, are presented in Chap. 9. Chapter 10 discusses the contribution to the radial (i.e. across the magnetic field) flux due to electrostatic fluctuations of density and plasma potential. The results obtained in the frequency domain allow one to relate the measured flux to the observed unstable modes. In Chap. 11 the analysis is extended to a broader region of the plasma cross-section. An experimental configuration, the so-called *SOL-like* scenario, is identified, for which a main plasma region and an edge region, connected by a transition region, can be clearly separated. Blobs are observed to form in the transition region and propagate to the wall. The two-dimensional heat and particle fluxes associated with plasma instabilities are measured from the plasma density and potential fluctuations, reconstructed via a boxcar-averaging technique. The particle flux carried by macroscopic plasma structures is calculated from their spatio-temporal evolution, obtained from simultaneous measurements of the plasma density over the plasma cross-section. The relationship between unstable modes and non-linear structures is investigated in detail. The results of this work are summarised and discussed in Part IV, which also provides an outlook for possible future lines of research on TORPEX.

Part I

The TORPEX experiment

Chapter 2

The TORPEX device: construction, design and main parameters

In this Chapter I summarise the technical and physical guidelines at the basis of the design of the TORPEX device, and the solutions adopted for its construction (Sec. 2.1). The main components of TORPEX are described, including the vacuum chamber, the vacuum and gas injection systems, the magnetic field coils setup and the plasma production system. The main parameters of the machine, and the ranges of typical operating conditions, are illustrated.

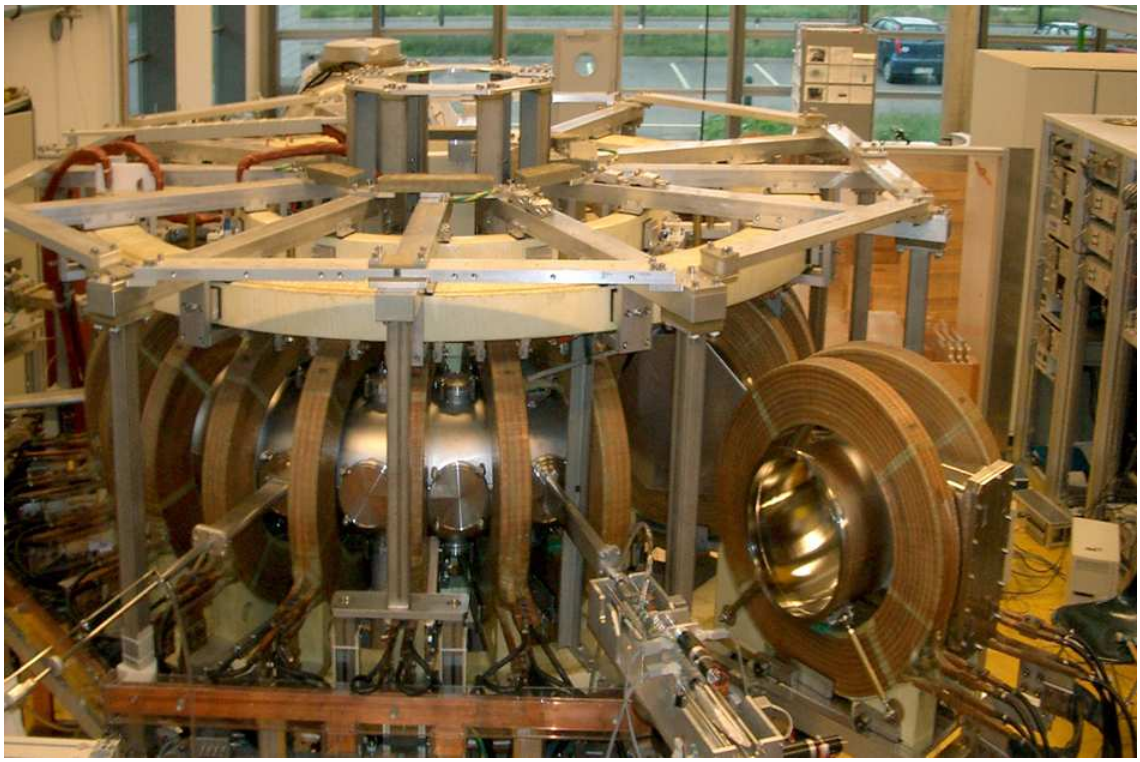

Figure 2.1: Picture of the TORPEX device. One of the 'movable' sectors is visible in the bottom-right corner.

2.1 Machine conception and design

The experiments presented in this Thesis work are performed on the toroidal device TORPEX [28], in operation at the CRPP-EPFL, Lausanne since March 2003.
The design of TORPEX started in November, 2001 with the goal of building a highly flexible device for basic plasma physics studies. The main research lines were the study of plasma instabilities and plasma-wave interaction physics, including their effect on particle and heat transport [27]. A third research avenue, namely the study of magnetic reconnection phenomena, was also envisaged but it has not been exploited to date. In order to study plasma instabilities and transport phenomena of interest for the fusion community, the main ingredients which are at the origin of tokamak turbulence were needed. These include gradients in the plasma profiles, providing the energy source for drift-like modes, and a curved magnetic field. This led, as a natural choice, to a toroidally shaped vessel. As an additional advantage with respect to linear machines, the effects of boundary conditions for the parallel (to the magnetic field, $\underline{B}$) dynamics, imposed by end-plates, are reduced.

Figure 2.2: The TORPEX vacuum vessel, composed of twelve sectors, four of which are 'retractable'. Several of the 48 ports are visible.

Vacuum chamber

The vacuum chamber [16], made of stainless-steel, is divided into twelve sectors, each spanning over 30° (Fig. 2.2). The fourfold symmetrical vessel is divided into four electrically insulated sets, of three sectors each, to limit the induced eddy currents. Four sectors, toroidally separated by 90° from each other, are extractable (Fig. 2.1). They can be easily removed from the machine to facilitate the installation, modification and reparation of diagnostics. Spare sectors can thus be modified to fit the requirements of new experiments, without stopping the experimental activity. The retractable sectors are attached to the fixed sectors by chain-like flexible brackets. A total number of 48 port-holes gives access for diagnostics and pumping. The diameter of the vessel was maximised, given the constraints imposed by the size of the pre-existing coils used to produce the toroidal magnetic field. The final value of 40cm corresponds to ~ 100 times the expected value of the ion sound radius, leading to negligible boundary effects on the plasma dynamics caused by plasma-wall interactions extending through a significant portion of the plasma volume.

Vacuum and gas injection systems

A schematic view of the TORPEX vacuum and gas injection systems is presented in Fig. 2.3. Four turbo-pumps with a nominal pumping speed of 345l/s (for N_2), backed by four primary pumps, maintain the vacuum inside the vessel at $\lesssim 5 \times 10^{-7}$mbar. Two primary pumps can be used to pump the vessel to $\approx 5 \times 10^{-3}$mbar, for example after a machine venting. A convenient system of valves allows one to isolate the turbo-pumps from the vacuum chamber ($TirV$), and the primary pumps from the turbo-pumps ($PrimV$). Another valve (BV) is used to by-pass the turbo-pump and evacuate the vessel through the primary pumps.
The working gas (Hydrogen or Argon, for the experiments reported herein) is injected at one toroidal position. The line can be isolated from the vessel by the so-called 'torpex valve' (TV). The injection rate for each gas is adjusted by flowmeters controlled by an electronic 'gas control' system. Combinations of different gases with arbitrary concentration is possible. An upgrade of the system is planned for the near future to double the number of different gases that can be injected, for example to perform systematic gas mass scans. A second line is used to inject Nitrogen during the openings of the machine. The injection rate is adjusted through a screw valve (IV). The pressure is monitored in the 'primary' and 'high-vacuum' branches of the circuit by vacuum gauges. In particular, two capacitive vacuum sensors are used to measure the pressure inside the vacuum chamber.

Magnetic field

An important element for the flexibility of the achievable experimental scenarios is the magnetic field configuration. Pre-existing coils (hereafter 'toroidal' coils) from the former LMP experiment [105][74] are used to produce a toroidal magnetic field up to 0.2T, with typical values ≤ 0.1T, which is high enough to have strongly magnetised electrons and magnetised ions. In addition to the main toroidal magnetic field, the possibility of imposing a poloidal magnetic field component, produced by external coils (hereafter 'poloidal' coils), was considered. An optimisation of the design and arrangement of the poloidal coils was conducted to achieve several possible magnetic field configurations, including a purely vertical and a cusp-shaped magnetic field (Fig. 2.4). The details on the optimisation process and on the technical specifications of the coils are extensively discussed in a previous Thesis work [67].
A subset of the poloidal coils can be used to induce a loop voltage inside the vessel, similarly to the standard ohmic operation in tokamaks. This was done, in particular, to study induced magnetic reconnection phenomena [25] and to force a transition from open to closed magnetic surfaces, which may determine a change in the character of the unstable modes and of the related turbulence [88]. Although the latter subject is not addressed in the present Thesis work, a first proof-of-principle has already been obtained [30].

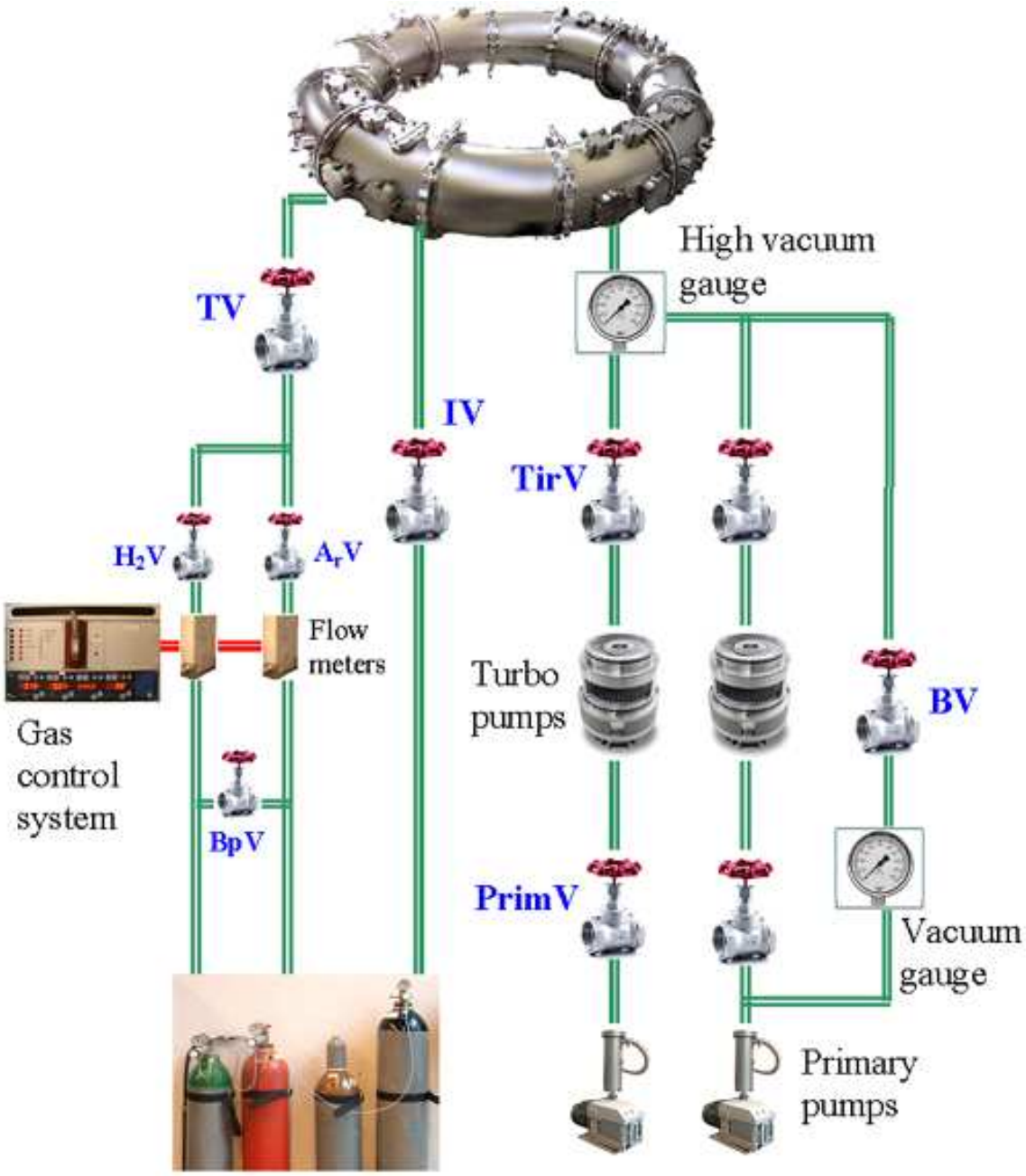

Figure 2.3: TORPEX vacuum system, including the gas injection system.

Plasma production

TORPEX plasmas are produced and sustained by microwaves at 2.45GHz, corresponding to the electron-cyclotron range of frequencies. This plasma production scheme has been preferred to other possibilities, e.g. a hot filament as a source of primary ionising electrons, because no net currents and charge unbalance are induced in the plasma. The choice of the frequency was based on the constraints imposed by the maximum available toroidal magnetic field, $B \leq 0.1$T, corresponding to frequencies ≤ 2.8GHz. The value of 2.45GHz has been finally chosen on the basis of the presently available commercial microwave sources. The wide use of these sources for industrial applications makes it easier to find off-the-shelf components, which results in a considerable reduction of development time and costs.
The microwave system installed on TORPEX is illustrated in Fig. 2.5. It consists of a commercial microwave source and a transmission line, which transmits the microwave power from the source to the vacuum chamber. The source can deliver up to 5kW of microwave power in continuous mode, or up to 50kW during 100ms in pulsed mode. In practice, the maximum available power is limited to 30kW to guarantee a safe operation of the system, for example by avoiding arcing in the circulator and on the microwave window. The microwave power can be modulated with frequencies up to 100kHz for a sinusoidal waveform, or 20kHz for a square waveform. The modulation amplitude is arbitrary, with a lower limit for the injected power of ≈ 200W. The injected and reflected power are measured on the transmission line. Neglecting the microwave leakage from the metallic vacuum chamber, their difference is taken as the value of the power absorbed by the plasma. For practical convenience, the microwaves are injected perpendicularly to the magnetic field from the low field side (LFS). A truncated waveguide is used as an antenna, which introduces finite $k_{\|}$ components in the injected spectrum. The ordinary (O-mode) polarisation has been chosen to avoid the cutoff for the extraordinary (X) mode at relatively low densities.
A complete description of the capabilities of the EC system and of its modifications, which were part of my responsibilities during the first part of this work, is given in Appendix A.

Diagnostics and data acquisition

To diagnose the plasma, the use of electrostatic probes was mostly envisaged. A copper ground plate, covering the whole experimental zone, was installed to minimise the risk of electromagnetic perturbations pick-up by the measured signals. The constraints and requirements for the development of the diagnostics set, and the solutions adopted, are extensively discussed in Chap. 3.

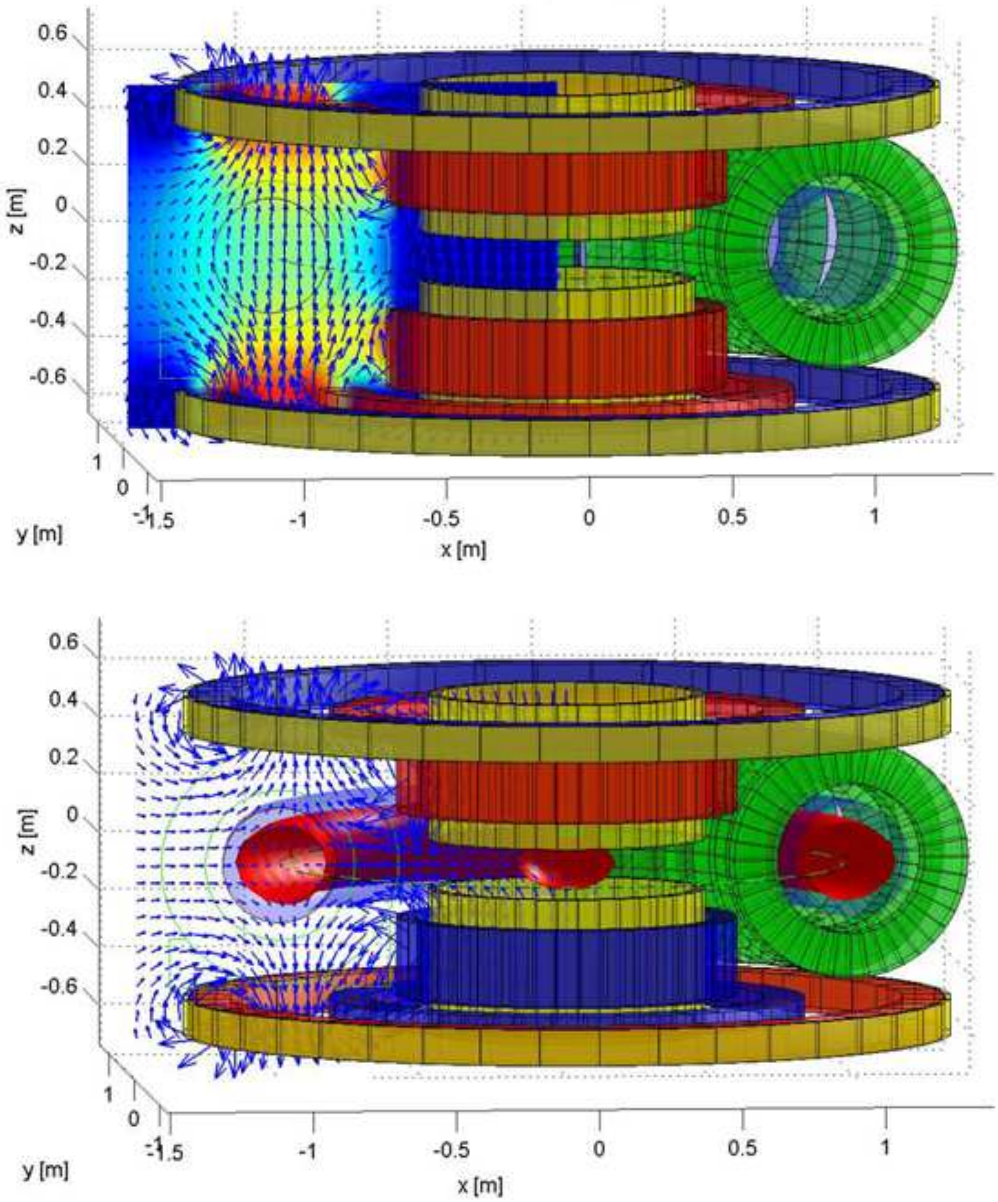

Figure 2.4: Two possible configurations of the poloidal magnetic field obtainable on TORPEX: purely vertical (*top*) and cusp-like (*bottom*) [67].

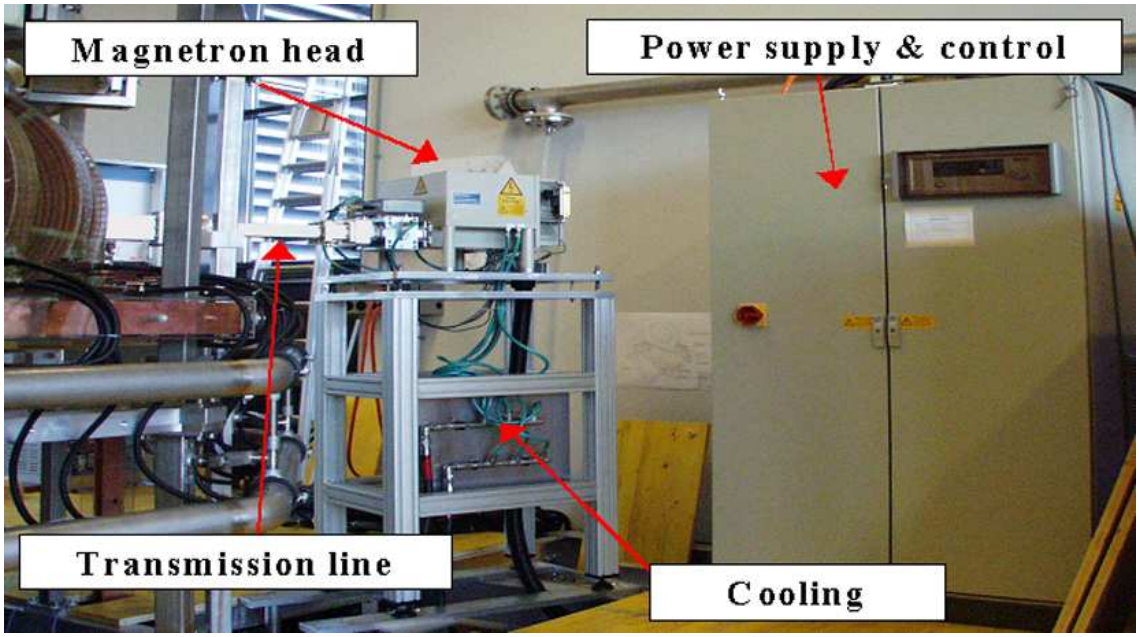

Figure 2.5: The EC system installed on TORPEX.

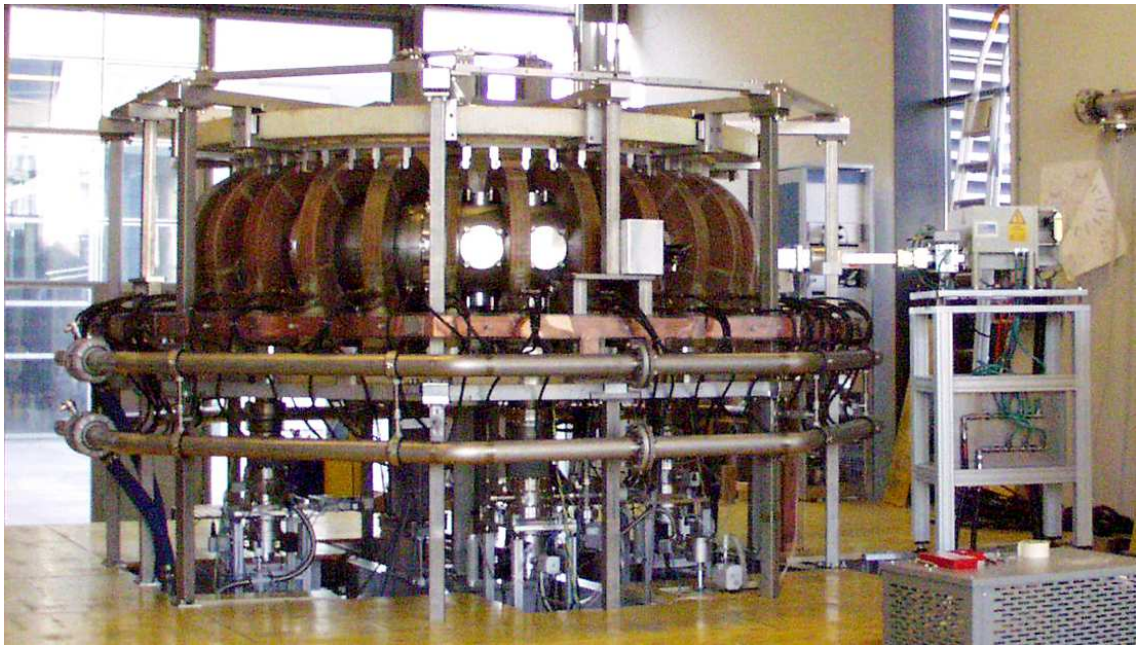

Figure 2.6: The TORPEX device. The microwave source is visible at right side of the picture.

Chapter 3

TORPEX diagnostics

Most of the experimental data from TORPEX are obtained by means of electrostatic Langmuir probes (LPs), designed and constructed by members of the TORPEX team in collaboration with the CRPP technical staff. The criteria which lead to a particular probe design are usually based on different needs and constraints, which span from physics to mechanics and electronics. These criteria and the solutions adopted on TORPEX are discussed in Sec. 3.1.
For practical convenience, multiple mechanical systems allowing a remote control of the probe position have been developed. The different solutions adopted so far are presented in Sec. 3.2.
All the experimental signals from the probes are usually pre-treated by dedicated electronic modules, then stored in a MDSplus[1] database. The architecture of the TORPEX database is discussed in Section 3.3. The acquired data requires specific analyses to extract the physical information. A set of routines have been developed in the Matlab environment for processing semi-automatically large amounts of data.
The different probes and their capabilities in terms of spatial resolution and frequency response are presented in Sec. 3.4. The names with which each probe is referred to throughout this Thesis are also introduced. An overview of the diagnostics layout, indicating the toroidal position of the probes, is shown in Fig. 3.5.

[1]Websites: *http://www.mdsplus.org* and *http://www.psfc.mit.edu/mdsplus.*

3.1 Probe design and construction

The main needs for the development of specific diagnostics for the TORPEX experiments are dictated by the general goals of the experiment. These include a systematic study of the instabilities which are potentially important for particle and heat transport across the magnetic field. The first requirement is to have a complete characterisation of the plasma in terms of the average profiles of density, temperature and potential. Second, one needs to characterise the instabilities which possibly develop on top of the average profiles in terms of frequency and wave-number spectra, and of their spatio-temporal patterns.
At the beginning of the TORPEX experimental activity, little information was available on the shape of the profiles, hence on the typical scale lengths for profiles variations, and on the properties of the unstable waves. Based on the results obtained in similar experiments [91][98], indicating for example typical gradient lengths $\sim 1-5$cm and fluctuation frequencies ≤ 10kHz, it was decided to install a first set of probes, including:

- A L-shaped array of 8 tips spaced by 1.8cm (SLP), used to measure the time-averaged plasma profiles. It was movable radially across the poloidal cross section and rotatable around its axis.
- A set of fixed probes, used to monitor the homogeneity of the plasma density at different toroidal positions.
- Three fixed arrays with 22 AC-coupled pins each (FLP), used to investigate the properties of the plasma fluctuations at ≈ 4cm from the edge.

The probes were made up of stainless-steel pins[2], encased in a ceramic holder. Particular attention was paid in the choice of the cables for the FLP array, in order to avoid noise pick-up and cross-talk between different pins, and to provide a large bandwidth. For that reason, the probe was built from Thermocoax, shielded cables. The associated electronics was characterised by a bandwidth ≤ 200kHz, with a flat frequency response up to ~ 120kHz. The signals were acquired at 250kSamples/s.
The results of the first experimental campaigns added more precise information on the spatial plasma profiles and on the fluctuations properties (Chap. 7), hence better defined requirements and constraints. The resulting guidelines for the different aspects involved in the probe construction and design, used for the 'second generation' of diagnostics, are listed below.

[2]Tungsten is commonly used for Langmuir probe tips, due to its good thermal resistance and high energy threshold for secondary electron emission. However, it is difficult to machine because of its fragility. A comparison between results obtained from probes with tungsten and stainless-steel tips has been carried out. For the stainless-steel tips there was no evidence of negative effects, such as secondary electron emission, for the low electron temperature characterising TORPEX plasmas.

- *Probe geometry* - To obtain as much information as possible on the spatial dependence of specific plasma parameters, one may wish to *maximise* the number of pins for each probe and cover a large portion of the plasma. By doing that, perturbations are introduced into the plasma because (i) probes are solid objects, representing a physical obstacle for the plasma, and (ii) they may drive a current, implying that charged particles are removed from the plasma altering its 'natural' charge balance. In this sense, the number of probes should be *minimised* and the coverage of the whole plasma region achieved by alternative methods. For example, small probes installed on a mechanical system which allows a 2-D movement inside the plasma are preferable. This concept led us to design probes such as SLP, TWEEDY and TRIP (Sec. 3.4).
  There are, however, cases for which a simultaneous coverage of an extended region is needed, e.g. to perform a spatio-temporal reconstruction of the dynamics of plasma 'structures' (Sec. 8.6). An example is provided by the HEXTIP probe. In this case the perturbations are minimised by reducing as much as possible the size of the probe tips and holders.

- *Contamination of the plasma* - During a plasma discharge, the probe electrode and its holder are subject to electron fluxes. Materials can heat up, especially in long discharges, and release impurities which alter the properties of the plasma. In addition, metallic electrodes hit by energetic electrons are subject to secondary electron emission, which can modify considerably the probe response. The choice of the probe materials is important to limit these negative effects. Ceramics, glass, tungsten should be preferred to softer materials, e.g. Teflon, PVC and other plastics. The latter are easier to machine, but more prone to releasing impurities, melting and outgassing. For the same reason, glues should be substituted by 'liquid ceramic' and a special tin, containing silver instead of lead, used for soldering.

- *Vacuum interfaces* - Vacuum-tight electrical feed-throughs are used to bring the probe signals out from inside the vacuum chamber to the electronics and acquisition. For movable probes, there exist also mechanical interfaces between the vacuum and the laboratory, at atmospheric pressure. In most cases, plastic O-rings are used. The number of feed-throughs should be minimised, for example by grouping together in a single multi-pin connector all the signals coming from a specific diagnostic.

- *Cables and electrical connections* - A single cable, without intermediate connections inside the vacuum, should be used to connect the probe tip to the feed-through. The cable type and size depend on the signal nature and amplitude. For small signals, and in general when a broad bandwidth is desired,

the cable should also include a screening jacket[3] to avoid electromagnetic interferences. The practical disadvantage of screened cables is that their typical bending radius is large, and can not be used for complicated probe geometries requiring, for example, a 90° bending over a few millimeters.

- *Electronics for signal processing and optimisation of the signal-to-noise ratio* - Probe signals are usually sent to an electronic module, which provides amplification and filtering in the required bandwidth. The amplification factors and the bandwidth must match the requirements of the acquisition boards, which ultimately collect the measured signals.
  In general, the amplitude of the probe signal depends on the plasma parameters and on the probe size. For example, the ion saturation current drawn by a probe is approximately given by $1/2\, q n_e A_{pr}\, (T_e/m_i)^{1/2}$, where q is the electron charge, n_e and T_e the electron density and temperature, A_{pr} the tip area and m_i the ion mass [47]. By imposing a lower limit on the measured current for the expected plasma parameters, one can easily derive a minimum value for the tip area. For TORPEX plasmas, assuming $n_e \sim 10^{16}\mathrm{m}^{-3}$ and $T_e \sim 5\mathrm{eV}$, it must be $A_{pr} \geq 6\mathrm{mm}^2$ to have a current $\geq 100\mu\mathrm{A}$.

- *Standardization and ease of repairing/replacing* - The use of standard components facilitates the design, installation and operations of the probes. For example, the same layout for the mechanical support of the probes is used on TORPEX for almost all the 'movable' probes. This allows us to move the same probe to different toroidal ports adopting the same flange type, or to install it on a remotely-controlled positioning system (Sec. 3.2) without unmounting it.

- *Microwave compatibility* - The use of microwaves with wavelength in vacuum of 12cm for the plasma production implies stringent constraints on the choice of the materials and on the design of the probe components. Microwaves can interact with metallic objects that are not conveniently grounded. Right angles of the probe cables should be avoided, because they represent a high impedance for the microwaves, leading to the formation of standing waves on the cables. In addition, microwaves can be partly absorbed by plastic materials, which can melt and release impurities into the plasma. Examples of damages caused by microwaves, collected during the first years of operation of TORPEX, are presented at the end of Sec. 3.4.

[3]Cables of this type are the 'Thermocoax' cables: *http://www.thermocoax.com/*

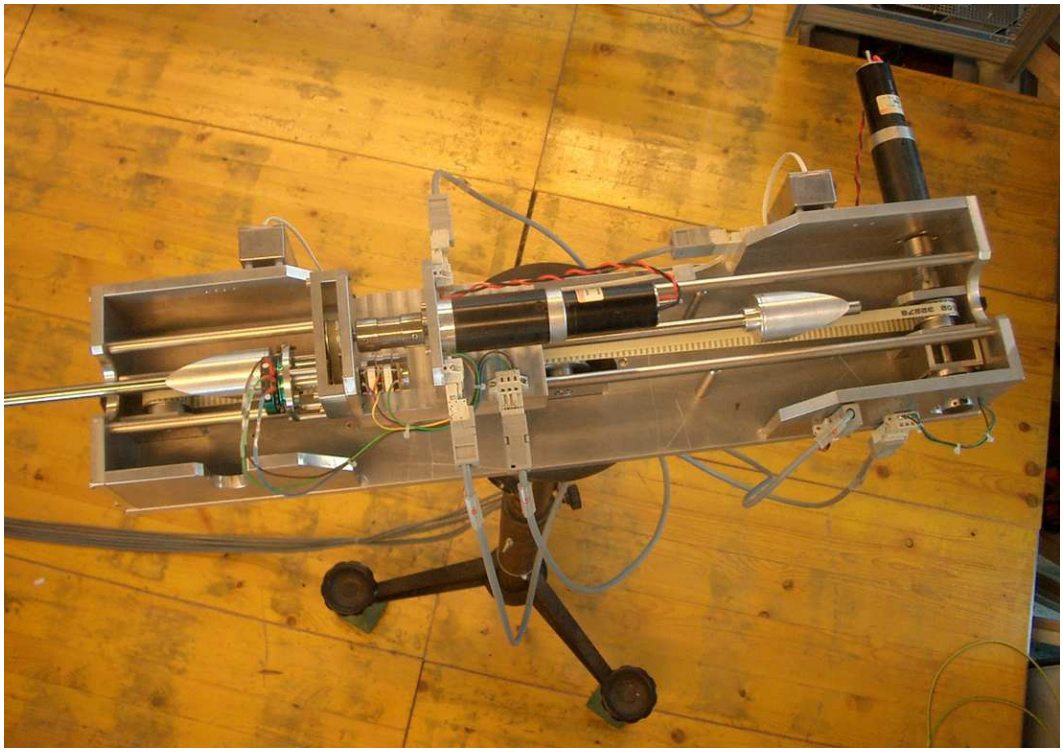

Figure 3.1: First generation of mechanical systems for the remote control of the probes position.

3.2 Probe positioning system

Some of the probes are installed on remotely-controlled movable systems, in order to adjust their position shot by shot from the TORPEX control room with high accuracy and reproducibility. A dedicated field in the TORPEX control graphical user interface allows the operator to adjust the position of each system before a discharge.
Three identical systems have been developed for the probes which are more often moved during a session, namely SLP, TWEEDY and TRIP. The system consists in a movable carriage, to which the probe arm is fixed through a rotating gear. The position of the carriage and the rotation angle of the gear, hence that of the probe, are controlled through stepping motors with an accuracy of $\pm$2mm and $\pm3^\circ$. The position and angle are measured via potentiometers before each discharge and their values stored in the database. Optical detectors are used to stop the probe movements before the maximum allowed range for radial displacement and rotation is exceeded.
Measurements over the poloidal cross section are possible with a convenient design of the probe. The movement of small probes consisting of closely-spaced tips, such

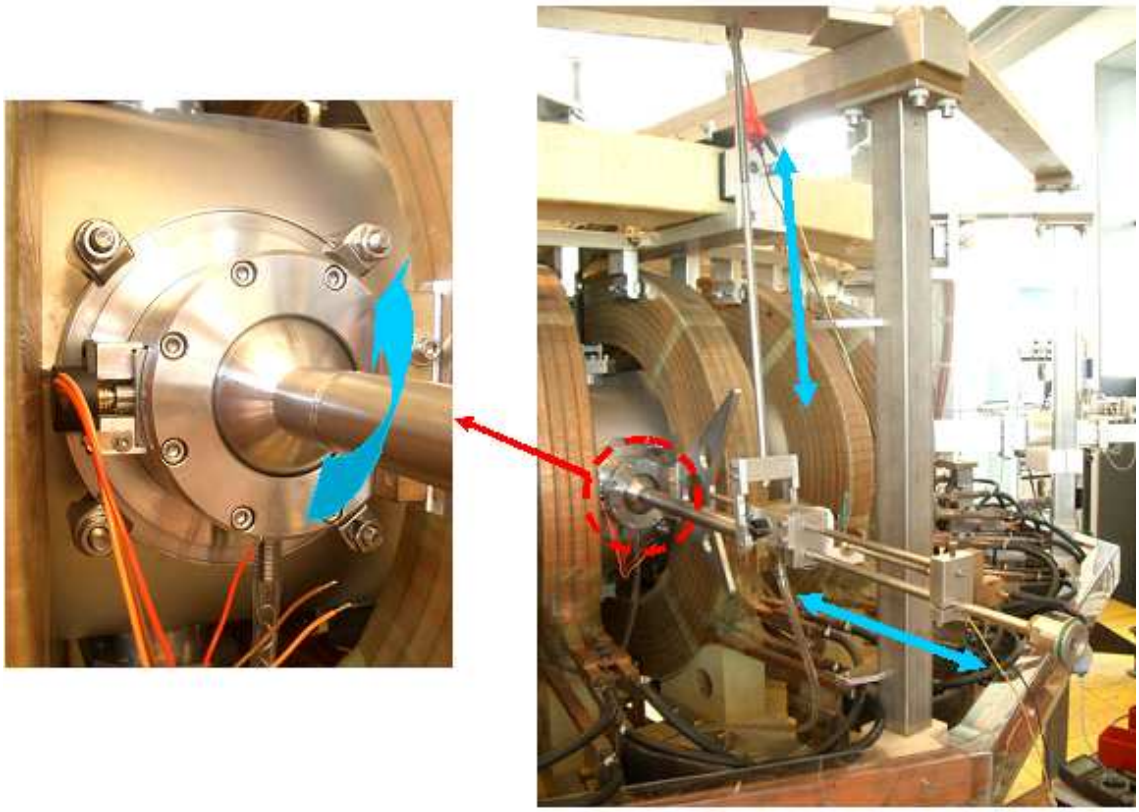

Figure 3.2: Second generation of mechanical systems for the remote control of the probes position.

as TRIP, is however limited to a chord at the midplane. A new design has been proposed to overcome this limitation, and a prototype is presently at work . The new system is presented in Fig. 3.2. The probe shaft slides inside a spherical joint, and the probe mounted on it (in this case a Rogowski coil, not used in this Thesis work) can span the whole cross section. The first and the second generation systems are controlled by the same electronic slave unit, connected to the control room through the BitBus (see Sec. 3.3).

3.3 Architecture of the data acquisition and network system

A simplified view of the architecture of the TORPEX data acquisition and network system[4] is shown in Fig. 3.3. The general principles are similar to those adopted for

[4]The development of the acquisition system and its integration with the MDSplus database has been followed by S. H. Müller, M. McGrath and X. Lobet. The Java GUI has been developed by

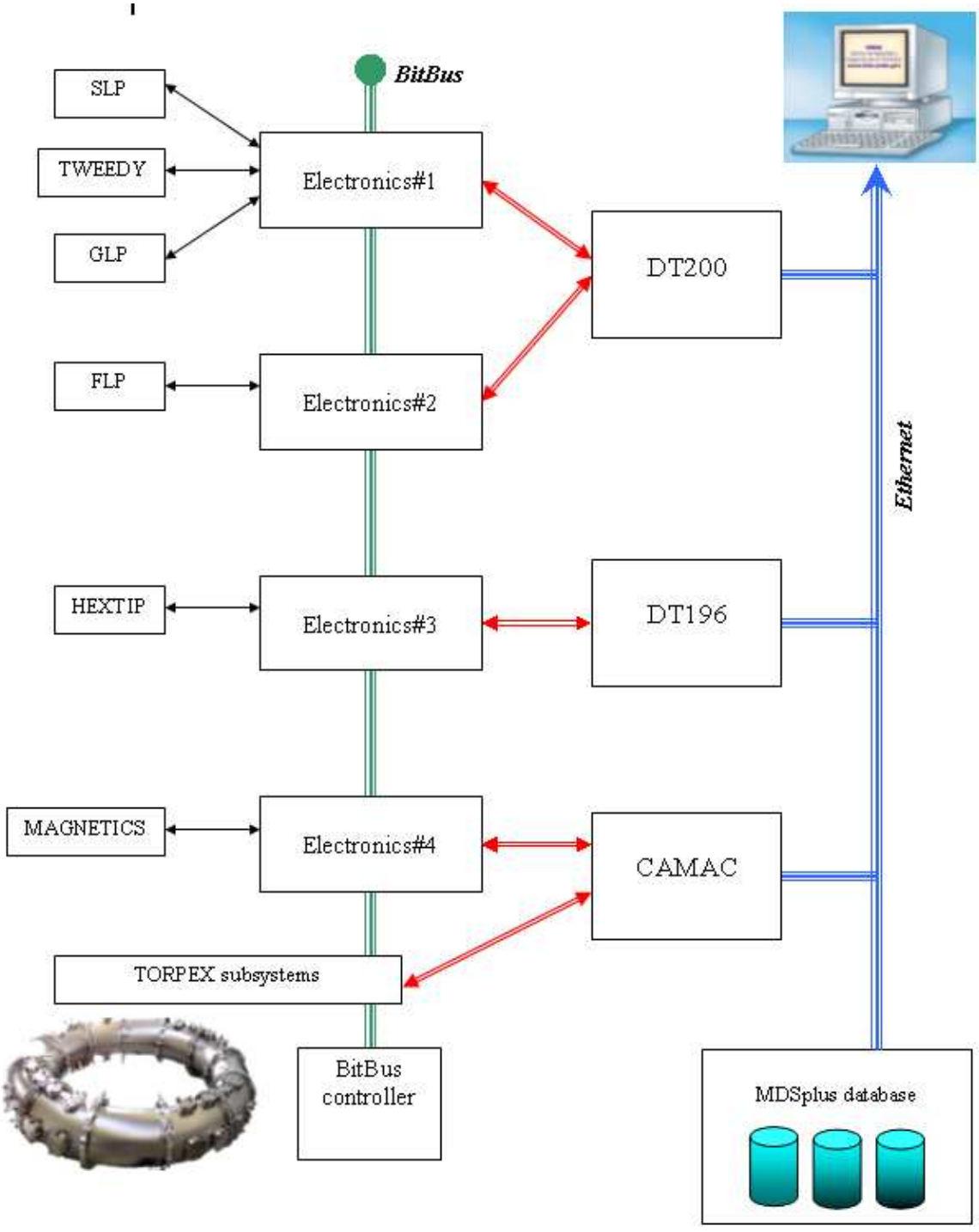

Figure 3.3: Schematic of the TORPEX acquisition and signal networking system.

the TCV tokamak [60].
Each probe, or set of probes, is connected to a dedicated electronic module from which the raw signals are sent to the acquisition. The acquisition systems are connected to an Ethernet link, allowing to download the data into the MDSplus database (see below). Each module represents a node of a 'bus', based on the BitBus protocol[5], which manages the flow of information from and to the different TORPEX subsystems. Through the BitBus it is possible to set remotely the bias voltage applied to some of the probes and the sensitivity of the current measurement. More details on the TORPEX acquisition system, including its possible upgrades, are found in Ref. [67].

3.3.1 Electronics

An electronic module for Langmuir probes has essentially two functions: (i) to provide the bias voltage required for a particular type of measurement, fixed or sweeping, and (ii) to perform specific operations on the measured signals, for example amplification and/or filtering. The bandwidth of the electronics is usually limited to below 125kHz, representing the Nyqvist frequency for most of the TORPEX acquisition systems (see below). A copper grounding plate, underlying the TORPEX experimental zone, provides a well defined, common ground to all the signals and electronics modules. A particular care must be spent when connecting elements located at different positions, mostly to avoid ground loops which can perturb the measurements. Signals from the probes as low as a few tens of millivolts can be detected, which corresponds to measurable densities, or density fluctuations, in the range 10^{15} to $10^{18}\mathrm{m}^{-3}$ and electron temperatures from ≈ 0.5 up to 50eV.

3.3.2 Data acquisition and data storage

The TORPEX data acquisition system consists of three groups, depending on the acquisition frequency:

- *Slow acquisition* - This system is based on CAMAC modules, with a maximum acquisition frequency of 10kSamples/s. It is commonly used to acquire the signals indicating the status of different technical elements, such as power supplies and constant voltage sources.

- *Fast acquisition* - At present, it consists of two D-TACQ digitizers[6] with 96 channel each, running up to 250kSamples/s. They are indicated as DT200 and DT196 (Fig. 3.3). On these modules are acquired most of the signals

M. Helletzgruber (Helletzgruber IT Solutions & Consulting).

[5]Website: *http://www.bitbus.org*

[6]Website: *http://www.d-tacq.com*

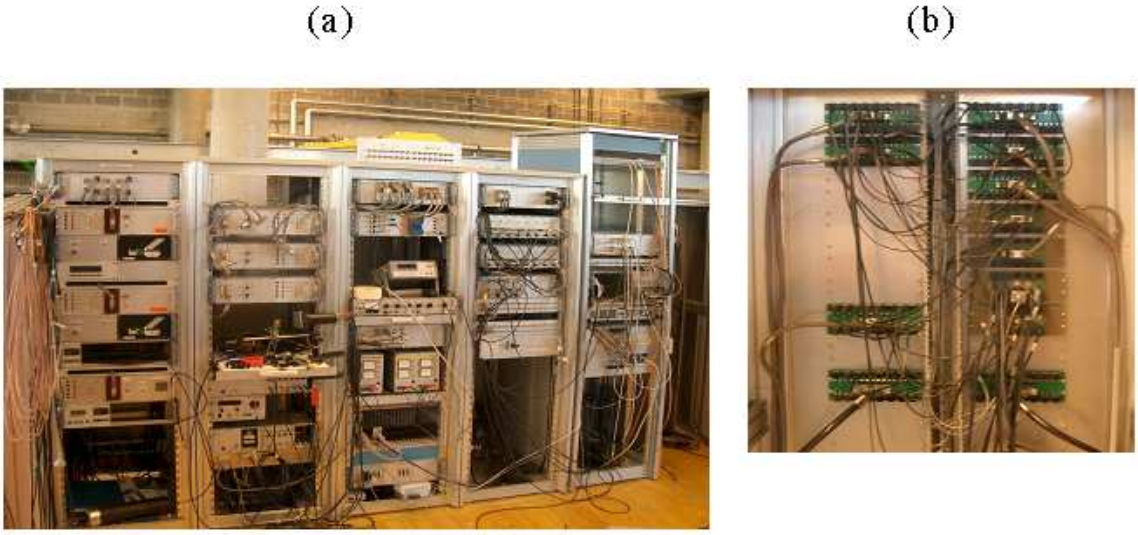

Figure 3.4: *(a)* Racks collecting the electronics modules. *(b)* Detail of the patch-panel, allowing one to connect a probe to a specific acquisition system.

coming from the different probes. The maximum frequency has been chosen on the basis of the typical time-scales of the phenomena observed in TORPEX plasmas (cfr. Chap. 7), which are usually below 10kHz.

- *Ultra-fast acquisition* - Two CAMAC-TRCF boards with 4 channels each are installed, with a maximum acquisition frequency of 10MSamples/s. So far, they have been mainly used for test purposes, for example to verify that no plasma fluctuations are present outside the frequency range covered by the D-TACQ modules.

After a discharge, the data is downloaded into the TORPEX database, based on a MDSplus architecture. Data from each discharge are organised into a tree-like structure, divided into sub-trees where control signals, raw signals from the probes and post-analysis results are stored. The database is accessible via a TDI[7] interface from standard data analysis languages, e.g. Matlab.

[7]Website: *http://www.mdsplus.org/tdi*

3.4 Overview of the diagnostics

In the following paragraphs, I describe the probes which are currently used on TORPEX. An overview is presented in Fig. 3.5, in which the toroidal position and the acronym of each probe are indicated. The probes data are analysed using standard techniques, which are shortly summarised in Appendix B. A complete description of the operation regimes of Langmuir probes and of the corresponding analysis techniques is found in Refs. [47][97][17] and [87].

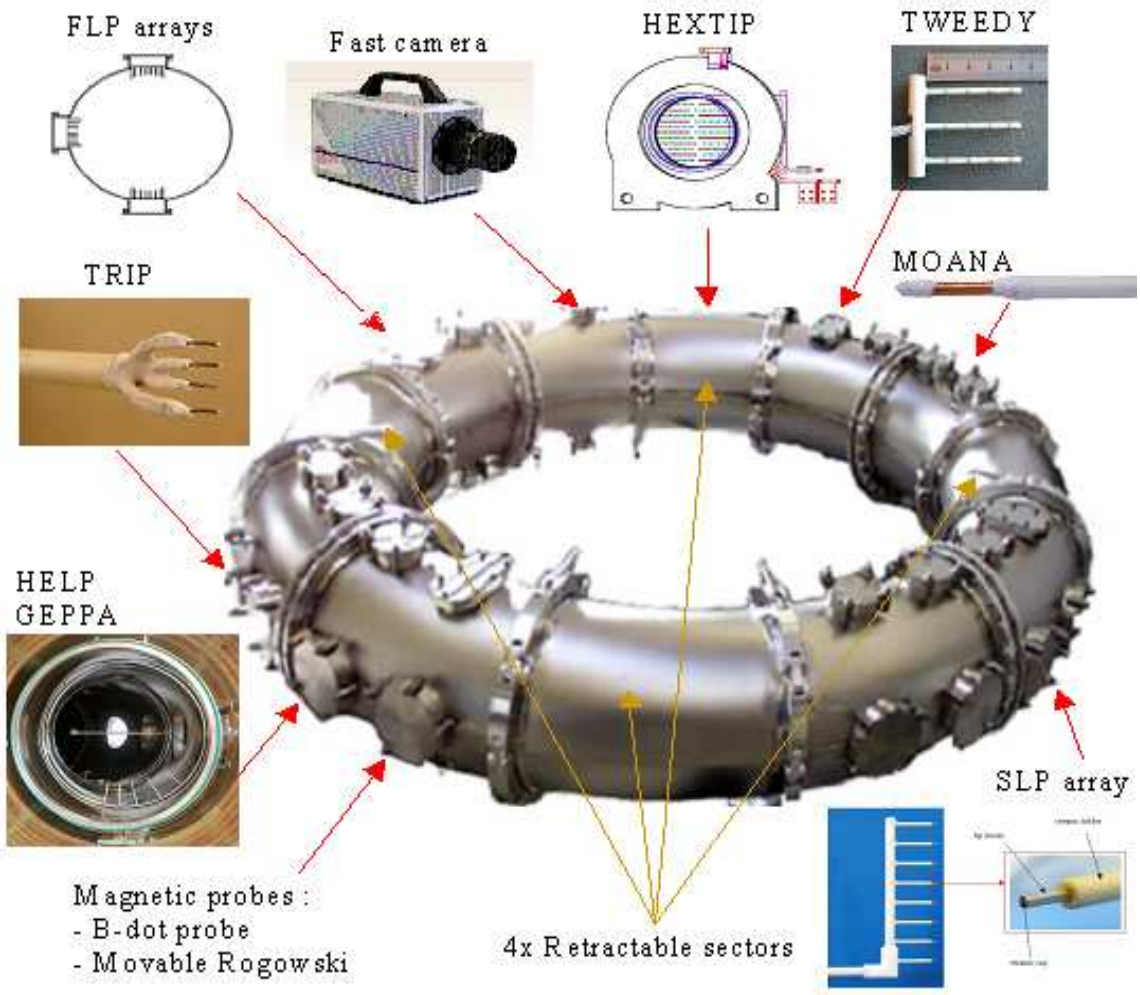

Figure 3.5: Overview of the main diagnostics installed on TORPEX.

SLP - Slow Langmuir Probe

It consists of 8 cylindrical pins, mounted in a comb-like structure and vertically separated by 1.8cm. SLP can be moved radially in the range $-14\text{cm} < r < 14\text{cm}$, and turned around its axis with an arbitrary angle. SLP is mainly used to measure density, electron temperature and plasma potential profiles over the poloidal cross-section. In conjunction with other probes, installed at different toroidal position, it is used to measure the parallel wave-number of plasma fluctuations [80]. When used in the swept voltage mode, the maximum time resolution is $\approx 500\mu$s.

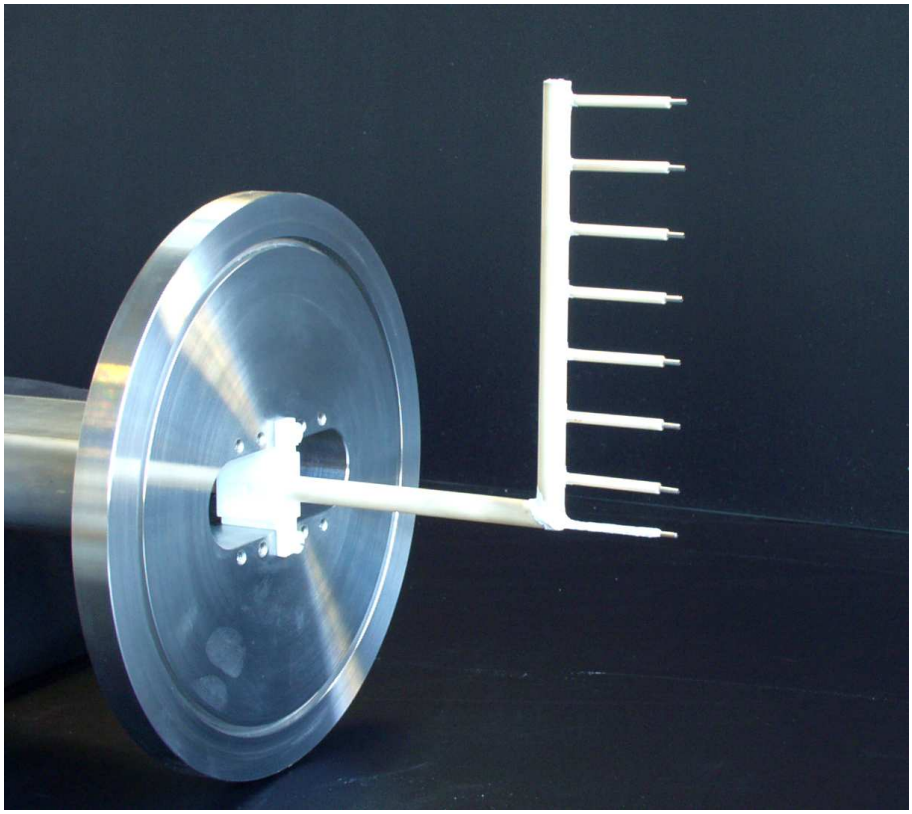

Figure 3.6: SLP

FLP - Fast Langmuir Probe

It consists of 3 arrays of 11 pin pairs each, located at the top, bottom and midplane (on the low-field side) at fixed positions. The distance between tips in the same pair is 1mm, and the pairs are spaced by 8mm. The probe has been designed to measure plasma fluctuations in the edge region [80]. Due to the AC (capacitive) coupling, only the fluctuating part of the signals is measured by a dedicated electronic module, with the advantage of a broader bandwidth with respect to the other probes.

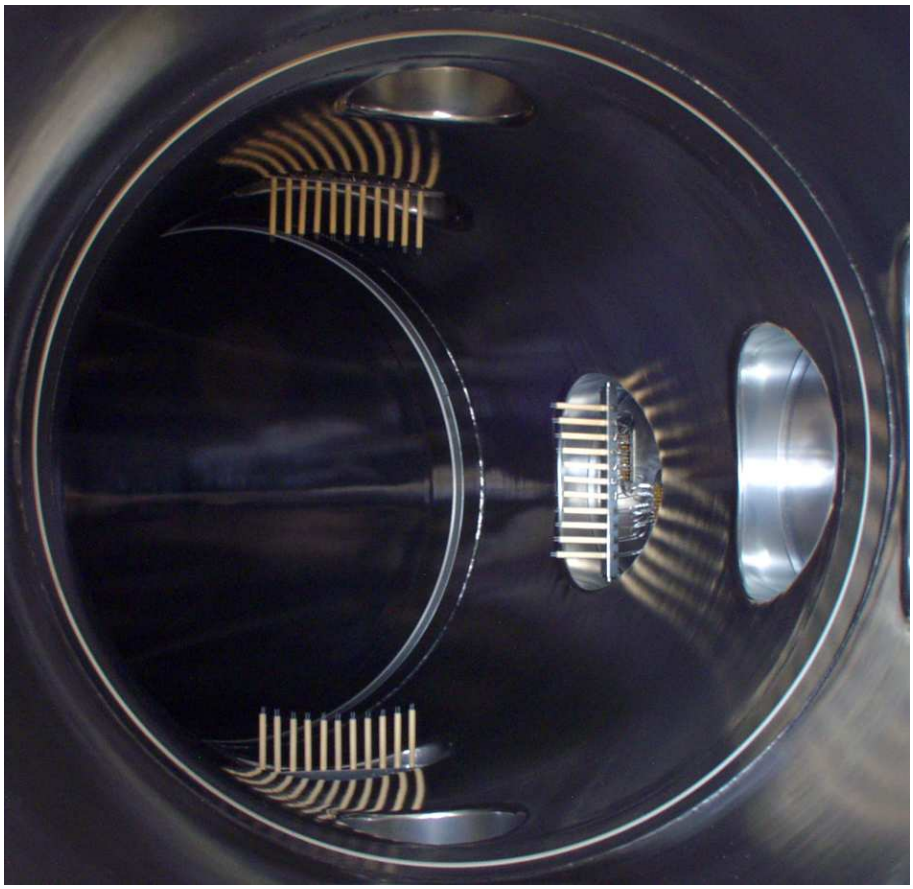

Figure 3.7: FLP

GLP - Gradient Langmuir Probe

GLP includes 8 pins mounted at different positions along the minor radius, with a relative spacing varying between 0.5cm and 1cm. It is fixed, installed on a horizontal port. GLP is used to measure the gradients of the plasma parameters along the radial direction around the position $r = 16$cm, at which FLP is measuring. The pins are made by thin rings wounded around the ceramic support. The same design, successfully tested first with GLP, was used later on as basis for the design of the HEXTIP and TWEEDY probes.

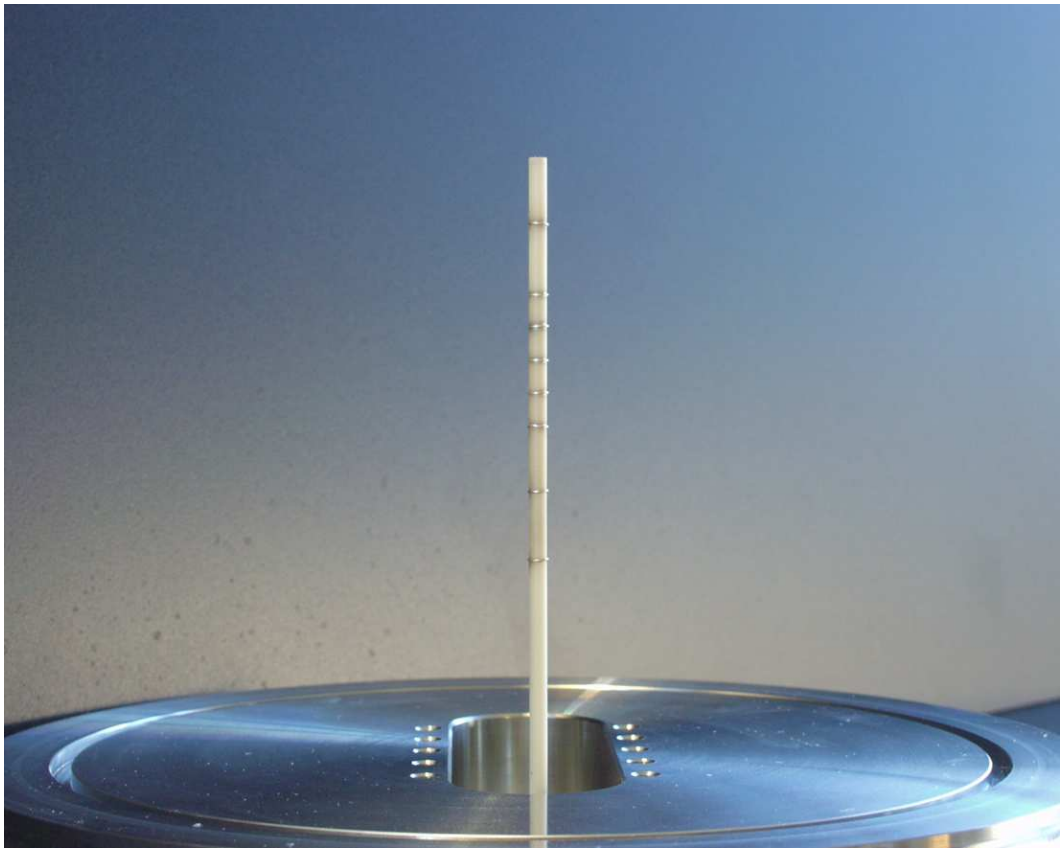

Figure 3.8: GLP

TWEEDY - Two-Dimensional probe

It consists of a 4×3 matrix of Langmuir probes, separated by 1cm radially and 1.8cm vertically. It is used for local, two-dimensional measurements of plasma profiles and fluctuations. The pins have the same geometry as the GLP probe. It can be moved radially in the range $-19\text{cm} < r < 19\text{cm}$ at the midplane, and turned around its axis.

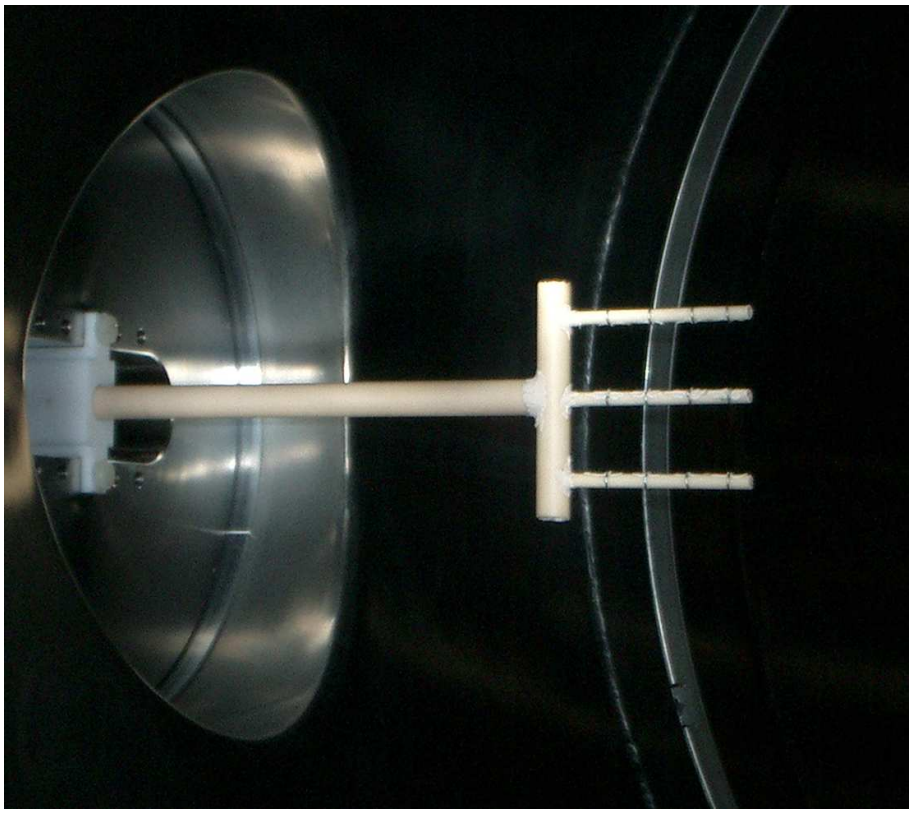

Figure 3.9: TWEEDY.

MOANA - Monogrid Omnidirectional ANAlyser

It is a simple gridded analyser, made by a single copper grid wrapped around a tungsten electrode. The grid is used to select only one class of particles, i.e. ions or electrons, that are collected on the electrode. The particle energy distribution function is calculated from the derivative of the measured ion or electron current as a function of the sweep voltage applied to the collector [47]. The response of the cylindrical probe head is insensitive to the orientation with respect to the magnetic field. More details on MOANA and on the experimental results obtained from it are presented in Chap. 6.

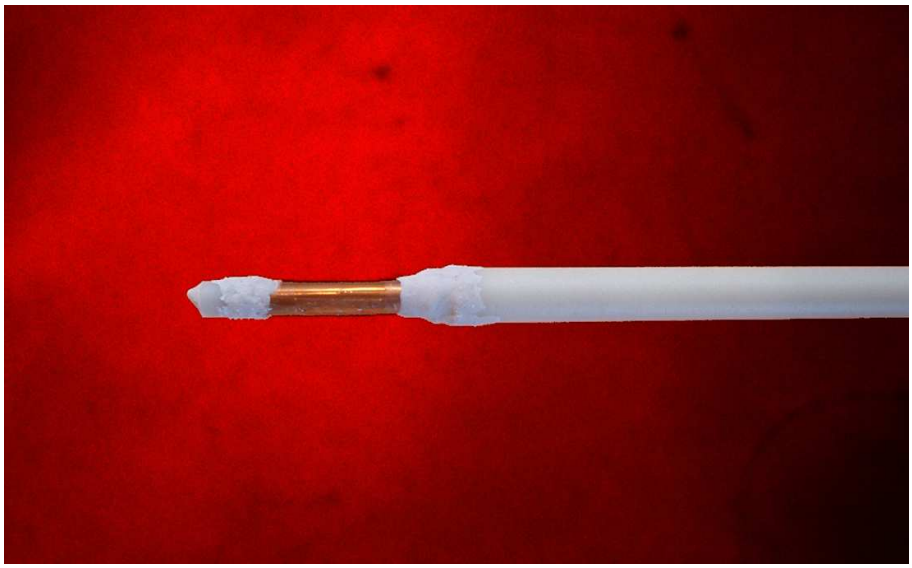

Figure 3.10: MOANA

GEA - Gridded Energy Analyser

The GEA probe, developed in collaboration with P. Weber and K. Schombourg [110][96], was initially intended to provide information on the ion and electron distribution function. The initial design includes four grids and the collector electrode, enclosed in a Macor box (Fig. 3.11a-b). A small Langmuir probe monitors the plasma parameters at the entrance of the first grid.
Several problems are identified during the tests, making the interpretation of the data difficult. The presence of four grids reduces the total transmission factor to $\leq 1\%$, resulting in a signal-to-noise ratio below unit for ion distribution function measurements. Along with the high level of density and, possibly, plasma potential fluctuations, this makes the measurements of the ion temperature practically impossible. For electron distribution function measurements, the low transmission factor makes it preferable to use simpler energy analysers, such as MOANA, instead of the GEA.

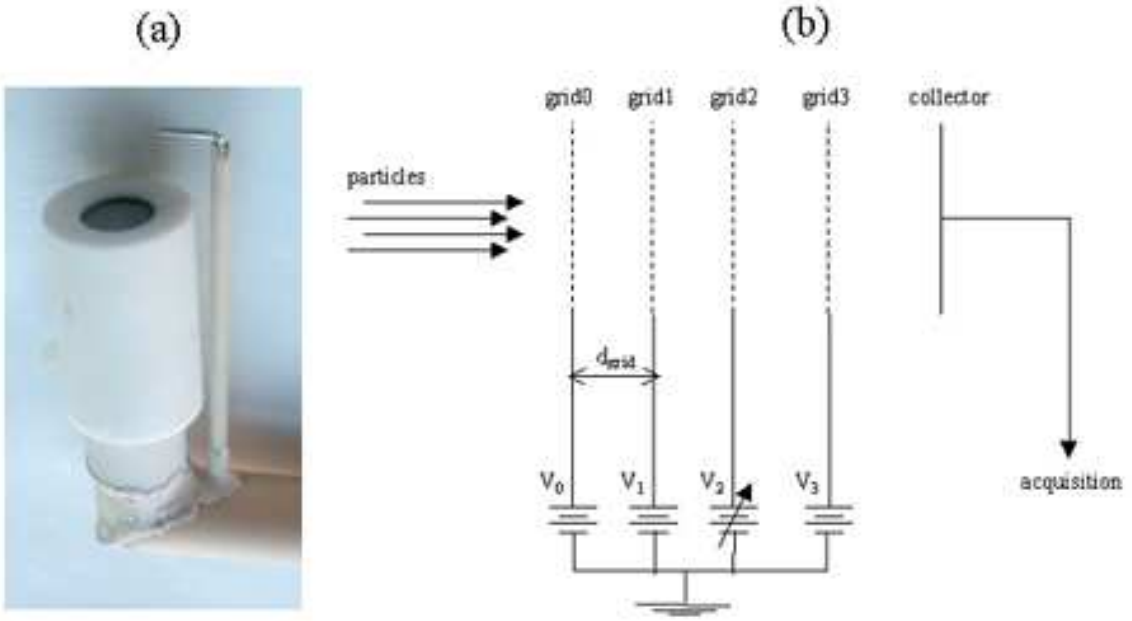

Figure 3.11: *Left:* The GEA operating on TORPEX. *Right:* principles of the original four-grid design.

HELP - Halo Edge Langmuir Probe

It consists of 25 pins that form a crown - or *halo* - in the poloidal cross-section. The distance of the pins from the walls varies between 2cm and 3.5cm to fit the hexagonal grid of the HEXTIP probe. The probe may provide boundary conditions for plasma parameters, for example to extrapolate the density profiles measured by HEXTIP to the whole poloidal section.

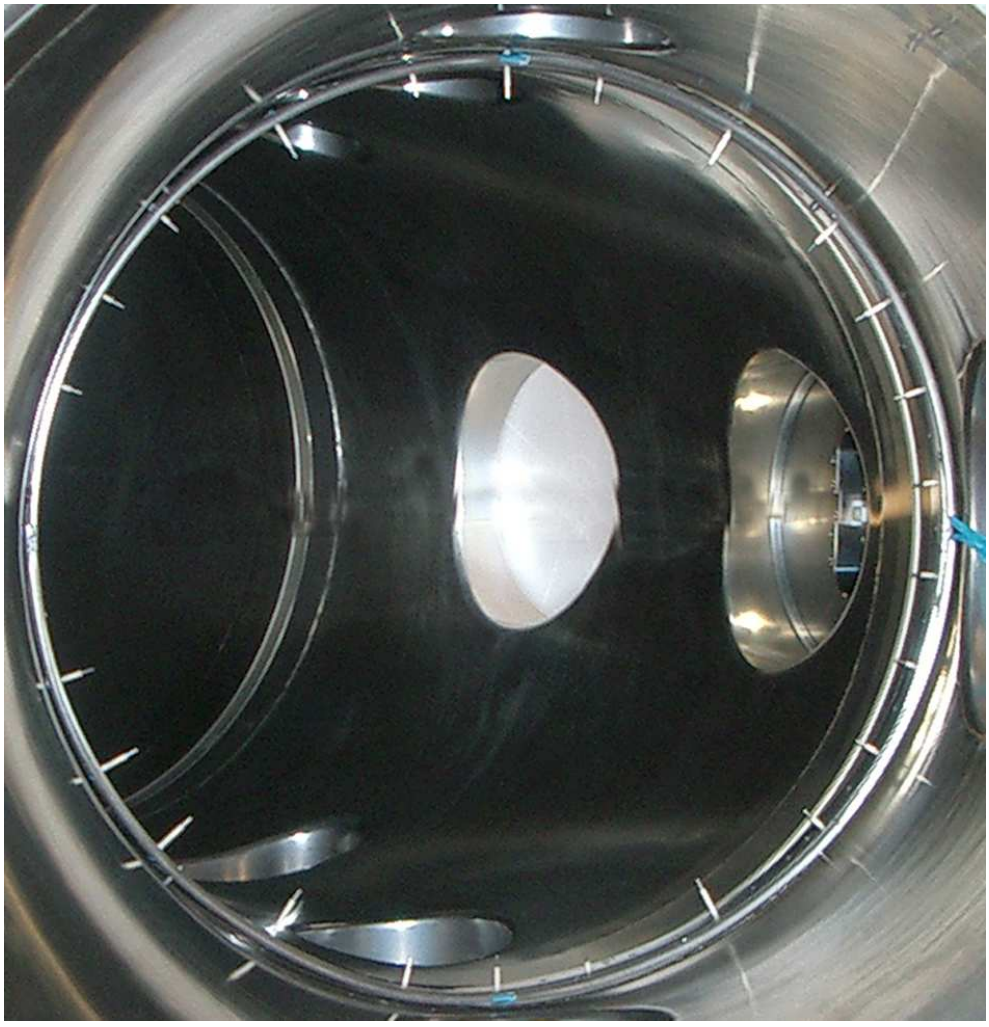

Figure 3.12: HELP

GEPPA - Gradients and Edge Parameters Probe Array

This probe is dedicated to measurements of gradients at the edge in the region from which most of the observed plasma instabilities originate. The spatial resolution is $\approx$ 1cm in the radial direction.

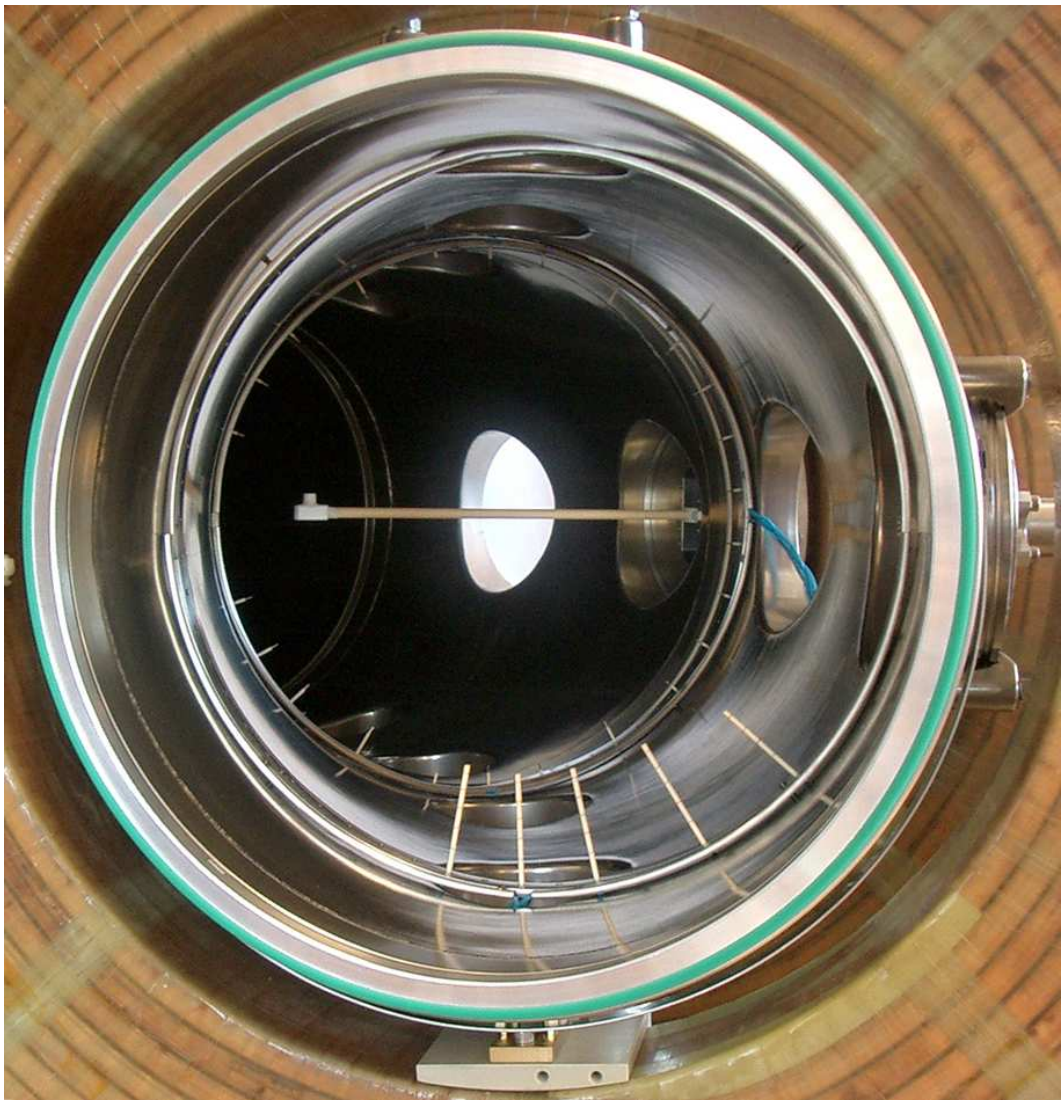

Figure 3.13: GEPPA

TRIP - TRansport Probe

Also referred to as 'flux' probe, this probe is dedicated to measurements of the electron temperature fluctuations (Sec. 8.1) and of the fluctuation-induced particle flux (Sec. 8.2). It consists of four tips, aligned vertically and separated by 2mm, measuring the ion saturation current and the floating potential. It can be moved radially in the range $-9\text{cm} < r < 19\text{cm}$ on the midplane [80].

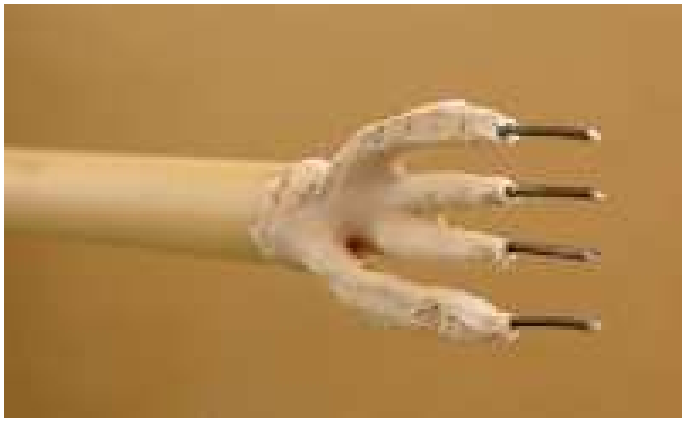

Figure 3.14: TRIP

HEXTIP - HEXagonal Turbulence Imaging Probe

HEXTIP is dedicated to the two-dimensional reconstruction of the density and floating potential signals over a poloidal cross-section. It consists of 86 tips, arranged on a hexagonal grid, with a spatial resolution is 3.5cm [67]. The bandwidth of the HEXTIP electronics is $\leq$ 20kHz.

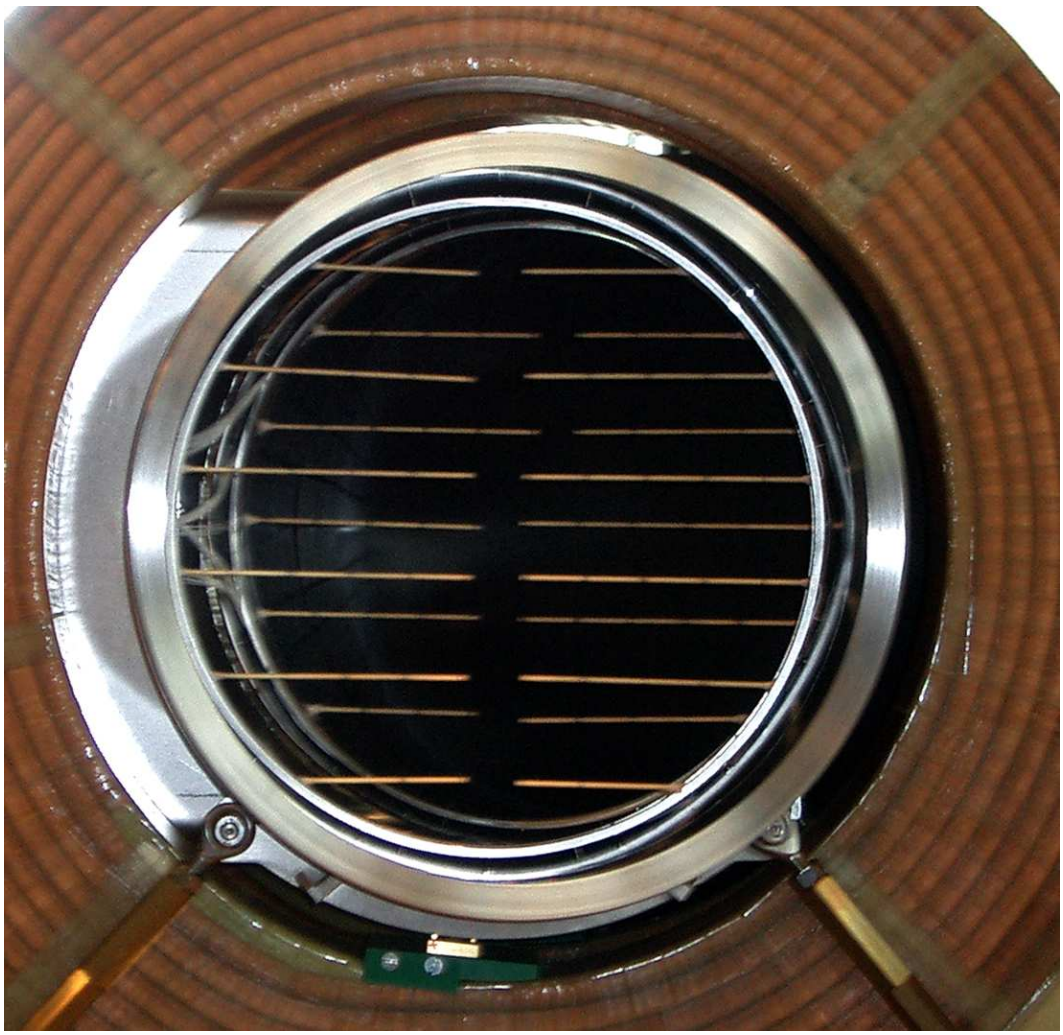

Figure 3.15: HEXTIP

Mach probes

Two Mach probes have been developed and installed, in collaboration with O. Pisaturo and C. Jan [76][51]. The Mach probe allows one to reconstruct the macroscopic plasma flows from the difference of the ion saturation current measured by tips facing two opposite directions [47]. The probe head is a cube with a circular electrode on each face, which allows one to measure the particle flows along three orthogonal directions. The two probes have different sizes, to investigate the influence of the probe dimensions on the measured flows [48].

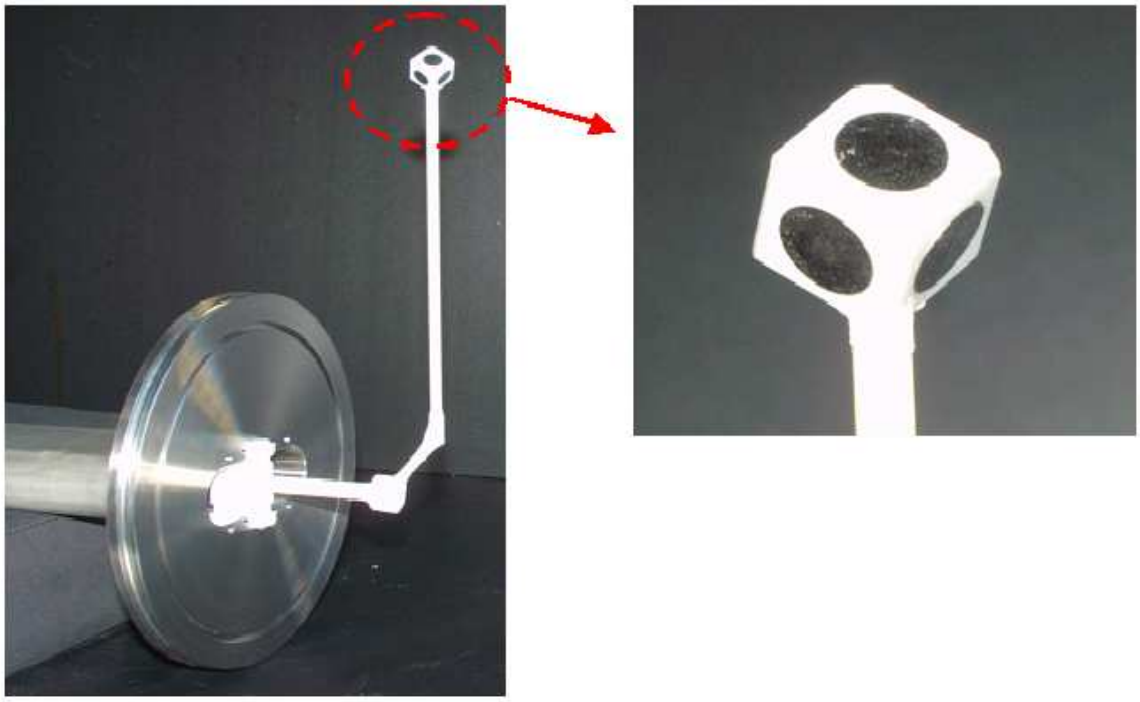

Figure 3.16: Mach probe.

Magnetic probes

TORPEX is equipped with a set of 'Ohmic' coils, which can be used to induce a toroidal loop voltage, hence a plasma current (Chap. 2). A set of fixed and movable Rogowski coils, designed and developed by G. Plyushchev, is used to measure the total plasma current and its spatial profile (Fig. 3.17a-c) [30]. The small coil for local plasma current measures has been recently installed on a 2D positioning system to reconstruct the current profile in the whole cross-section. A B-dot probe (Fig. 3.17b) is used to measure the magnetic field fluctuations [65]. The goal is to investigate the changes in the character of instabilities when a plasma current is driven and closed magnetic flux surfaces form [30].

Optical diagnostics

Different optical diagnostics are used to perform non-perturbative measurements of plasma fluctuations. For example, a small telescope insertable into the plasma can be used to collect light from a limited plasma volume of $\approx 1\text{cm}^3$ (Fig. 3.18a). The telescope is movable along a horizontal chord at the midplane [85]. It can be connected through an optical fiber to an OMA spectrometer for measuring the spectral properties of the emitted light, with a temporal resolution ≤ 50Samples/s. For fluctuations studies, the fiber is connected to an external telescope providing line-integrated measurements. Single photons can be counted using a photomultiplier tube (Fig. 3.18c). The results, presented in [8], are preparatory for the development of LIF methods on TORPEX. Line-integrated measurements have been also obtained with photodiodes looking at the plasma from horizontal or vertical ports (Fig. 3.18c), as reported in [76]. The same line of research may benefit from the use of an ultra-fast camera[8], with a speed of up to 250kFrames/s, recently purchased for a full 2-D imaging of the plasma fluctuations and turbulence [30].

[8]Photron Ultima APX-RS.

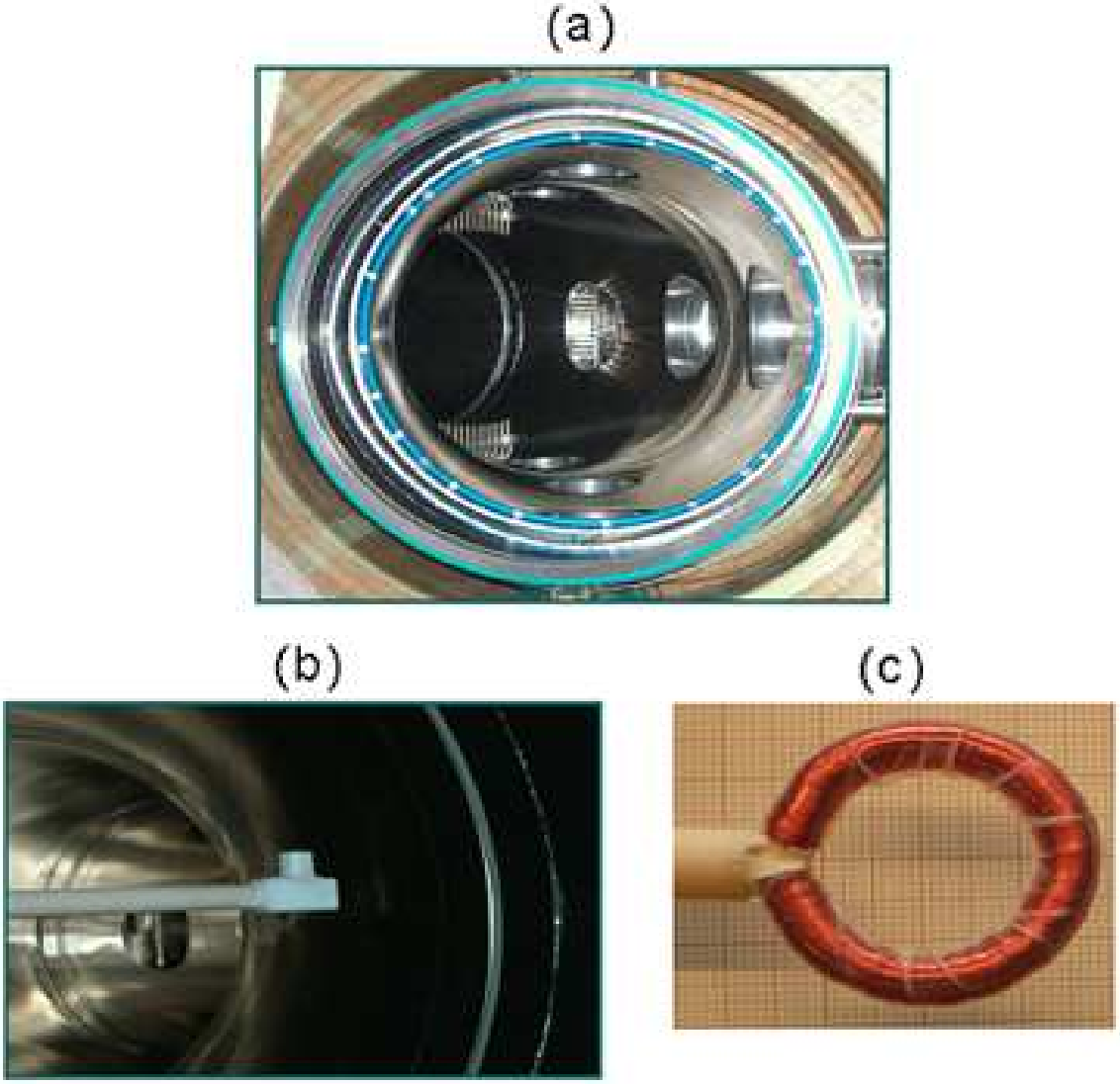

Figure 3.17: Magnetic probes installed on TORPEX: Fixed *(a)* and movable *(c)* Rogowski coil for measuring the total plasma current and its spatial profile. *(b)* Three-dimensional B-dot probe for magnetic fluctuations measurements.

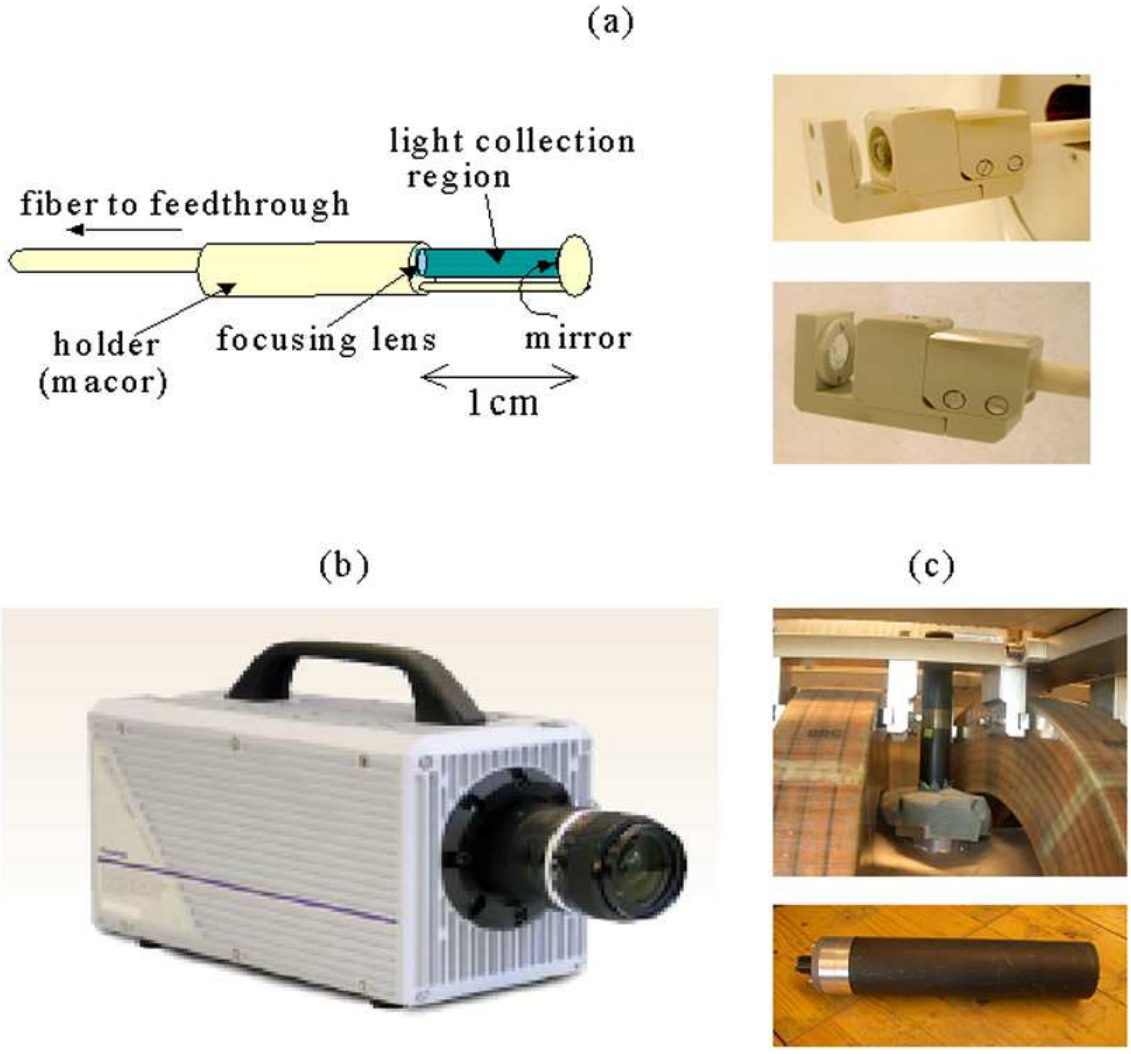

Figure 3.18: Optical diagnostics in use on TORPEX: *(a)* a small telescope for local measurements, *(b)* an ultra-fast camera and *(c)* photodiodes and photomultiplier detectors.

Proposal for a 39GHz interferometer

One of the main limitations of Langmuir probes is that they do not provide an *absolute* measurement of the plasma density. In fact, parameters as the effective collection surface and electron temperature, both known with relative accuracy, enters in the formula used to convert the measured current into density values [47]. An interferometer could provide the information required for an absolute calibration of Langmuir probes. Figure 3.19 illustrates a possible layout for a 39GHz interferometer for TORPEX. Many elements are already available, such as a 100mW Gunn-diode source, detectors, waveguide elements and power sensors. The emitting and receiving horns could be installed on existing ports, looking at the plasma along a vertical line of sight. The phase shift expected for typical TORPEX plasmas is within the measurable range, if mechanical vibrations of the machine support are limited.

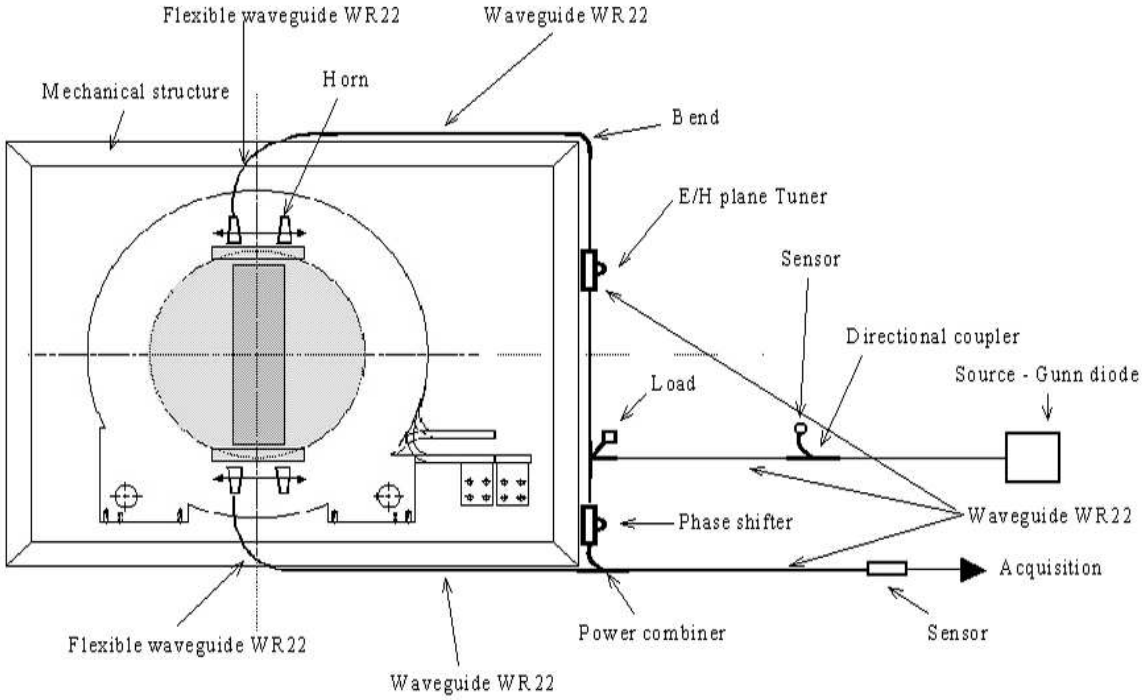

Figure 3.19: Layout of the 39GHz interferometer proposed for absolute density measurements on TORPEX.

Undesired effects of microwaves

Figure 3.20 illustrates some examples of the effect of the interaction between microwaves, probes and other metallic structures.
A prototype of the SLP probe, destroyed after a few days of operations, is shown in Fig. 3.20a. By coincidence, the probe tip length was close to a quarter of the microwave wavelength in vacuum, thus forming an efficient antenna [2]. The probe was quickly damaged, probably due to the formation of standing waves along the probe cables. A similar problem occurred to another probe with much smaller tips (Fig. 3.20b), though the reason why the probe broke is still unknown.
A different problem occurred to the telescope. The plastic case surrounding the telescope melted on one side of the box, and opaque structures formed on the mirror, reducing the light collection efficiency (Fig. 3.20c). Also note the two metallic screws, which were not electrically grounded. The presence of electrically *floating* metallic objects must be avoided.
Finally, in Fig. 3.20d it is shown a detail of a microwave quartz window installed at the end of the microwave transmission line (Fig. A.2). A small gap was present between the window gasket and the flange, where arcs occurred repeatedly with a permanent damage of the window.

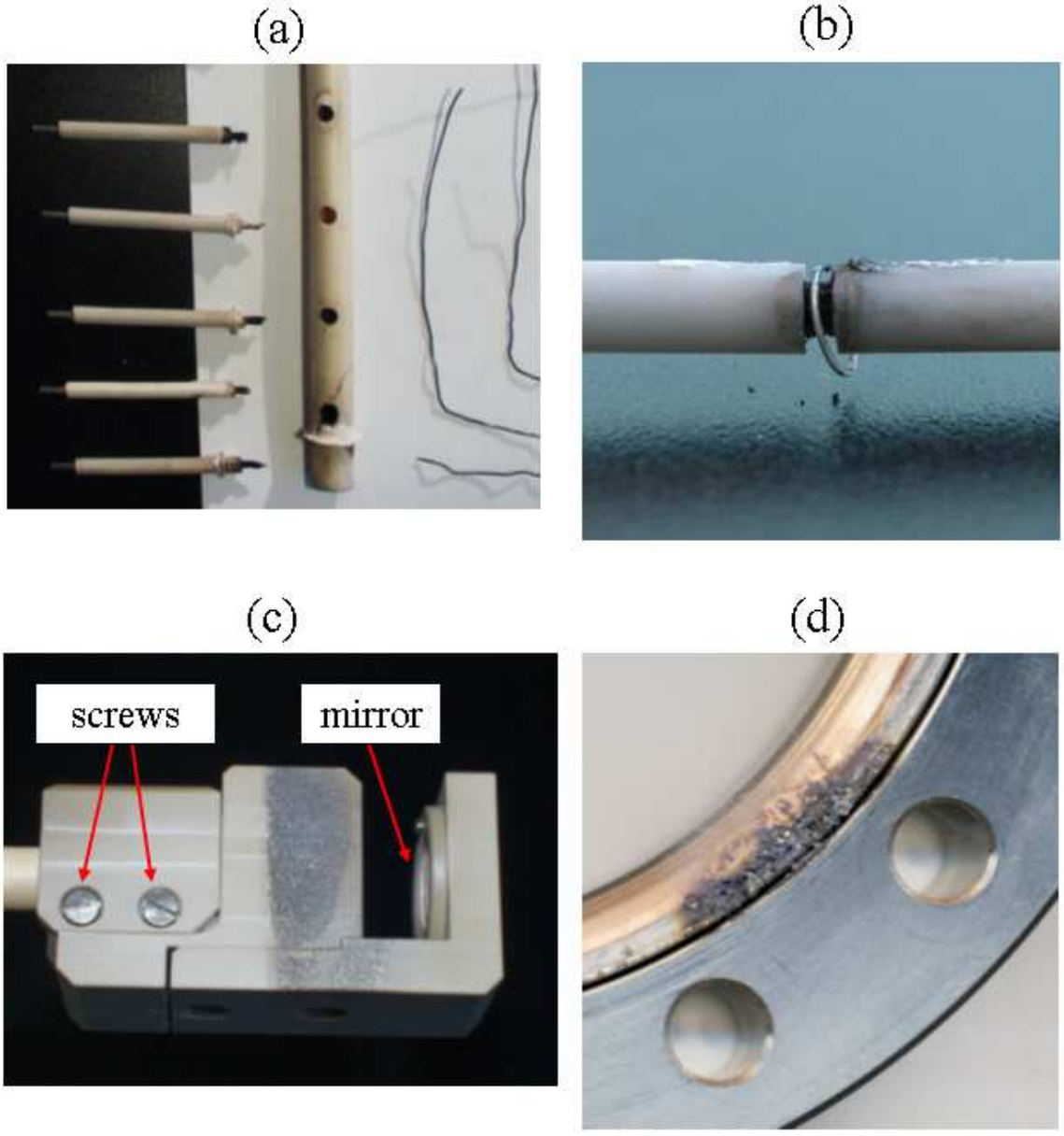

Figure 3.20: Effects of the interaction of microwaves at 2.45GHz with probes and other metallic structures.

Part II

Plasma production and properties of the time-averaged profiles

Chapter 4

Plasma production by microwaves

Plasmas generated and heated by means of waves in the electron cyclotron (EC) range of frequencies are widely used in industrial applications [36][58], in basic plasma physics studies [28][91][98] and in tokamaks (e.g. to assist the plasma startup [50][114]). A good understanding of the basic mechanisms that lead to absorption of EC waves, ionisation of the neutral gas and sustainment of the plasma is important in all these cases. A knowledge of the spatial profile and the dynamical behaviour of the particle and heat sources as a function of magnetic field, background gas pressure and EC injected power can lead to establishing the link between these control parameters and the resulting plasma characteristics. For example, the possibility of modifying the density gradient lengths is a crucial issue for the study of instabilities and turbulence [28][102][98]. For fusion plasmas, the size of the device is usually large compared to the wavelength of the injected waves. Approximations based on WKB and geometrical optics apply [101], and the main features of the propagation and absorption processes can be modelled satisfactorily [84]. This is not the case for smaller devices dedicated to basic plasma physics or industrial applications, where the typical dimensions are comparable to, or smaller than, the wavelength of the injected EC waves. Despite the widespread use of low density, low electron temperature EC plasmas, there exists little quantitative information on the ionisation processes and on the spatial distribution of the particle and heat sources.
Most of the studies in this field have focused on the use of EC waves in industrial applications [36][58]. Only a few studies exist for configurations, such as the one exploited in TORPEX, in which plasmas are confined in a toroidal vacuum chamber by a mainly toroidal magnetic field, often referred to as *simple magnetised tori* [91][98]. These studies highlighted the importance of the upper hybrid (UH) resonance for the absorption of EC waves. An estimate of the obtainable plasma densities and temperatures on the basis of a power and particle balance was given [91]. However, the ionisation of the neutral gas was entirely ascribed to a thermal electron population with a given electron temperature, without a clear distinction between the background thermalised population and the suprathermal electrons resulting from a possible, localised absorption of the microwave power. No systematic study of the ionisation processes and the spatial dependence of the particle source was carried out. This topic will be extensively investigated in Chap. 5.
In this Chapter, the basic mechanisms responsible for the ionisation of the neutral gas are investigated. A method based on the modulation of the microwave source to identify the microwave power deposition locations is presented. The link between the source and external control parameters is shortly discussed, as an introduction to the next Chapter. Examples of the average plasma profiles obtained in TORPEX are given, in order to highlight the influence of the plasma production mechanisms, although a more extensive discussion on the plasma profiles is given in Chap. 7.

4.1 Basic principles of plasma production by EC waves

4.1.1 Microwave injection scheme

The microwave injection scheme adopted on TORPEX is illustrated in Fig. 4.1. Microwaves are injected from the low-field side (LFS), which provides a better accessibility to the machine for technical reasons[1]. At the output of the waveguide the waves are in the ordinary mode (O-mode) polarisation. However, a first transition from rectangular to circular cross-section, required to match the waveguide to the vacuum chamber, already contributes in changing the original polarisation [86]. As no focusing elements, viz. a microwave horn antenna [2], are present, microwaves are actually injected into the vessel with a mixed polarisation, which can be represented as a superposition of O-mode and extraordinary (X-) mode.

4.1.2 Plasma-wave interaction mechanisms

Before the beginning of the plasma discharge, only the naturally present free electrons can be accelerated at the EC resonant layer, where $f_{rf} = f_{ec}$, by single particle interaction with the microwaves injected at the frequency f_{rf}. If the energy of the accelerated electrons exceeds the ionisation potential of the neutral gas, electron impact ionisation occurs and new electron-ion pairs are created.
Once a plasma is formed, its dielectric properties determine the wave dynamics. Depending on the model describing the plasma, different kinds of resonance can be found. While in the frame of the fluid model the O-mode is not subject to any resonance, the kinetic model predicts resonant acceleration of electrons at the EC layer. However, only a fraction of the wave power is absorbed at the EC layer in the experiments reported herein, due to the small value of $k_\perp \rho_l$ [7], where ρ_l is the electron Larmor radius. The remaining fraction is reflected from the vacuum chamber walls at the high-field side (HFS), leading to a loss of the original polarisation. Both X and O-mode waves propagate back in the plasma. At the UH layer, where $f_{rf} = f_{uh} \approx (f_{ec}^2 + f_p^2)^{1/2}$, the X-mode encounters a fluid plasma resonance, the refractive index tends to infinity and the wave E-field is strongly enhanced, leading to significant particle acceleration. The details of the acceleration mechanisms are not yet completely understood [58]. Non-linear mechanisms, such as parametric instabilities excited by the injected pump wave, may play a considerable role [39][82]. Linear mode conversion into short wavelength electron Bernstein waves (EBWs) can also take place [82][114][91]. The details of the mode conversion process, of the back propagation to the HFS and of the subsequent absorption of the EBWs depend

[1]The distance between the toroidal field coils on the high-field side is too small to install a waveguide for the 2.45GHz frequency.

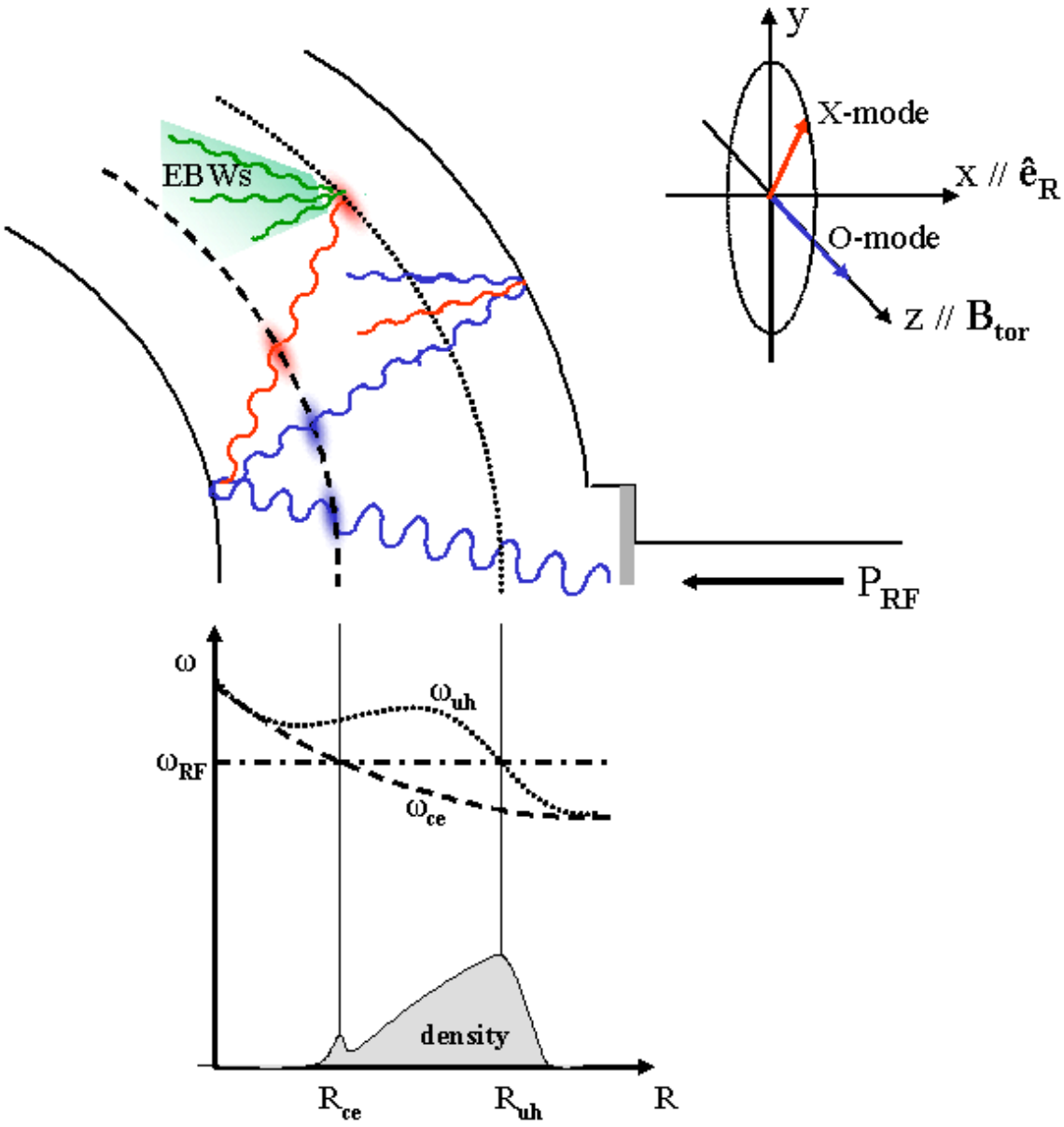

Figure 4.1: Illustration of the injection scheme adopted in TORPEX. Microwaves are injected from the low-field side (on the right of the figure) with O-mode polarisation. After multiple reflections on the vacuum chamber walls, we can consider that the original polarisation is lost.

on the plasma profiles and are beyond the scope of this Thesis.
The dependence of f_{uh} on the density through the plasma frequency f_p leads to a complication in the study of the dynamical behaviour of density, electron temperature and plasma potential (n, T_e and V_{pl}). The value of n for which $f_{rf} = f_{uh}(R)$ is

$$n_{uh}(R)[10^{17}\,\mathrm{m}^{-3}] \approx \frac{f_{rf}^2[\,\mathrm{GHz}]}{8}\left[1-\left(\frac{R_{ec}}{R}\right)^2\right] \tag{4.1}$$

where R_{ec} is the radial position of the EC resonance. If the density profile is known from the experiments, this relation allows one to estimate the position of the resonant UH layer. Equation 4.1 implies that density fluctuations reflect in fluctuations of the position of the UH layer. In our experiments we see from the measured density profile and relevant fluctuations that the UH layer spans typically a region of width $\sim$ 1cm during a period $\geq 200\mu$s. On the other hand, the time-scale that characterises the ionisation can be roughly estimated as $1/\nu_{iz} \leq 100\mu$s, where ν_{iz} is the ionisation rate. Therefore, in the following we neglect density fluctuations, as their effects are experimentally separable from those related to ionisation due to the different time-scales.

4.2 Experimental profiles

Figure 4.2 shows typical background profiles of n, T_e and V_{pl} measured in Argon and Hydrogen. The density profiles are steeper on the LFS for both gases. Higher values of n are measured in Argon, where both the ionisation efficiency and the particle confinement time are expected to be higher than in Hydrogen, due to the higher ionisation cross section and ion inertia [70]. The single particle confinement time is determined by the combined effect of direct losses along the magnetic field and ∇B and curvature drifts (see Chap. 7). For electron energies $\approx T_e$ and typical values of B_z, it is estimated to be $\geqslant 200\,\mu$s (Sec. 7.3). The electron temperature has similar values for the two gases, in the range from 3eV to 8eV, with values slightly higher in Hydrogen. The profile of T_e is also peaked on the low-field side. A less pronounced peak is sometimes observed at the EC resonance. The profiles of V_{pl} are similar to those of n, except at the HFS in Hydrogen, where an increase of V_{pl} does not correspond to an increase in the density. The typical experimental conditions for the two gases and the corresponding calculated collision frequencies and mean-free-paths are summarised in Tab. 4.1 and Fig. 4.3.
To investigate the role of f_{uh} and f_{ec} in the ionisation process, the microwave source is modulated with square pulses between two values of power (Fig. 4.6). The time intervals Δt_{off} and Δt_{on} correspond to the background plasma and to the perturbed plasma. The analysis is performed over the time intervals τ_{low} and τ_{high}, chosen within the perturbed and unperturbed plasma phases, respectively. Note that τ_{low}

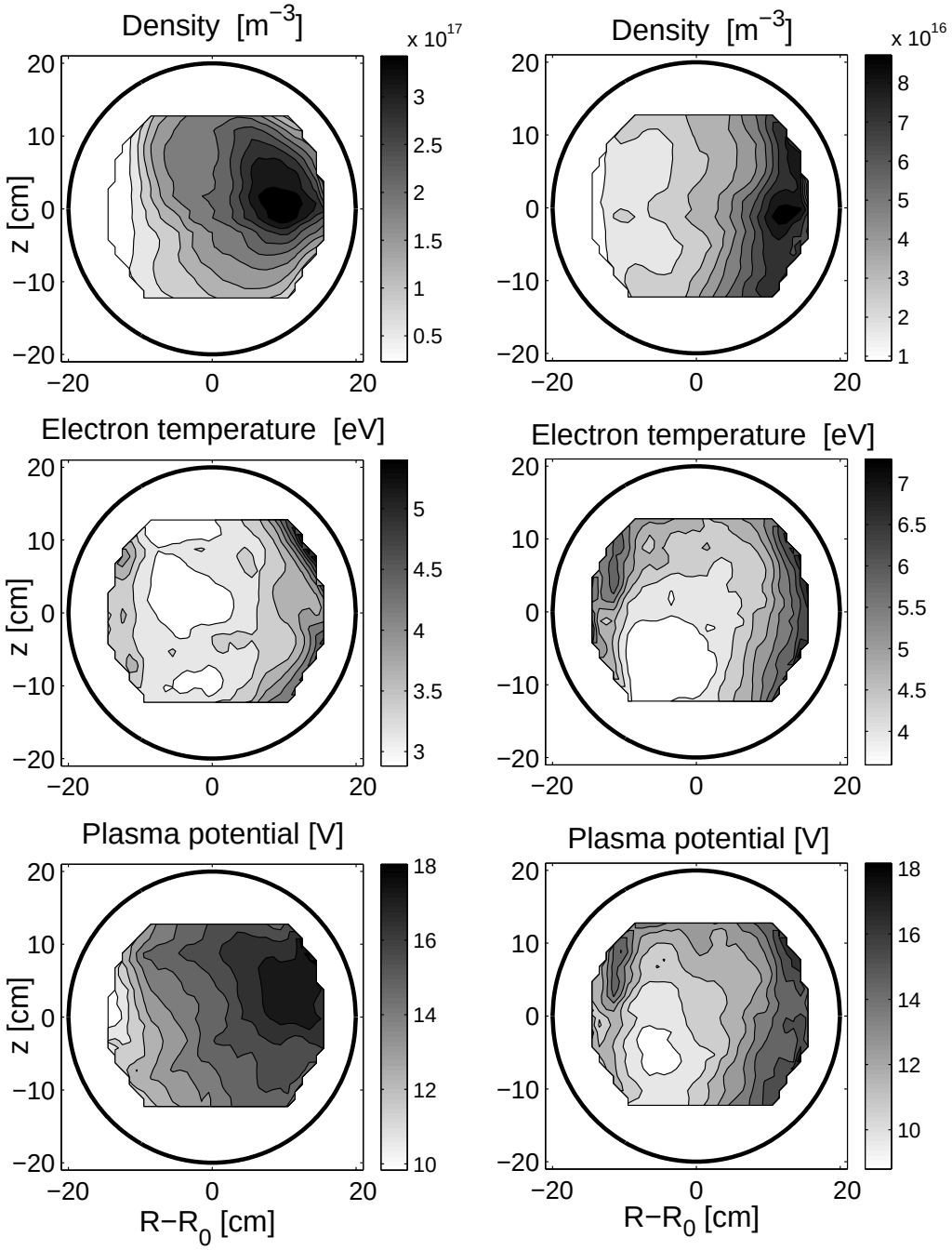

Figure 4.2: Typical profiles in Argon (left) and Hydrogen (right) plasmas. Here and in the following discussion for Argon plasmas $B_z = 1$mT and $p_g = 2\times10^{-5}$mbar, and for Hydrogen $B_z = 0.6$mT and $p_g = 3.5 \times 10^{-5}$mbar. The EC resonance is located at $R - R_0 = -12.5$cm, corresponding to a toroidal magnetic field $B_\phi = 76$mT on the axis.

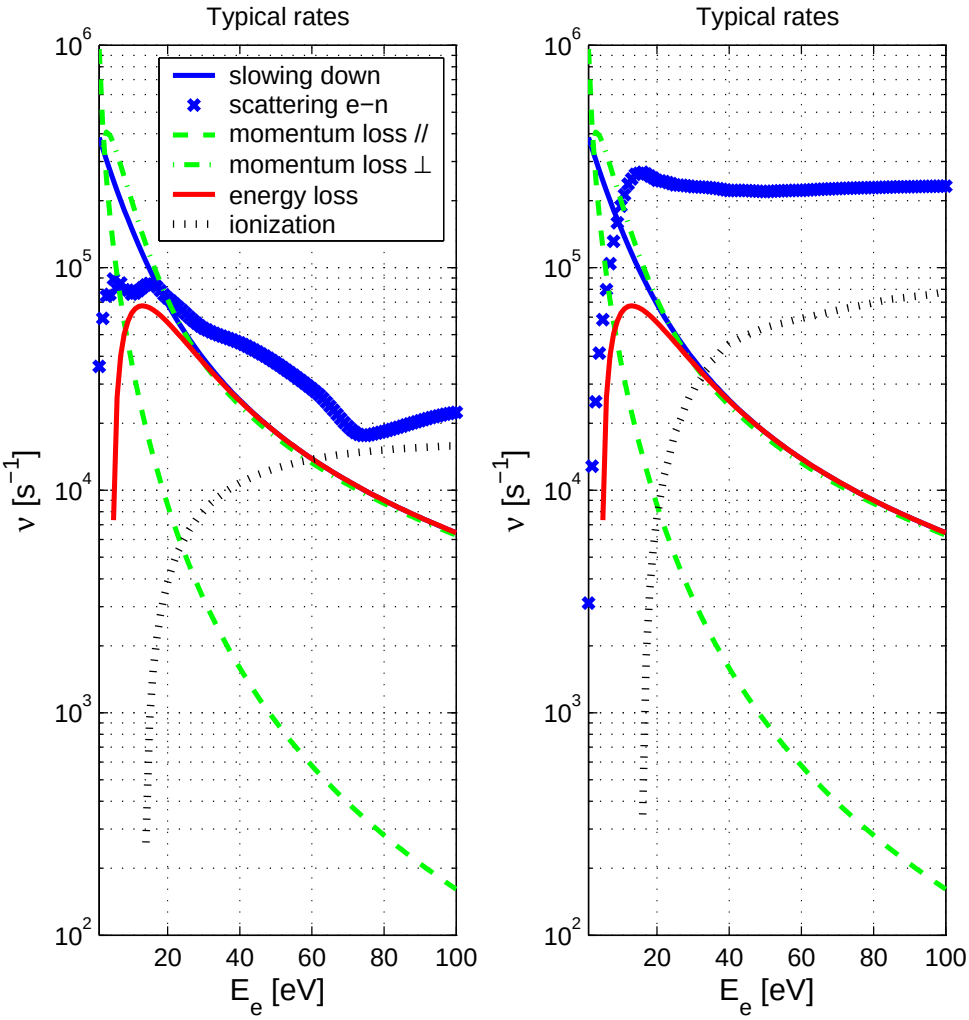

Figure 4.3: Collision rates for a test electron with energy E_e in Hydrogen ($l$eft) and Argon ($r$ight) plasmas with $n = 5 \times 10^{16}\mathrm{m}^{-3}$ and $T_e = 5\mathrm{eV}$. A neutral gas pressure of 2×10^{-5}mbar is assumed.

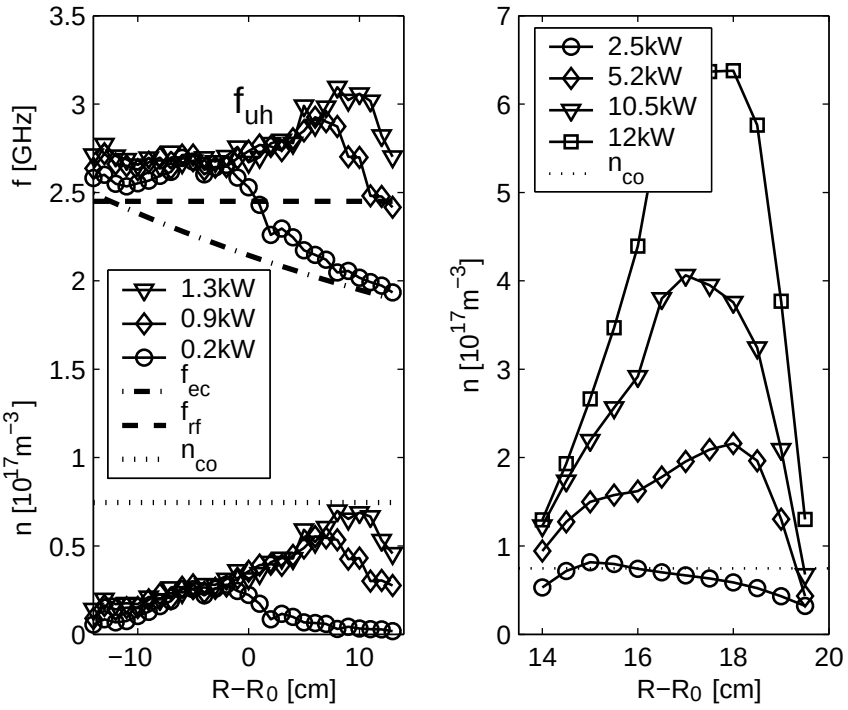

Figure 4.4: *Left:* Density and frequency profiles on the axis $z = 0$ in Hydrogen for three values of absorbed power. *Right:* Density profiles in Hydrogen at the edge (LFS) for values of absorbed power $>$ 2kW. n_{co} is the cutoff density for O-mode propagation.

and τ_{high} can be only a fraction of the overall *low* and *high* phases defining the duty cycle. The plasma density response to the modulation can then be measured by means of electrostatic probes operated in the ion saturation regime and moved on a shot-to-shot basis over the plasma cross section. For each spatial position, the density response is characterised in terms of the average fractional variation, $\Delta n/n = (n_{high} - n_{low})/n_{low}$, where n_{low} and n_{high} are the densities averaged over all the time intervals τ_{low} and τ_{high}.

The optimisation of the τ_{low} and τ_{high} values is based on two requirements. First, the 'low' phase must be far enough from the injected power pulse in order for the plasma to relax toward the stationary background state. Second, τ_{high} must be much shorter than the typical time scales characterising the macroscopic density fluctuations (Chap. 7), in order to clearly distinguish the changes of n related with a change of the power. The amplitude of the power pulse is chosen to be small enough to avoid too strong perturbations of the background plasma and large enough to have a well discernable response from the measured signals. For the experiments reported in this Chapter, the modulation frequency is chosen in the range 0.5kHz to

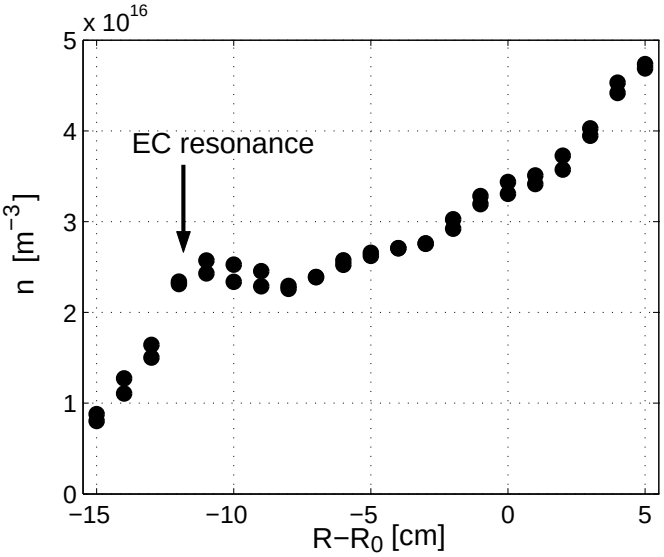

Figure 4.5: Radial density profiles at the midplane in Hydrogen for $P_{rf} = 1$kW. The EC resonance is at $R - R_0 = -12.5$cm. Note the change in the slope of n around the EC resonance, indicating the presence of a particle source at this location. The increase of the density toward the LFS, on the right of the picture, is due to a second source location, namely at the UH resonance (not shown in the figure).

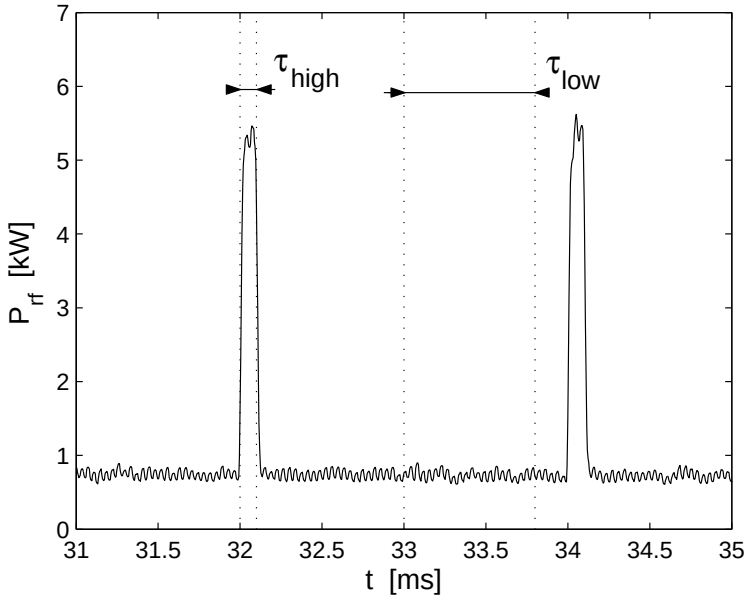

Figure 4.6: Illustration of the modulation technique based on square pulses of the injected microwave power. The density in the background and perturbed states results from an average over all the τ_{low} and τ_{high} intervals.

	Argon		*Hydrogen*	
neutral pressure [mbar]	2×10^{-5}		3.5×10^{-5}	
B_z [mT]	1		0.6	
connection length [m]	42		58	
plasma density [m^{-3}]	5×10^{16}		5×10^{16}	
electron temperature [eV]	5		5	
ionisation degree [%]	~ 10		~ 10	
collision type	σ [10^{-20} m^2]	λ_{mfp} [m]	σ [10^{-20} m^2]	λ_{mfp} [m]
Coulomb	8.2	76	8.2	76
e/n scattering	10.7	5.8	1.87	20
ionisation	2.6	23	0.61	60

Table 4.1: Typical experimental conditions, collision cross-sections and corresponding mean-free-paths for Coulomb collisions, scattering of electrons on neutrals and ionisation for Argon and Hydrogen plasmas. Values refer to a test electron with parallel energy equal to T_e. A representative value of 50eV is assumed for the perpendicular energy of the suprathermals responsible for ionisation (cfr. Chap. 6). Plasma density and electron temperature are average values. For comparison, the length of a field line connecting the bottom to the top of the vacuum vessel (the *connection length*) for $R = R_0$ is reported.

1kHz, with a duty cycle between 5 and 20% and $\tau_{high} \approx 20\,\mu$s. The injected power goes from 0.2 up to 5kW.

4.2.1 Absorption at the EC and UH resonances

Figure 4.4 shows the radial profiles of n and of the EC and UH frequencies at the midplane for different values of absorbed power in Hydrogen plasmas. One can clearly see that the UH resonance shifts toward the walls on the LFS as P_{abs} increases. For $P_{abs} > 1.5$kW there are regions where the density is maintained above the O-mode cutoff value (overdense plasma), and the maximum continues to increase with the power. On the other hand, the density in the EC resonant region is essentially independent of the absorbed power. The observed shift of the density maximum to the LFS as the injected power is increased, together with the change in the slope of the radial profile systematically observed around $R = R_{ec}$ (an example is shown in Fig. 4.5), confirm that the plasma is produced at both the EC and UH resonances.
The fraction of power absorbed at each resonant location depends on the total amount of power coupled to the plasma, hence on the density profile, due to the intrinsic dependence $f_{uh} = f_{uh}(n)$. Fig. 4.7 shows the dependence of the fractional density variation, $\Delta n/n$, obtained with the modulation technique described above

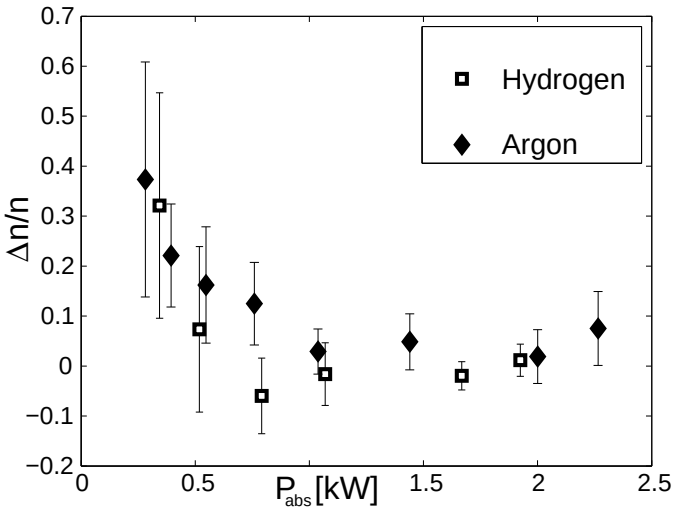

Figure 4.7: Fractional density variation, $\Delta n/n$, with modulated EC power, measured in Argon (diamonds) and Hydrogen (squares) on the midplane at $R = R_{ec}$ as a function of the injected microwave power in the 'low' phase. The error bars represent the standard deviation of the values measured for all the microwave power pulses.

and measured on the midplane at $R = R_{ec}$, upon the injected power. No data are shown for the UH layer because the layer is outside the region of measurement for most of the microwave power values, especially for Argon. The results are similar for the two gases. We observe that $\Delta n/n$ is reduced for increasing values of total absorbed power, suggesting that the power is progressively absorbed elsewhere, namely at the UH layer.

The density profiles also indicate that the UH resonance is located at just one radial position (for a fixed vertical position). Although in principle scenarios with multiple UH resonant regions and cutoffs are possible (Fig. 4.8), the feature of a single resonance along R is common to all the time-averaged profiles analysed so far (Chap. 7).

Experiments in which the microwave power is modulated can also provide a 2-D reconstruction of the ionisation profile. An example is shown in Fig. 4.9, for P_{abs} changing from 0.2 to 1.8kW. The experiments in Hydrogen show a sudden, localised increase in the density, coherent with the modulation of the microwave power. The location where this occurs coincides with the position of the resonant UH layer estimated from Eq. 4.1. For Argon plasmas the UH layer is outside the region accessible by the probes and its position can only be inferred from an extrapolation of the measured density profiles. The observable peak of $\Delta n/n$ coincides with the EC layer, confirming that both resonances lead to ionisation. By using the boxcar-averaging method described above (see also Sec. 8.4) one can also investigate the evolution

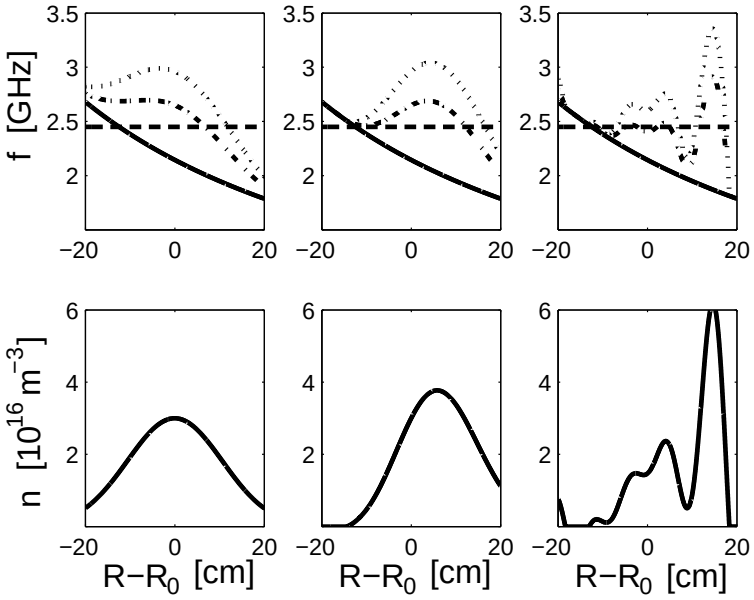

Figure 4.8: Possible scenarios of radial profiles for the resonances (*top*) involved in the propagation and absorption of waves injected at $f = f_{rf}$ and corresponding density profiles (*bottom*). Top figures: f_{rf} (dash), f_{ec} (solid), f_{uh} (dot-dash), f_r (dot). f_r is the frequency of the right-cutoff for X-mode propagation. The LFS is on the right of the figures. Note the possible sequences of UH resonances and cutoffs encountered by a wave propagating in the X-mode from the HFS to the LFS. Only first scenario sketched (*top left*) seems to be fully compatible with the experimental data shown in Figs. 4.4 and 4.5.

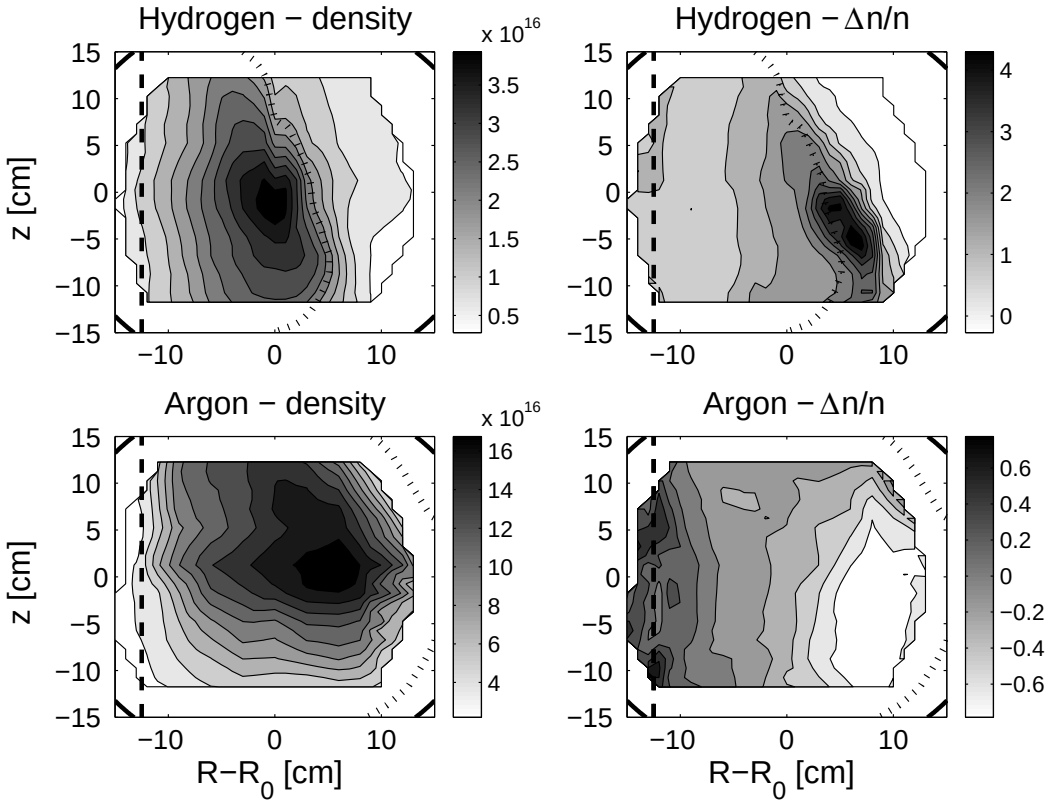

Figure 4.9: Background density profiles (*left*) and measured fractional density variation $\Delta n/n$ (*right*) with modulated EC power (square pulses, modulation frequency = 500Hz, duty cycle 20%) in Hydrogen and Argon (absorbed power between P_{abs} = 0.2kW and 1.8kW). Dashed line: EC resonance; dotted line: UH resonance extrapolated to the whole poloidal section.

of T_e and V_{fl} during a microwave power pulse. Data for Hydrogen plasmas show that T_e and V_{fl} remain almost constant in time over most of the poloidal section. Around the EC and UH layers the electron temperature rises together with P_{abs} (see Fig. 8.11). Along with the dip observed in V_{fl}, this may be interpreted as a signature of additional suprathermal electrons accelerated at the resonant layers [100], cfr. Chap. 6.
In addition to the processes described above, a contribution to the ionisation rate can come from the particles in the tail of the thermal electron distribution:

$$R_{th} = \int_{\Omega} n_g n(R,z) \langle \sigma_{iz}(v) v \rangle_{T_e(R,z)} d\Omega \tag{4.2}$$

where Ω is the plasma volume, the average $\langle \ldots \rangle$ is performed over energies above the ionisation potential assuming a maxwellian electron distribution with temperature $T_e(R,z)$ and n_g is the neutral density. This particle source has a spatial distribution that depends on that of T_e and n_e, and in general is much broader than the thin layer where ionisation by suprathermal electrons accelerated at the resonant layers occurs. The average values of T_e that would correspond to the measured volume-integrated density are in the range from 5eV to 9eV, i.e. about twice the measured values averaged over the poloidal cross section. Therefore, the contribution of the thermal population alone is insufficient to explain the observed plasma densities.

4.3 Summary and discussion

In this Chapter, we show that the power absorption at the EC resonance is in general quite poor, and most of the wave power is instead absorbed at the UH resonance. Nevertheless, the presence of the EC resonance inside the vacuum chamber is required to initiate the breakdown of the neutral gas. Experimental evidence that suprathermal electrons, responsible for most of the ionisation events, are generated at both resonances is presented. The spatial profile of the particle source is identified by measuring the plasma density response to a fast modulation of the EC power, which allows one to separate the fast phenomena related to ionisation from the slower mechanisms leading to the stationary background profiles. These experiments can be used to establish a link between the ionisation processes and experimental control parameters such as the vertical magnetic field, the injected power and the geometry of the device. The influence of the particle source on the density makes it possible to act on the profiles via the same control parameters that are relevant for the ionisation processes.
From the experiments, we conclude that the electrons can experience an energy gain sufficient to give rise to ionisation at both the EC and the UH layers, despite the different nature of the acceleration mechanisms at the two resonances. The electrons that acquire sufficient energy ionise the neutral gas within a few centimeters

	Argon	*Hydrogen*
δ_{res}/v_{the} [s]	5×10^{-7}	1.5×10^{-5}
ν_p^{-1} [s]	2×10^{-6}	10^{-5}

Table 4.2: Mean interaction time at the UH resonance for thermal electrons (T_e = 5eV is assumed), evaluated from the experimental density profiles. ν_p is the collision rate for momentum change.

around the two resonances, as highlighted by the experiments with modulation of the injected power (see Fig. 4.9). Each resonant layer, then, represents a possible particle source, and it is worth discussing the parameters that determine their relative contribution to the total source.
The number of ionisations from a particular layer depends on how many electrons are accelerated and on their energy. The average energy gain of an electron at $f_{rf} = f_{uh}$ and $f_{rf} = f_{ec}$ depends on the local value of the wave electric field and on the average wave-particle interaction time, τ_{int} [58]. Depending on the experimental conditions, different mechanisms are responsible for a finite interaction time [10]. For practical purposes we can set $\tau_{int} = min\{\delta_{res}/v_{the}, \nu_p^{-1}\}$. Here ν_p is the total electron momentum transfer rate and δ_{res} is the length of the path of electrons travelling along the magnetic field through the resonant region at the thermal speed v_{the}. The values of τ_{int} and δ_{res} are affected by the experimental parameters in a different way for the two resonances.
At the EC layer the resonant condition $f_{rf} = f_{ec}(R)$ is independent of the vertical coordinate. The finite bandwidth Δf_{rf} broadens the resonant location along the major radius, with $|\Delta R_{ec}/R_{ec}| \propto |\Delta f_{rf}/f_{rf}| \sim 10^{-2}$, but does not affect δ_{res}, which corresponds to the connection length between the top and the bottom of the vessel. As $\delta_{res}/v_{the} \gg \nu_p^{-1}$, at the EC layer the interaction time is determined by the collision rate, $\tau_{int} = \nu_p^{-1}$ (cfr. Tab. 4.2).
For the UH layer several parameters, such as the bandwidth of the injected beam, the vertical field B_z, the density profile and the geometry of the vacuum vessel, determine the value of δ_{res}. Due to the dependence $f_{uh} = f_{uh}(n)$, with $n = n(R, z)$, $\delta_{res} \propto \Delta f_{rf}/f_{rf}$, except in the limit $\Delta f_{rf} \to 0$, when other mechanisms are responsible for a finite interaction time [10]. For the magnetic field configuration used on TORPEX, the value of δ_{res} is inversely proportional to that of the vertical magnetic field, $\delta_{res} \propto B/B_z \sim B_\phi/B_z$. The dependence on the density leads to an additional broadening in the vertical direction. In summary, for the UH layer

$$\delta_{res} \propto \left| \frac{\Delta f_{rf}}{f_{rf}} \left(\frac{1}{n} \frac{\partial n}{\partial z}\Big|_{n=n_{uh}} \right)^{-1} \frac{B}{B_z} \right| \tag{4.3}$$

The width δ_{res} is enhanced in regions where $\partial n/\partial z \to 0$, which could explain the peak of $\Delta n/n$ observed in the Hydrogen case, where the UH layer is almost vertical

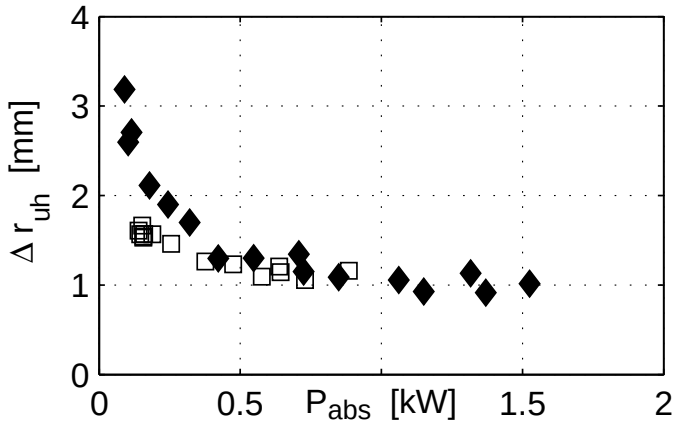

Figure 4.10: Average width of the resonant UH layer along the vertical direction, Δr_{uh}, as a function of P_{abs} for Hydrogen (diamonds) and Argon (squares), evaluated from an interpolation of the density profiles and assuming a bandwidth of the injected waves $\Delta f_{rf} = 20$MHz .

(Fig. 4.9). For sufficiently high absorbed power the UH layer gets close to the vacuum chamber walls (Fig. 4.4). The density gradient increases, reducing the width and the volume of the layer (Fig. 4.10). Assuming that the number of electrons accelerated at $f_{rf} = f_{uh}$ is proportional to the density inside the UH layer, this mechanism may result in a decreased efficiency of the plasma production. Moreover, if the density in front of the microwave antenna (at the LFS) rises above the cutoff value, the fraction of power coupled to the plasma becomes smaller as n increases, giving a negative feedback action between P_{abs} and n. Both effects may explain the observed saturation of the density with the injected microwave power (Fig. 4.11). Thus the minor radius and, more generally, the size and the geometry of the vacuum vessel are expected to influence the dependence of the density profile upon the absorbed power.
The features discussed above highlight the coupling between the plasma production processes and the density profile. Further evidence is provided by experiments with relatively large toroidal field and microwave power, in which large amplitude oscillations with frequency $\leq$ 10kHz are observed in the absorbed power and the density (Fig. 4.12). The two quantities are strongly correlated, with phase and amplitude of the density oscillations which depend on the spatial location. The coupling between density and absorbed power may be understood on the basis of a predator-prey model [65]. To provide a better interpretation to this type of phenomena and, more in general, to complete the study of the plasma production mechanisms, more information on the particle source and its spatial profile is needed. This is the subject of the next Chapter.

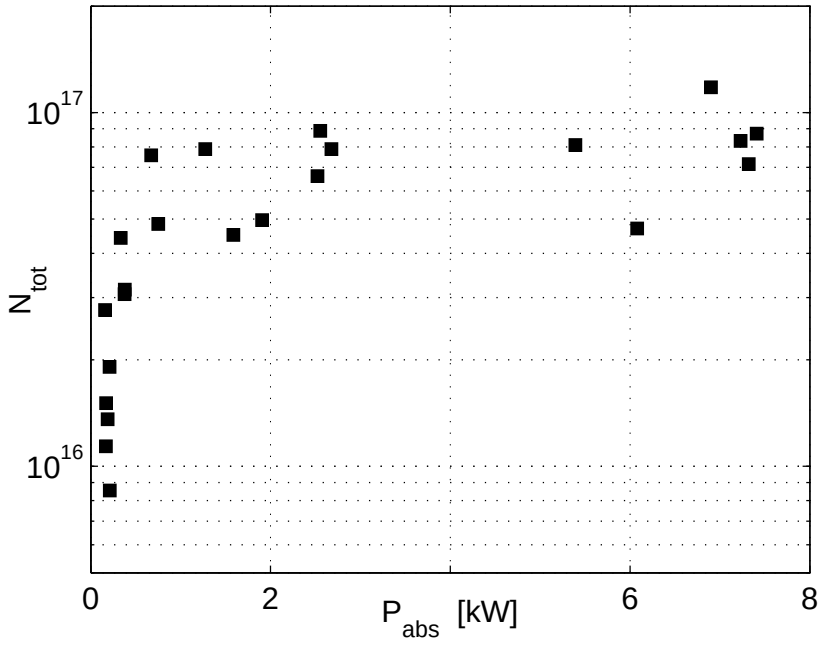

Figure 4.11: Total number of ions (assuming $n_e \approx n_i$) as a function of the absorbed power for Argon plasmas. Note the saturation of the total plasma particle content for $P_{abs} > 2$kW.

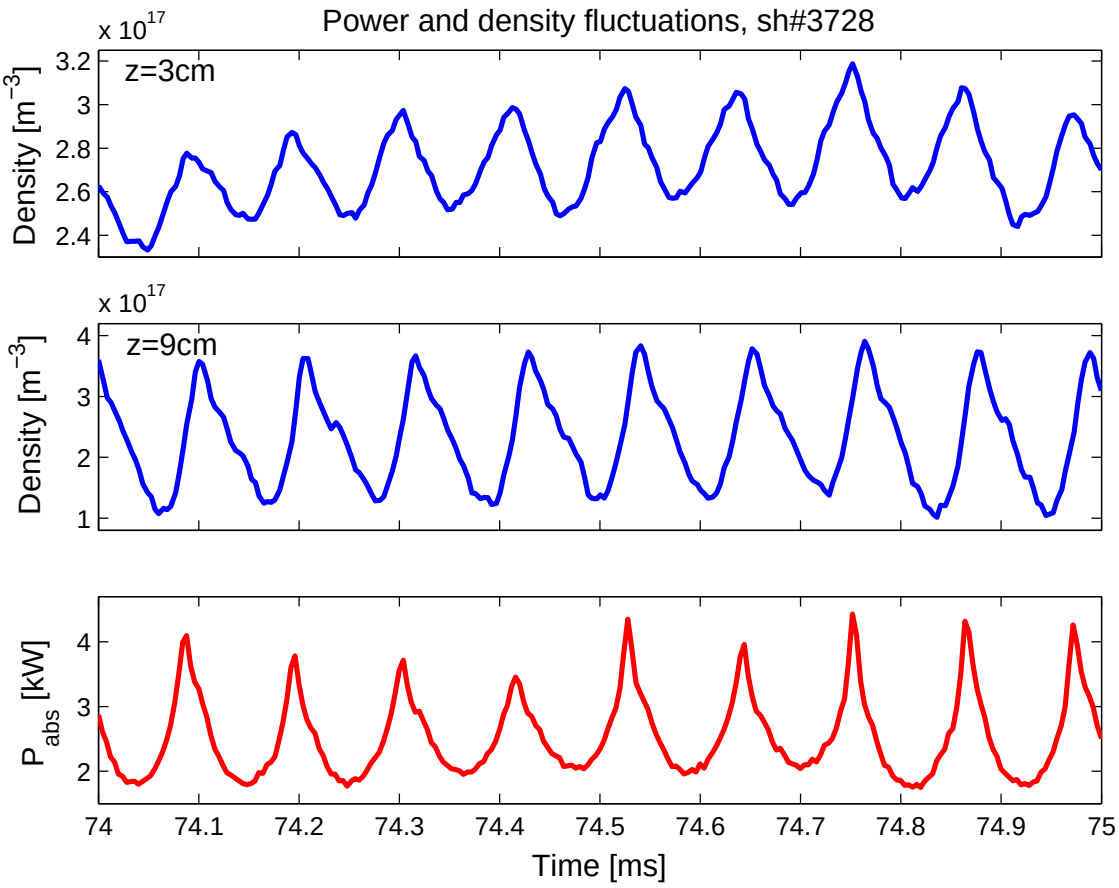

Figure 4.12: Example of plasma density oscillations, measured at two vertical positions for an Argon plasma, which show a strong coupling with the absorbed microwave power.

Chapter 5

Experimental characterisation of the particle source in the microwave plasma production scheme

The study of transport and associated plasma losses, which represents an important part of this Thesis, is naturally coupled to that of energy and particles sources. Their knowledge is also important for implementing numerical codes to simulate specific experiments. By including as much information derived from the experiment as possible, in fact, the number of unknowns quantities in the codes can be reduced. A direct comparison between the code outputs, for example in terms of instabilities and associated phenomena, and the experimental results would then be easier.
The mechanisms behind the plasma production by microwaves in the electron-cyclotron (EC) frequency range were described in detail in the previous Chapter. It is shown that the ionisation occurs primarily close to the EC and upper-hybrid (UH) resonances, and that for sufficiently high microwave power the dominant source of ionisation is the UH layer. The contribution to the total ionisation rate from electrons in the tail of the thermal electron distribution function is negligible. However, a quantitative estimate of the source profile is made difficult by the fluctuations of the position of the UH layer, resulting from the coupling between the UH frequency and the plasma density.
In this Chapter, an accurate reconstruction of the spatial profile of the plasma particle source in TORPEX is provided. The different contributions to the particle source are quantified on the basis of a global particle balance, and the crucial role played by the UH resonance is confirmed. A simple numerical code is developed to estimate the local properties of the source profile as a function of adjustable experimental parameters, namely the injected microwave power, the magnetic field configuration and the neutral gas pressure. Finally, the results of the experiments and of the numerical code are cast into a semi-empirical expression for the source profile. The typical parameters for the experiments reported in this Chapter are summarised in Tab. 5.1.

5.1 Quantification of the different contributions to the ionisation rate

Three mechanisms can bring electrons up to energies above the ionisation potential, W_{iz} (see [78] and Chap. 4): wave absorption (i) at the EC resonance, (ii) at the UH resonance and (iii) electrons in the tail of the thermal electron distribution function. Here we look for an expression for the contribution of each of these three mechanisms to the ionisation rate as a function of the absorbed microwave power.
Assuming that via the EC resonance a fraction of the absorbed power corresponding to $\eta_{ec}P_{abs}$ goes into the acceleration of electrons up to a typical energy E_f, the ionisation rate related to the EC channel is defined as

$$R^{ec} = \eta_{ec}(P_{abs})\,\frac{P_{abs}}{E_f^{ec}}\,\eta_{iz}^{ec}(E_f^{ec}) \tag{5.1}$$

Here η_{iz}^{ec} is the number of electron-ion pairs created by each suprathermal electron. Similarly, at the UH layer

$$R^{uh} = \left[1-\eta_{ec}(P_{abs})\right]\,\frac{P_{abs}}{E_f^{uh}}\,\eta_{iz}^{uh}(E_f^{uh}) \tag{5.2}$$

i.e. it is assumed that the microwave power is transferred to the plasma via the EC and UH channels only. In general, $E_f^{ec} \neq E_f^{uh}$ due to the different physics involved in the acceleration process at the two resonant layers [78]. The ratios η_{iz}^{uh}/E_f^{uh} and η_{iz}^{ec}/E_f^{ec} represent the ionisation efficiency per unit energy acquired by the electrons accelerated at the UH and EC layers.
The next step consists in deriving a convenient expression for $\eta_{ec} = \eta_{ec}(P_{abs})$. We define $\Delta n/n$ as the normalised density increase associated with an increase of the absorbed microwave power, ΔP_{abs}. Based on the data shown in Fig. 5.1, at the EC layer we can take $\Delta n/n \propto \Delta P_{abs}/P_{abs}$. Assuming that $\Delta n \propto R^{ec}$ and that

gas	Argon	Hydrogen
neutral pressure p_{gas} [10^{-5} mbar]	2	3.5
Position of the EC resonance, $R-R_0$ [cm]	-12.5	-12.5
B_ϕ *on the axis* [mT]	76	76
B_z [mT]	1	0.6
plasma density [10^{16} m^{-3}]	≤ 10	≤ 3
electron temperature [eV]	5	5
plasma potential [V]	≤ 20	≤ 20

Table 5.1: Typical conditions for the experiments reported in this Chapter.

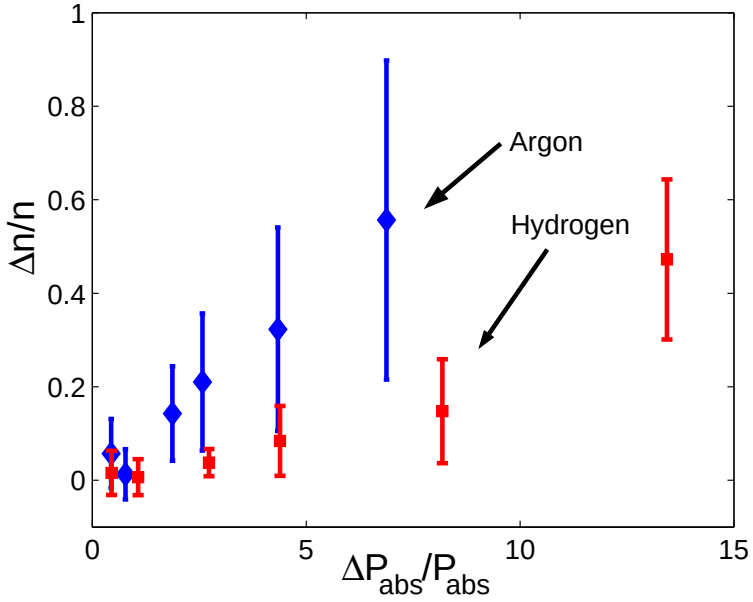

Figure 5.1: Measured $\Delta n/n$ at the EC resonance for $z = 0$ as a function of $\Delta P_{abs}/P_{abs}$. The microwave power was modulated with square pulses (modulation frequency = 500Hz, duty cycle 20%).

$\eta_{iz}^{ec,uh}(E_f)/E_f^{ec,uh}$ does not depend upon P_{abs} (see Sec. 5.2), we find from Eq. 5.1

$$\eta_{ec}(P_{abs}) = const. \times n\frac{\Delta P_{abs}}{P_{abs}^2} \tag{5.3}$$

Note that both n and ΔP_{abs} are unknown functions of P_{abs}. The dependence of η_{ec} upon P_{abs} can be experimentally reconstructed, as shown in Fig. 5.2. The complete empirical relation $\eta_{ec} = \eta_{ec}(P_{abs})$ must account for the fact that at the breakdown all the power is absorbed at the EC resonance but, as the density increases, the ionisation occurs preferentially at the UH layer. We put

$$\eta_{ec}(P_{abs}) = \eta_\infty + (1 - \eta_\infty)\exp\left(-\frac{P_{abs}}{\gamma}\right) \tag{5.4}$$

where η_∞ is the fraction of power absorbed at the EC layer for $P_{abs} \to \infty$. The parameter γ can be interpreted as a characteristic power value above which the efficiency of the EC channel starts decreasing. The validity of the expression for $\eta_{ec}(P_{abs})$ proposed in Eq. 5.4 is confirmed by a least mean square fit of the experimental data (Fig. 5.1).

In addition to the ionisation associated with the two resonant regions we have to include the contribution R^{th} from electrons in the tail of the thermal distribution:

$$R^{th} = \int_\Omega n_g n(R,z)\,\langle\,\sigma_{iz}(v)\,v\,\rangle_{T_e(R,z)}\,d\Omega \tag{5.5}$$

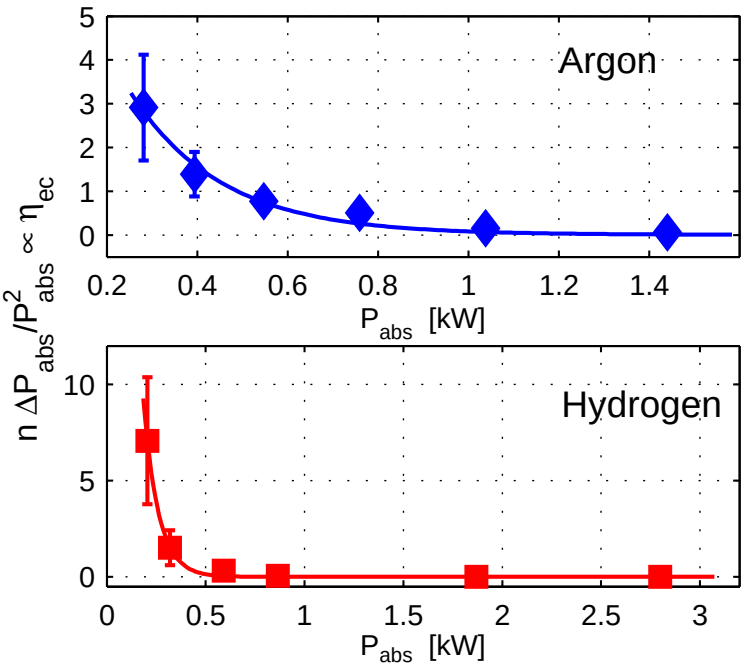

Figure 5.2: Estimate of $\eta_{ec}(P_{abs})$ from Eq. 5.3. Data from Argon (*top*) and Hydrogen (*bottom*) plasmas on the midplane at the EC resonance. The solid lines represent a fit based on Eq. 5.4. The error bars represent the standard deviation from the ensemble of microwave power pulses.

Here Ω is the plasma volume and the average $\langle \ldots \rangle_{T_e(R,z)}$ is performed over energies above W_{iz}, assuming a Maxwellian distribution with temperature $T_e(R,z)$. The neutral density, n_g, is assumed to be uniform.
By summing the three contributions, we obtain for the total ionisation rate

$$R_{iz} = R^{th} + P_{abs}\left[\alpha + \beta \exp\left(-\frac{P_{abs}}{\gamma}\right)\right] \tag{5.6}$$

where we have defined

$$\alpha = \eta_\infty \left(\frac{\eta_{iz}^{ec}}{E_f^{ec}} - \frac{\eta_{iz}^{uh}}{E_f^{uh}}\right) + \frac{\eta_{iz}^{uh}}{E_f^{uh}}, \qquad \beta = (1-\eta_\infty)\left(\frac{\eta_{iz}^{ec}}{E_f^{ec}} - \frac{\eta_{iz}^{uh}}{E_f^{uh}}\right) \tag{5.7}$$

Under stationary conditions the global particle balance can be written as $N_{tot}/\tau_p = R_{iz}$, where N_{tot} is volume-integrated density and τ_p is the average particle confinement time. We assume that τ_p does not depend explicitly on the injected power [70]. The value of τ_p can be estimated as the characteristic time of the density decay after the shutdown of the microwave source (Sec. 7.3.1). For practical convenience,

a single time-constant is used here. The results do not differ substantially from what it is found with a more accurate analysis in Sec. 7.3. For our experimental conditions we find $\tau_p \approx 0.2$ms (Hydrogen) and $\tau_p \approx 0.4$ms (Argon).
Equation 5.6 can be used to fit the data from a series of experiments providing $N_{tot} = N_{tot}(P_{abs})$, taking α, β and γ as fitting parameters. The contribution to N_{tot} from the thermal population, estimated from Eq. 5.5, can be neglected. The value of N_{tot} is obtained from the measured density profiles, extrapolated to the whole poloidal section and integrated over the entire plasma volume. To vary P_{abs}, the injected microwave power is slowly ramped up from 0 to 10kW within the same plasma discharge, while B_z and p_{gas} are varied on a shot-to-shot basis. The density profile is measured by HEXTIP (Sec. 3.4). A constant $T_e = 5$eV is assumed. Once the parameters α and β are determined, the quantities η_{iz}^{uh}/E_f^{uh} and η_{iz}^{ec}/E_f^{ec} can be evaluated from Eq. 5.7. The condition $\eta_{iz}^{ec,uh}/E_f^{ec,uh} \geq 0$ provides an upper limit for η_∞, namely $\eta_\infty \leq \alpha/(\alpha+\beta)$. For the data presented here $\alpha \ll \beta$, and we can approximate $\eta_\infty \approx 0$, consistently with the data (Fig. 5.1). The experimental data for Hydrogen plasmas and the results of the fits are shown in Fig. 5.3 and Fig. 5.4. The dependence of N_{tot} on p_{gas} and B_z for two characteristic values of absorbed microwave power is summarised in Fig. 5.5. The strong influence of p_{gas} on the obtainable densities is clear, with the plasma production becoming less efficient for higher pressures. As no clear dependence of τ_p upon p_{gas} is observed, we conclude that, for these operating conditions, the ionisation efficiency, η_{iz}/E_f, is decreased for higher neutral pressures. The dependence of N_{tot} on the vertical magnetic field is weaker. In this case $\eta_{iz}^{ec,uh}/E_f^{ec,uh}$ slightly increases with B_z. However, τ_p shows a monotonic decrease, which can be ascribed to the enhanced direct losses along the magnetic field lines. Both the plasma production and the loss rate are increased, resulting in an almost constant total density.

5.2 Spatial profile of the particle source

To proceed with the modelling of the particle source profile, information on the width of the region around the resonant layers where ionisation occurs, and its dependence upon the plasma profiles and E_f is required. A simple numerical code based on a Monte Carlo approach has been implemented for this purpose. The details on the code implementation are given in Appendix C.

5.2.1 Simple code for estimating the source profile

The dynamics of an electron in the plasma depends on a number of events (scattering, ionisation, losses) that can be conveniently represented by cross sections. The value of the macroscopic cross sections as a function of the particle energy are known

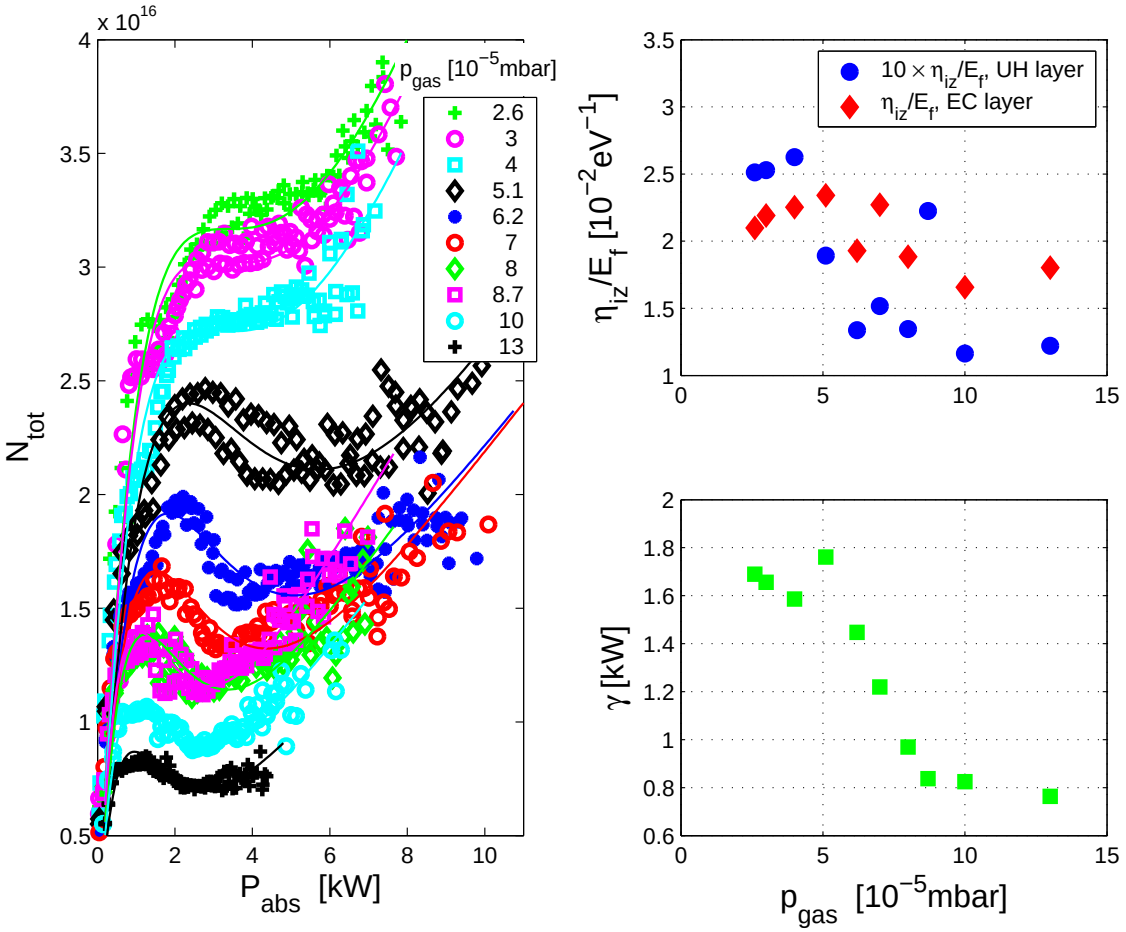

Figure 5.3: Volume-integrated density as a function of the absorbed microwave power for different values of the neutral gas pressure (Hydrogen plasmas). *Left:* experimental results of $N_{tot}(P_{abs})$ (symbols) and fit of the experimental data with Eq. 5.6 (solid line). *Right:* Coefficients η_{iz}^{uh}/E_f^{uh}, η_{iz}^{ec}/E_f^{ec} and γ resulting from the fit.

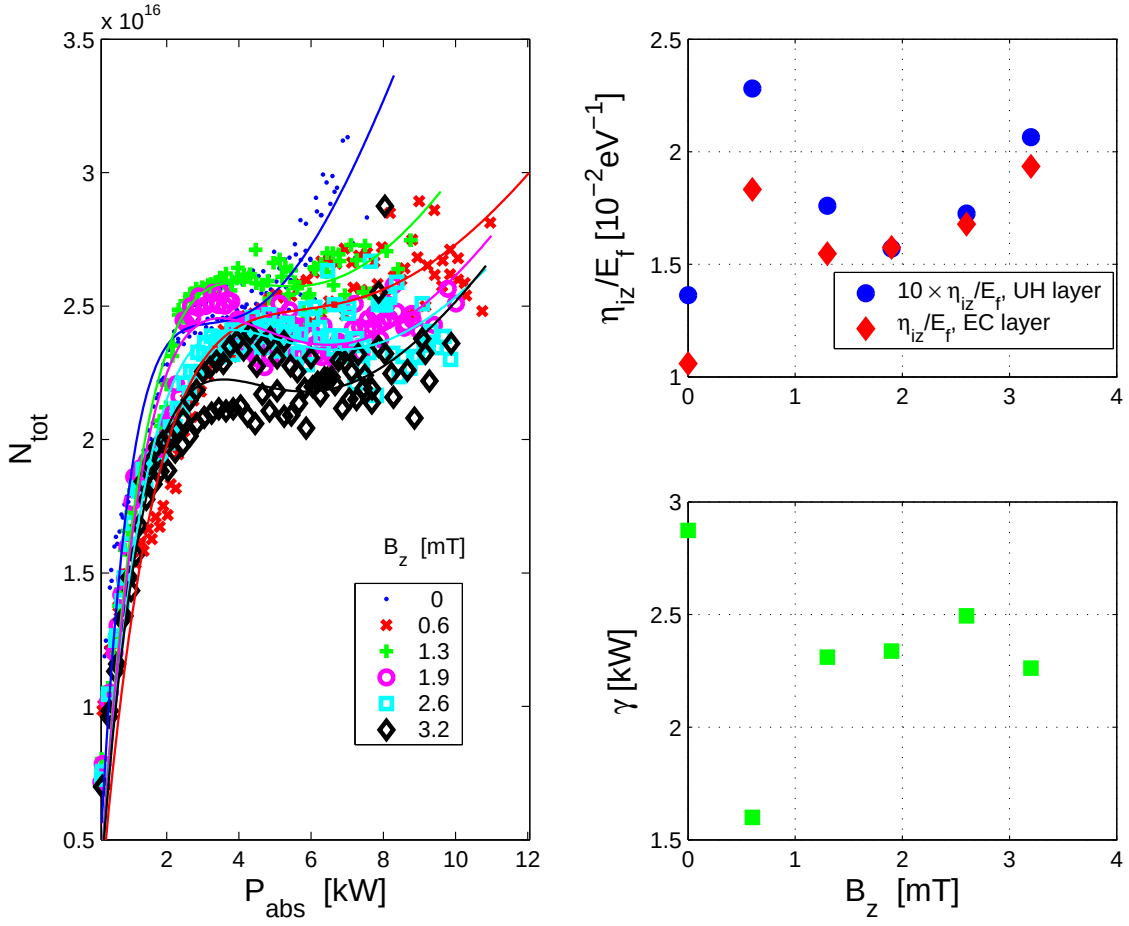

Figure 5.4: Same as in Fig. 5.3, but for different values of the vertical magnetic field, B_z.

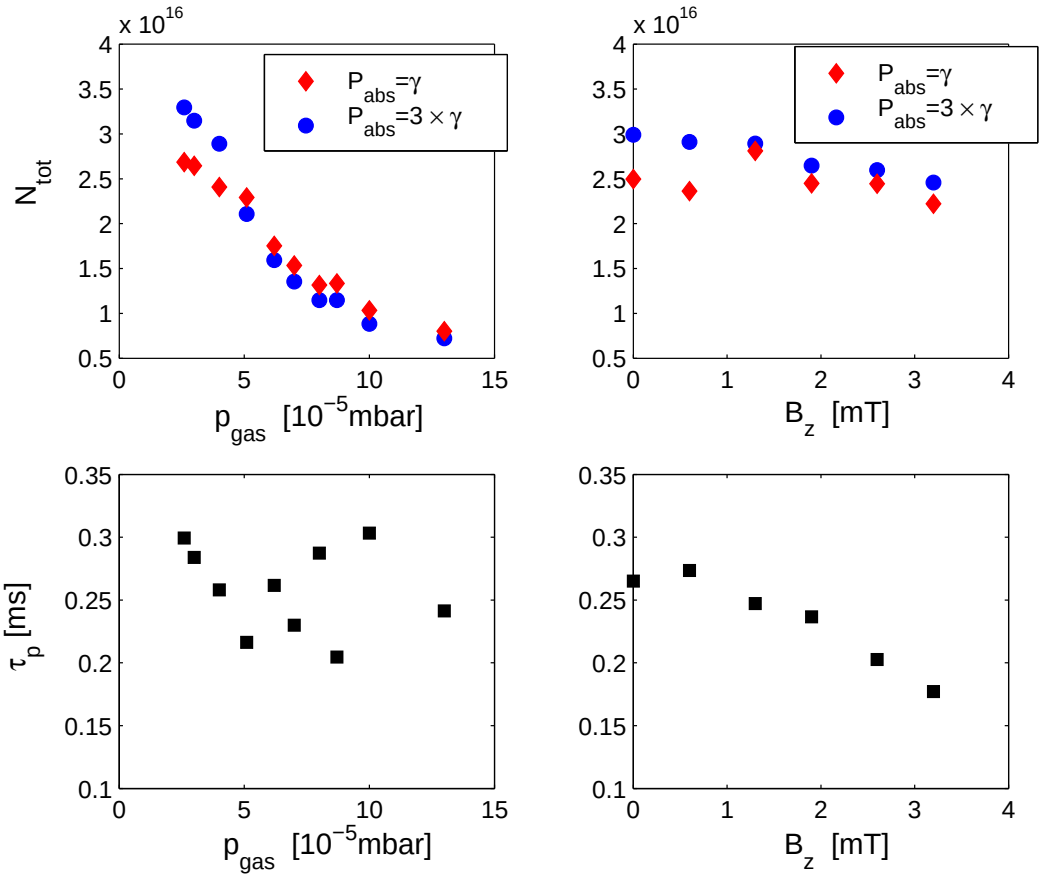

Figure 5.5: Dependence of N_{tot} and τ_p on p_{gas} and B_z for two characteristic values of absorbed microwave power, $P_{abs} = \gamma$ (diamonds) and $P_{abs} = 3\,\gamma$ (circles). The parameter γ is the power level above which the efficiency of the EC channel starts decreasing.

from the background density profiles of plasma and neutrals. It is then possible to calculate the relative probabilities that electrons experience a particular event after travelling a distance Δx. The 'life' of the electron can be reconstructed from all the events occurred from its generation to its loss. This representation of the electron dynamics in terms of events, characterised by probabilities, justifies the use of a code based on Monte Carlo techniques ([62] and references therein). By reconstructing the 'statistical life' of a large number of particles, and averaging over the *ensemble*, one can obtain useful information on the system under investigation, especially for problems that can not be solved analytically.

Electron trajectories and background profiles

The trajectories of the test electrons, also called *primary* electrons, start at the resonance position. The code simulates the dynamics of the test particles only in one dimension, i.e. along a vertical path (direction z) in the poloidal plane for a given radial position. The vertical path represents a projection of the real motion, characterised by a velocity component parallel to the magnetic field and drifts in the vertical direction. A finite tilt angle, $\theta_{tilt} = atan(B_z/B_\varphi)$, is taken into account. The experimental density and electron temperature background profiles are used. For computational convenience, they are extrapolated to the whole poloidal section with a boundary condition $n = 0$ on the walls. A uniform density profile is assumed for the neutral gas.
As an example, we estimate the mean free path, λ, of a test electron with $E_0 = 50$eV in a uniform plasma with $n = 10^{17}\mathrm{m}^{-3}$ and $T_e = 5$eV. For any kind of event, we define $\lambda = 1/n\,\sigma(v, T_e)$, where v is the velocity of the electron. For an Argon plasma is $\lambda_{sc,g} \approx 8$m, $\lambda_{iz} \approx 380$m, where $\lambda_{sc,g}$ and λ_{iz} are the mean free paths for scattering on the neutrals and for ionisation. The length of a magnetic field line inside the vessel for typical values $B_z = 1$mT and $B_\varphi = 76$mT is about 40m. The mean free path for Coulomb collisions, $\lambda_{sc,coul}$, is smaller than $\lambda_{sc,g}$, but these are small-angle collisions and are not very relevant, as discussed below.
We conclude that scattering events dominates with respect to ionisation events. The ionisation probability is quite small, and its cross section for Hydrogen is even smaller than for Argon.

Collisions with charged and neutral particles

The rate for small-angle Coulomb collisions is higher than that for scattering on neutrals. For this reason, Coulomb scattering is treated in the code as a 'continuous' process, thus allowing one to use a spatial grid step greater than $\lambda_{sc,coul}$. The collisions on the neutrals have a probability distribution function for the scattering angle, θ, equal to $p(cos\theta) = 1/2$. An interchange between perpendicular and parallel energy can take place after a single collision with a neutral.
From these considerations, and from the fact that the energy slowing down is negligible, it follows that Coulomb collisions play a minor role in the model. In practice, they are neglected in order to reduce considerably the computing time.
Another important conclusion is that, as a consequence of the scattering on neutrals, the electron distribution function, $f_e(\underline{v})$, is isotropic, though most of the energy absorbed from the injected waves goes into the perpendicular velocity.

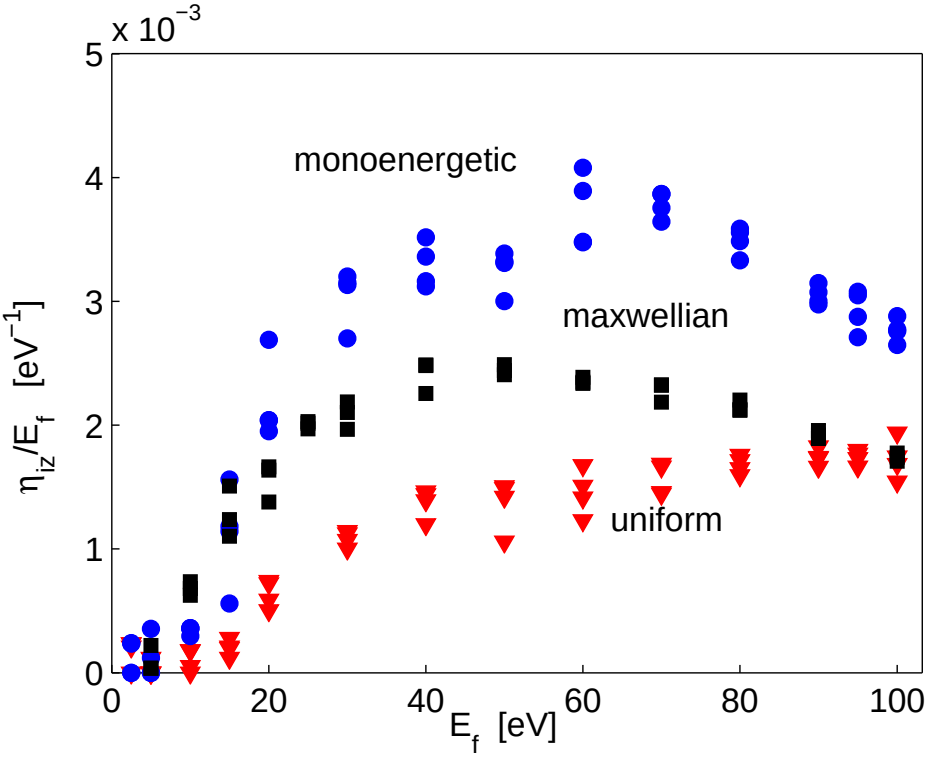

Figure 5.6: Results of the numerical estimates of η_{iz}/E_f for Hydrogen plasmas. The energy of the suprathermal electrons is extracted from a mono-energetic distribution (circles), a maxwellian with temperature E_f (squares) and from a uniform distribution between W_{iz} and E_f (triangles).

Code implementation

The code calculates the trajectories of suprathermal electrons for a given experimental density profile, assuming a bandwidth $\Delta f_{rf} = \pm 20$MHz for the injected microwaves. The test electrons start with perpendicular energies, E_f, extracted from different test distributions (mono-energetic, uniform or maxwellian). The parallel velocities are randomly extracted from a Maxwellian distribution with temperature T_e. Note that the acceleration due to the wave-particle interaction enters only in this initialisation phase. The modelling of the acceleration mechanisms is therefore by-passed in the code by *ad hoc* assumptions on E_f.
Starting energies $\leq$ 100eV are used in the simulation. The upper limit of 100eV has been estimated from measurements with a gridded energy analyser, see Chap. 6, and from the fact that spectroscopic measurements in Argon provide no evidence of doubly ionised ions. The cross section for double ionisation has a threshold of 40eV and increases slowly up to about 7% of the single ionisation cross section for

a 100eV electron [113].
The code gives $\eta_{iz}^{uh}/E_f^{uh} \lesssim 4 \times 10^{-3}\text{eV}^{-1}$ for typical background profiles and a wide range of energies E_f (Fig. 5.6). This is in excellent agreement with the results shown in Fig. 5.3 and Fig. 5.4 for the UH layer, in particular for suprathermals characterised by a maxwellian distribution, cfr. Chap. 6. On the other hand, there exists a discrepancy for the EC layer, suggesting that the code does not model properly the EC resonance, for which a different acceleration mechanism is at play [58]. Therefore the results of the code are accurate in the limit of high absorbed power, when ionisation at the UH layer is dominant.
In general, the particle source profile estimated from the code peaks at the resonant locations and decays along z as a superposition of two exponentials with different decay lengths (cfr. Fig. C.3). This feature is determined by the collisions on neutrals, which mix parallel and perpendicular energies of the test electrons that have been accelerated at the resonance, where they acquire primarily perpendicular energy. An electron initially moving along B with a velocity $v \sim v_{the}$ has a high probability of ionising close to the resonance. After a collision, its velocity along B can go up to $v \sim (E_f/m_e)^{1/2} \gg v_{the}$, therefore the next ionisation event will occur far from the resonance.

5.2.2 Semi-empirical expression for the source profile

An analytical expression can be used to summarise the information obtained from the experiments and from the simple numerical code. The normalised source profile can be recovered by summing the contributions from the electrons accelerated at different positions z':

$$r_i(R,z) = \frac{1}{G} \int e^{-\left(\frac{f_i(R,z')-f_{rf}}{\Delta f_{rf}}\right)^2} \times \left[e^{-\frac{|z'-z|}{\Delta z_1}} + A\, e^{-\frac{|z'-z|}{\Delta z_2}} \right] dz' \tag{5.8}$$

where the index i indicates either the EC or the UH layer and G is a normalisation factor such that $\int_\Omega \sum_i r_i(R,z)\, d\Omega = 1$. The first term in the integrand models the resonance condition. The terms in square brackets come from the finite mean-free-path of electrons accelerated at (R,z') and travelling for a finite distance before they ionise a neutral. The parameters A, Δz_1 and Δz_2, whose physical interpretation is given in Appendix C, are determined by means of the numerical code. An example of the calculated particle source profile is shown in Fig. 5.7. If the density profile is known, Eq. 5.8 allows one to retrieve the normalised spatial profile of the particle source. More quantitative information on the ionisation rate is based on the knowledge of τ_p, required to quantify R^{uh} and R^{ec} and to rescale the normalised profile. If this information is available, the particle source profile can finally be expressed as

$$S(R,z) = n_g n(R,z) \left\langle \sigma_{iz}(v)\, v \right\rangle_{T_e(R,z)} + R^{ec}\, r_{ec}(R,z) + R^{uh}\, r_{uh}(R,z) \tag{5.9}$$

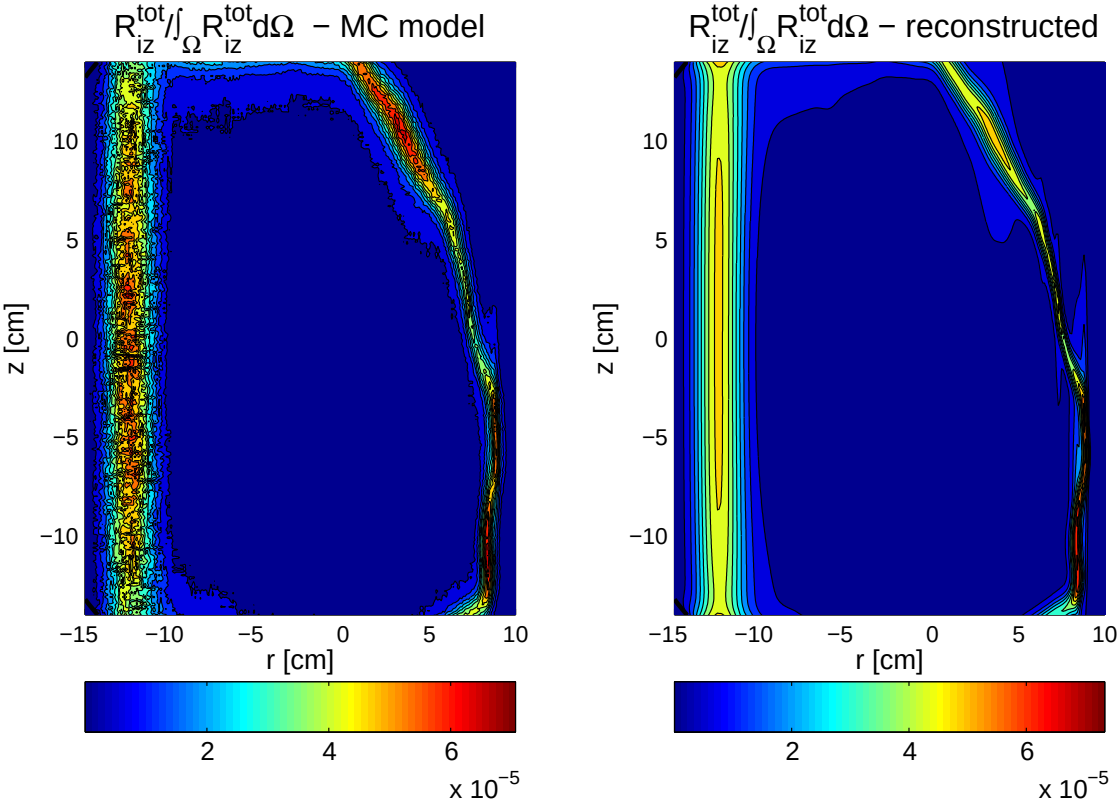

Figure 5.7: Particle source profile, output of the simple numerical code (*left*) and reconstruction based on Eq. 5.8 (*right*) for a Hydrogen plasma.

5.3 Summary and discussion

The particle source profile and its dependence on the experimental conditions have been investigated in the EC wave produced plasmas of TORPEX. A method is proposed to quantify the contributions to the global ionisation rate for different experimental conditions. The results show that the main contribution to the particle source comes from suprathermal electrons generated at the EC and UH resonant layers, as the electrons in the tail of the thermal distribution give only a negligible correction to the total ionisation rate. To confirm the role of electrons with different energies in the ionisation processes, information on the electron distribution function is required, which is the subject of the next Chapter.
A simple numerical code has been developed to get information on the local properties of the particle source, taking as input the experimental density and electron temperature profiles. The normalised plasma source profile can thus be estimated as a function of experimental parameters such as the neutral gas pressure and the vertical magnetic field. The code results are accurate for sufficiently high absorbed

power, i.e. when most of the ionisation occurs close to the UH resonant layer. More theoretical and experimental investigations on the detailed acceleration mechanisms at play at the EC resonance are required to improve the numerical simulation.
The two-dimensional profile of the particle source is reconstructed on the basis of the available information and a semi-empirical expression is proposed. This expression can be included in numerical codes simulating the plasma dynamics, viz. the fluid code ESEL [34] which is recently being adapted to the TORPEX experiment [67].

Chapter 6

Measurements of the electron energy distribution function

The energy distribution function (EDF) provides the most exhaustive information on the behaviour of a plasma. In practice, plasmas are often assumed to be in a thermodynamical equilibrium state and maxwellian EDFs are adopted to describe the ion and electron populations. This assumption may not be justified in devices where the plasma is confined for a time much shorter than its typical relaxation time-scales, or when additional sources of heat and particles are present. An EDF far from the maxwellian may affect the estimates of important quantities such as collision frequencies, instabilities growth rate and reaction rates. Moreover, in practice, the knowledge of the shape of the EDF is the basis for the interpretation of many diagnostic signals [47]. Examples of devices where non-maxwellian EDFs are commonly found include plasma-processing reactors [36] and tokamaks, in which the plasma can be heated by externally launched waves, e.g. electron-cyclotron (EC) waves [9][54][42]. Strongly non-maxwellian EDFs can also be expected when the plasma is produced and sustained by EC waves [36][58].
Experimentally, different methods are available to measure the EDF. Techniques based upon polarisation spectroscopy [29] and D_α light emission [42] can be used in tokamaks. In colder plasmas, the most widely used techniques are based on electrostatic Langmuir probes [47][22]. The EDF is derived from the derivative of the current measured by the probe with respect to the sweep voltage. However, the accuracy of the method may be affected by a number of factors, such as a non-saturating ion current for a large, negative probe bias voltage ([37] and references therein). To reduce the effect of incomplete ion saturation, and improve the determination of crucial parameters such as the plasma potential, on TORPEX we use an electrostatic energy analyser to characterise the electron EDF.
This Chapter describes the results of the EDF measurements performed on TORPEX to conclude the investigation of the plasma production mechanisms, and the resulting particle source term. The goal is to relate the local properties of the electron EDF in TORPEX with the plasma production mechanisms. The possible implications for a correct modelling of the particle source are discussed.

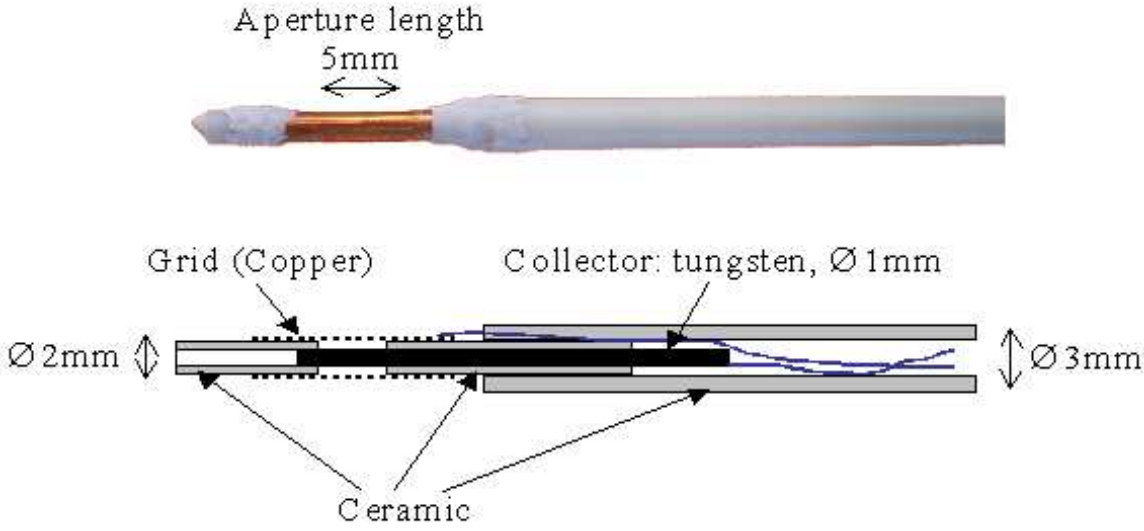

Figure 6.1: The MOANA probe installed on TORPEX.

6.1 Experimental setup

The results presented in this Chapter for the EDF are obtained by means of an electrostatic energy analyser (EEA). The basic idea behind EEAs is to filter and measure particles depending on their charge and energy [47]. We focus here on the measurements of the electron EDF. The current density measured on the collector as a function of the grid voltage, V_g, is

$$j(V_g) = q\sqrt{\frac{2}{m_e}}\, n_e \int_{V_g}^{\infty} T_{tr}(E)\,\sqrt{E}\, f_c(E)\, dE \tag{6.1}$$

where $f_c(E)$ is the EDF of particles reaching the collector, m_e is the electron mass, q the elementary charge and n_e the density in the unperturbed plasma. The term T_{tr} is the grid transmission factor. Assuming a plasma potential $V_{pl} = 0$, the EDF in the unperturbed plasma is then $f(E) \propto (T_{tr}\, V_g^{1/2})^{-1}\, \partial j/\partial V_g$.
A picture and a schematic of the EEA installed on TORPEX are shown in Fig. 6.1. The collector is made of a cylindrical tungsten electrode with diameter of 1mm and length of 5mm. The grid is wrapped around the collector holder, and the separation between grid and electrode is 0.5mm. This design makes the probe response insensitive to the orientation of the probe with respect to $\underline{B}$, hence the name MOANA (Monogrid Omni-directional ANAlyser). The probe can be inserted from the bottom of the vacuum vessel, spanning a strip $-20\text{cm} < z < 6.5\text{cm}$, or horizontally at the midplane, covering the range $-8\text{cm} < r < 20\text{cm}$.
The geometrical transmission factor of the grid can be estimated as $(l_g - d_g)^2/l_g^2$,

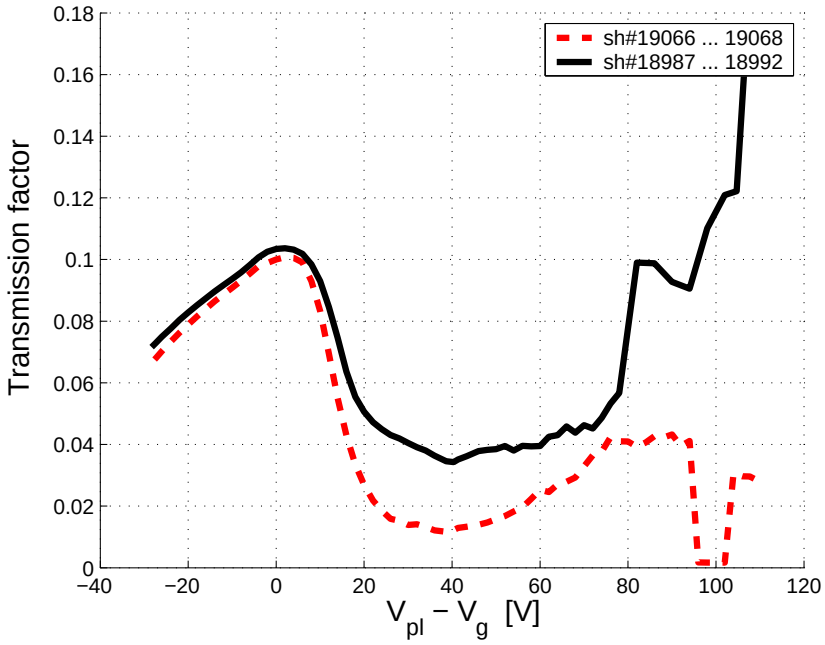

Figure 6.2: Measured grid transmission factor, $T^e_{tr}(E)$, at two different locations, corresponding to the EC (dashed line) and UH (solid line) resonance layers. The energy of the electrons collected by the probe is here expressed as the difference between the local plasma potential and the grid voltage, V_g. The strong dependence of T^e_{tr} on the electron energy makes it crucial to include the measured $T^e_{tr}(E)$ in the analysis.

where l_g is the mesh step and d_g the thickness of the wires. For MOANA is $l_g = 12.5\mu$m and $d_g = 5\mu$m, which gives a transmission of $\approx 36\%$. In practice, a different transmission factor is measured due to the different dynamics of ions and electrons and the specific geometry of the probe. For the electron current it is found experimentally that $T^e_{tr} \approx 8\%$ when V_g approaches the plasma potential. In the previous estimate the dependence of T^e_{tr} on the particle energy is neglected. Particles with low parallel (to $\underline{B}$) and high perpendicular velocity, i.e. with a large Larmor radius compared to l_g, will be lost on the grid with higher probability than particles with a dominant parallel velocity. If the collector and grid electron currents, j_c and j_g, are known, then T^e_{tr} can be estimated as $T^e_{tr} = j_c/(j_c + j_g)$. Note that improper assumptions on the ion component of j_g [37] may result in an inaccurate estimate of $T^e_{tr}(E)$, which mainly leads to uncertainties in the estimated densities. The measured $T^e_{tr}(E)$ confirms that high energy particles may be collected with lower efficiency, see Fig. 6.2.
For $5 \leq V_{pl} \leq 20$V, to measure a full EDF the grid voltage is swept from -100V to $+40$V with a triangular waveform at a frequency of 330Hz. A fixed bias voltage of

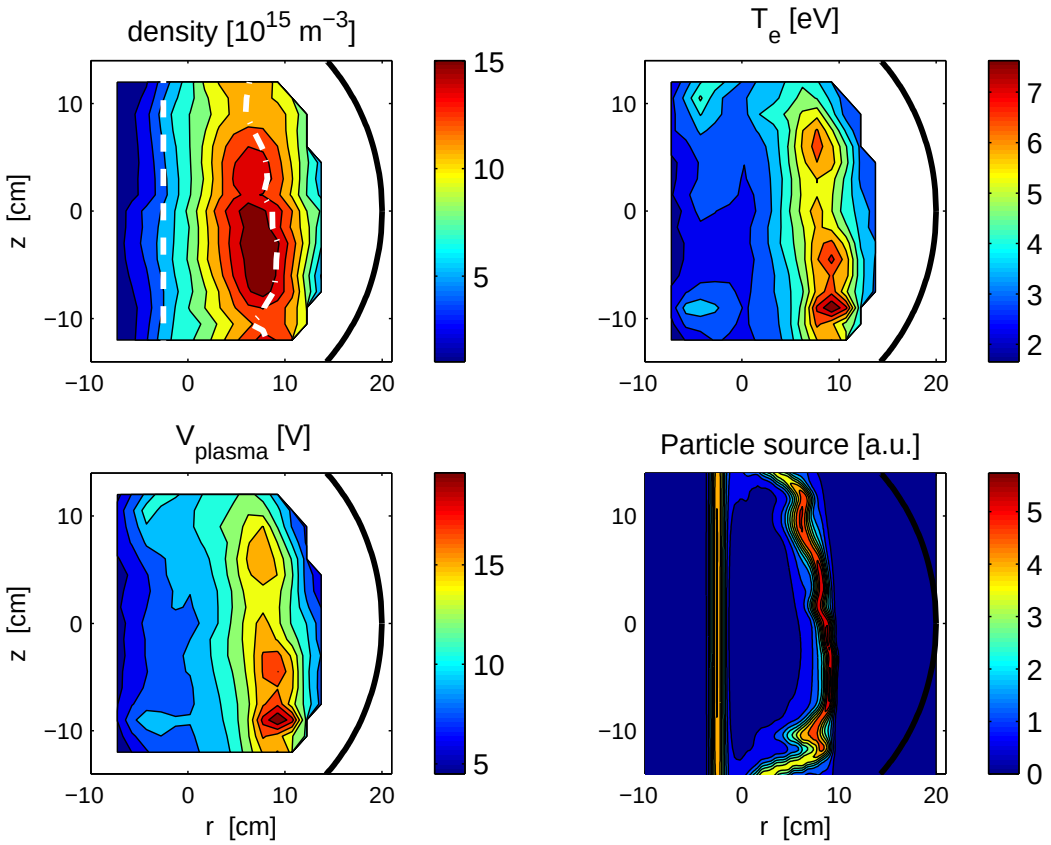

Figure 6.3: Density, electron temperature, plasma potential and particle source profiles. The thick, white lines represent the EC (dashed) and UH (dash-dotted) resonances.

+40V is applied to the collector. As for standard Langmuir probes, an average $I-V$ curve can be recovered by averaging over multiple sweep periods and, possibly, over different shots. This average curve, corrected for the measured $T^e_{tr}(E)$, can then be differentiated to obtain $f(E)$.

6.2 Measurements of the electron EDF

The results shown hereafter refer to Hydrogen plasmas obtained from a base pressure of 6×10^{-5}mbar with an injected microwave power of ≈ 400W. The time-averaged profiles of n, T_e and V_{pl} are shown in Fig. 6.3. A toroidal magnetic field of 86mT on the axis and a uniform vertical magnetic field of 1.2mT are used. The positions of the resonant layers are highlighted with dashed and dash-dotted lines, and the particle source is estimated following the procedure described in the previous Chapter,

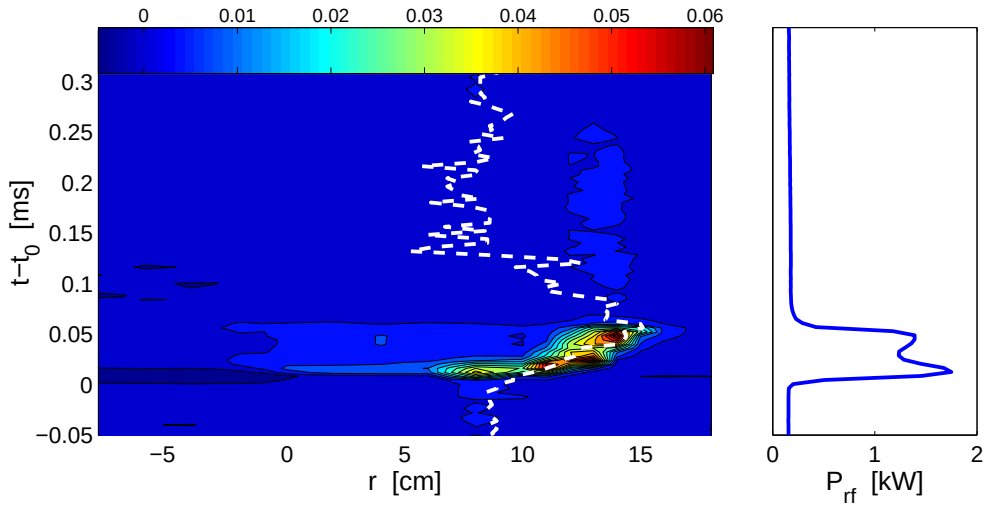

Figure 6.4: Collector current amplitude, in arbitrary units, during a pulse of the injected microwave power (shown on the right) along an horizontal chord at the midplane. The dashed line indicates the position of the UH resonance, calculated from the grid current. Note the small increase with respect to the background value of j_c at $r = 14$cm after the pulse, lasting for $\approx 150\mu$s.

see Eq. 5.9.
The temporal behaviour of the collector current for $V_g \leq -40$V is shown in Fig. 6.4. A positive voltage of +40V is applied to the collector. With this configuration, the plasma density, hence the position of the UH resonance, can be inferred from the grid ion saturation current, and electrons with energy $> V_{pl} + |V_g|$ are detected on the collector. The figure refers to discharges where short pulses of the injected power (modulation frequency 1kHz, duty cycle 5%) are superimposed to a stationary level of ≈ 400W. The data is taken along an horizontal chord on the equatorial plane. Under these conditions, an increase of the measured T_e is observed during the pulses in regions close to the EC and UH resonances (see, for example, Figs. 8.11 and 8.14). However, this is not enough to explain the increase of j_c by a factor ≈ 5. Such increase is instead ascribed to the enhancement of the suprathermal population following the abrupt change of the injected power. This happens at positions corresponding to the resonant UH layer, whose location evolves in time during the pulse accordingly to the density evolution. The complete EDFs, measured without modulation of the microwave power, are shown in Fig. 6.5. In the same figure the results for regions corresponding to the EC and UH resonances are detailed. The results from regions where no interaction between the plasma and the injected microwaves is expected to occur are also reported for comparison.
For practical convenience, the total distribution can be modelled by a linear com-

bination of maxwellian distributions, each characterised by a weight a_k and a temperature $T_{e,k}$:

$$f_k(E)dE = a_k \left(E/T_{e,k}^3\right)^{1/2} \exp\left(-E/T_{e,k}\right) dE \tag{6.2}$$

For most of the plasma regions located on the low-field side with respect to the EC resonance the EDF is well recovered by a bi-maxwellian curve. In these regions, electrons accelerated at the UH layer are expected to be present due to the dominant electron motion along $\underline{B}$. The example in Fig. 6.6 shows that the temperature of the two populations is well distinct, with the suprathermal being ≈ 4 times the bulk temperature. The density of suprathermals represents a few percent of the total. Inside the EC layer, and in regions on the high-field side of the EC resonance, where in principle there should be no suprathermals, a more complex EDF is measured. Only for low energies, $E \leq 15$eV, can it be represented by a single maxwellian. An energy cutoff, above which the measured signals drop below the electronics noise level, is observed for $E \geq 15$eV. It is worth noting that the normalised EDFs do not vary substantially when the background pressure, the vertical magnetic field or the injected microwave power are changed. This suggests that the local plasma-wave interaction mechanisms are not strongly affected by those parameters, in contrast to the resulting plasma profiles.

More information on the dynamics of the suprathermal electrons can be inferred from the analysis of the collector current signals. For sufficiently negative grid voltages, when j_c is dominated by the suprathermal electrons, j_c exhibits a spiky behaviour. An important parameter that can be extracted from the time series is the time delay between spikes, τ_d. To evaluate τ_d a threshold value, I_{th}, is chosen for the current. The time delay is defined as the time interval between adjacent crossings of the threshold. Crossings with positive and negative slopes are counted separately. The number of crossings corresponding to different values of τ_d can then be represented in a histogram. For threshold values $I_{th} < \sigma$, where σ is the standard deviation of the signal, the histogram peaks around $\tau_d \approx 0.05$ms for both the EC and UH layers. This indicates the presence of small-amplitude oscillations with frequencies > 20kHz. At the UH layer, a second peak becomes visible at $\tau_d \approx 0.25$ms when I_{th} exceeds σ (Fig. 6.7a). This peak is associated with intermittent, high amplitude spikes in the collector current. A peak at the same frequency, $1/\tau_d$, is detected by other probes, measuring density fluctuations, which are on the same magnetic field line as MOANA (Fig. 6.7b). This feature is explained by the dependence of the UH frequency on the density, $f_{uh} = (f_{ec}^2 + f_p^2)^{1/2}$, where f_{ec} is the EC frequency and $f_p = f_p(n)$ is the plasma frequency. A confirmation is provided by discharges where the microwave power is modulated with short rectangular pulses, thus forcing a modulation of the density at the UH layer. The histogram shows a sharp peak where $1/\tau_d$ coincides with the modulation frequency (Fig. 6.7c-d).

These observations suggest that density fluctuations, leading to oscillations of the UH resonant layer and modifications of the density gradient, may affect the wave

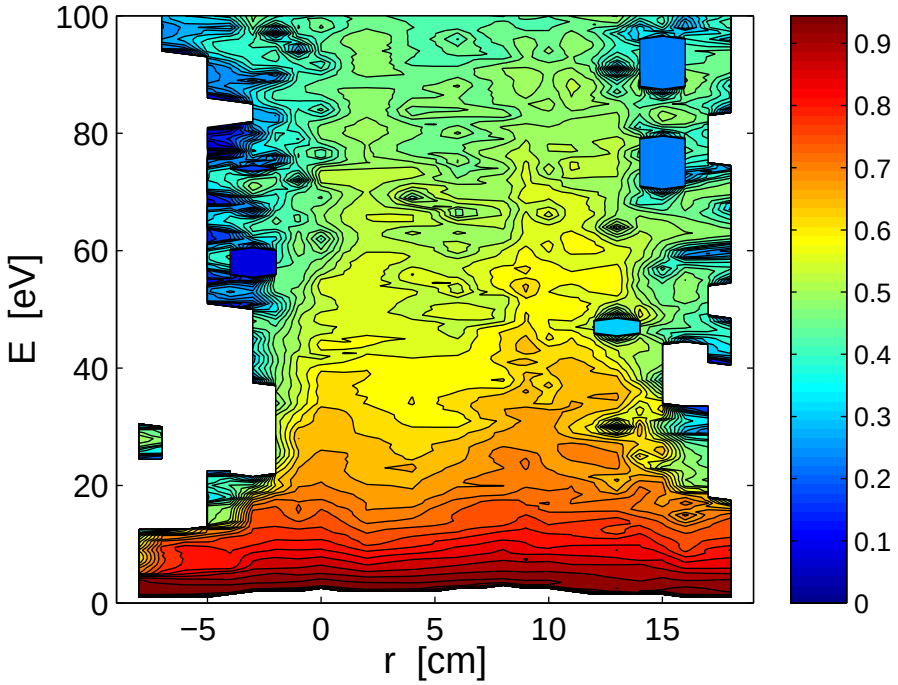

Figure 6.5: Electron EDF ([a.u.], normalised to the local density) measured at the midplane. The EC resonance is at $r = -2.5$cm. The UH resonance spans a region from $r = 8$cm to $r = 11$cm.

absorption efficiency [78], hence the acceleration of the suprathermals.

6.3 Summary and discussion

Measurements of the electron energy distribution function in TORPEX show that a substantial difference exists between electrons accelerated at the EC and UH resonances, the suprathermals from the UH layer being much more energetic than those from the EC layer. This observation provides a strong evidence for the different nature of the interactions at the two resonances. When averaged in time, the suprathermal population originating from the UH layer can be modelled with a maxwellian EDF. However, on short time-scales ($\approx 100\mu$s), it appears that suprathermal electrons are ejected intermittently from the UH layer. A characteristic frequency can be identified as $1/\tau_d$, and corresponds to that observed in the density fluctuations. A scan of the relevant experimental parameters, such as the neutral gas pressure, the vertical magnetic field and the injected microwave power, has been carried out. The measured EDFs do not show any systematic dependence on these parameters. This is consistent with the observations that the average magnitude of the plasma param-

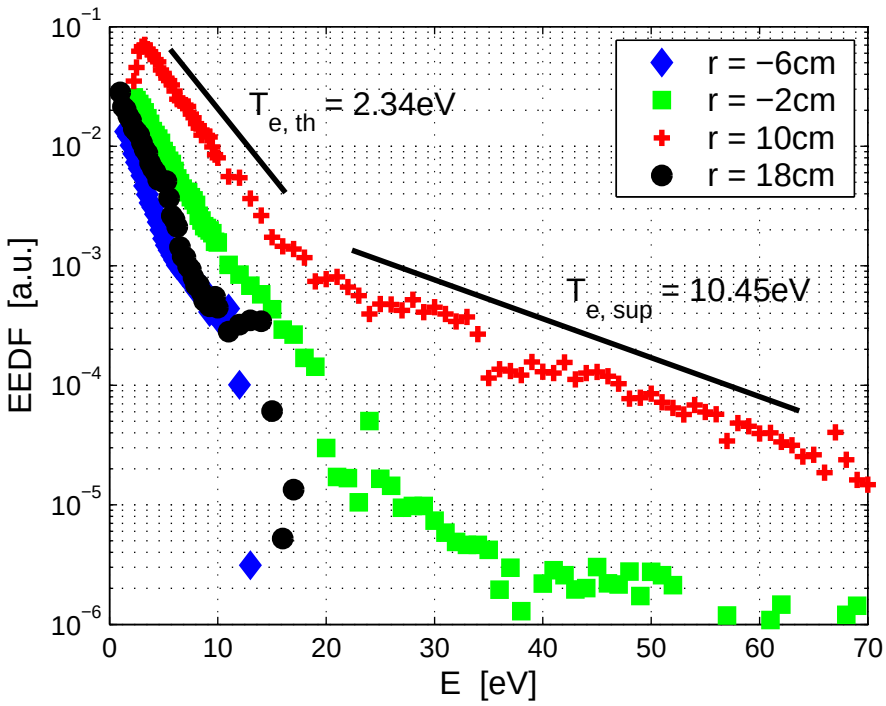

Figure 6.6: Electron EDF measured at four different positions. The results of a least-mean-square fit with a bi-maxwellian function is shown for the data from the UH layer ($r = 10$cm). $T_{e,th}$ and $T_{e,sup}$ are the temperatures of the bulk and suprathermal components.

eters do not vary significantly for the different experimental conditions, though their spatial profiles and the position with respect to the vessel can change substantially [78]. These observations confirm the applicability of simple models for the plasma particle source term, which can be simply based on the macroscopic, time-averaged density and electron temperature profiles [77].
Beside its relevance for a complete characterisation of the plasma production processes, the possibility of measuring the EDF makes the interpretation of the experimental data more robust. For example, even a small fraction ($\leq 1\%$) of suprathermal electrons with a temperature of ≈ 4 times the bulk temperature, may affect the results of standard Langmuir probes. In practice, the standard assumption of identifying floating and plasma potential fluctuations fails, as the floating potential signals are dominated by the suprathermal population. Analysis of density fluctuations deduced from measurements of the ion saturation current would also be affected if the probe voltage is not kept low enough with respect to the suprathermal energy.

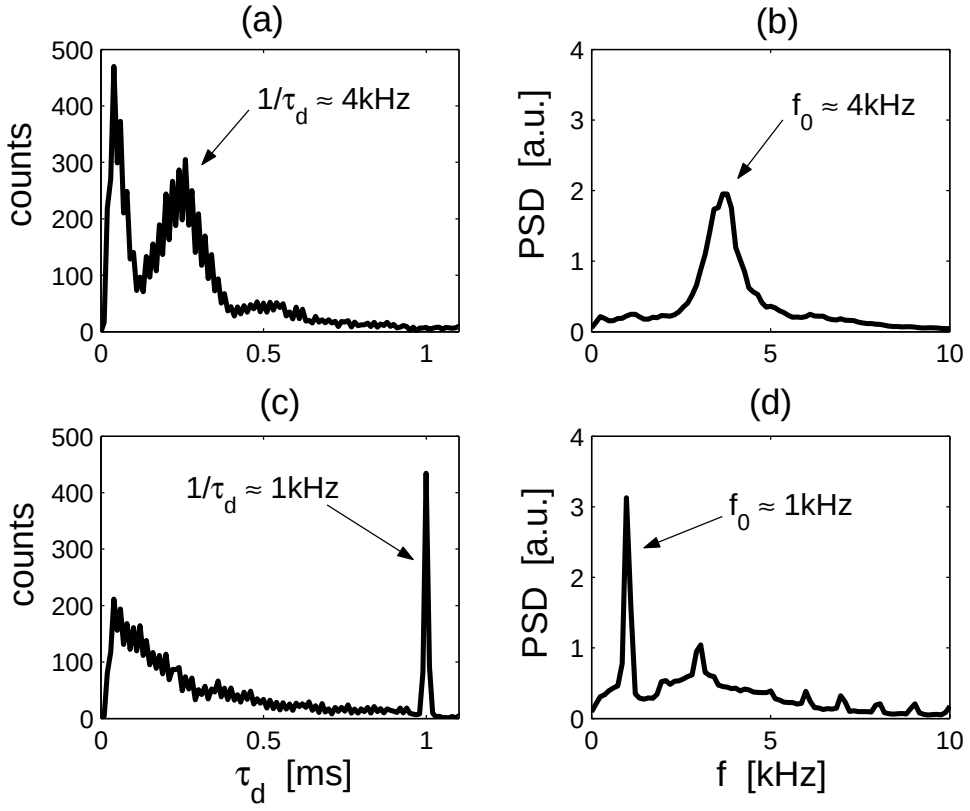

Figure 6.7: *Left:* Histograms of the time delay between spikes in j_c for shots without (a) and with (c) modulation of the injected microwave power (rectangular pulses, frequency 1kHz, duty-cycle 5%). Only data for regions where suprathermals from the UH layer are expected to reach the probe are shown. The threshold level is $I_{th} = 2\,\sigma$. *Right:* Power spectral density of ion saturation current, without (b) and with (d) power modulation, from a probe which is close to the UH layer. The probe and MOANA are aligned along the same magnetic field line. The correspondence between the frequencies of the peaks observed in the probe current and $1/\tau_d$ indicates a link between the dynamics of the suprathermal and fluctuations of the density.

Chapter 7

Basic properties of TORPEX plasmas

This Chapter discusses the basic properties of TORPEX plasmas in the *simple magnetised torus* configuration, used for the study of plasma instabilities and transport. The Chapter is divided into three main parts.
In Sec. 7.1 I illustrate the properties of the time-averaged plasma profiles. The effects of a number of experimental control parameters, such as the injected microwave power and the magnetic field configuration, are discussed. The goal is to vary in a controlled way quantities of importance for the investigated physics, such as the shape of the plasma profiles, their gradient scale lengths and the connection length of the magnetic field lines. Section 7.2 provides an overview of the electrostatic plasma instabilities developing in TORPEX plasmas. The specific experimental scenario used in Part III to investigate transport phenomena is discussed in detail.
Apart from plasma instabilities, flows associated with the creation of the pseudo-equilibrium are responsible for the intermediate time-scales characterising the macroscopic plasma dynamics. This subject is discussed in Sec. 7.3.

7.1 Time-averaged plasma profiles

This Section presents the time-averaged plasma profiles obtained under different experimental conditions. In the following, I refer to the time-averaged profiles as the *background* profiles, on top of which other phenomena, such as the development and the propagation of instabilities, can be present. It should be noted that there are cases for which this operational definition may become less meaningful and even misleading, in particular when the amplitude of the fluctuating quantities is comparable with the mean value of the corresponding background profiles.
As a first example, the profiles of density, electron temperature and plasma potential obtained from Hydrogen with a neutral gas pressure of 6×10^{-5}mbar and an injected microwave power of 400W are reproduced in Fig. 7.1. The currents in the toroidal and vertical magnetic field coils are $I_{tf} = 380$A and $I_{vf} = 60$A, corresponding to $B_\varphi = 76$mT on the axis and $B_z = 1.2$mT. With these parameters, a relatively good up-down symmetry is achieved (see Section 7.1.2).
The density is peaked on the LFS of the EC resonance, with a maximum value slightly higher than the calculated value n_{uh} defining the position of the UH resonance, given in Eq. 4.1. The electron temperature has a similar behaviour. It is almost constant at $T_e \sim 5$eV in the region between the two resonances and drops to ≤ 1.5eV in the outermost regions on the LFS. Similar considerations hold for the plasma potential.
The gradients of all the three quantities, hence of the plasma pressure, have a maximum on the LFS. The same region is characterised by a 'bad' curvature of the magnetic field, relatively to the destabilisation of plasma instabilities [80], and by the maximum of the particle source profile.

7.1.1 Plasma confinement principles and pseudo-equilibrium formation

Simple magnetised tori, such as TORPEX, are characterised by 'open' magnetic field lines intersecting the vessel walls. Therefore, the plasma confinement provided by the magnetic field topology is poor, in contrast to fusion-oriented devices.
The confinement principles and the mechanisms leading to the formation of a pseudo-equilibrium[1] for TORPEX plasmas have been investigated in [70], where a global model, including the effect of the vertical field on the plasma losses, is developed. Two main loss terms are identified. The first term accounts for the direct losses along the open magnetic field lines. The second term is related to the $E_{cs} \times B$ fluid drift, where E_{cs} is a vertical electric field that arises as a consequence of the charge separation induced by the ∇B and curvature drifts [72]. The friction provided by

[1] I call it *pseudo-equilibrium* to differentiate it from a magneto-hydrodynamic equilibrium, that can not be achieved in simple magnetised tori [92].

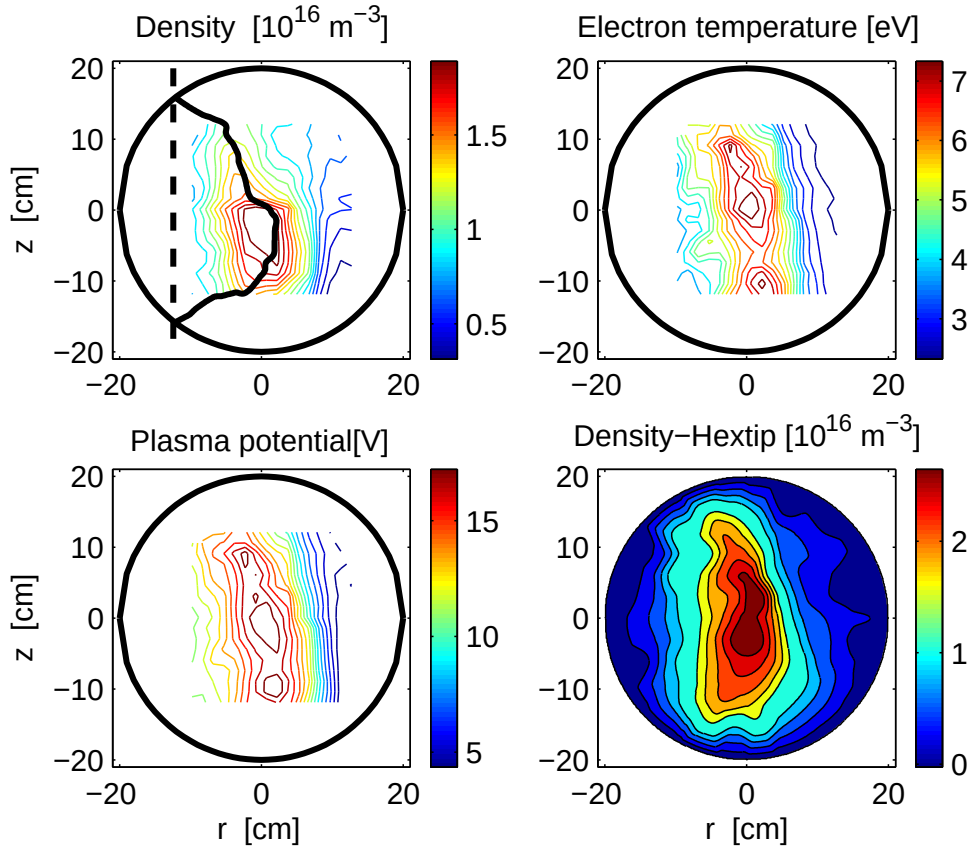

Figure 7.1: Plasma density, electron temperature and plasma potential profiles for a typical Hydrogen plasma. The density measured by HEXTIP is also shown.

Coulomb collisions limits the acceleration parallel to $\underline{B}$. Other loss terms, such as recombination, are neglected. The two loss mechanisms have a different dependence on the pitch angle of the magnetic field. An optimum value for the pitch angle, which results in a maximum confinement time, can be derived from the theory [70][67] and compared with the experimental results, cfr. Section 7.3.3.
Once this pseudo-equilibrium is formed, the fluid drifts characterising inhomogeneous plasmas embedded in a curved magnetic field [32] affect considerably the macroscopic plasma profiles and dynamics. The dominant drifts are the $E \times B$ drift, due to a non uniform plasma potential, and those due to the curvature and the gradient of the magnetic field.
The $E \times B$ drift velocity, $\underline{v}_{E\times B} = (\underline{E} \times \underline{B})/B^2$, can be calculated if the plasma potential profile and the magnetic field are known (Fig. 7.2). The curvature and

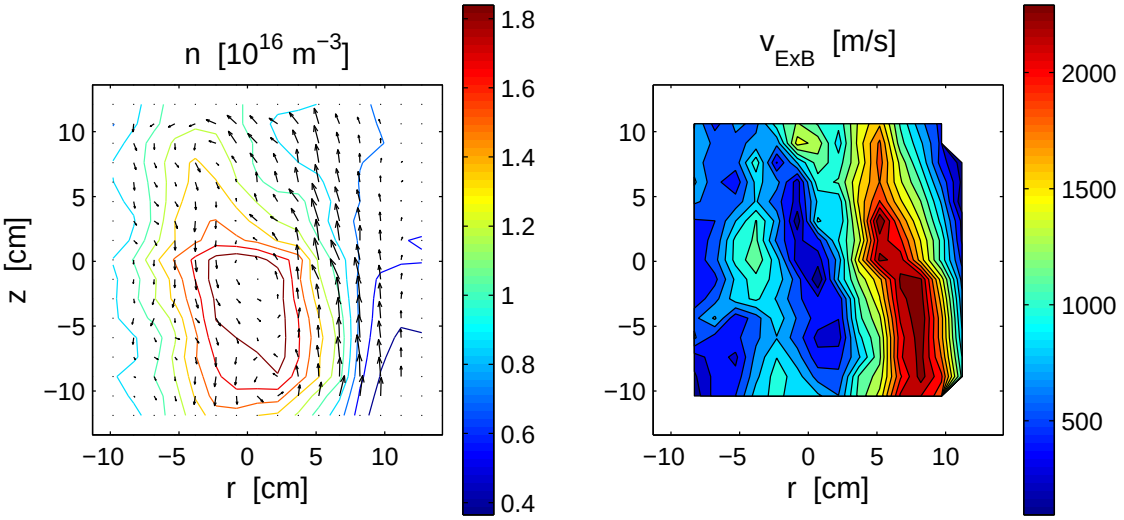

Figure 7.2: $E \times B$ velocity pattern (*left*) and speed magnitude (*right*) for the profiles shown in Fig. 7.1.

∇B drifts are cast into a drift velocity, $\underline{v}_d$ [32]

$$\underline{v}_d = \frac{1}{q\,n\,B}\,\underline{b} \times \nabla p_\perp + \frac{p_\perp}{q\,n\,B}\,\frac{\hat{e}_z}{R_{curv}} \tag{7.1}$$

where $\hat{e}_z$ is the unit vector in the vertical direction, z. Here $\underline{b} = \underline{B}/B$, R_{curv} is the curvature radius and the subscripts $\parallel$ and $\perp$ refer to the direction of $\underline{B}$. The magnetic field, $B \approx B_0 R_0/R$, is generated by currents in the external coils, thus $\nabla \times B = 0$. The pressure tensor is split in its parallel and perpendicular components, $\underline{\underline{P}} = p_\perp(\underline{\underline{I}} - \underline{b}\underline{b}) + p_\parallel\,\underline{b}\underline{b}$ ($\underline{\underline{I}}$ is the unit tensor).
In total, the drift of a fluid element is $\underline{v}_{E\times B} + \underline{v}_d$. Other contributions, such as the polarisation drift $\underline{v}_p = m_e/qB^2\,d\underline{E}/dt$, are found to be negligible. The direction of $\underline{v}_d$ in a poloidal cross section depends on the sign of the charge, q, i.e. is opposite for ions and electrons, with $v_{di} \ll v_{de}$. For a 'positive' toroidal magnetic field[2], ions tend to drift upward and electrons downward, resulting in a vertical electric field component. The total electric field, determining the charge-independent $\underline{v}_{E\times B}$, can be calculated from the measured plasma potential profile. For usual experimental conditions there are regions where $\underline{v}_{E\times B}$ and $\underline{v}_d$ are co-linear, namely on the HFS, and regions where they are opposed, on the LFS.
From Eq. 7.1 it can be seen that the presence of a finite B_z implies a non-zero projection of the drift velocity in the toroidal direction. This suggests that net plasma flows could be present, although only indirect measurements are available at present (Sec. 9.3).

[2]Looking the machine from the top, a positive B_φ goes in the counter-clockwise direction.

In summary, ion and electron drifts depend on external parameters, such as the magnetic field configuration, and on the local profiles of n, T_e and V_{pl}. The latter are self-consistently coupled to each other. The picture becomes more complicated when other populations are considered, for example the suprathermal electrons accelerated at the EC and UH resonances (Chap. 6).

7.1.2 Plasma profile shaping

It is possible to modify in a systematic way the plasma profiles by acting on experimental parameters such as the injected power, the magnetic field configuration and the neutral pressure. In the following, the HEXTIP probe (Sec. 3.4) is used for a qualitative estimate of the density profiles from ion saturation current measurements. When a higher spatial resolution and a more accurate estimate, including the information on T_e, are needed, for example to evaluate the gradient scale-lengths, the SLP probe is used instead. A comparison between the density profiles measured by HEXTIP and by SLP, i.e. taking into account the electron temperature variations, is shown in Fig. 7.1. The two profiles look qualitatively similar, though there are differences in the absolute value of the measured densities and the profiles from SLP show more pronounced peaks. Possible reasons for this discrepancy are inaccuracies in the value of the effective collecting surface used in the analysis. It should be also noted that the geometry of the tip is different for the two probes. A difference in the measurements done with cylindrical and ring-like tips is usually observed on TORPEX. For example, ring-like tips seem to be more sensitive to fast electrons, which results in an overestimated T_e with respect to cylindrical tips.

Effect of the injected power

The effect of the injected microwave power, P_{rf}, on the density profiles is shown in Fig. 7.3. The measurements are done along an horizontal chord on the midplane. Except for P_{rf}, the other parameters are kept constant, with $B_\varphi = 76$mT on the axis, $B_z = 0.6$mT A and $p_{gas} = 3.5 \times 10^{-5}$mbar.
As mentioned in Section 4.2.1, the main effect of an increased absorbed power is to make the density maximum shift to the low-field side (LFS). As a consequence, the position of the UH resonance also shifts to the LFS, until the profile is squeezed on the walls. At this point, a further increase of the absorbed power leads to a local increase of the density, while the volume-integrated density is almost saturated (cfr. Figs. 5.3 and 5.4).
From the examples described above, it results that a careful adjustment of the injected power makes it possible to modify gradually the profiles, thus the derived quantities such as the gradient scale length, with an excellent reproducibility.
However, the tight coupling between the effective absorbed power and the density

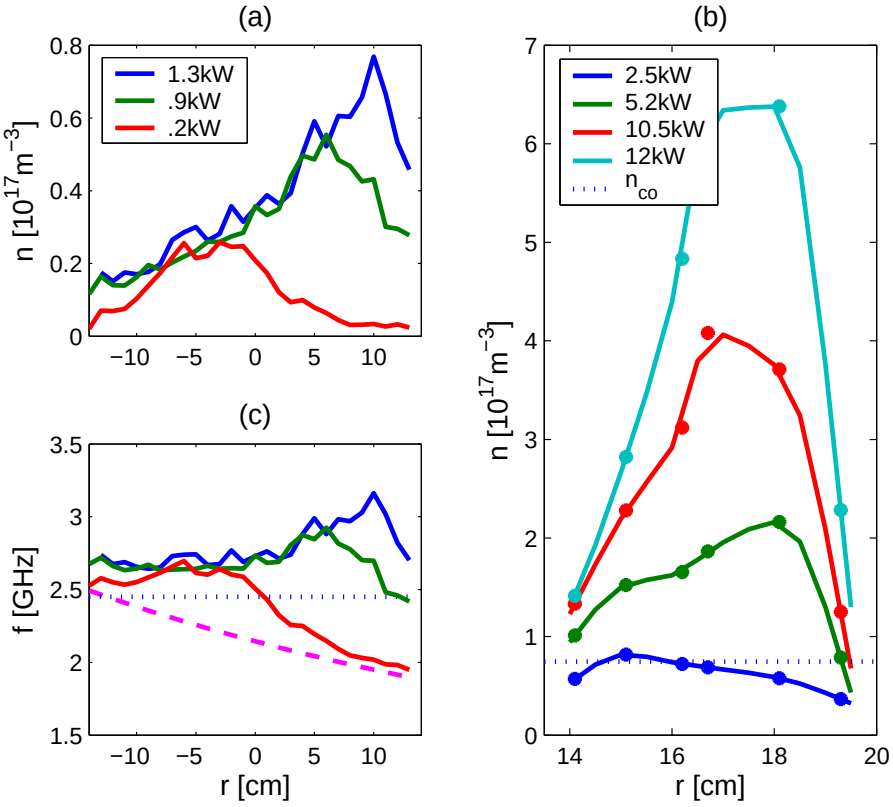

Figure 7.3: *(a)-(b)* Radial density profiles as a function of the absorbed microwave power. Profiles in *(b)* are measured by GLP. *(c)* Corresponding profiles of the EC (dashed) and UH (solid) frequencies. The resonances occur where these frequencies intersect the $f_{rf} = 2.45$GHz line (dotted). n_{co} is the density cut-off value for O-mode propagation.

itself does not allow us to consider P_{rf} as a *control* parameter, independent of the plasma state. To overcome this limitation, one should be able to control the absorbed power, rather than the injected power. The potentiality of this improvement has already been demonstrated in TORPEX (see Appendix A.2.4), but a stable operation of the EC system with this configuration can not yet be ensured for technical reasons, related to the non-linear relation between the voltage controlling the amount of delivered microwave power and the measurements of the power.

Effect of the toroidal magnetic field

The amplitude of the toroidal magnetic field can be adjusted by imposing the current, I_{tf}, flowing in the toroidal field coils. The sign of I_{tf} can be inverted, thus changing the direction of the toroidal field. By fixing I_{tf}, the position of the EC

resonance, R_{ec}, is determined. For standard operations, the EC layer is positioned on the HFS, so that the plasma can expand to the LFS in the remaining portion of the vessel. The most commonly value set for I_{tf} is 380A, implying $R_{ec} = -12.5$cm. Apart from the position of the EC resonance, hence of the plasma profiles, the variations in I_{tf} do not determine substantial changes in the values of the plasma parameters. Referring to Fig. 7.4, when I_{tf} is increased the profile shifts to the LFS, following the change of R_{ec}. For $I_{tf} \geq 440$A, the maximum of the density approaches the wall on the LFS, and a further increase brings the plasma too close to the wall to have a valid experimental configuration.
At present, the range of variations of I_{tf} is limited by the fact that the EC resonance must lie inside the vacuum chamber to initiate the discharge. The range of allowed toroidal magnetic field amplitudes could be broadened by installing other microwave sources at higher frequencies.

Effect of the vertical magnetic field

For a fixed value of I_{tf}, the amplitude of the vertical magnetic field, B_z, determines the pitch angle of the total magnetic field. A larger pitch implies higher direct losses along $\underline{B}$, but also a better compensation of the particle drifts due to the curvature and the gradient of B [70]. The vertical magnetic field is necessary to guarantee the up-down symmetry of the profiles. For values above 0.5mT, B_z has only little effect on the background profiles. In practice, B_z is determined by the current, I_{vf}, flowing in the vertical, or poloidal, field coils. I_{vf} can be arbitrarily adjusted before the discharge, and the direction of B_z reversed by inverting the polarity at the output of the vertical field power supply.
Examples of density profiles for different values of B_z are shown in Fig. 7.5. For $I_{vf} = 0$, the magnetic field is purely toroidal, and particles accumulate in the upper half under the effects of the fluid drifts. As I_{vf} is increased, a better up-down symmetry is achieved. For $I_{vf} \geq 40$A, the profiles are symmetric. In practice, there exist an upper limit, $I_{vf}^{max} \sim 150$A, above which the good toroidal symmetry is lost. A further increase of I_{vf}, hence an increase of the pitch angle, reduces the top-to-bottom connection length, making the ionisation efficiency of the primary electrons so poor that no breakdown occurs.
A relevant parameter that is varied by changing I_{vf} is the *connection length*, L_c, i.e. the length of a field line connecting the bottom to the top of the vessel. With a toroidal magnetic field $B_\phi = B_0 R_0 / R$ and a constant vertical field, the connection length is a function of the major radius (Fig. 7.7).

Effect of the neutral gas pressure

The neutral pressure, p_{gas}, is, in practice, the least effective among all the experimental parameters that can be used to act on the background profiles. This can be

seen in Fig. 7.8, where an increase of p_{gas} by a factor > 3 determines no appreciable variations of the profiles. The neutral pressure is usually set within the range 2×10^{-5}mbar $< p_{gas} < 2 \times 10^{-4}$mbar. For lower pressures, the ionisation efficiency is poor, and no breakdown occurs. For higher pressures, an overdense plasma forms just in front of the microwave antenna, preventing the microwaves to spread around the torus to form toroidally symmetric profiles. On the other hand, p_{gas} is an interesting parameter to vary other important physical quantities, such as the collision rate between plasma particles and neutrals.

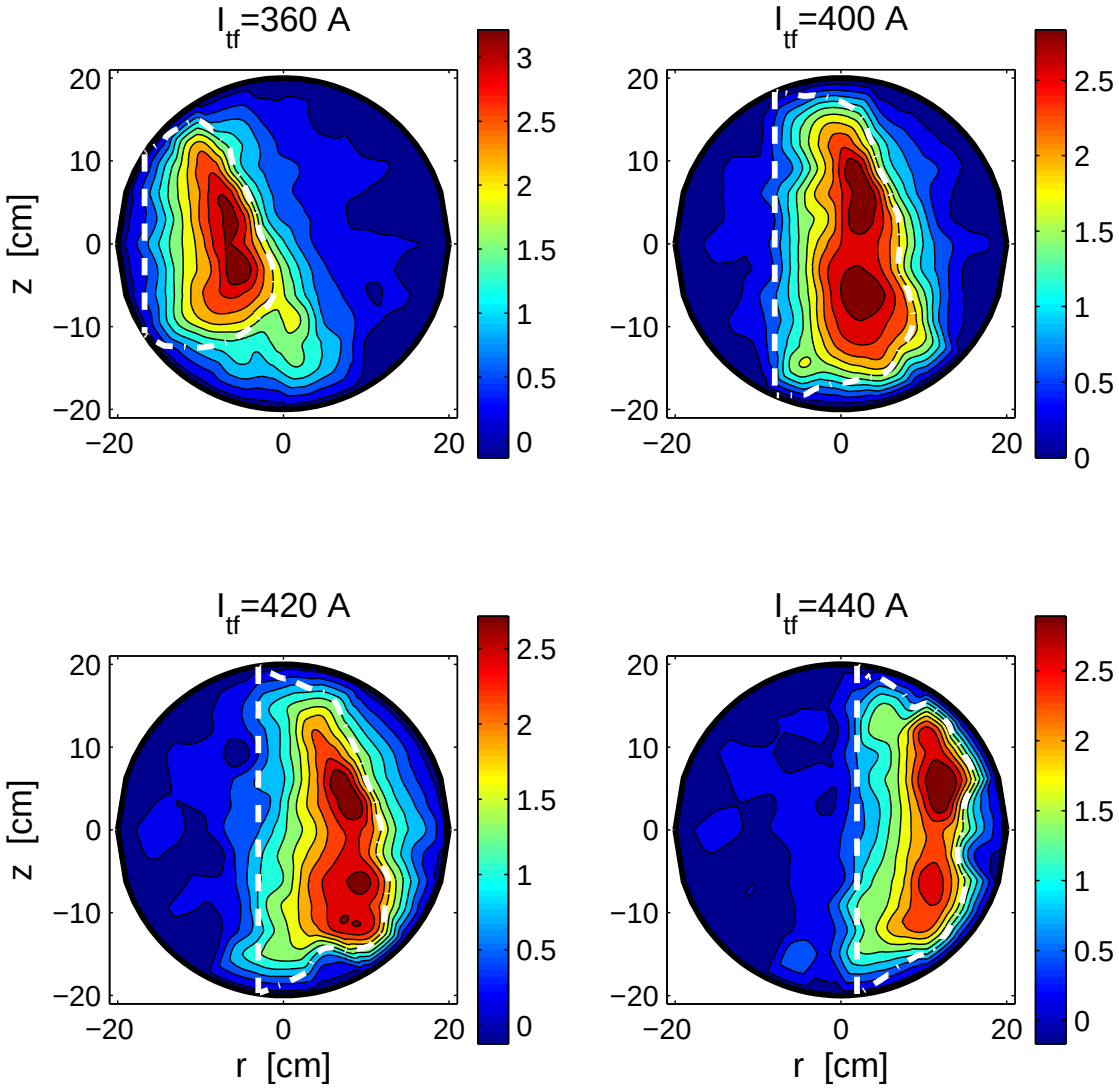

Figure 7.4: Density profiles from the HEXTIP probe for different values of the toroidal magnetic field. The position of the EC (dashed) and UH (dash-dotted) resonances are shown.

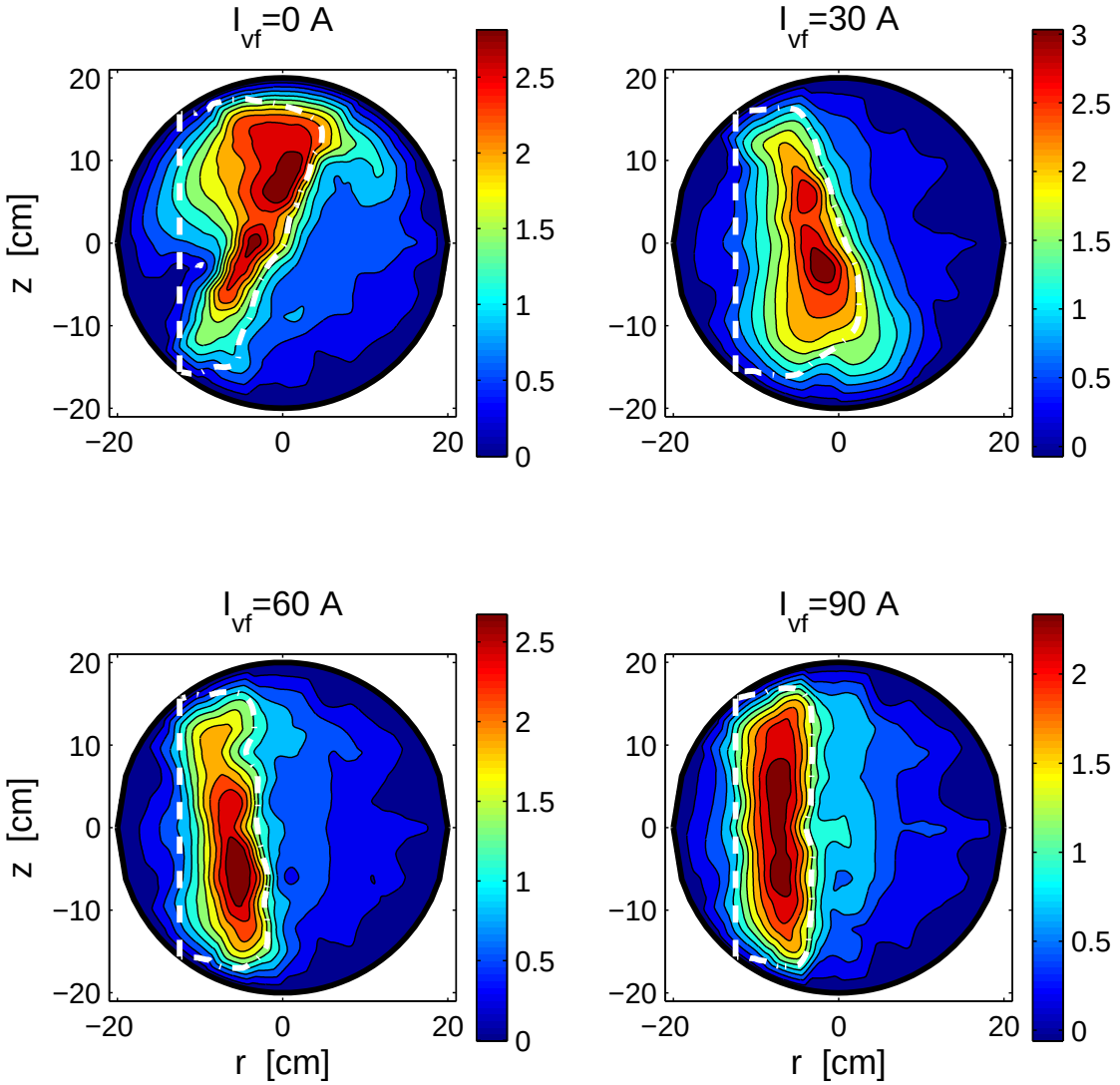

Figure 7.5: Density profiles from the HEXTIP probe for different values of the vertical magnetic field. The position of the EC (dashed) and UH (dash-dotted) resonances are shown.

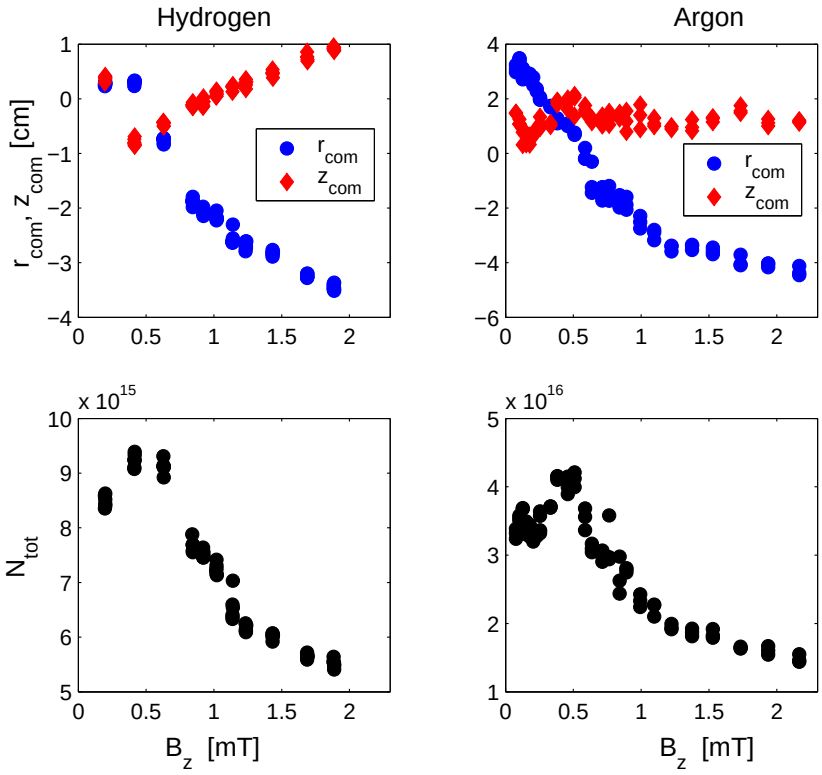

Figure 7.6: *Top:* Radial and vertical position of the plasma centre-of-mass as a function of B_z for Hydrogen and Argon plasmas. *Bottom:* Volume-integrated density as a function of B_z.

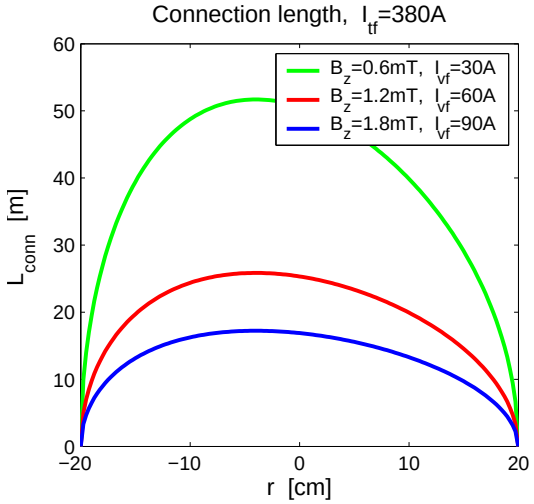

Figure 7.7: Connection length as a function of the radial position for $I_{tf} = 380A$ and three different values of vertical field, B_z.

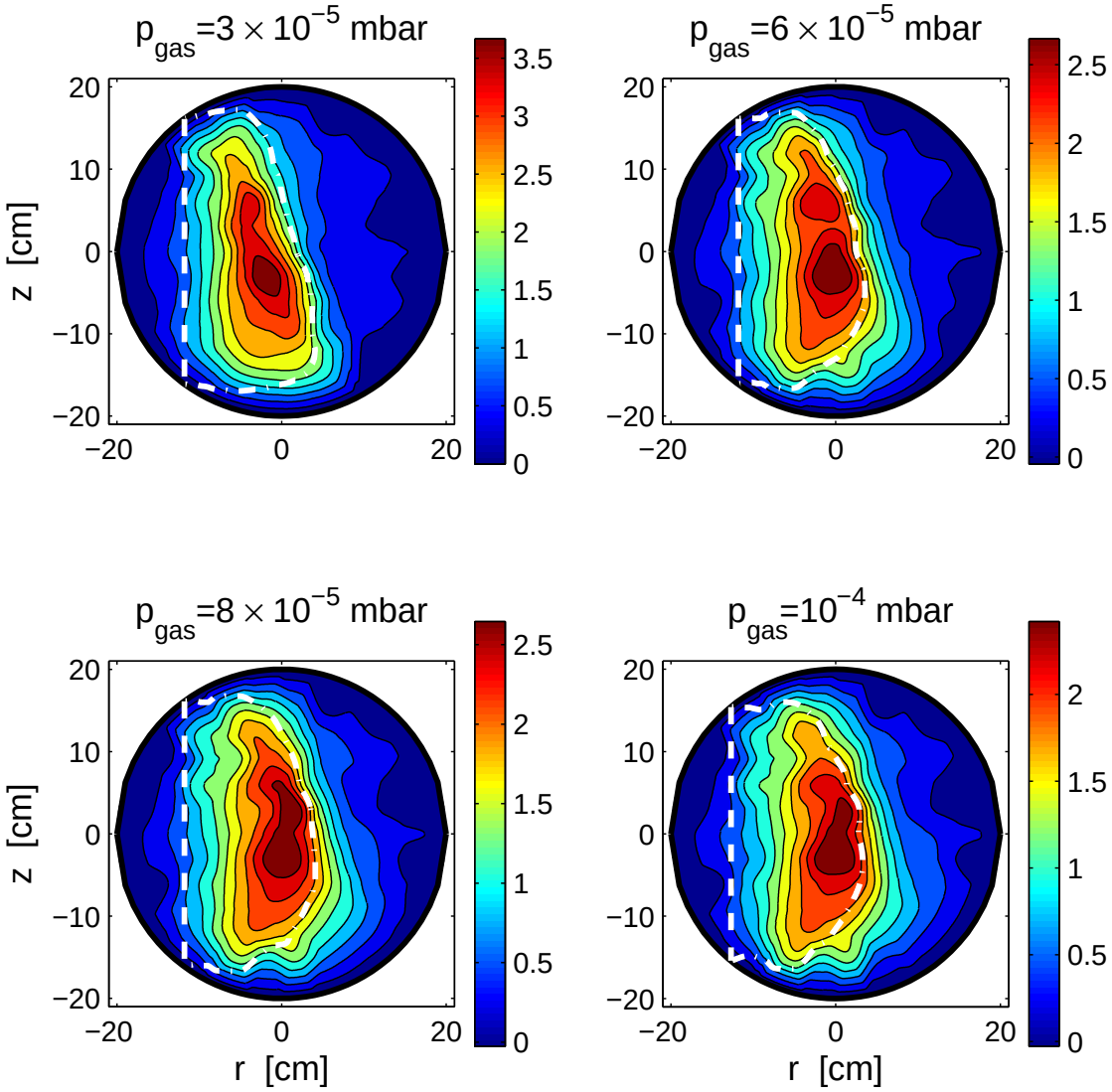

Figure 7.8: Density profiles from the HEXTIP probe for different values of the neutral gas pressure. The position of the EC (dashed) and UH (dash-dotted) resonances are shown.

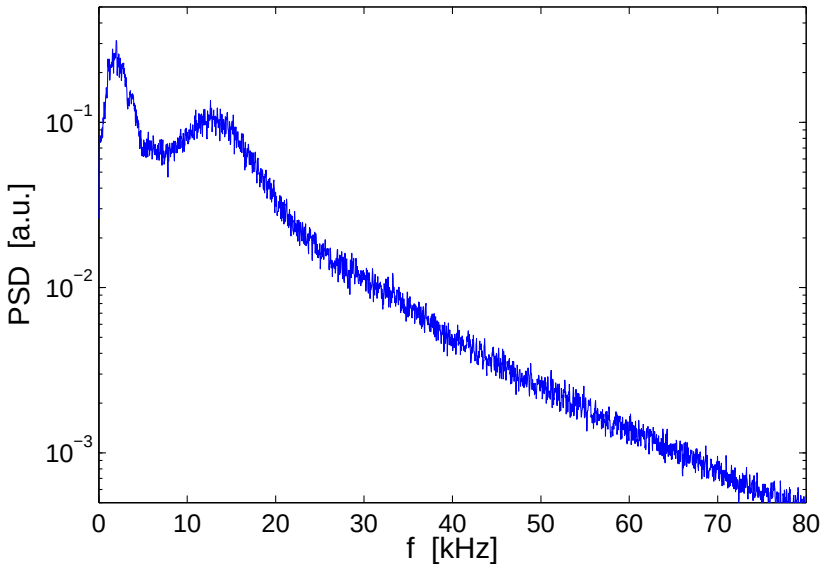

Figure 7.9: Example of a power spectral density of density fluctuations (PSD, in arbitrary units) measured at $r = 0$, $z = 0$ for $B_z = 1.2$mT.

7.2 Electrostatic instabilities in TORPEX

As shown in the previous Section, TORPEX plasmas are characterised by spatial gradients in density and electron temperature, hence in the plasma pressure. This non-uniformity of the plasma pressure provides a free energy source for drift waves [45], characterised by a low frequency, $f < \omega_{ic}/2\pi$, where ω_{ic} is the ion-cyclotron frequency. The presence of a curved magnetic field provides an additional drive for the destabilisation of modes in regions where the pressure and magnetic field gradients are co-linear [80]. The unstable modes may be characterised by a non-zero phase between density and potential fluctuations, which results in a net particle and heat flux. This *fluctuation-induced* flux can be higher than the classical flux due to Coulomb collisions by several order of magnitude, and may contribute significantly to the high flux level observed in the core of fusion devices [112].
The main features of the instabilities observed in TORPEX are described in this Section, as part of the illustration of the experimental background for the investigation of the transport mechanisms at play in TORPEX plasmas, presented in Part III. Their complete study and characterisation are the subject of the PhD thesis of F. M. Poli, see Ref. [79]. We focus here on a particular experimental scenario, with $B_\varphi = 76$mT on the axis, $B_z = 1.2$mT and $P_{rf} \approx 400$W, for which the background profiles are shown in Fig. 7.1. The role of a particular experimental parameter, the vertical magnetic field, is also discussed to generalise the results.
A power spectrum from an ion saturation current signal, measured by the TRIP

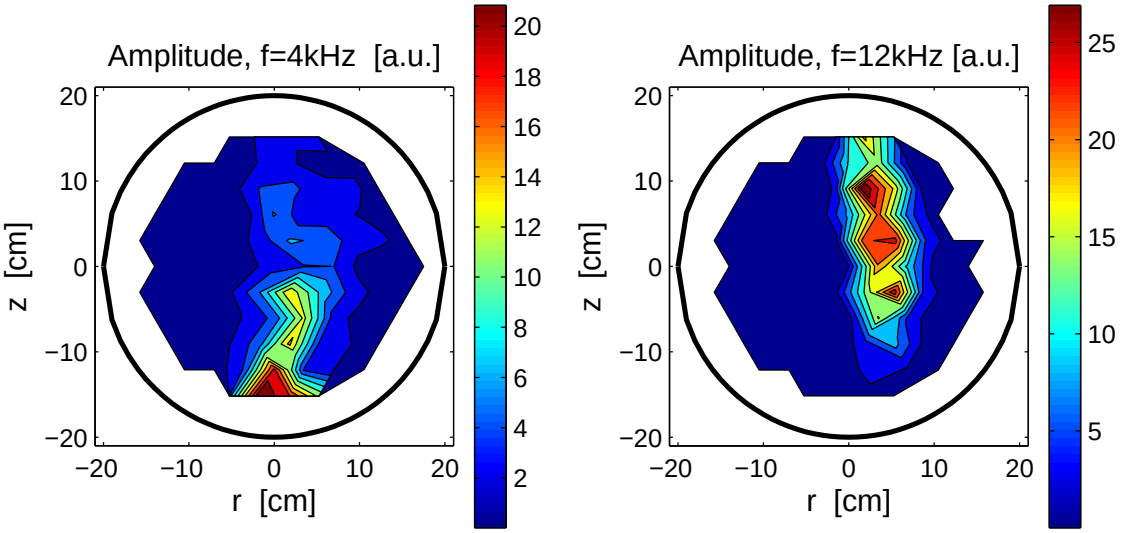

Figure 7.10: 2-D profiles of the amplitude of fluctuations with frequency around 4kHz and 12kHz. The plasma profiles are the same as in Fig. 7.12.

probe (Sec. 3.4) at the midplane at $r = 0$, is shown in Fig. 7.9. Two spectral regions can usually be distinguished, centred around[3] $f = 4$kHz and $f = 12$kHz. Figure 7.10 shows the two-dimensional profiles of the density fluctuations amplitude for the two frequency bands. It can be seen that the fluctuations are maximum where strong plasma pressure gradients, co-linear with the magnetic field gradient, ∇B, are present. Only low-amplitude fluctuations are observed on the high-field side, where the density gradient has opposite direction with respect to ∇B. Note that another peak, with $f = 2$kHz, appears for $B_z \leq 1.2$mT and lower values of the neutral gas pressure. This mode is also localised in the region of high density gradient, with an amplitude profile more centred on the midplane with respect to the 4kHz mode. Examples of this experimental scenario are given later, in Part III, where Hydrogen plasmas obtained from $p_{gas} = 3.5 \times 10^{-5}$mbar are studied.
The instability at $f = 4$kHz originates in the bottom region of the poloidal cross section. From here, it is convected upward by the underlying $E \times B$ drift, almost perpendicularly to the density gradient (Fig. 7.2). This is consistent with the fact that, as a first approximation, the waves propagate with the electron diamagnetic velocity, v_{de}, in the plasma frame of reference, moving with respect to the laboratory frame because of the macroscopic plasma drifts, dominated by the $E \times B$ drift. Since at the low-field side[4] is $v_{E\times B} > v_{de}$, the net direction of propagation

[3]The exact values of these frequencies may change slightly for different experimental sessions. I refer here to the typical values, which are usually reproducible within ±1kHz.

[4]The velocities $\underline{v}_{E\times B}$ and $\underline{v}_{de}$ are, in practice, almost parallel. Their relative direction may change, depending on the local plasma profiles.

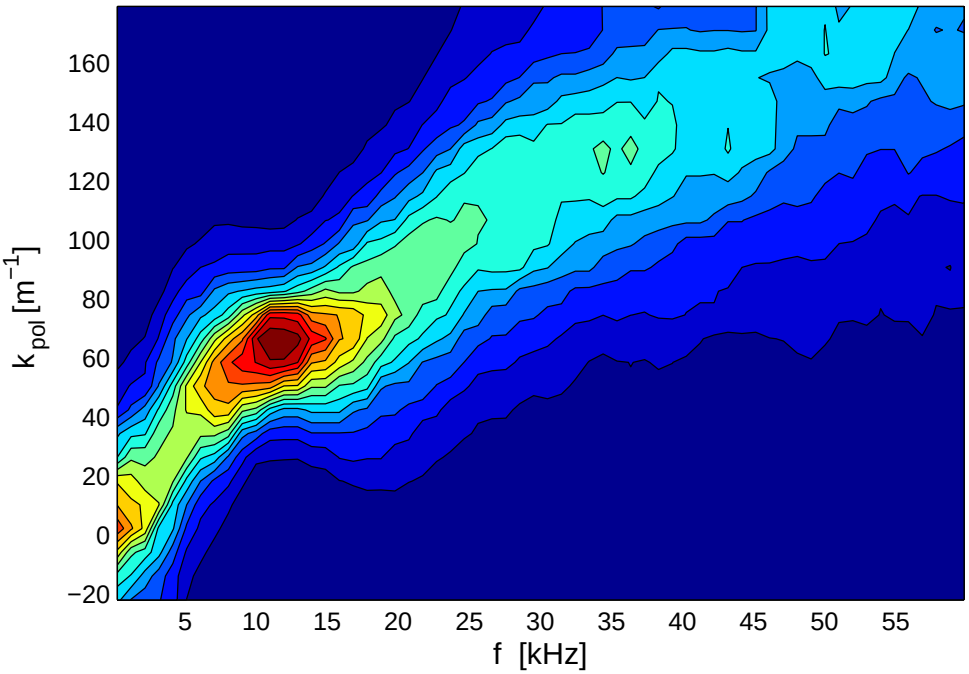

Figure 7.11: Conditional frequency-wavenumber spectrum measured at the midplane at $r = 16$cm [79].

in the laboratory frame is that of $\underline{v}_{E\times B}$ [80]. The mode amplitude is attenuated in the upper half of the poloidal section, consistently with a loss of energy to higher frequencies modes due to non-linear mode-mode coupling [81]. The wave-numbers in the directions perpendicular[5] and parallel to the magnetic field, k_{pol} and $k_{\|}$, have been measured by means of two-points correlation techniques [3]. The conditional frequency-wavenumber spectrum, measured by the FLP probe (Sec. 3.4) at $r = 16$, $z = 0$cm, is shown in Fig. 7.11 and gives $k_{pol} \sim 20\text{m}^{-1}$ for $f = 4$kHz. For the same frequency, a parallel wavenumber, $k_{\|} \sim 0.5\text{m}^{-1}$, is measured by means of two toroidally separated probes aligned on the same magnetic field line, following the method described in Ref. [80]. For the mode at $f = 4$kHz, the condition $k_{\|}/k_{pol} \ll 1$, typical for drift waves, is satisfied. The measured parallel wave-number is small but finite, thus ruling out the possibility that the observed modes are in this case pure interchange, or 'flute', modes. Similar considerations hold for a mode at frequency $\lesssim 2$kHz, which is measured for values of the vertical magnetic field ≤ 1.2mT, and is also identified as a drift mode [80].
The mode at $f = 12$kHz presents different features. From Fig. 7.10 we observe that it originates on the low-field side around $z = -10$cm, then develops in a region of

[5]We define k_{pol} as the wavenumber perpendicular to $\underline{B}$ and to the density gradient, in the direction which roughly corresponds to the propagation direction of the waves in the plasma frame.

strong $E \times B$ flow, cfr. Fig. 7.2. The perpendicular and parallel wavenumbers are $\approx 70\text{m}^{-1}$ and ≈ 0, suggesting that this mode is an interchange mode.
The coexistence of modes with different nature is a common feature for different experimental conditions. In particular, a systematic dependence of the relative strength of the modes is observed upon the value of B_z, hence of the tilt angle of the vertical magnetic field and of the connection length. For $B_z \leq 0.6\text{mT}$ only the drift modes, with $f \leq 5\text{kHz}$, are observed. As B_z is increased a broad-band peak at $\approx 15\text{kHz}$, an interchange mode, appears and becomes dominant for $B_z \geq 1.2\text{mT}$. A further increase in B_z makes its frequency to decrease from 15kHz to $\approx 5\text{kHz}$ for $B_z = 2\text{mT}$, probably because the reduced connection length prevents the occurence of unstable modes with extremely long parallel wavelengths.

7.3 Intermediate time-scales of the macroscopic plasma dynamics

This Section discusses the time-scales that characterise the macroscopic variations of density, electron temperature and plasma potential other than the fluctuations associated with plasma waves and instabilities, already addressed in the previous Section. The particle confinement time, τ_p, is investigated. Different methods are presented, which provide information on local and global values of τ_p.
The confinement time can be inferred from local measurements of the density decay time after a fast switch-off of the microwave power source. This method is useful to get information on the spatial dependence of τ_p, although in the interpretation of the results one should take into account that measurements are taken during a non-stationary plasma phase. The same technique can be applied to estimate the *total* plasma confinement time, i.e. the typical time scale over which the volume-integrated density decays. A similar technique was used in [70], where the measurements were limited to a few positions in a poloidal cross section and a single decay-time constant was inferred. In reality, different mechanisms can simultaneously regulate the density decay, leading to a competition between different time-scales.
More sophisticated techniques are based on the plasma response to a modulated injected power. In this case the plasma is maintained in a stationary state by a constant level of injected power, to which small perturbations are superimposed. These techniques are extended to the study of the decay time of electron temperature and plasma potential by means of a software-implemented boxcar-averaging technique, described in Sec. 8.4. An overview of the results obtained with the different techniques is given below, when possible for the same target plasma. The reference background plasma profiles are shown in Fig. 7.12. The injected power is $\approx$ 200W, the toroidal and vertical magnetic fields are $B_\varphi = 76$mT, $B_z = 1.2$mT, and the neutral gas pressure is 6×10^{-5}mbar.
A first calculation of τ_p can be done considering the single-particle confinement mechanisms in TORPEX. Neglecting the weak electrostatic confining forces, ions and electrons flow along $\underline{B}$ toward the walls, but are subject to the ∇B and curvature drifts. The confinement time corresponds to the average time-of-flight from the source region to the walls. We associate a time-of-flight to each of the two drift velocities, $v_{\nabla B}$ and v_{curv}, and evaluate τ_p as their average. The mean distance that a particle covers before it reaches the walls is taken as the minor radius, a, therefore

$$\tau_p = \left(\frac{v_{\nabla B}}{a} + \frac{v_{curv}}{a} \right)^{-1} \tag{7.2}$$

For $T_e = 5$eV and standard values of the magnetic field we obtain $\tau_p \sim 250\mu$s for electrons.

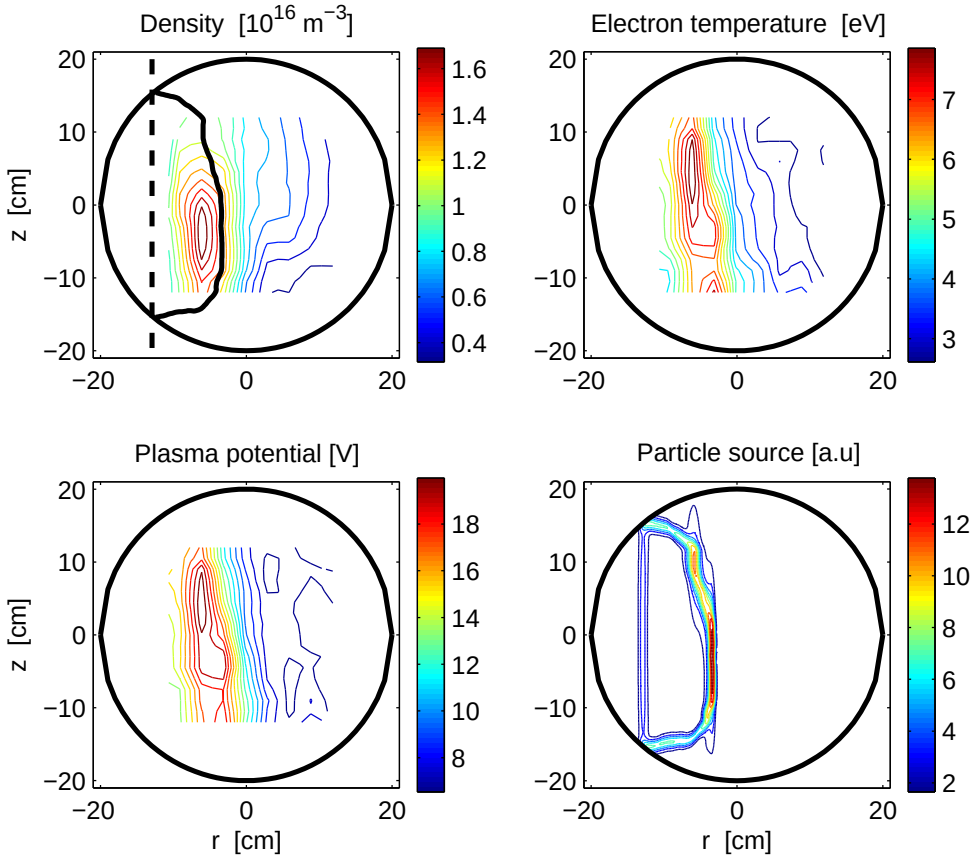

Figure 7.12: Plasma density, electron temperature, plasma potential and particle source profiles for the Hydrogen plasma investigated in this Section.

7.3.1 Decay time analysis

We assume that the plasma density response to perturbations is governed by N typical time constants, that we identify with $\tau_{p,i}$. The density decay after a switch-off of the power source can be modelled as $n(t) = n_0 \sum_{i=1}^{N} k_i \exp(-t/\tau_{p,i})$, with $\sum_{i=1}^{N} k_i = 1$. Here the density is assumed to be simply proportional to the ion saturation current, i.e. electron temperature variations are neglected (cfr. Appendix B.1). The validity of this assumption is discussed in Sec. 7.3.3, on the basis of the available information on the electron temperature dynamics.
An example of a raw density trace after switch-off of the microwave source is shown in Fig. 7.13, from which we note that two distinct τ_p's can be identified, and the normalised density decay is well fitted by

$$n(t)/n_0 = \alpha \exp(-t/\tau_{p,s}) + (1-\alpha) \exp(-t/\tau_{p,f}) \tag{7.3}$$

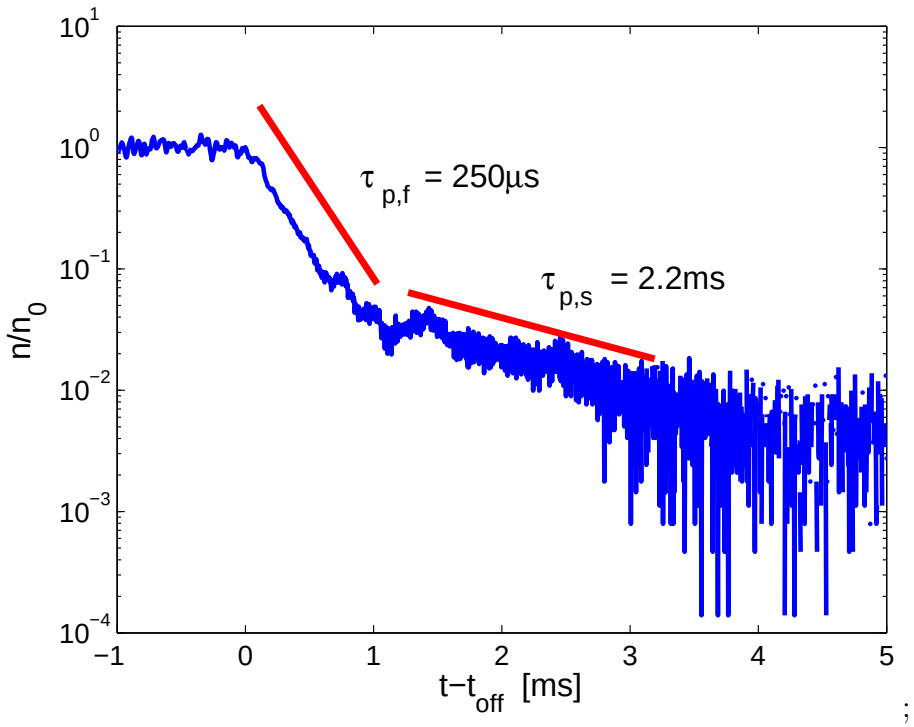

Figure 7.13: Example of a decaying density signal after switch-off of the microwave power. Two distinct time-constants are identified.

where n_0 is the density in the stationary phase and the 'fast' and 'slow' time-constants, $\tau_{p,f}$ and $\tau_{p,s}$, are introduced. This feature is common to most plasma regions. The coefficient α, with $0 \leq \alpha \leq 1$, gives the relative weight of the two time constants in regulating the decay. Just after the power switch-off the plasma is lost at the rate $\tau_{p,f}$, which is of the same order as the one derived from a simple estimate of the particle drifts. After a few times $\tau_{p,f}$, the higher time constant dominates the decay.
Additional information is obtained by comparing the results of the typical *global* and *local* decay times. In the first case the density is integrated over the whole cross-section. In the second case the evolution of the local density, as measured by a single probe tip, is considered. The dependence of τ_p on experimental parameters such as the injected power, the magnetic field configuration and the neutral gas pressure has been investigated. The main results, presented in the next paragraphs, are discussed in Sec. 7.3.3.

Global decay time

To evaluate the global decay time, it is convenient to use data from the HEXTIP probe, which provides the density profile and its temporal behaviour over most of the poloidal cross section in a single discharge. The signals from HEXTIP are summed up to get the time evolution of the volume-integrated density, $N_{tot}(t)$. The fit of $N_{tot}(t)$, normalised to its stationary level during the plasma discharge, with Eq. 7.3 gives the two time-constants and the parameter α. The procedure can be repeated for different experimental conditions to investigate the dependence of τ_p on specific experimental parameters.
An example of a scan of B_z is shown in Fig. 7.14. The integrated density and the slow time-constant exhibit a clear trend with B_z, with a maximum for $B_z \approx 0.5$mT (cfr. Figs. 7.6 and 7.21), while $\tau_{p,f}$ and the parameter α are almost constant. A very similar behaviour is observed for Argon plasmas, with a maximum of N_{tot} and $\tau_{p,s}$ occurring for $B_z \approx 0.5$mT.
The maximum of $N_{tot} = N_{tot}(B_z)$ can be understood by looking at the position of the density centre-of-mass as a function of B_z, shown in Fig. 7.6. When no vertical magnetic field is applied, the density is shifted with respect to the centre of the chamber, under the effects of the curvature and ∇B drifts. By increasing B_z the drifts are partly compensated by a motion of the plasma along B and the profile is almost symmetric with respect to the midplane. When $B_z > .5$mT the direct losses along B are more and more relevant. The integrated density is decreased and, consistently, the radial position of the centre-of-mass shifts to the high-field side. The dependence of τ_p on other parameters, such as the neutral gas pressure, does not show any clear trend for this value of injected power (Fig. 7.14), which is consistent with a negligible dependence of the plasma profiles on that parameter.

Local decay time

Instead of summing up the density signals to obtain $N_{tot}(t)$, the time-constants $\tau_{p,f}$ and $\tau_{p,s}$ can be measured locally as a function of the position in the poloidal plane. An example is shown in Fig. 7.15 for the same case presented in Fig. 7.12. This exercise allows one to compare the profiles of the decay time with the profiles of n, T_e and V_{pl}, and with the local values of derived quantities and geometrical parameters, for example the collisionality and the connection length. We observe that the fast time-constant dominates the density decay in regions characterised by high density and electron temperature. At the low-field side the decay is dominated by the slow time-constant, as can be seen from the fact that the parameter $\alpha \to 1$. The same behaviour is observed on the high-field side with respect to the EC resonance, as highlighted in discharges where the EC resonance is close to $r = 0$ and the plasma can expand to the high-field side.

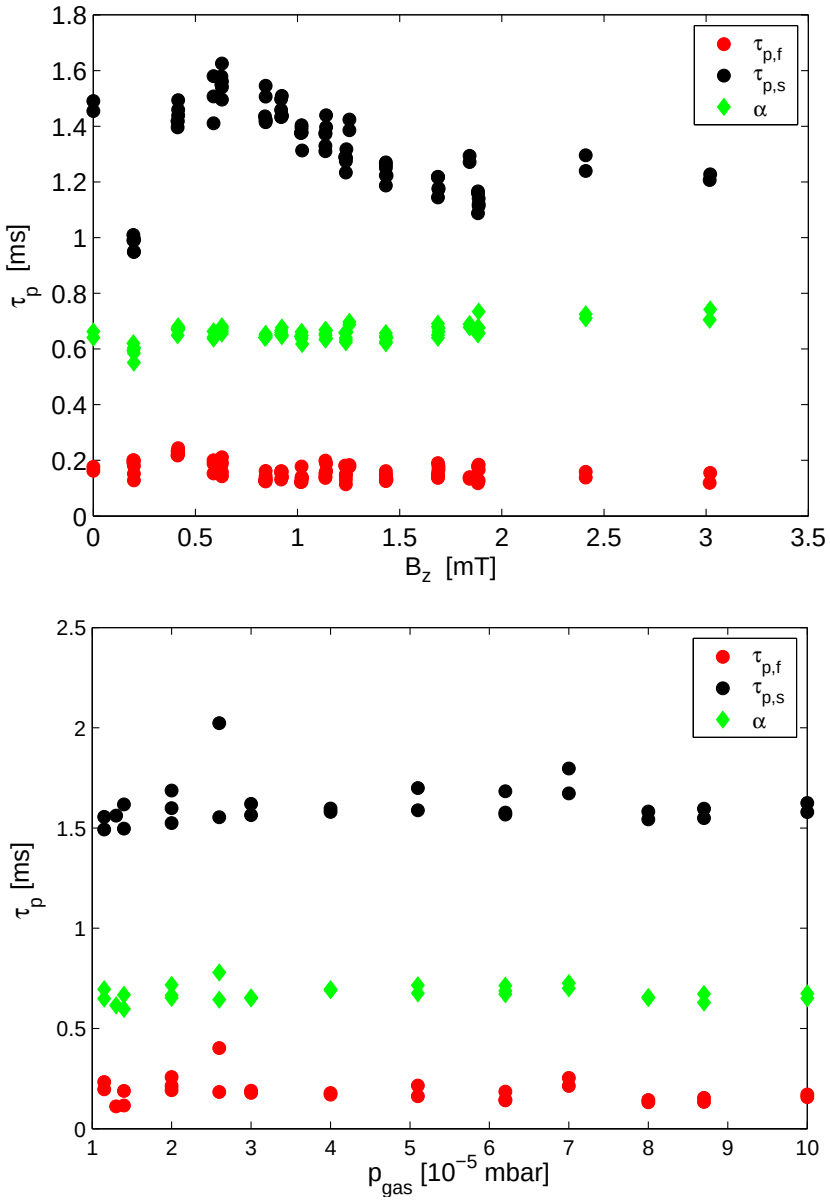

Figure 7.14: *Top:* Time-constants characterising the density decay for different values of the vertical magnetic field, B_z. The parameter α (cfr. Eq. 7.3) is also plotted. *Bottom:* Time-constants for different values of the neutral gas pressure, p_{gas}. The magnetic field values are $B_\phi = 76$mT and $B_z = 0.6$mT.

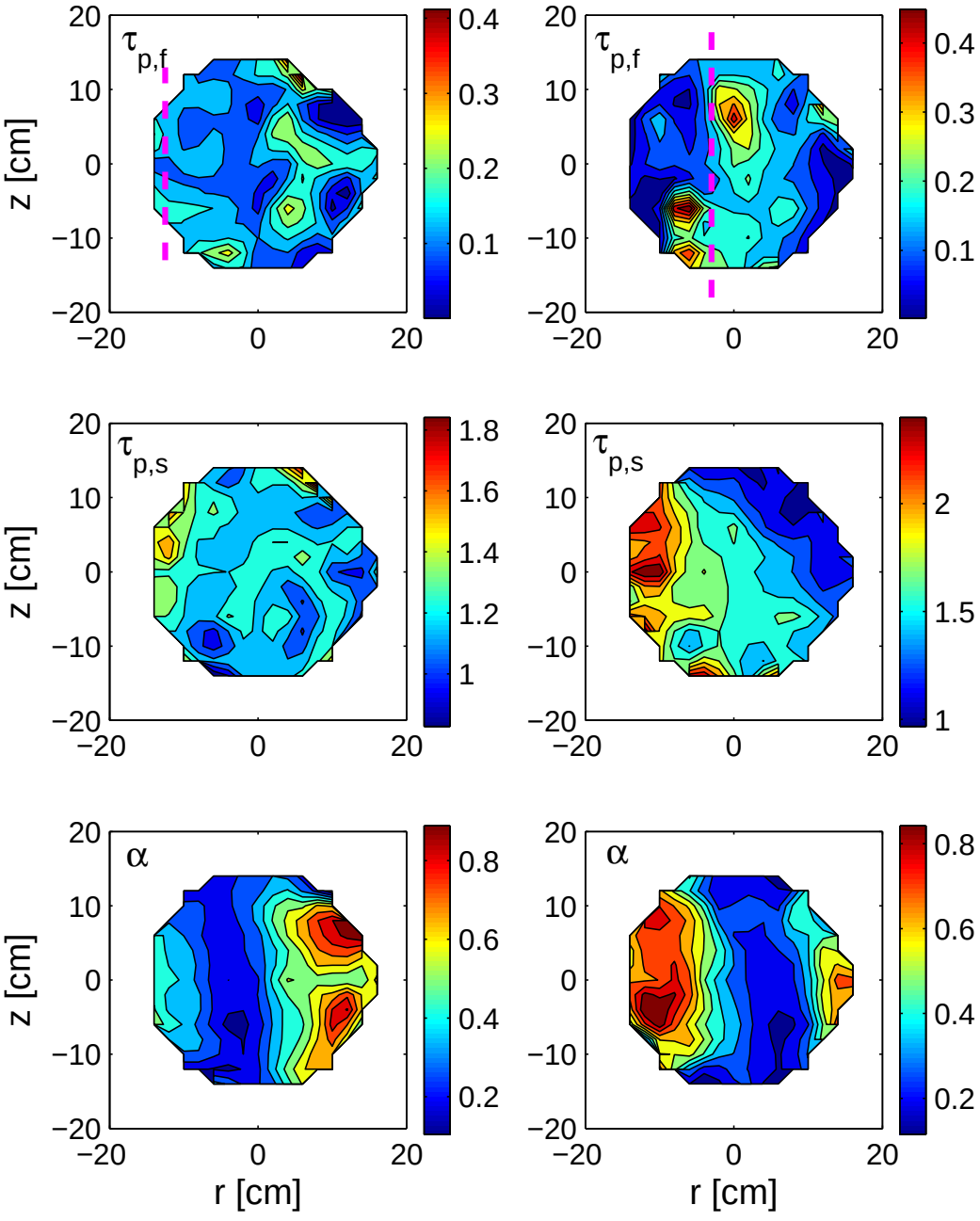

Figure 7.15: Density decay times, in [ms], and parameter α (cfr. Eq. 7.3) measured in a poloidal cross section for two values of toroidal magnetic field, $B_\phi = 76$mT (*left column*) and $B_\phi = 86$mT (*right column*), corresponding to $I_{tf} = 380$A and $I_{tf} = 420$A. The corresponding density profiles are shown in Fig. 7.4. The dashed line in the upper figures indicate the position of the EC resonance.

7.3.2 Analysis of the plasma dynamical response

The plasma response to a modulation of the injected power can be measured to determine the time scales over which the plasma reacts to an external stimulus [71]. The advantage with respect to the time-decay analysis is that the plasma is maintained in a stationary state, to which small perturbations are applied. In this Section I review the two possibilities that have been explored in TORPEX to establish the transfer function between density and modulated injected power:

- The density response to small-amplitude sinusoidal perturbations with different modulation frequencies is analysed in Fourier space.
- The plasma is perturbed with fast pulses, ideally representing 'delta' functions in time. The *poles* of the transfer function, representing the time-constants of the system, are recovered by means of Laplace space analysis [61].

Fourier techniques

We start from the density continuity equation

$$\frac{\partial n}{\partial t} = -\frac{n}{\tau} + S \tag{7.4}$$

where all the loss channels, including particle fluxes, are modelled by the loss term $-n/\tau$, and the particle source, S, is taken into account. Equation 7.4 is linearised by separating n and S in a stationary and a time-dependent part (subscripts '0' and '1'). Since $\partial n_0/\partial t = 0$ we obtain, after Fourier transformation for the time variable:

$$-i\,\omega\, n_1 = -\frac{n_1}{\tau} + S_1 \tag{7.5}$$

where we have assumed that the perturbed density and source simply vary in time as $\exp(-i\,\omega\, t)$. The transfer function n_1/S_1 calculated from Eq. 7.5 is

$$\frac{n_1}{S_1} = -\frac{\tau}{1 + i\,\omega\,\tau} \tag{7.6}$$

and is characterised by a cut-off frequency $= 1/\tau$. Note that S_1 is a local particle source term, which is *a priori* unknown. The only information we have from the experiments is the amplitude of the power modulation, p_1. We assume that S_1 can be expressed as $S_1 = \alpha(\underline{x})\, p_1$, where the position dependent coefficient $\alpha = \alpha(\underline{x})$ is independent of the modulation frequency. Both the density and the power modulation signals can be measured, thus τ can be obtained by fitting the experimental response of n_1 with Eq. 7.6. Examples of this procedure are shown in Fig. 7.16, from which we note that this simple approach works only for regions close to the particle source locations.

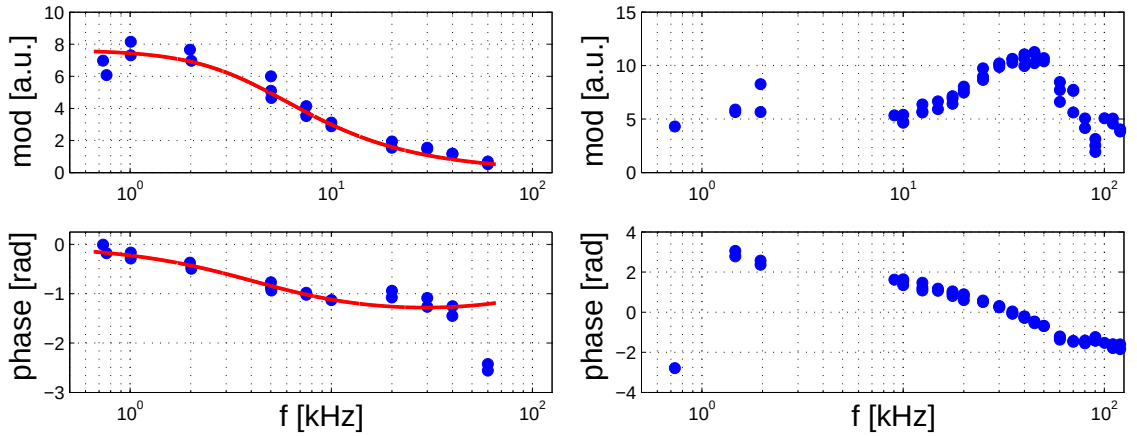

Figure 7.16: Full circles: amplitude and phase of the measured transfer function n_1/S_1 for a sinusoidal modulation of the injected microwave power. The results from two different positions are shown. *L*eft: Close to the UH resonance the transfer function is well fitted by the single time constant model (thick line), cfr. Eq. 7.6. *R*ight: Far from the resonances, a more complex transfer function is measured, that cannot be represented by the simple model of Eq. 7.6.

A further hypothesis on the dominant transport mechanisms at play is required for a correct analysis. For an extensive discussion, see Part III. We assume here that density perturbations originating in the particle source region are subject to convection only. Recombination occurs at rates $< 10^2 \mathrm{s}^{-1}$, and is neglected. In this case, there exists a phase shift, $\Delta\phi$, between n_1 measured at a generic point and the perturbed source signal, S_1. The term $\Delta\phi$ is measured from the density and injected power signals. We substitute $n_1 \rightarrow n_1\, e^{i\,\Delta\phi}$ and from Eq. 7.5 we obtain

$$\frac{1}{\tau} = i\,\omega + \frac{S_1}{n_1}\, e^{-i\,\Delta\phi} \tag{7.7}$$

The coefficient α can be calculated by imposing that the time constant τ be real:

$$\Im\left[i\,\omega + \alpha\,\frac{p_1}{n_1}\, e^{-i\,\Delta\phi}\right] = 0 \;\Rightarrow\; \alpha = -\frac{\omega\, n_1}{p_1}\,\frac{1}{\Im\left[e^{-i\,\Delta\phi}\right]} \tag{7.8}$$

The real and imaginary parts are indicated with $\Re$ and $\Im$. At this point the only unknown in Eq. 7.7, τ, is given by

$$\tau = \left(\Re\left[i\,\omega + \frac{S_1}{n_1}\, e^{-i\,\Delta\phi}\right]\right)^{-1} \tag{7.9}$$

In practice, it is preferable to have many independent realisations of n_1, namely with different modulation frequencies and/or amplitudes.

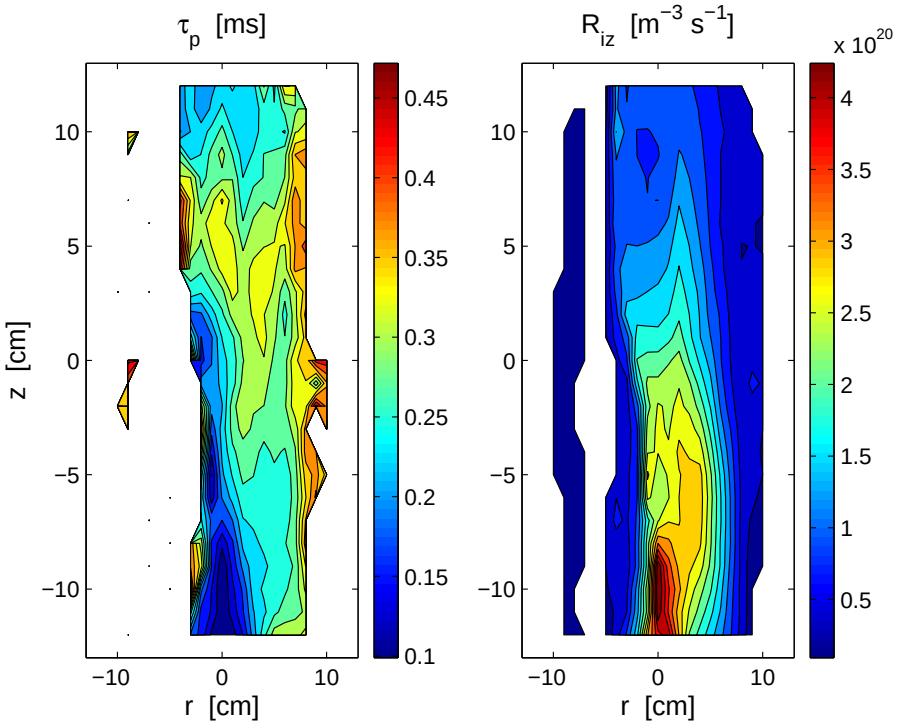

Figure 7.17: Example of Fourier analysis for estimates of the particle confinement time and of the perturbed ionisation profile by means of Eqs. 7.8 and 7.9. Three different modulation frequencies are used, 120, 360 and 720Hz. Another example is shown in Fig. 9.6 for a different set of experimental parameters.

In addition to τ, the ionisation source profile is obtained. An example over a limited region in the poloidal cross section is shown in Fig. 7.17 for the same data shown in Fig. 7.15. There is a good agreement with the decay time method, although from Eq. 7.9 only an average τ_p can be deduced.

Laplace techniques

The *poles* of the transfer function between injected power and density response can be deduced from the response to a step change of the microwave power [71][110]. In practice the power is modulated with rectangular pulses, ideally representing 'delta' perturbations in the time domain. The response can be averaged over many modulation cycles to improve the signal-to-noise ratio.
The poles measured in this way can be used to estimate the natural time-constants, such as the confinement time, that regulate the dynamics of the system.
In general, the results agree well with those derived from the Fourier space and decay time techniques. As a disadvantage, it turns out that, for standard discharge

lengths $\leq$ 1.5s, the modulation amplitude must be high (of the order of 2kW for a stationary injected power $\leq$ 500W) in order to have a good signal to noise. Moreover, it is observed on TORPEX that a fast increase in the injected power originates fast electrons (see Chap. 6), which makes it difficult to separate ion and electron responses in the data. A signature of the presence of suprathermal electrons dominating the probe response may be, for example, the fast initial drop of the measured ion saturation current at the beginning of a power pulse.
To overcome the limitations of the ion saturation current measurements, the Laplace analysis technique can be extended to the results of a software-implemented boxcar-averaging technique. The details on the implementation of the boxcar method for Langmuir probes data are given in Sec. 8.4. Here we focus on its application to the investigation of the plasma dynamics time-scales, including the behaviour of electron temperature and plasma potential. A characterisation of the dynamics of the suprathermal electron component is attempted.
This technique has two advantages. First, it allows a better measurement of the density response, since the variations of T_e are included. Second, a knowledge of the electron temperature and plasma potential response provides more information than the density response alone. Figure 7.18 shows an example of the time evolution of the main plasma parameters following a short pulse of the injected power. The data is taken in a region corresponding to the UH resonant layer. The time traces result from an average over $\geq$ 150 modulation cycles. The samples obtained in this way can then be analysed to extract the poles of the plasma response for each specific parameter. From Fig. 7.18 we observe that the plasma parameters vary on different time-scales. The time constant characterising the density decay, $\tau_{p,f} \approx 300\mu$s, is recovered.
More interesting is the response of the plasma potential and of the electron temperature, which slightly increase after the pulse and decay considerably faster than n. The increase of V_{pl} is probably responsible for the fast decrease of the density observed at the beginning of the pulse. The same feature is observed when the density is estimated from the ion saturation current. The fast rise of the absorbed microwave power would then perturb the local plasma potential, hence the electric field, which in turn expels ions out of the UH layer. Note that a similar mechanism is invoked to explain the density pump-out observed in tokamaks during strong EC heating [116], although the issue is still debated and other explanations have been proposed [111][26].
The same analysis can be applied to reconstruct the dynamics of the suprathermal electrons. The details on the measurements of the suprathermals are given in Chap. 6. Two examples are shown in Fig. 7.19. The results are compatible with those presented in Fig. 7.18. The increase in the plasma potential and a first decrease of n, followed by an increase and a decay with a time-constant $\tau_{p,f} \approx 300\mu$s, are confirmed. From Fig. 7.19 it appears that the energy and density of the suprathermals

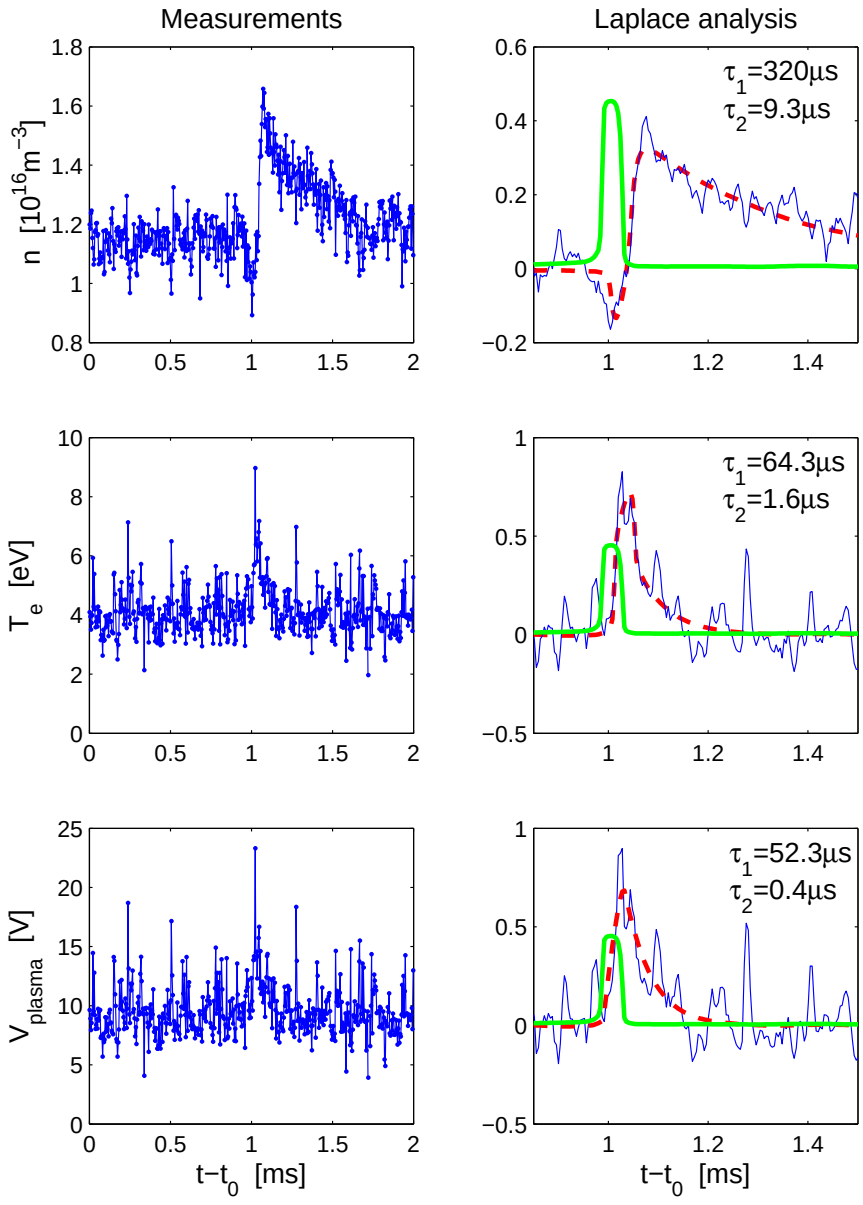

Figure 7.18: Coupled Laplace analysis and boxcar-averaging technique for estimating the density, electron temperature and plasma potential relaxation time constants. The three parameters vary with different time-scales. The time-constant for density relaxation is comparable with that obtained from decay-time analysis. *Left column:* Reconstructed signals. *Right column:* Signals variations after a pulse of the injected power (thin, blue lines) and the best fit resulting from the Laplace analysis (dashed, red lines). The injected power pulse, in arbitrary units, is shown for reference (thick, green lines).

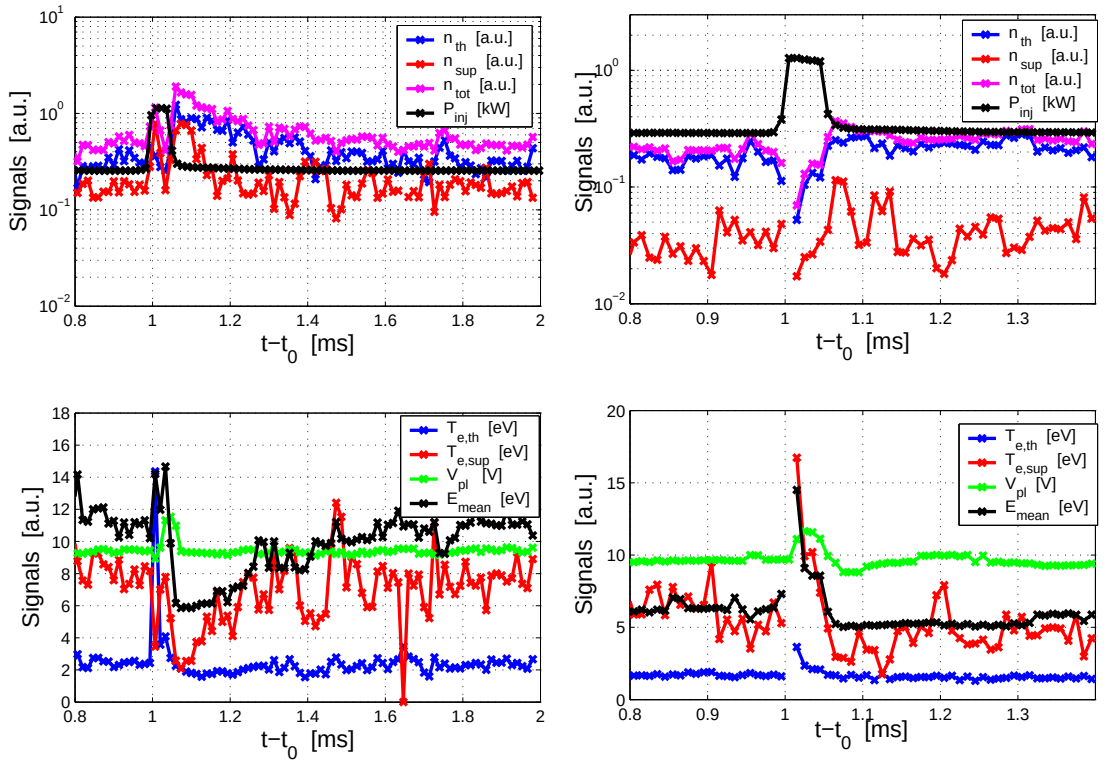

Figure 7.19: Boxcar-averaging technique applied to data from MOANA to investigate the dynamics of plasma potential, including the effects of suprathermal electrons, measured at $r \approx 10$cm (*left*) and $r \approx 5$cm (*right*). The UH layer is at $r = 10$cm. The traces show the density and temperature for the bulk (n_{th}, $T_{e,th}$) and for the suprathermals (n_{sup}, $T_{e,sup}$), the plasma potential V_{pl} and mean energy of the electron population. The injected microwave power, P_{inj}, is also shown for reference.

increase during the power ramp-up, then decrease below the stationary value, which is re-established on a time-scale comparable with $\tau_{p,f}$. As we move away from the UH layer inside the main plasma these features are preserved, but the 'bulk' density increase is much less evident, compatibly with the fact that ionisation mostly occurs in a narrow layer around the resonances (cfr. Chap. 4 and Chap. 5). No clear result has been obtained so far for regions corresponding to the EC resonant layer, where the boxcar method fails due to the low density and low energy of the suprathermals.

7.3.3 Discussion

The previous results show that simple measurements of the density decay time can provide information on the macroscopic plasma dynamics as a function of experimental parameters, such as the vertical magnetic field and the neutral gas pressure. Other methods, namely a combination of Laplace analysis of the plasma response to a modulated microwave power with boxcar-averaging techniques, are more suitable when more complete information is needed, for example to investigate the simultaneous dynamics of n, T_e and V_{pl}.
Within the limits of each method, the results obtained from the decay time analysis and from the Fourier and Laplace analysis agree fairly well. The density decay time calculated from I_{sat} (Eq. 7.3) is usually smaller than that measured with the Laplace analysis. A possible explanation is suggested by Fig. 7.19, where one can see that T_e decays faster than n after a perturbation. For practical convenience, an average decay time, $\tau_{1/2}$, is introduced as the time required to observe a density drop to 50% of its original value, and therefore includes all the three parameters which appear in Eq. 7.3. By noting that the decay time is actually estimated from $I_{sat} \propto n\, T_e^{1/2}$, neglecting T_e variations leads to underestimating $\tau_{1/2}$.
On the basis of the measured local density decay time, the plasma can be divided into two regions, characterised by values $\tau_{1/2} \leq .2$ms and $\tau_{1/2} \geq .2$ms:

- The first region corresponds to the *main plasma* region[6], where the particle source is located and n, T_e and V_{pl} have their maximum values. The measured $\tau_p \approx \tau_{p,f}$ is almost constant.

- The second region corresponds to a *source-free region*, characterised by low density and electron temperature, $n \leq 5 \times 10^{15}\mathrm{m}^{-3}$ and $T_e \leq 2$eV. The plasma profiles are almost flat and the drift velocity low, which may suggest a 'stagnation' of the plasma. In fact, here the typical confinement time is $\approx \tau_{p,s}$ and increases for decreasing n, T_e and V_{pl}.

These results are summarised in Fig. 7.20. They can be used for a comparison between the experiments and the predictions of a theoretical model [67], cfr. Sec. 7.1.1. Note that the model is *global* and assumes uniform profiles, therefore the comparison is made using the volume-averaged density and the average decay time. The theoretical model predicts a strong influence of B_z on the confinement time, and weaker variations upon parameters like p_{gas} and T_e. An example of the dependence of $\tau_{1/2}$ and N_{tot} upon B_z for Hydrogen and Argon is shown in Fig. 7.21. It can be seen that B_z has an influence on N_{tot} which is maintained for different values of the toroidal magnetic field. The variations of $\tau_{1/2}$ with B_z, dominated by variations of the slow time-constant (cfr. Fig. 7.14), are not systematic, as results when different values

[6] A complete characterisation of the different plasma regions is given in Sec. 11.1.2.

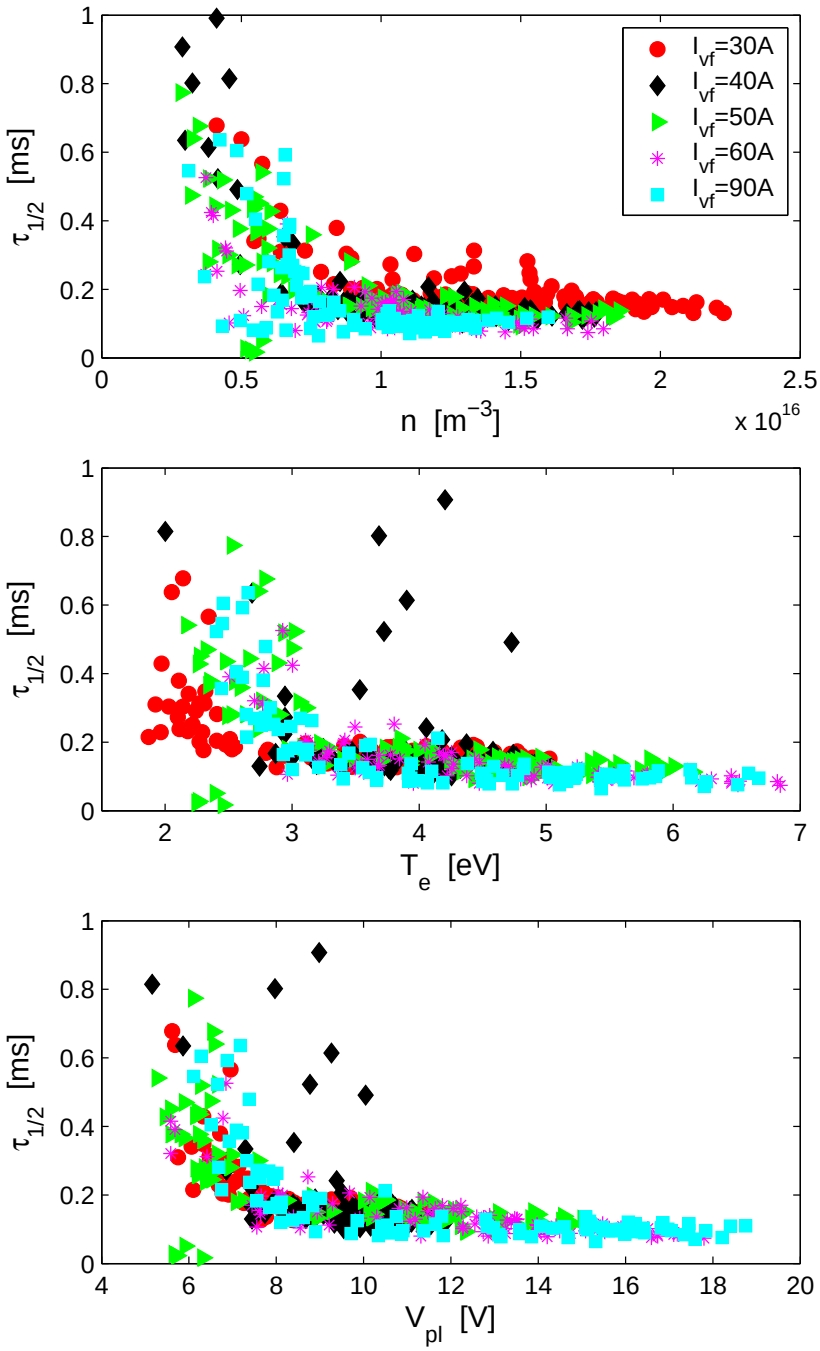

Figure 7.20: Local $\tau_{1/2}$ as a function of plasma density, electron temperature and plasma potential for five values of B_z.

of toroidal magnetic field are compared. The dependence on the gas mass and the predicted inverse dependence of $\tau_{1/2}$ on N_{tot} are not observed in the experimental data.

In general, we note that inhomogeneities in the plasma profiles are common to all the discharges analysed, while the model assumes spatial homogeneity. A model including possible spatial variations of the plasma parameters should then be used for more precise predictions. In conclusion, apart from the correlation with the time-averaged density, electron temperature and plasma potential, the measured $\tau_{1/2}$ does not show any unambiguous dependence on other quantities such as drift velocity, pressure gradient, connection length and electron collisionality. Note that all these quantities refer to the plasma before the power is switched off, and they are expected to vary along with the density decay.

No further conclusions on the transport mechanisms at play in TORPEX can be attempted on the basis of these results. Dedicated experiments and appropriate experimental techniques are needed, as discussed in Part III.

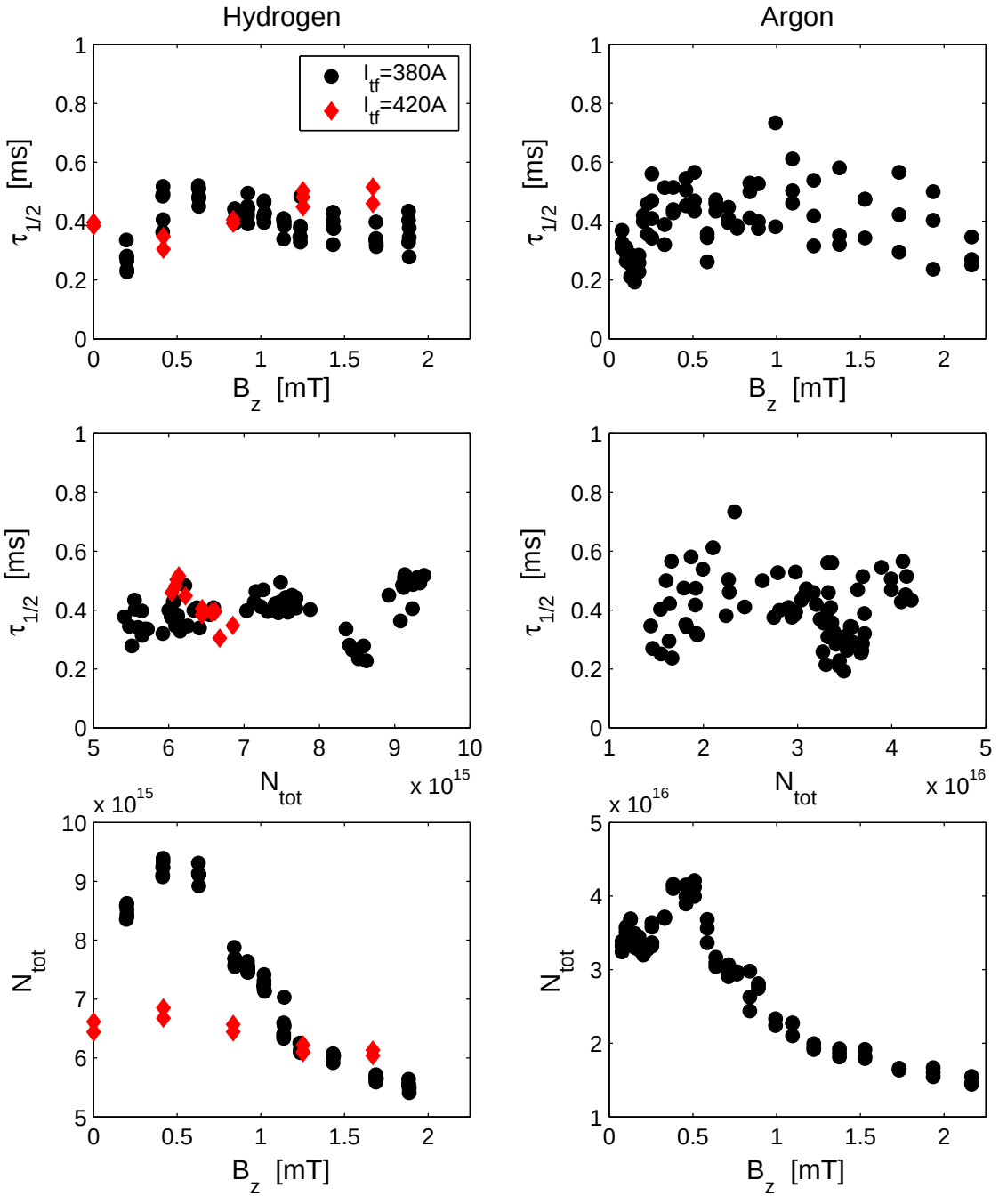

Figure 7.21: Relation between B_z, N_{tot} and $\tau_{1/2}$ used for a comparison with a theoretical model for the particle confinement time [67]. Data from Hydrogen (*left column*) and Argon (*right column*) plasmas are presented.

Part III

Particle and heat transport in TORPEX

Chapter 8

Experimental and analysis techniques for transport studies

In this Chapter, I present the techniques that are used on TORPEX to measure the particle transport and identify the basic mechanisms behind it. A major part of the Chapter is dedicated to the measurement of the fluctuation-induced flux, performed using analysis in the frequency domain, via standard Fourier methods, and in the time domain. Despite the relative simplicity of the Fourier-based method, described in Sec. 8.2, a correct interpretation of the data requires the simultaneous knowledge of density and plasma potential fluctuations. In practice, the plasma potential is recovered from measurements of the *floating* potential. Additional measurements of electron temperature fluctuations, described in Sec. 8.1.2, are needed to relate unambiguously the two quantities.
The second approach is based on a conditional reconstruction of the time-space evolution of density, plasma potential and electron temperature (Sec. 8.5). It combines the standard 'conditional average sampling' technique (Sec. 8.3) with a software-implemented boxcar-averaging technique (Sec. 8.4).
To gain more insight into the *statistical* properties of the transport, a method based on the identification of plasma 'structures' and their dynamics in real-space, developed in a previous Thesis work [67], can be used (Sec. 8.6).
The methods mentioned above are used to measure the flux related to fluctuations, but they do not provide any information on the *total* fluxes. This can be inferred by means of a technique, presented in Sec. 8.7, based on the plasma response to a modulation of the injected microwave power.

8.1 Measurement of electron temperature fluctuations

By a convenient setup of the signals acquired on each tip, the TRIP probe installed on TORPEX can be used as a *triple probe* [22][18] to measure electron temperature fluctuations. The triple probe method is discussed in the next Sections, along with an example of the results obtainable on TORPEX.

8.1.1 Triple probe method

A triple probe consists of three pins. Two tips, floating with respect to ground, are connected to each other through a fixed voltage source (Fig. 8.1). Their voltages are indicated as V^+ (tip#1) and V^- (tip#2), with $\Delta V = V^+ - V^-$. The third tip measures the floating potential, V_{fl}. Since $V^- < V_{fl} < V^+$, a negative (electron) current flows in tip#1 and a positive (ion) current in tip#2.
The analysis is based on the continuity of the current flowing in the two tips at $V = V^+$ and $V = V^-$ (Fig. 8.2). The current in each tip, I_1 and I_2, is

$$I_1 = I_{i,1} - I_{e,1}\, e^{-\frac{V_{fl,1}-V^+}{T_e/e}} \tag{8.1}$$

$$I_2 = I_{i,2} - I_{e,2}\, e^{-\frac{V_{fl,2}-V^-}{T_e/e}} \tag{8.2}$$

where

$$V_{fl,1} = V_{fl,2} = V_{fl}\ ,\quad I_{i,1} = I_{i,2} = I_i\ ,\quad I_{e,1} = I_{e,2} = I_e \tag{8.3}$$

assuming that the tips are identical and close enough to each other. By imposing $I_1 \equiv -I_2$ we obtain:

$$\frac{2\, I_i}{I_e} = e^{-\frac{V_{fl}-V^+}{T_e/e}} + e^{-\frac{V_{fl}-V^-}{T_e/e}} \tag{8.4}$$

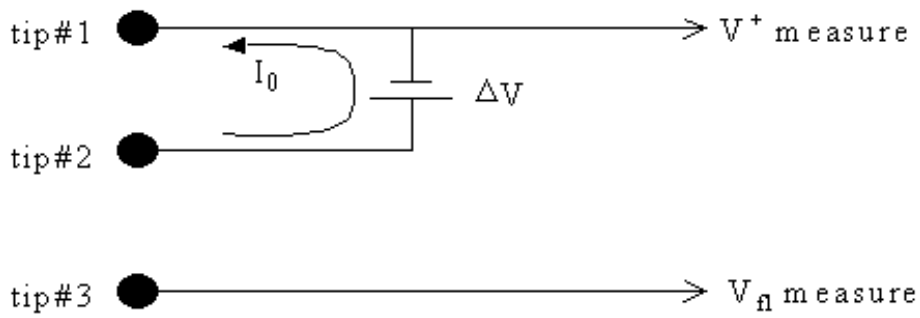

Figure 8.1: Layout of the tip connections used to exploit the triple probe method.

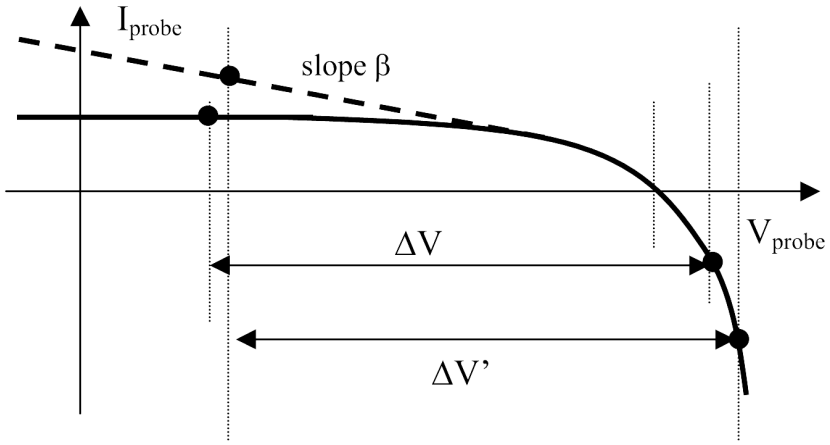

Figure 8.2: Illustration of the triple probe method.

and, by replacing $V^- = V^+ - \Delta V$

$$\frac{2\,I_i}{I_e} = e^{\frac{V^+ - V_{fl}}{T_e/e}} \left(1 + e^{-\frac{\Delta V}{T_e/e}}\right) \tag{8.5}$$

Equation 8.5 can be simplified if $\Delta V \gg T_e/e$. In addition, if the ion current does saturate for a sufficiently negative probe voltage, Eq. 8.5 becomes [22]

$$2 = e^{\frac{V^+ - V_{fl}}{T_e/e}} \tag{8.6}$$

from which T_e can be obtained

$$T_e = \frac{e\,(V^+ - V_{fl})}{log\,2} \tag{8.7}$$

The expression in Eq. 8.7 is commonly used to infer T_e from a triple probe [22]. However, the time-averaged T_e values obtained for TORPEX plasmas from Eq. 8.7 are almost twice the average values given by SLP and TWEEDY. We identified two main sources of errors [18]:

- The condition $\Delta V \gg T_e/e$ is not fulfilled. The resulting T_e is underestimated.
- The ion current does not saturate (see Fig. 8.3). The resulting T_e is overestimated.

The first point can be accounted for by solving Eq. 8.5 iteratively. To address the second point, the I-V curve for that specific probe must be known, in order to infer the correct expression for $I_i = I_i(V_{pr})$. For the TRIP probe we have

$$I_i(V_{pr}) \approx I_{i,0}\,(1 + \beta\,V_{pr}) \tag{8.8}$$

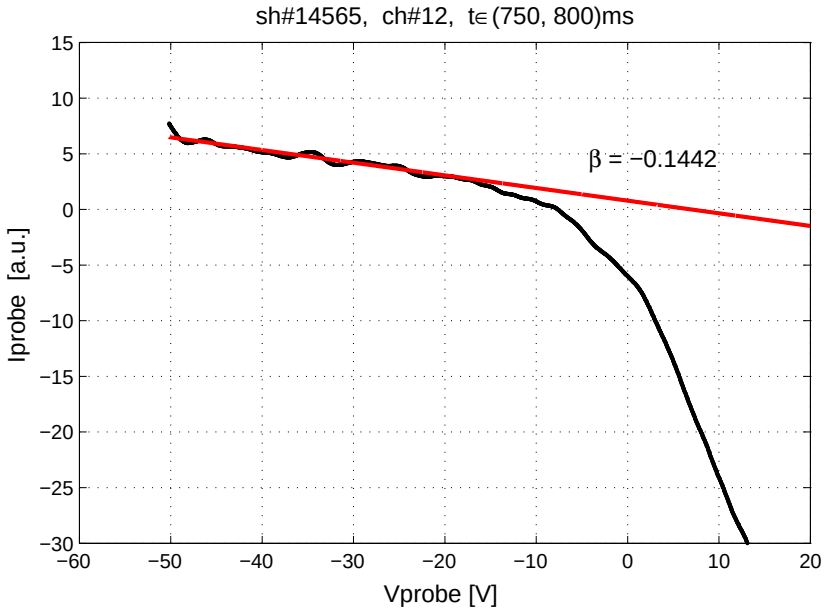

Figure 8.3: Example of an I-V curve for TRIP probe (Hydrogen plasma).

with $\beta \approx -0.01 \rightarrow -0.2$ for the experiments reported in this Thesis (Fig. 8.4). By inserting Eq. 8.8 into Eq. 8.5 and taking $I_e \approx I_{i,0}$, one obtains

$$2\,(1+\beta\,V_{pr}) = e^{\frac{V^+ - V_{fl}}{T_e/e}}\,\left(1+e^{-\frac{\Delta V}{T_e/e}}\right) \tag{8.9}$$

Equation 8.9 is used in this Thesis to evaluate T_e from the triple probe data, with the approximation $V_{pr} \approx V_{fl} + V^-$ and an average value $<\beta> \approx -0.05$ (Fig. 8.4).

Tests of the triple probe

The results reported herein refer to Hydrogen plasmas with $p_g = 6 \times 10^{-5}$mbar, $B_\varphi = 76$mT on the axis, $B_z = 0.6$mT and $P_{rf} \approx 300$W. Different values of ΔV are used, and the results compared for simultaneous radial scans of the SLP and TRIP probes. The measurements are taken on the equatorial plane. Figure 8.5 shows the background density, floating potential and electron temperature radial profiles measured by SLP. The average floating potential and electron temperature measured by TRIP are also shown. There is an excellent agreement between the two probes for all the values of ΔV, which is not the case when Eq. 8.7 is used to interpret the data instead of Eq. 8.9.

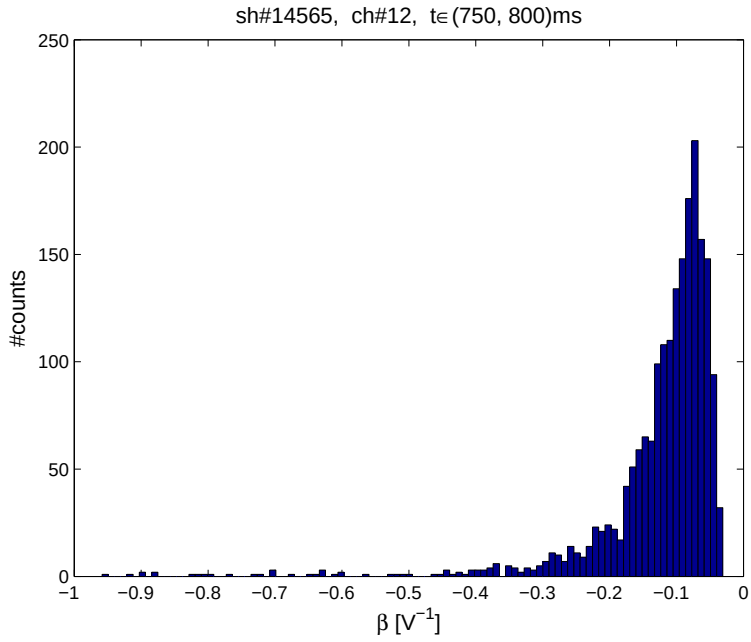

Figure 8.4: Histogram of the coefficient β for the TRIP probe for Hydrogen plasmas and a number of different experimental conditions.

8.1.2 Examples of electron temperature fluctuation measurements

Figure 8.5 shows the measured T_e and δT_e (time-averaged and fluctuations amplitude) for the same experimental conditions reported above. The voltage difference for the triple probe is $\Delta V = 24$V. The electron temperature profile is in excellent agreement with the one measured by SLP. The normalised fluctuation level, estimated as the rms value of $T_e(t)$ for each discharge, is $\leq 20\%$ for all the radial positions. The maximum of δT_e is shifted to the LFS with respect to the maximum of T_e. These features are common to all the experimental conditions for which the TRIP probe was used in the triple probe configuration. It should be noted that the triple probe results may be sensitive to the presence of suprathermal electrons, as the standard Langmuir probes. It is not possible to discriminate between the contributions to δT_e from the bulk and the suprathermals.

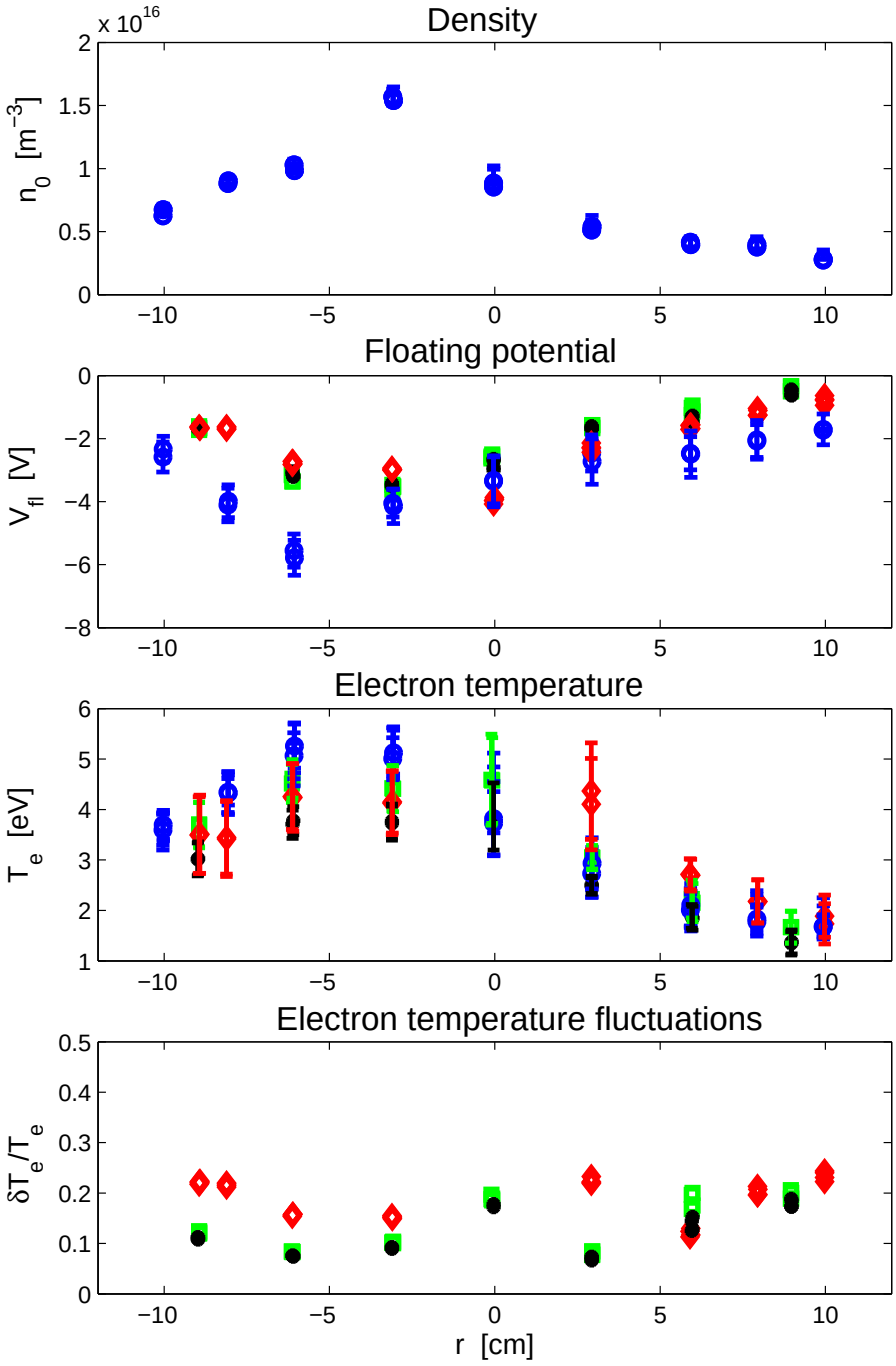

Figure 8.5: Example of density, floating potential and electron temperature radial profiles measured by SLP (blue circles), to be compared with the results from TRIP for different values of ΔV (red, green, black symbols). The relative fluctuation level, $\delta T_e/T_e$, is estimated as the rms of the time series.

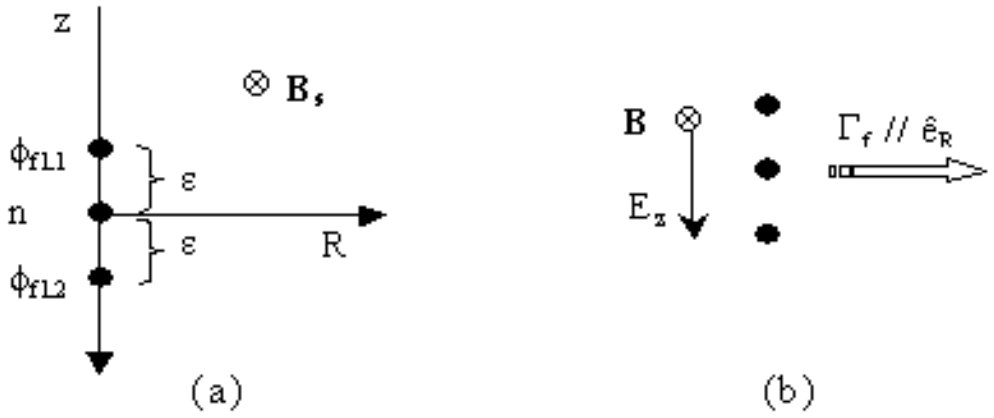

Figure 8.6: *(a)* Notation and layout of a three-tips electrostatic probe used to measure the fluctuation-induced particle flux. *(b)* With this notation the flux is positive, i.e. in the direction of $\hat{e}_R$, when $E_z < 0$. For practical convenience, in this Section the axis z is inverted with respect to the standard notation adopted in this Thesis work.

8.2 Measurement of the fluctuation-induced particle flux

This Section discusses the method used to measure the particle flux induced by correlated fluctuations of density and electric field [112]. For electrostatic fluctuations ($B_1 \equiv 0$) the time-averaged particle flux is [4]

$$\langle \Gamma_f \rangle = \langle n_1 \, v_1 \rangle = \frac{1}{B} \langle \, n_1 \, E_1 \, \rangle \tag{8.10}$$

Here n_1 and v_1 indicate the fluctuating part of the plasma density and of the fluid $E \times B$ velocity, with E_1 the fluctuating electric field and $\langle \ldots \rangle$ denotes a time average.

In a local slab geometry we put

$$v_1 = v_{1,x} \parallel \hat{e}_R \, , \quad E_1 = E_{1,z} \, , \quad B = B_s = B_0 \tag{8.11}$$

where the x, z and s axes lie along the major radius, the vertical direction and the toroidal direction, see Fig. 8.6. Therefore

$$v_1 \equiv v_{1,x} = \frac{E_{1,z}}{B_0} \tag{8.12}$$

In Fourier space, the time-averaged particle flux along x is given by

$$\langle \Gamma_f \rangle = \Re\{ \frac{1}{B_0} \mathcal{F} \{ n_1 \, E_{1,z} \}_{\omega=0} \} \tag{8.13}$$

where $\mathcal{F}\{.\}$ indicates the Fourier transform in time and $\Re\{.\}$ the real part. Introducing the convolution product, $*$, one obtains

$$\mathcal{F}\{n_1 E_{1,z}\} = \mathcal{F}\{n_1\} * \mathcal{F}\{E_{1,z}\} = \frac{1}{2\pi}\int_{-\infty}^{\infty} d\omega' \mathcal{F}\{n_1\}(\omega-\omega')\,\mathcal{F}\{E_{1,z}\}(\omega') \quad (8.14)$$

Note that in Eq. 8.13 we take the limit $\omega \to 0$, corresponding to the time average, and that $\mathcal{F}\{n_1\}(-\omega') = \mathcal{F}\{n_1\}^\star(\omega')$ as $n_1 \in \mathbb{R}$ (* indicates the complex conjugate). We obtain for the time-averaged flux:

$$\langle \Gamma_f \rangle = \Re\{\, \frac{1}{\pi B_0}\int_0^{\infty} d\omega \mathcal{F}\{n_1\}^\star(\omega)\,\mathcal{F}\{E_{1,z}\}(\omega)\,\} \quad (8.15)$$

The electric field fluctuations are related to plasma potential fluctuations, φ_1. The electric field is derived from measurements of φ_1 at two locations, separated by a distance $2\epsilon = y_2 - y_1$ (Fig. 8.6*a*). Assuming that y_1 and y_2 are symmetric with respect to the origin $y = 0$, i.e. $y_1 = \epsilon$ and $y_2 = -\epsilon$, one can obtain the electric field at $y = 0$ as

$$E_{1,z}(y=0,t) = \lim_{\epsilon\to 0}\frac{\varphi_1(-\epsilon,t) - \varphi_1(\epsilon,t)}{2\epsilon} \quad (8.16)$$

As $\mathcal{F}\{\tilde{E}_y\} = -i\,k_z\,\mathcal{F}\{\varphi_1\}$,

$$\langle \Gamma_f \rangle = \Re\{\, \frac{1}{\pi}\int_0^{\infty} d\omega\, \frac{-i\,k_z}{B_0}\,\mathcal{F}\{n_1\}^\star(\omega)\,\mathcal{F}\{\varphi_{1,z}\}(\omega)\,\} \quad (8.17)$$

We introduce the following quantities:

- Cross-power spectrum:

$$P_{n_1\varphi_1} = \mathcal{F}\{n_1\}^\star\,\mathcal{F}\{\varphi_{1,z}\} \quad (8.18)$$

- Coherence:

$$\gamma_{n_1\varphi_1} = \frac{|P_{n_1\varphi_1}|}{\sqrt{P_{n_1n_1}}\,\sqrt{P_{\varphi_1\varphi_1}}} \quad (8.19)$$

- Phase angle $\alpha_{n_1\varphi_1}$:

$$\alpha_{n_1\varphi_1} = \angle\, P_{n_1\varphi_1} \quad (8.20)$$

By noting that

$$\mathcal{F}\{n_1\}^\star\,\mathcal{F}\{\varphi_{1,z}\} \equiv \gamma_{n_1\varphi_1}\, e^{i\,\alpha_{n_1\varphi_1}}\,\sqrt{P_{n_1n_1}}\,\sqrt{P_{\varphi_1\varphi_1}} \quad (8.21)$$

the definitions introduced above allows one to rewrite Eq. 8.17 in the form

$$\langle \Gamma_f \rangle = \Re\{\, \frac{-1}{\pi\, B_0}\int_0^{\infty} d\omega\, i\,k_z\,\gamma_{n_1\varphi_1}\, e^{i\,\alpha_{n_1\varphi_1}}\,\sqrt{P_{n_1n_1}}\,\sqrt{P_{\varphi_1\varphi_1}}\} \quad (8.22)$$

From Eq. 8.22 we finally identify the *spectral flux*, $\Gamma_{f,\omega}$, such that

$$\Gamma_{f,\omega}\, d\omega = \frac{k_z}{\pi\, B_0}\, \gamma_{n_1\varphi_1}\, \sin\left(\alpha_{n_1\varphi_1}\right) \sqrt{P_{n_1 n_1}\, P_{\varphi_1\varphi_1}}\, d\omega \tag{8.23}$$

represents the contribution to the fluctuation-induced flux of fluctuations with a frequency in the range $(\omega, \omega + d\omega)$. The spectral flux is at the basis of the combined analysis of instabilities and the related flux. In practice, a direct evaluation of $\Gamma_{f,\omega}$ from Eq. 8.23 is difficult, due to constraints on the measurable quantities and on the probe geometry, which are discussed in detail here below.

Coherence between signals

From Eq. 8.23, the spectral flux is proportional to the coherence between density and potential signals. In practice, a minimum coherence might be measured also for physically uncorrelated signals[1]. A condition on the minimum acceptable coherence, determined on the basis of the background noise level, should be set to consider the data as representative of a physically meaningful signal.

Dependence $k_z = k_z(\omega)$

The wave-number $k_z = k_z(\omega)$ must be known to quantify the spectral flux, Eq. 8.23. Its value is usually derived from the cross-phase between two potential measurements, $\Delta\phi$:

$$k_z(\omega) = \frac{\Delta\phi(\omega)}{2\,\epsilon} \tag{8.24}$$

where a bi-univocal relation $k_z = k_z(\omega)$ is implicitly assumed. In practice, k_z may exhibit a spectrum of values for a fixed ω. Statistical methods allow one to estimate the wave-number-frequency spectrum [3], from which it is possible to check the validity of Eq. 8.24.
When a finite k_z-spectrum is considered, Eq. 8.23 should be modified by introducing an additional integration over the k's:

$$\Gamma_{f,\omega}\, d\omega = \int dk'_y\, k'_y(\omega) \frac{S(\omega|k'_y)}{S(\omega)}\, \frac{1}{\pi\, B_0}\, \gamma_{n_1\varphi_1}\, \sin\left(\alpha_{n_1\varphi_1}\right) \sqrt{P_{n_1 n_1}\, P_{\varphi_1\varphi_1}}\, d\omega \tag{8.25}$$

where $S(\omega|k'_y)/S(\omega)$ is the normalised conditional spectrum [3]. Note that also the phase angle, $\alpha_{n_1\varphi_1}$, is an implicit function of k'_y when a finite tip separation is considered.

[1] Examples are pick-up between tips, disturbances injected by the electronics and RF disturbances. These effects add the same spurious components to each measuring channel, which result in an artificially increased coherence.

Tip separation and measurable wave-numbers

The gap between the tips measuring the potential imposes the maximum value of k_z, i.e. the minimum wavelength, that can be unambiguously resolved:

$$\frac{\lambda^{min}}{2} = 2\epsilon \quad \Rightarrow \quad k_z^{max} = \frac{2\pi}{\lambda^{min}} = \frac{\pi}{2\epsilon} \tag{8.26}$$

Therefore, measured wave-numbers $\geq k_z^{max}$ probably originate from measurements affected by aliasing, and should be discarded.

Phase measurements

In practice, one should look at the behaviour of $\Delta\phi$ as a function of ω and impose a condition on the smoothness of $\Delta\phi(\omega)$, assuming that phase jumps greater than some given value are unphysical and must be rejected. This value may depend on the specific settings used for the analysis, such as the number of points used for the FFT and the sampling frequency.

Tip separation and cross-phase measurements

In principle, density and electric field fluctuations should be measured at the same spatial location, see Eq. 8.16. This is not the case in a real experiment, where a finite separation between the tips measuring the potential is needed in order to recover the 'spatial' information, namely the k_z value. The gap ϵ cannot be indefinitely small, because this implies an extremely small measured phase difference, which would be badly affected by the noise in the measurements.
For finite k_z's, the finite gap introduces an additional phase shift, $\pm k_z\,\epsilon$, between n_1 and the potential signals. In order to evaluate correctly the term $\alpha_{n_1\varphi_1}$,the average of the phase angles between n and *each* plasma potential signal should be considered:

$$\alpha_{n_1\varphi_1} = \frac{\alpha_{n_1\tilde{\varphi}_1} + \alpha_{n_1\tilde{\varphi}_2}}{2} \tag{8.27}$$

The additional phase shift, which is anti-symmetric with respect to $y = 0$, cancels out.

Plasma potential, floating potential and electron temperature fluctuations

Contrary to the standard notation adopted in the rest of the Thesis, in this Section the potential was indicated with the symbol φ. The ambiguity between plasma and *floating* potential is now removed and the usual notation, V_{pl} and V_{fl}, can be reintroduced, with $V_{pl} = V_{fl} + \mu\, T_e/e$ (Appendix B). In fact, for most experimental

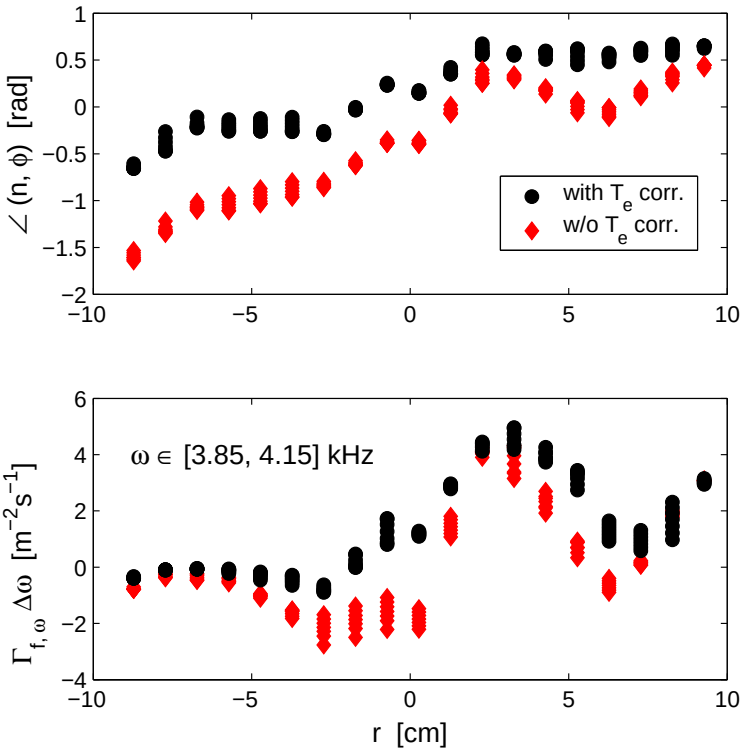

Figure 8.7: *Top:* Measured phase between density and potential, calculated with and without $\tilde{T}_e$ corrections, as a function of the radial position at the midplane. *Bottom:* Corresponding spectral flux for a selected frequency range, where a coherent mode is present.

situations the only information available on the electric field is derived from the floating potential. It is assumed that $\varphi_1 = V_{pl,1} \equiv V_{fl,1}$, which is valid only in the limit $\tilde{T}_e \to 0$ or, for practical cases:

$$\mu \tilde{T}_e \ll V_{fl,1} \tag{8.28}$$

For the general case with $\tilde{T}_e \neq 0$, the measurements of the fluctuation-induced flux based on the assumption $V_{pl} \equiv V_{fl}$ data alone can be misleading, because the estimated amplitude of $V_{pl,1}$ and the phase between n_1 and $V_{pl,1}$ might be strongly inaccurate [117][43].
For the reasons mentioned above, the measurements of $\Gamma_{f,\omega}$ are corrected for finite a $\tilde{T}_e$. In practice, the time-traces $T_e(r,t)$ and $V_{fl}(r,t)$ are obtained from T_e fluctuations measurements (Sec. 8.1) for the positions of interest. Assuming that $\mu \neq \mu(t)$, the plasma potential, $V_{pl}(r,t)$, is also calculated. After Fourier transforming the three

signals, the amplitude and phase correction factors are evaluated:

$$C_{|V_{fl}|\rightarrow|V_{pl}|}(r,\omega) = \frac{|V_{pl}|}{|V_{fl}|} \quad , \quad \Psi(V_{fl} \rightarrow V_{pl})(r,\omega) = \angle V_{pl} - \angle V_{fl} \tag{8.29}$$

The two factors are used to correct the results for $\Gamma_{f,\omega}$ by setting, in Eq. 8.25, $\varphi_1 = V_{fl,1}\, C_{|V_{fl}|\rightarrow|V_{pl}|}\, e^{i\Psi}$. An example of the flux calculated with and without the finite $\tilde{T}_e$ effects is shown in Fig. 8.7. The importance of finite electron temperature fluctuations is confirmed. For instance, there are regions where the flux sign in reversed when $\tilde{T}_e$ is taken into account (for $r < 0$ in the example of Fig. 8.7), and the differences in the phase $\alpha_{n_1\varphi_1}$ can be as large as 1rad. These results are significantly different from those obtained in tokamak edge plasmas, where usually n and T_e fluctuations are in phase, and the corrections for finite $\tilde{T}_e$ have a minor impact on the measurements fluctuation-induced flux [43].
It should be noted that the method described above can be applied when fluctuations have wavelengths $\gg \epsilon$, which is the case for all the scenarios investigated on TORPEX. The same considerations discussed in pag. 139 about the effect of a finite tip separation hold for $\tilde{T}_e$ measurements as well, from which the correction factors (Eq. 8.29) are calculated. For typical values of wavelengths measured on TORPEX, the correction to the phase related to a finite tip separation would be $2\pi\epsilon/\lambda \approx 20 \times 2 \times 10^{-3} \sim 5\%$, which is within the error in the measurement of the phase due to noise.

8.3 Conditional average sampling technique

A useful technique for studying the spatio-temporal behaviour of macroscopic structures is the Conditional Average Sampling (CAS) [53][57]. A complete overview of the capabilities and limitations of the method is found in Ref. [5] and references therein. The method consists in extracting through ensemble averages the signal part that is correlated with a specific *event*, defining a 'trigger' condition, C. For example, the event could be a burst in the measured density and

$$C = \{n > n_{th}\,;\, n = n_{loc.max}\} \tag{8.30}$$

where n_{th} is a convenient threshold and $n_{loc.max}$ a local maximum in the density signal (Fig. 8.8). Another possibility could be to impose a condition of the type

$$C = \{n_{low} < n < n_{high}\,;\, n = n_{loc.max}\} \tag{8.31}$$

where only events with an amplitude within a certain range are considered. As a further example, C could be defined in terms of the difference of the signals measured at two spatial positions, i.e. on a spatial gradient, or extracted from the coefficients of a wavelet decomposition of the reference signal [106].
The N times at which the condition C is satisfied, $t_{C,i}$, are recorded (Fig. 8.8), and the conditionally averaged signal is calculated

$$s_0 = \frac{1}{N}\sum_{i=1}^{N} n(t = t_{C,i}) \tag{8.32}$$

Similarly, the conditionally averaged signal at a time shifted by τ with respect to $t_{C,i}$ is

$$s_\tau = \frac{1}{N}\sum_{i=1}^{N} n(t = t_{C,i} - \tau) \tag{8.33}$$

The reconstructed signal $s = s(\tau)$ in a time window of width Δt centred around the event is obtained by letting τ vary between $t_{C,i} - \Delta t/2$ and $t_{C,i} + \Delta t/2$. Note that the events are not directly related to the absolute timing of the plasma discharge. Providing that the discharges are highly reproducible, 2-D profiles with high spatial resolution can be obtained by moving probes on a shot-to-shot basis.
In this simple version of the CAS method there are two parameters to optimise, namely n_{th} and Δt.

- The value of n_{th} has a direct impact on the condition C, hence on the number and type of the events which are detected. In practice, n_{th} is a trade-off between a good statistics and an effective discrimination of the most representative events.

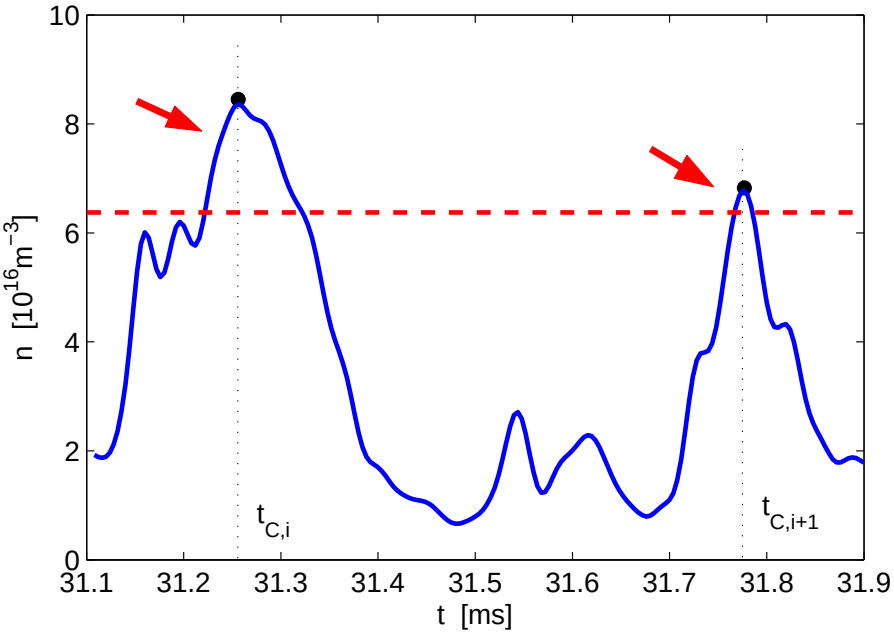

Figure 8.8: Example of a density trace from a fixed 'reference' probe used to implement the CAS technique. In this example the threshold value is set to $1 \times \sigma$ (red, dashed line), where σ is the standard deviation of $n(t)$. Two *events*, indicated by the arrows, are clearly identified. The times $t_{C,i}$ and $t_{C,i+1}$ correspond to the local maxima of the signal.

- The parameter Δt must be smaller than the minimum delay between events to avoid including the same event twice in the average, Eq. 8.33. In general, it is set equal to a few auto-correlation times of the raw density signals.

An example of a 2-D reconstruction of the spatio-temporal pattern of a coherent mode, commonly observed in TORPEX plasmas (see Sec. 7.2), is shown in Fig. 8.9. In this case, the discriminating condition is defined as in Eq. 8.30, with n_{th} equal to the standard deviation of the reference signal, which is measured at $r = 0$, $z = 0$, where the amplitude of the fluctuations is maximum.

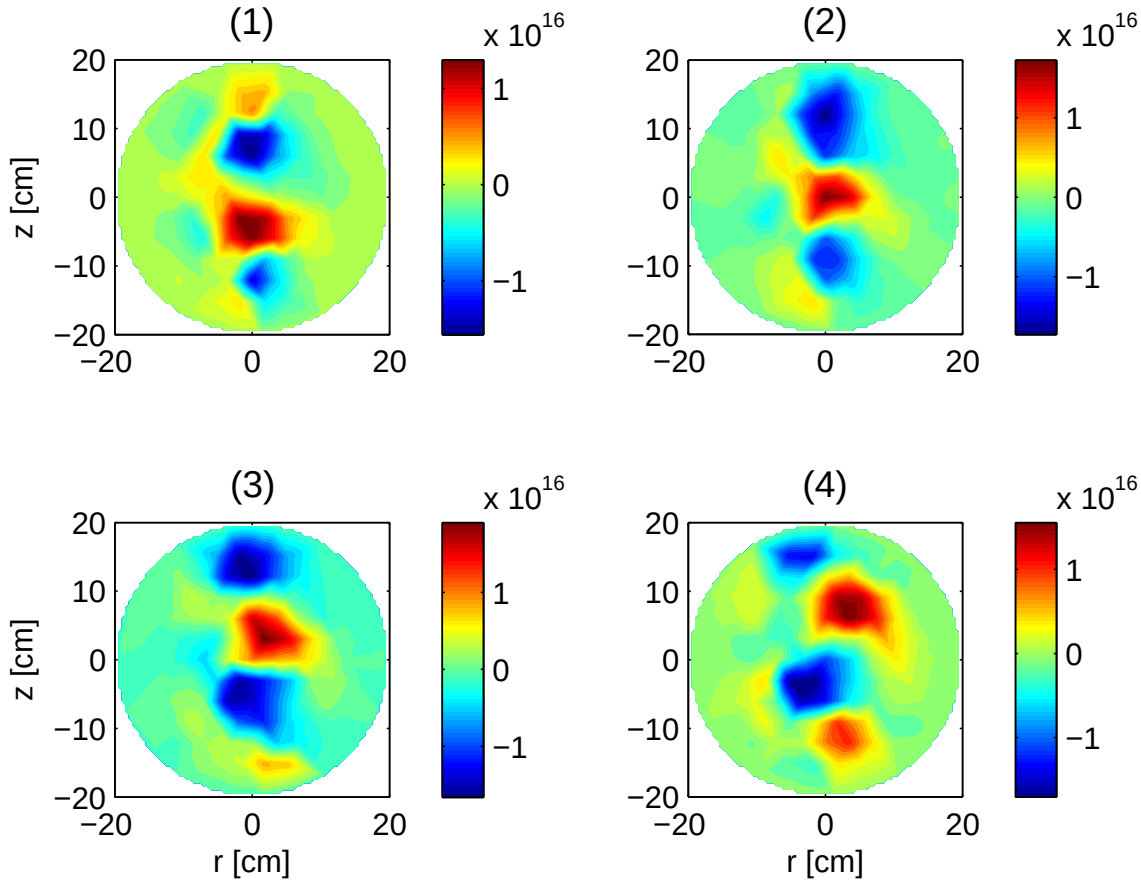

Figure 8.9: Reconstruction of the spatio-temporal pattern of density fluctuations by means of the CAS technique for a Hydrogen plasma (data from the HEXTIP probe) [104]. A coherent mode, propagating in the vertical direction, is clearly observed. Figures (1) to (4) refer to four time frames from the same discharge, with a time interval between frames of 40μs.

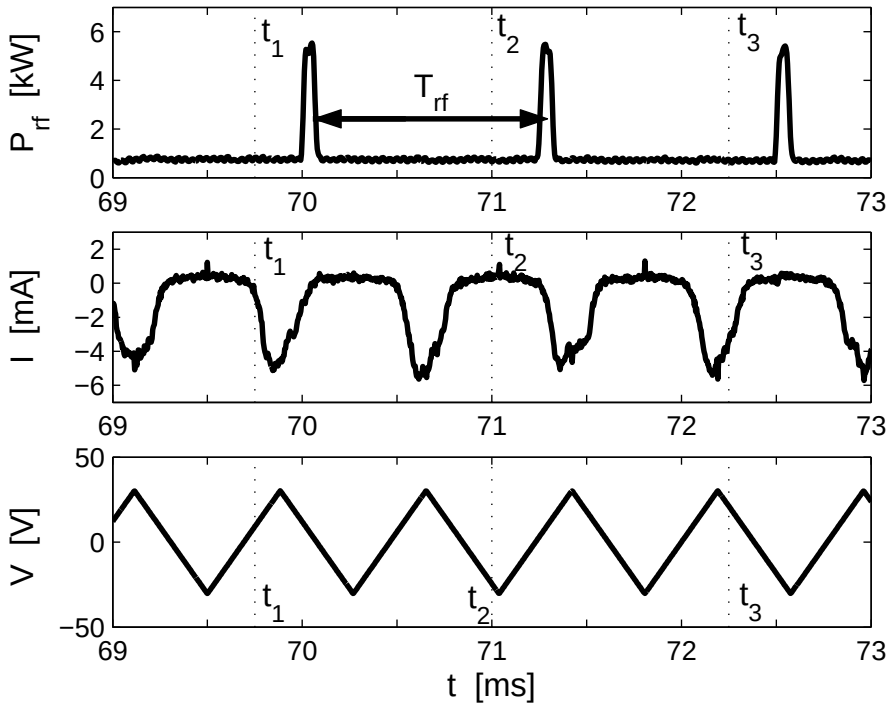

Figure 8.10: Illustration of the boxcar-averaging technique used to estimate the simultaneous variation of n, T_e and V_{pl} during a power modulation period, T_{rf}.

8.4 Boxcar-averaging technique

Most of the experimental results presented in this Thesis are obtained by means of electrostatic probes. The mode in which the probe is operated determines the maximum time resolution of the results. For the simultaneous determination of n, T_e and V_{pl} the double of the sweep period, typically $\geq 500\mu$s, constitutes the maximum time resolution. However, there are cases for which a higher temporal resolution is needed. For example, one might be interested in the evolution of n, T_e and V_{pl} in connection with fast events, for which only n can be usually measured with high temporal resolution with probes operating in I_{sat} mode.
To evaluate simultaneously the time evolution of the three parameters and estimate the errors made by assuming $n \propto I_{sat}$, i.e. without including changes of T_e and/or V_{pl}, a boxcar-averaging technique can be used. To illustrate the technique we refer to the case of discharges with power modulation.
Referring to Fig. 8.10, the power signal is taken as reference to reconstruct the average behaviour of the probe current and voltage signals within a modulation period, T_{rf}, containing $N_s = T_{rf}\, f_{acq}$ samples (f_{acq} is the acquisition frequency). The probe voltage is swept at a frequency which differs from the power modulation frequency,

and the probe current is measured. The voltage and current time series are resampled at the rate $1/T_{rf}$, taking as starting time the first N_s points. At the end of this procedure one obtains a set of N_s probe characteristics containing information on the evolution of the plasma parameters during a modulation cycle. The curves are then analysed with standard fitting techniques to get n, T_e and V_{fl}, from which, for example, V_{pl} can be calculated (see Appendix B.2).
Fig. 8.11 shows a reconstruction of the behaviour of the main plasma parameters during a modulation cycle in Hydrogen, for regions close to the EC and UH layers, where the presence of suprathermal electrons could affect the interpretation of the ion saturation current data. Although changes of T_e and V_{fl} are clearly observed, especially close to the UH layer, the density traces from I-V curves and I_{sat} are in good agreement. These results justify in this case the use of I_{sat} data as representative of the density dynamical behaviour.

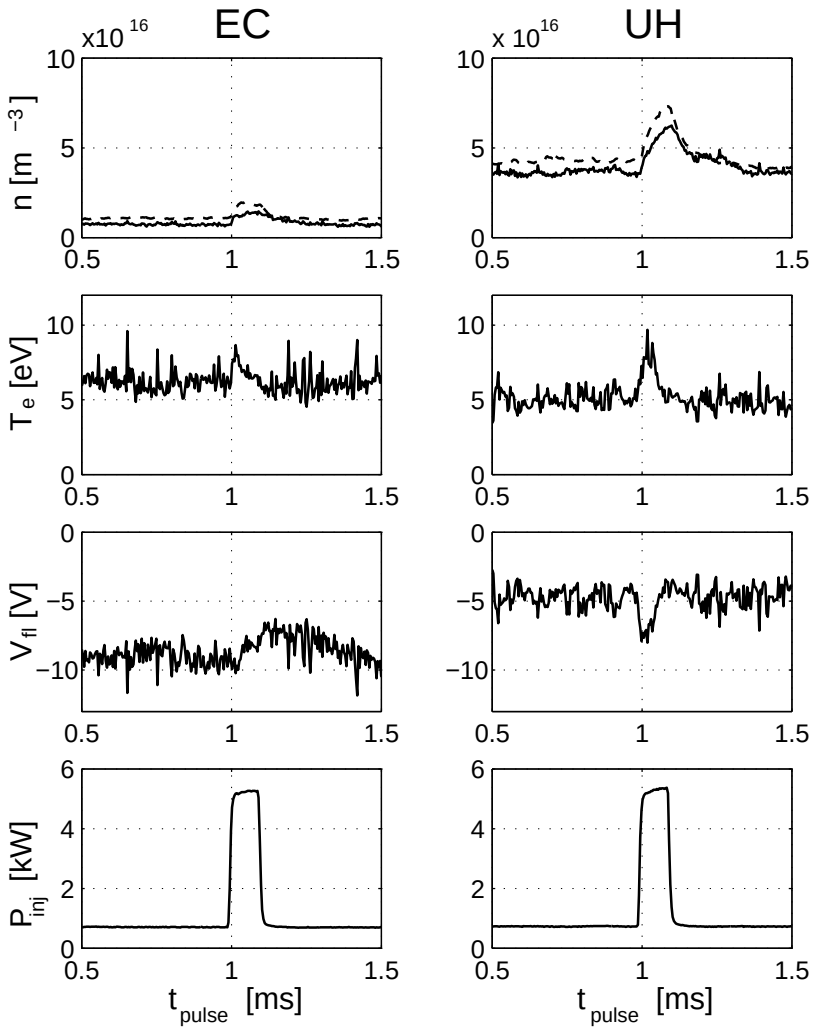

Figure 8.11: Evolution of n, T_e and V_{fl} from swept Langmuir probes during a power modulation cycle, reconstructed by means of the boxcar-averaging technique. For comparison, the dashed line shows the density measured from I_{sat}, assuming a constant $T_e = 5\,eV$. Measurements are done in Hydrogen at the EC (*left column*) and UH (*right column*) layers.

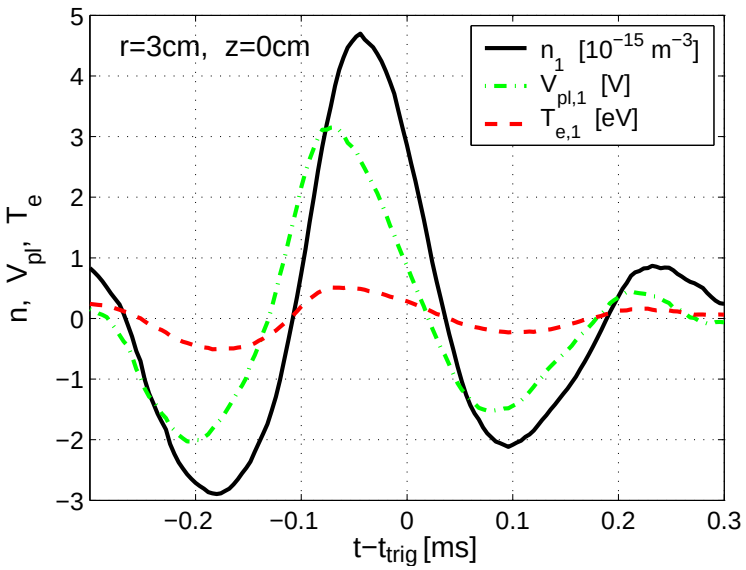

Figure 8.12: Example of average n, T_e and V_{pl} in a time-window centred around a density spike detected on the reference probe. Note the finite relative phases between density and plasma potential.

8.5 Combined CAS-Boxcar technique

The boxcar-averaging technique illustrated in Sec. 8.4 can be also applied, in combination with the CAS method (Sec. 8.3), to study plasma instabilities [75] and transport. In this case the reference signal is the ion saturation current measured by a fixed probe, instead of the injected microwave power signal. Once the trigger events are identified, the reconstruction of the average I-V Langmuir curves proceeds as for the boxcar method. By means of the combined CAS-boxcar technique, poloidal profiles and time evolution of density and plasma potential are obtained (Fig. 8.12). This makes it possible to calculate the particle transport due to correlated fluctuations of n and V_{pl} (Sec. 11.4). Moreover, the heat flux can be calculated since the electron temperature is also known.
The choice of the reference probe is dictated by the phenomenon under investigation. Referring to the standard TORPEX plasmas, the probe can be chosen at the location where a coherent mode is present, and the method is used to reconstruct the spatio-temporal pattern of the instability. The example in Fig. 8.13 shows the density, electron temperature and plasma potential perturbations due to a coherent mode at 4kHz, convected by the background $E \times B$ velocity.
Another field of interest is the study of 'intermittent' events, i.e. strong, local perturbations of the plasma parameters which can not be described by a wave representation. A complete discussion of this class of phenomena is given in Sec. 11.4. In

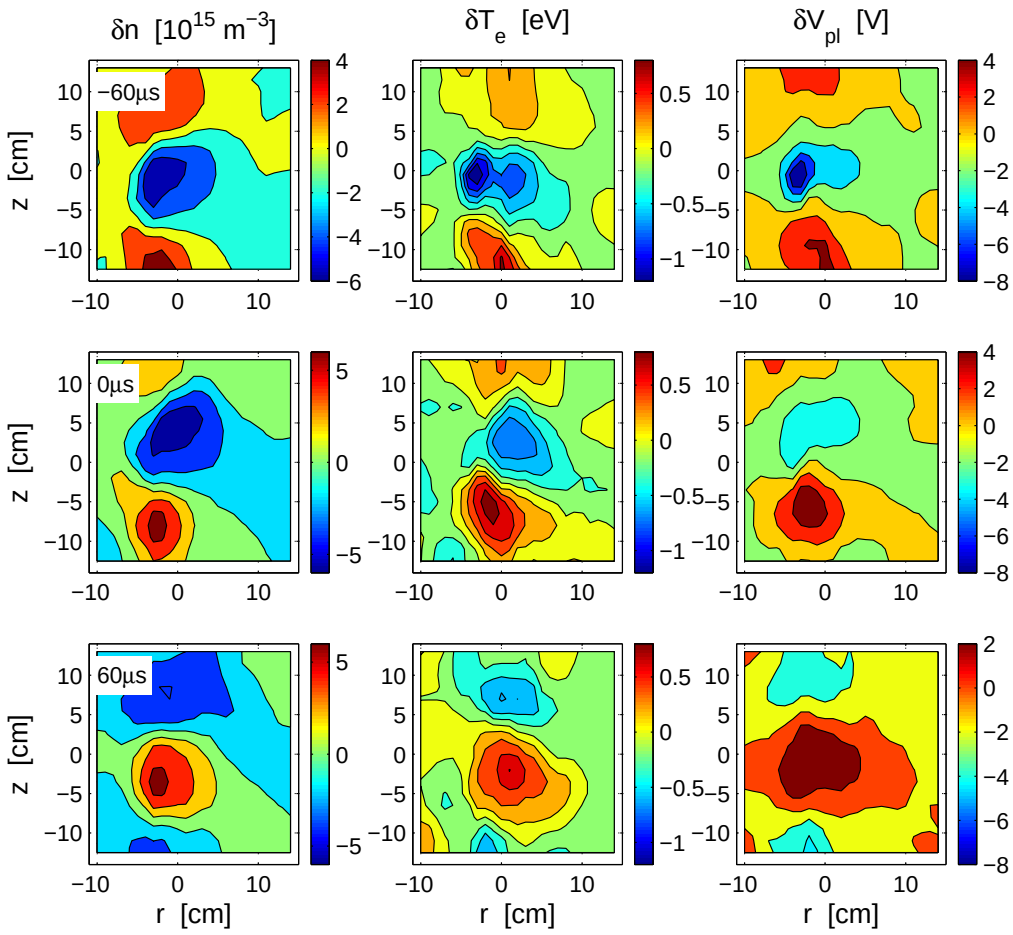

Figure 8.13: Reconstruction of the time-dependent fluctuations of n, T_e, V_{pl} over a 2D cross-section. The inserts show the times, with respect to the detection of a trigger event ($t = 0$), at which the profiles are calculated.

this case the reference probe must be located where the density spikes are detected, which usually corresponds to the LFS plasma region. An example of reconstructed traces is shown in Fig. 8.14.
For TORPEX discharges, the method gives stable results for a discharge duration ≥ 1.5s. Up to ~ 1500 trigger events are detected, depending on the threshold level chosen to define the trigger condition. The probes measuring the I-V curves are swept at 1kHz, and the sweep voltage is limited to $(-20, +5)$V to maximise the number of points in the range useful for the fit of the I-V curve.

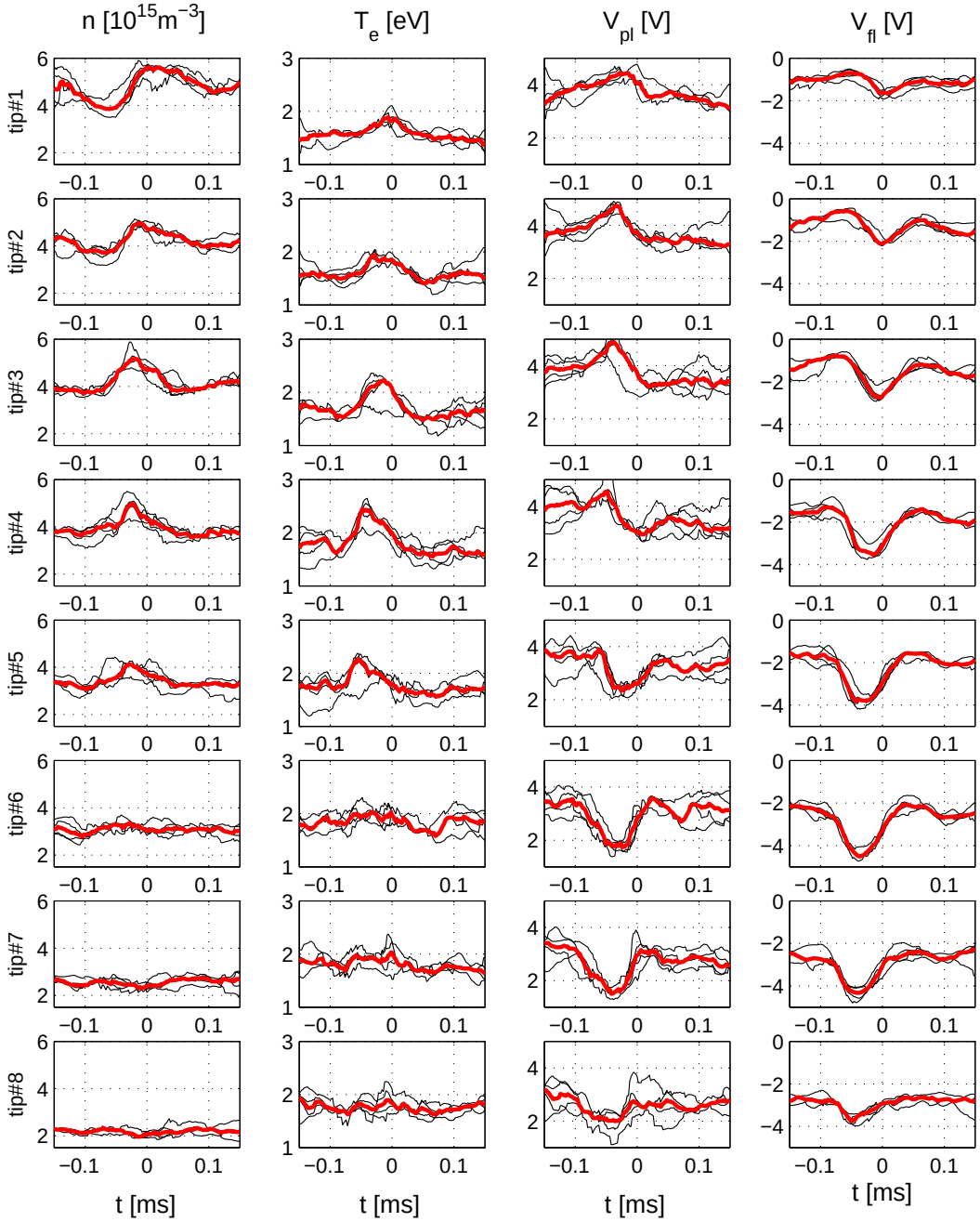

Figure 8.14: Reconstruction of the simultaneous behaviour of n, T_e, V_{pl} and V_{fl} from the 8 tips of SLP, using the combined CAS-boxcar technique. The trigger condition is a threshold on a I_{sat} signal (cfr Eq. 8.30). Measurements are done in Hydrogen. Data (thin lines) refers to four discharges with the same experimental conditions. The thick line is the average of the four repetitions.

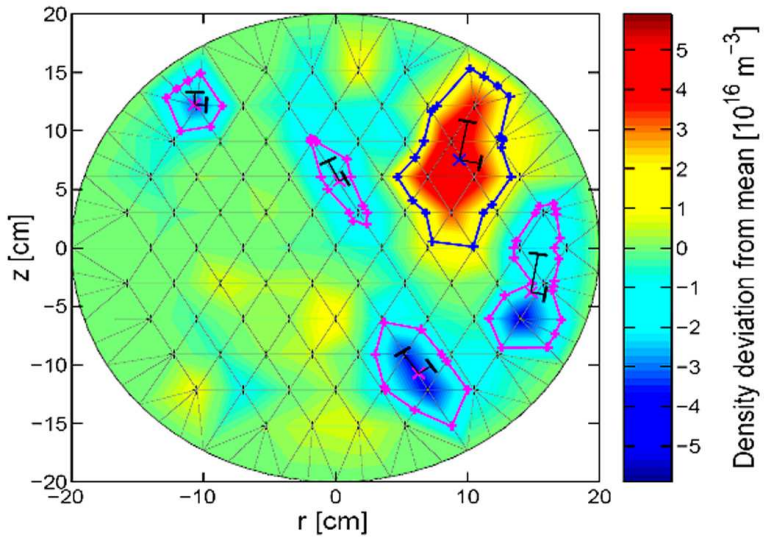

Figure 8.15: A single time-frame representing the instantaneous density fluctuations, reconstructed from HEXTIP data with a spatial resolution of 3.5cm. Five macroscopic 'structures' are identified and characterised by their contours, orientation and associated mass.

8.6 Real-space statistical analysis

This Section briefly summarises the space-time analysis and visualisation technique developed by S.H. Müller in the frame of his PhD thesis [67].
The method is based on simultaneous measurements of the plasma density over a poloidal cross section, obtained from HEXTIP (Sec. 3.4). By comparing the density profile evolution frame by frame one can reconstruct the temporal behaviour of macroscopic density 'structures' within the same discharge. The structures are defined as bounded regions in which the instantaneous density exceeds the time-average value by a convenient factor. Analogously, *negative* structures are defined by considering a threshold smaller than the average density. An example is shown in Fig. 8.15, where one positive and four negative structures are identified.
For each time frame, the structures are characterised in terms of size, associated mass, centre of mass and orientation. Their velocity and trajectory are calculated by tracking a structure during subsequent time frames. By knowing the velocity, the mass and the trajectory of each structure, a net flux through 'virtual surfaces' intersecting the poloidal plane can be calculated [67].
All the information from a single discharge is collected in a database, and used to calculate the statistics associated with particular events, such as trajectory patterns, birth and death locations of the structures and particle fluxes [68].

8.7 Plasma response to a modulated microwave power: multi-harmonics analysis

Methods based on measurements of the plasma response to externally imposed perturbations are widely used in tokamaks to study transport phenomena (see [89][11][63] and references therein). In particular, a modulation of the injected EC power can be used to infer the value of the particle and heat transport coefficients, on the basis of specific assumptions on the form of the transport equations.
To our knowledge, these techniques have not been exploited yet on basic devices like TORPEX. A first reason is that the injection system must be able to provide a well controlled modulation of the output power. This was the motivation behind the upgrades of the TORPEX microwave system, described in Appendix. A.1. Second, modulation techniques are expected to give information on the global plasma losses, regardless of the physical mechanisms behind the measured fluxes. For a simple magnetised torus the dominant loss channel is the flow along the open magnetic field lines, which is of little interest for the magnetic confinement physics community compared to other more general issues, such as the flux related to plasma instabilities. Nevertheless, the information on the total fluxes is relevant for a complete characterisation of transport phenomena at play, and provides an upper limit to which the results from other techniques can be compared.
In this Section, I describe the analysis method of data from discharges with modulated EC power used on TORPEX. It is based on the combined analysis of the response to perturbations with different amplitude and/or frequency. A convective model is adopted, as it results to be the most appropriate to describe the observed plasma dynamics.

Description of the 'multi-harmonics' method

The multi-harmonics analysis method is discussed here in three steps. The general lines are depicted adopting a simplified, one-dimensional model. Then, the obtained equations are extended to the general three-dimensional case. The practical implementation of the method is finally illustrated at the end of the Section.
The interpretation of the density response to a modulated microwave power is based on the density continuity equation

$$\frac{\partial n}{\partial t} = -\underline{\nabla} \cdot \underline{\Gamma} + S \tag{8.34}$$

where $\underline{\Gamma}$ is the particle flux and S the source term. For the one-dimensional case $\Gamma = \Gamma(x)$ and $S = S(x)$, and the flux is assumed to be purely convective[2], $\Gamma = n\,U$. This assumption will be justified in Sec. 9, on the basis of the experimental results.

[2]In this Section, I use the symbol U to indicate the time-averaged, macroscopic velocity field.

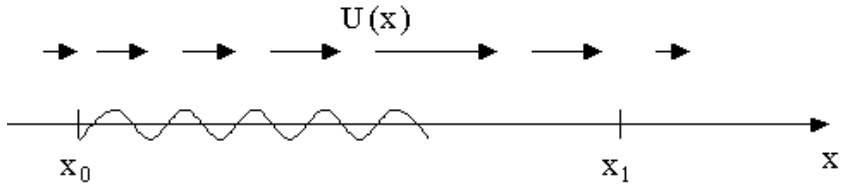

Figure 8.16: Effect of a background velocity field, $U(x)$, on the measurements of the phase of a signal excited at x_0 and detected at x_1.

We decompose n, U and S into a constant, time-independent part plus a first-order fluctuating part (subscripts '0' and '1'). The time Fourier transform of Eq. 8.34 for the first-order part is

$$i\omega\, n_1 = -\nabla(n_1\, U_0) - \nabla(n_0\, U_1) + S_1 \tag{8.35}$$

with

$$n_1 = A\, e^{i\omega\, t}\, e^{i\varphi}\ ; \quad U_1 = B\, e^{i\omega\, t}\, e^{i\gamma}\ ; \quad S_1 = p\,\alpha\, e^{i\omega\, t} \tag{8.36}$$

for the component at frequency $\omega/2\pi$, and the amplitude of the coefficients A and B depend on x and ω. The term $p\,\alpha$ represents the amplitude of the *local* source perturbation, with $p = p(\omega)$ and $\alpha = \alpha(x)$ (see Sec. 7.3.2).
Note the additional terms, $e^{i\varphi}$, $e^{i\gamma}$ in Eq. 8.36, which originate from the presence of a background velocity field. Referring to Fig. 8.16, a density perturbation generated at $x = x_0$ and detected at $x = x_1$ is subject to a phase shift

$$\varphi = \omega\Delta t = \omega \int_{x_0}^{x_1} \frac{dx'}{U_0(x')} \tag{8.37}$$

If the source location and the macroscopic convection velocity are independent of ω, i.e. $\Delta t \neq \Delta t(\omega)$, the phase is simply proportional to the perturbation frequency. From Eq. 8.35 we obtain

$$U_0\Big(\frac{\partial\, A}{\partial\, x} + iA\frac{\partial\, \varphi}{\partial\, x}\Big) + A\frac{\partial\, U_0}{\partial\, x} + e^{i(\gamma-\varphi)}\Big[B\frac{\partial n_0}{\partial\, x} + n_0\,\Big(\frac{\partial\, B}{\partial\, x} + iB\frac{\partial\, \gamma}{\partial\, x}\Big)\Big] - i\omega A = -p\alpha e^{-i\varphi} \tag{8.38}$$

Suppose now that two sets of measurements, labelled as i and j, are available. The two sets may correspond, for example, to two different modulation frequencies, ω_i and ω_j. We make the further assumption that the modulation of the microwave power does not affect the convective velocity, i.e. $U_1 \equiv 0$, see Sec. 9.
By writing Eq. 8.38 for the two sets, taking their ratio, and splitting the resulting equation into real and imaginary part, one obtains two linear equations which can be solved to get U_0 and $\partial U_0/\partial x$ from the measured quantities $A_{i,j}$, $\varphi_{i,j}$ and $p_{i,j}$. The

same procedure can be easily extended to multiple sets of modulation parameters, leading to an over-determined set of equations for the transport coefficients. Note that the plasma response from different modulation parameters was qualitatively compared in a number of experiments aimed at estimating the transport coefficients (see [64] and references therein). To our knowledge, the combination of this information in a unique system of equations has not been reported yet.
An alternative procedure would be to obtain a system of equations by simply combining Eq. 8.38 for the different sets of modulation parameters. However, it should be noted that by taking the ratio of the two equations all the proportionality coefficients between measured quantities and the corresponding physical parameters[3] are cancelled out, making the method more accurate.

Extension to the three-dimensional case

Equation 8.38 can be easily extended to the general 3-D case, for which $A = A(x, z, s)$ and $\varphi = \varphi(x, z, s)$ (x, z and s are the coordinate along the major radius, vertical and toroidal directions).
Contrary to the time-averaged source profile, the instantaneous perturbed source profile term is assumed to depend on s, under the effect of fluctuations and finite time-scales of the ionisation processes. Such an asymmetry is consistent with the dependence of the plasma response upon the toroidal direction, observed in the experiments. Note that, in the absence of any attenuation, the perturbations can propagate around the torus and contribute to the signal measured at different vertical positions, depending on the convection path. It is assumed here that 'local' perturbations produce the strongest signal, which is only weakly affected by this 'return signal' after one (or more) toroidal turns.
The equations for the 3-D case can be cast in the form

$$\underline{\underline{T}} \cdot \underline{X} = \underline{Y} \tag{8.39}$$

where, for each pair of sets i and j

$$\underline{X} = \left[V_{0,x},\ V_{0,z},\ V_{0,s},\ \frac{\partial U_{0,x}}{\partial x} + \frac{\partial U_{0,z}}{\partial z} + \frac{\partial U_{0,s}}{\partial s} \right]^T \tag{8.40}$$

$$\underline{\underline{T}} = \begin{bmatrix} a^{ij} & b^{ij} & c^{ij} & d^{ij} \end{bmatrix} \tag{8.41}$$

$$\underline{Y} = \left[s^{ij} \right] \tag{8.42}$$

By introducing the quantities

$$k_{ij} = \frac{p_i}{p_j}\ ,\ \Delta\varphi_{ij} = \varphi_j - \varphi_i \tag{8.43}$$

[3] In particular, these include the conversion from ion saturation current into plasma density and from the RF diode signal into the injected microwave power.

the coefficients of the matrix $\underline{\underline{T}}$, in its complex form, are

$$a^{ij} = \frac{\partial A_i}{\partial x} + iA_i \frac{\partial \varphi_i}{\partial x} - k_{ij}\, e^{i\Delta\varphi_{ij}} \left(\frac{\partial A_j}{\partial x} + iA_j \frac{\partial \varphi_j}{\partial x} \right) \tag{8.44}$$

$$b^{ij} = \frac{\partial A_i}{\partial z} + iA_i \frac{\partial \varphi_i}{\partial z} - k_{ij}\, e^{i\Delta\varphi_{ij}} \left(\frac{\partial A_j}{\partial z} + iA_j \frac{\partial \varphi_j}{\partial z} \right) \tag{8.45}$$

$$c^{ij} = \frac{\partial A_i}{\partial s} + iA_i \frac{\partial \varphi_i}{\partial s} - k_{ij}\, e^{i\Delta\varphi_{ij}} \left(\frac{\partial A_j}{\partial s} + iA_j \frac{\partial \varphi_j}{\partial s} \right) \tag{8.46}$$

$$d^{ij} = A_i - k_{ij}\, e^{i\Delta\varphi_{ij}}\, A_j \tag{8.47}$$

and

$$s^{ij} = i \left(A_i\, \omega_i - A_j\, k_{ij}\, e^{i\Delta\varphi_{ij}}\, \omega_j \right) \tag{8.48}$$

Implementation of the method on TORPEX data

In order to solve the system 8.39, at least $N = 3$ distinct sets of measurements are needed, leading to eight independent equations for the four unknown. In practice, $N \gg 3$ independent sets, leading to an over-determined system, are needed to overcome the effect of the noise. The latter can be considerably reduced by increasing the length of the discharge. For the experiments reported in the following, a pulse length of ≈ 3.5s is used for modulation frequencies ~ 80Hz.
The method requires a large amount of experimental data to reconstruct the 3-D profiles of the amplitude and phase for each modulation frequency. The number of required plasma discharges can be considerably reduced by choosing a convenient waveform for the modulated microwave power, for example short, rectangular pulses containing a large number of harmonics of the fundamental modulation frequency (Sec. 9), see Fig. 8.17. The measurements are done with the SLP probe (Sec. 3.4), which can be rotate about its axis to collect data from regions $s \lesseqgtr 0$. A spatial resolution of 1cm radially and 1.8cm vertically and toroidally is sufficient to provide accurate profiles of the background plasma parameters.

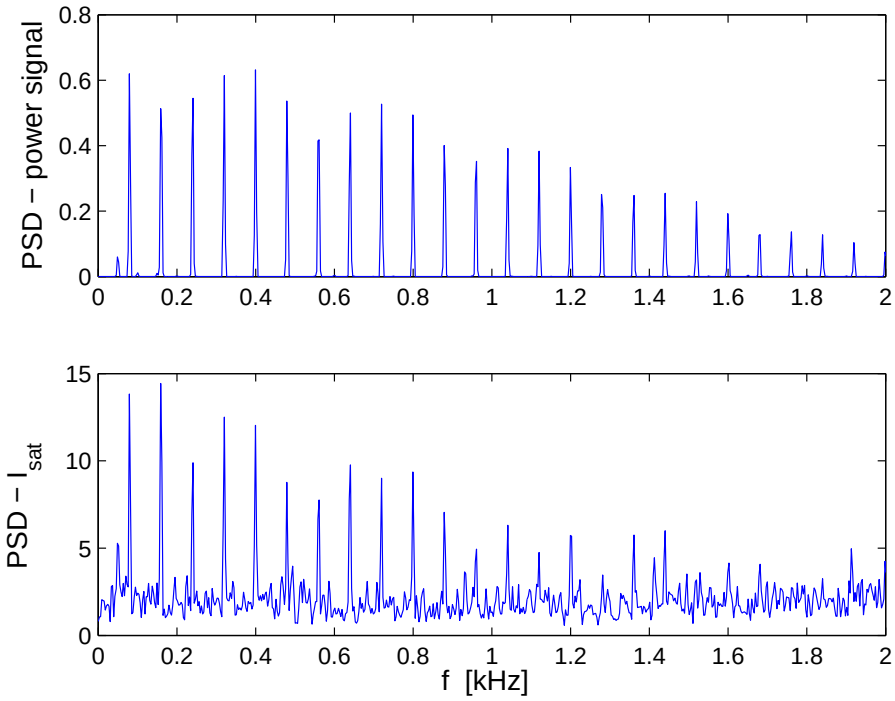

Figure 8.17: Power spectral density of the modulated microwave power signal and of an ion saturation current signal.

Chapter 9

Measurements of the total particle flux via EC power modulation

In this Chapter, the particle transport is investigated by means of the EC power modulation technique discussed in Sec. 8.7. This technique represents an extension of the simple method used in Sec. 7.3.2 to estimate the particle confinement time from the plasma dynamical response to a perturbation of the injected microwave power. The goal here is to measure the particle fluxes along the radial, vertical and toroidal directions, which play the role of loss terms in the density continuity equation. The fluxes are then interpreted in terms of a convective velocity.
The target plasma is obtained from Hydrogen, with 400W of injected microwave power. The toroidal and vertical magnetic fields are 76mT and 1.2mT, corresponding to $I_{tf} = 380$A and $I_{vf} = 60A$. The neutral gas pressure is 3.5×10^{-5}mbar. The background profiles of density, electron temperature and plasma potential are presented in Fig. 9.1.
The choice of the modulation parameters is discussed in Sec. 9.1. In Sec. 9.2 the plasma density response, in terms of amplitude and phase, is illustrated and the validity of the hypotheses introduced in Sec. 8.7 is verified. The 'multi-harmonics' method is then applied to derive the three-dimensional plasma fluxes (Sec. 9.3). Finally, the results of this Chapter are summarised and discussed in Sec. 9.4.

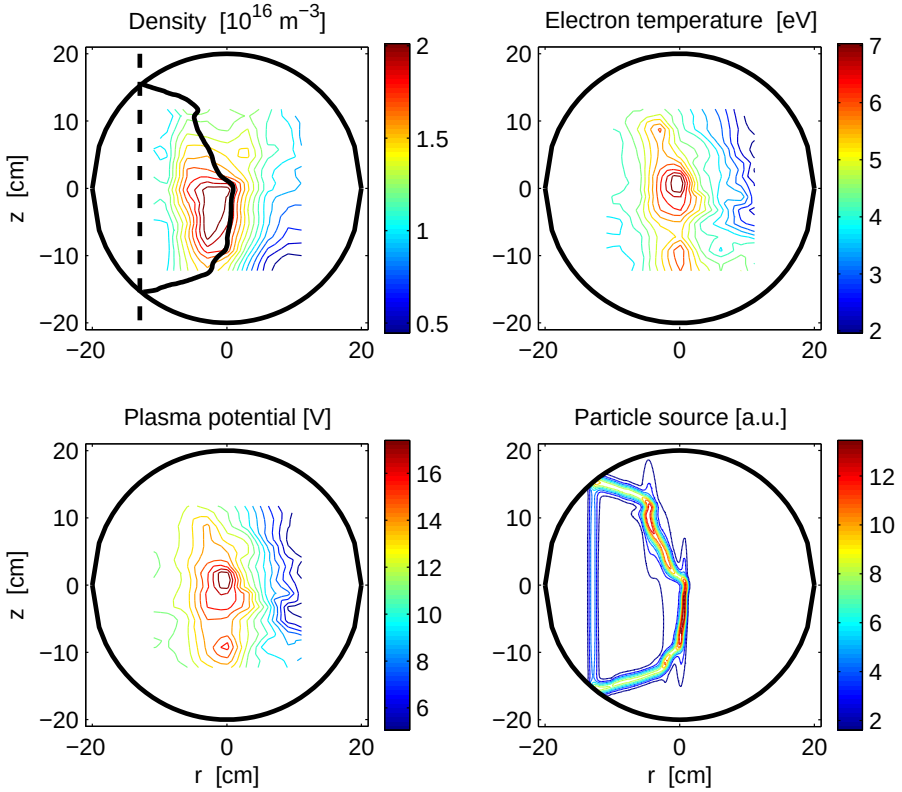

Figure 9.1: Plasma density, electron temperature, plasma potential and particle source profiles for the target plasma investigated in this Chapter.

9.1 Modulated power signal

Two types of power modulation waveforms are used, whose parameters are summarised in Tab. 9.1. The modulation frequency is 80Hz, much lower than the typical frequency of instabilities and the inverse of the intermediate time-scale of the macroscopic plasma dynamics (cfr. Chap. 7). Both waveforms consist of rectangular pulses, which allows one to inject simultaneously a large number of harmonics of the modulation frequency. The number of discharges required to measure the plasma response in a poloidal cross-section is thus considerably reduced, with respect to using a purely sinusoidal modulation. The amplitude and the duty-cycle of the power perturbation are minimised, in order to avoid a strong departure from the stationary background profiles during the pulses, while preserving a clearly detectable density response. The main difference between the two sets of modulation parameters is the sign of the power perturbation (Fig. 9.2). For regions on the high-field side with respect to the UH resonance, the signal-to-noise of the density response to a

Pulse shape	*min. power* [W]	*max. power* [W]	f_{mod}	*Duty cycle* [%]
Positive	400	500	80	3
Negative	300	400	80	10

Table 9.1: Parameters of the two sets of modulated microwave power.

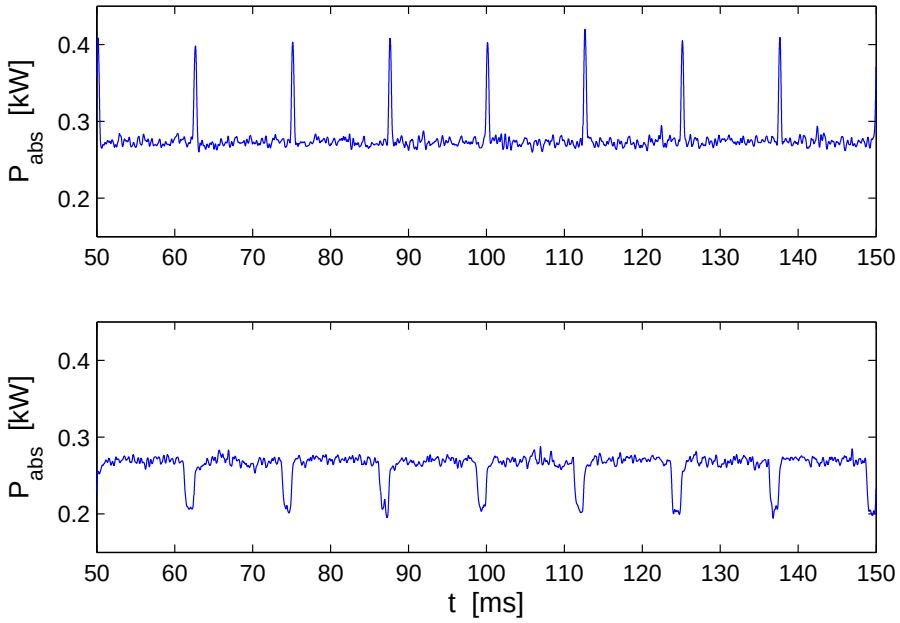

Figure 9.2: Time traces of the modulated microwave power used to investigate the plasma response.

positive pulse of the injected microwave power is very low. On the other hand, a net response is measured for negative pulses. The possibility of interpreting within the same analysis the plasma response to modulated power signals with different modulation parameters is discussed below.
The power spectra of the power modulation signals are shown in Fig. 9.3. Multiple harmonics of the fundamental modulation frequency at 80Hz are visible, especially for the 'positive' pulses. The same harmonics are detected in the I_{sat} signals, with different amplitudes depending on the probe position.

9.2 Consistency of the plasma response

In order to infer from the multi-harmonics technique the three-dimensional particle flux, a number of hypotheses need to be verified:

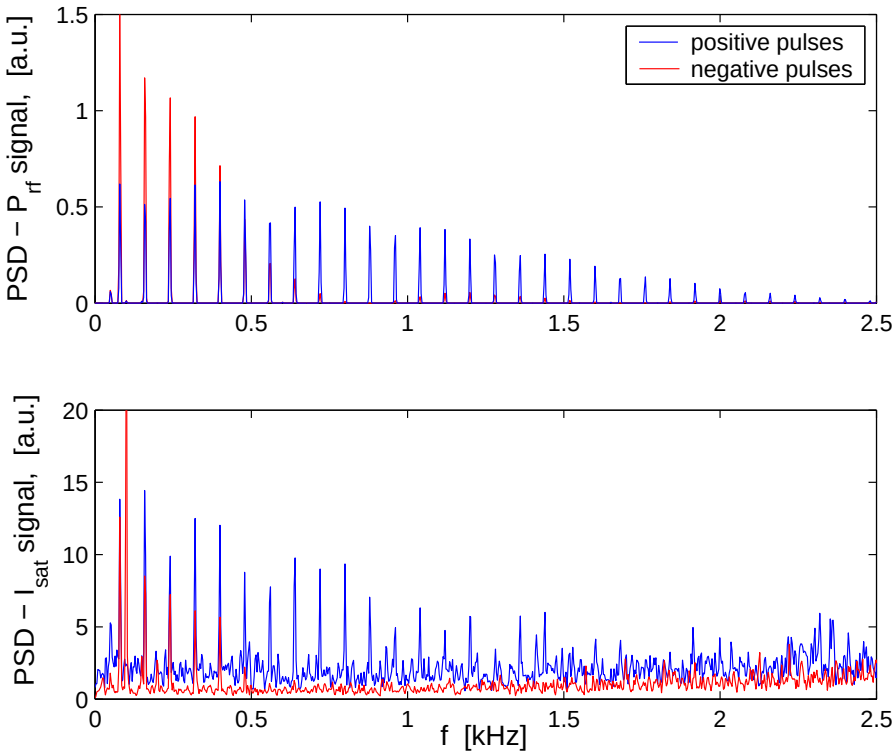

Figure 9.3: Power spectral density of the microwave power signals shown in Fig. 9.2.

1. The particle transport is dominated by convection with a phase between density and modulated power depending linearly upon the modulation frequency.

2. The spatial profile of the perturbed particle source is independent of the modulation frequency.

3. Amplitude and phase of the transfer function between modulated power and density response must be consistent with the particle source profile. In particular, a maximum amplitude and a phase ≈ 0 are expected where the source term is maximum.

4. The perturbations of the convection velocity induced by the microwave power modulation are negligible.

Examples of the density response at the fundamental modulation frequency are presented in Fig. 9.4. The corresponding amplitude and phase, combined in the same figure, refer to positive and negative pulses for regions $r \geq -2.5$cm and $r < 0$cm. Average values between data from positive and negative modulation pulses are taken in the overlapping region. The background density profile and the $E \times B$ velocity

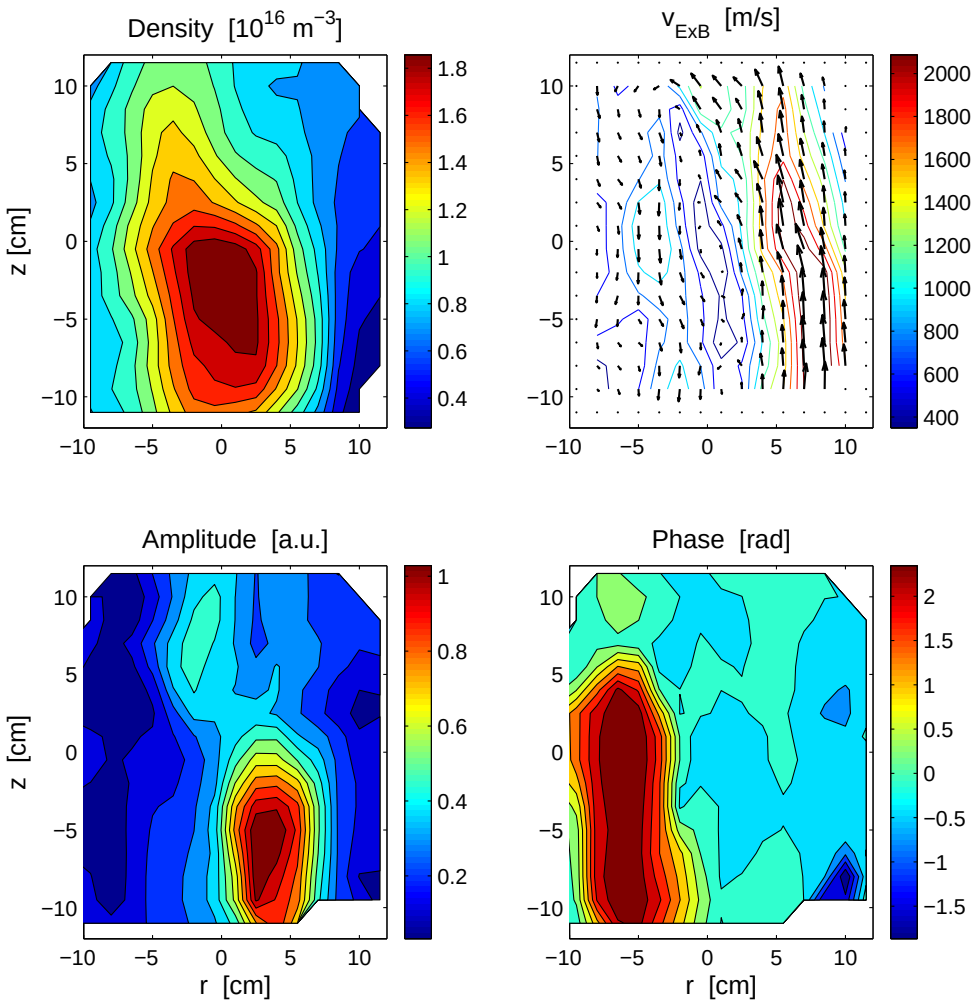

Figure 9.4: *Top:* density profile and $E \times B$ velocity for the case investigated in this Chapter. *Bottom:* amplitude and phase of the density response for the fundamental modulation frequency of 80Hz. The phase is measured in $[-\pi, \pi]$.

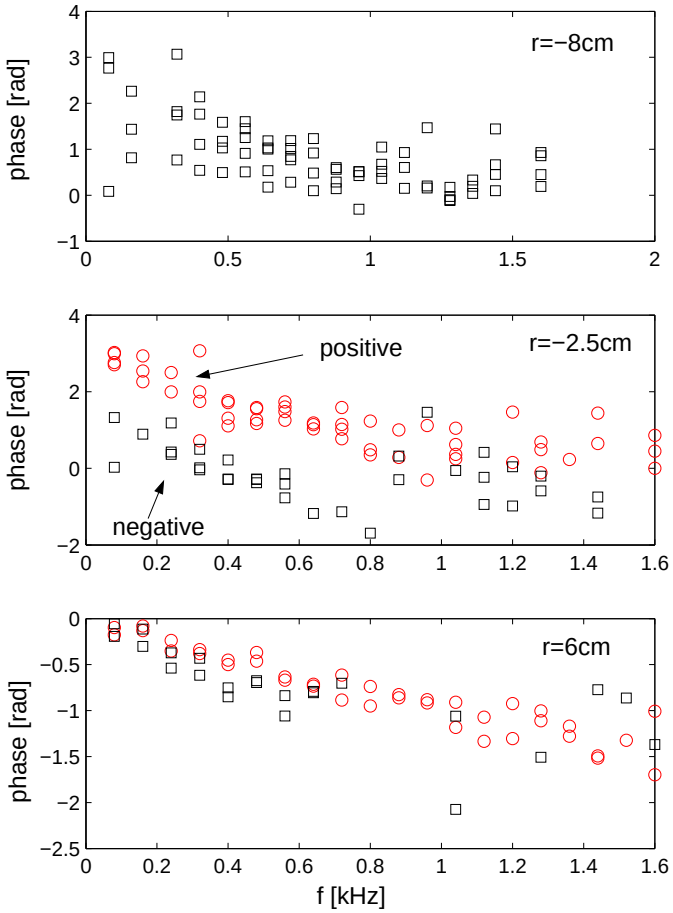

Figure 9.5: Measured phase of the density response at different radial positions at the midplane. Results from discharges with positive and negative density bursts are indicated by circles and squares.

pattern and magnitude are also shown. The validity of the hypotheses on which the multi-harmonics method is based is verified below.

- *Hypothesis no. 1*
  A first argument for excluding that diffusion is the dominant transport mechanism in TORPEX plasmas is the systematic spatial separation between regions of maximum density and position of the particle source, that could be explained only by a negative diffusion coefficient. In addition, diffusive processes lead to a spatially symmetric amplitude of the density response around the source region. This is not observed on TORPEX, even for high modulation frequency $\geq$ 50kHz, for which the contribution to the density response from convective terms should vanish [11].

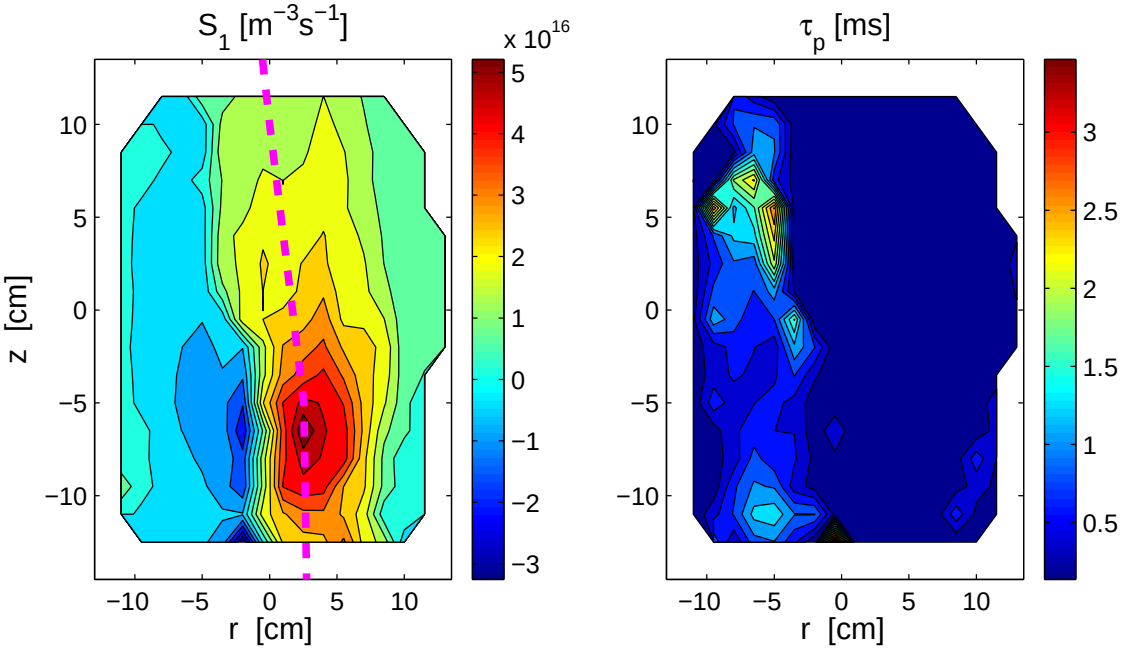

Figure 9.6: Ionisation rate associated with the microwave power perturbation (*left*) and particle confinement time (*right*). The thick, dashed line represents the position of the UH layer.

For different positions, a linear dependence between the phase of the density response and the modulation frequency is observed (Fig. 9.5). The slope is almost constant up to $\approx$ 1kHz, compatibly with purely convective transport mechanisms. On the high-field side, where negative pulses are used, the phase measurements are confused and the convective character of the transport can not be confirmed. Therefore, the hypothesis no. 1 is confirmed only for regions with $r \geq 2.5$cm.

- *Hypothesis no. 2*
  The density response data can be used to calculate the confinement time, τ_p, and the profile of the perturbed particle source, S_1, (Fig. 9.6), as described in Sec. 7.3.2. The profile of S_1, evaluated from the combined analysis of all the harmonics up to 1kHz, is consistent with the position of the UH layer, calculated from the time-averaged profiles. A 'negative' source, indicating a decreased ionisation rate with respect to the unperturbed value, is found when negative power pulses are used, i.e. for $r < 0$. From the results of S_1 calculated for each harmonic separately, we conclude that hypothesis no. 2 is qualitatively verified, although the measured confinement time for regions $r < 0$ is much larger than that measured in Sec. 7.3.

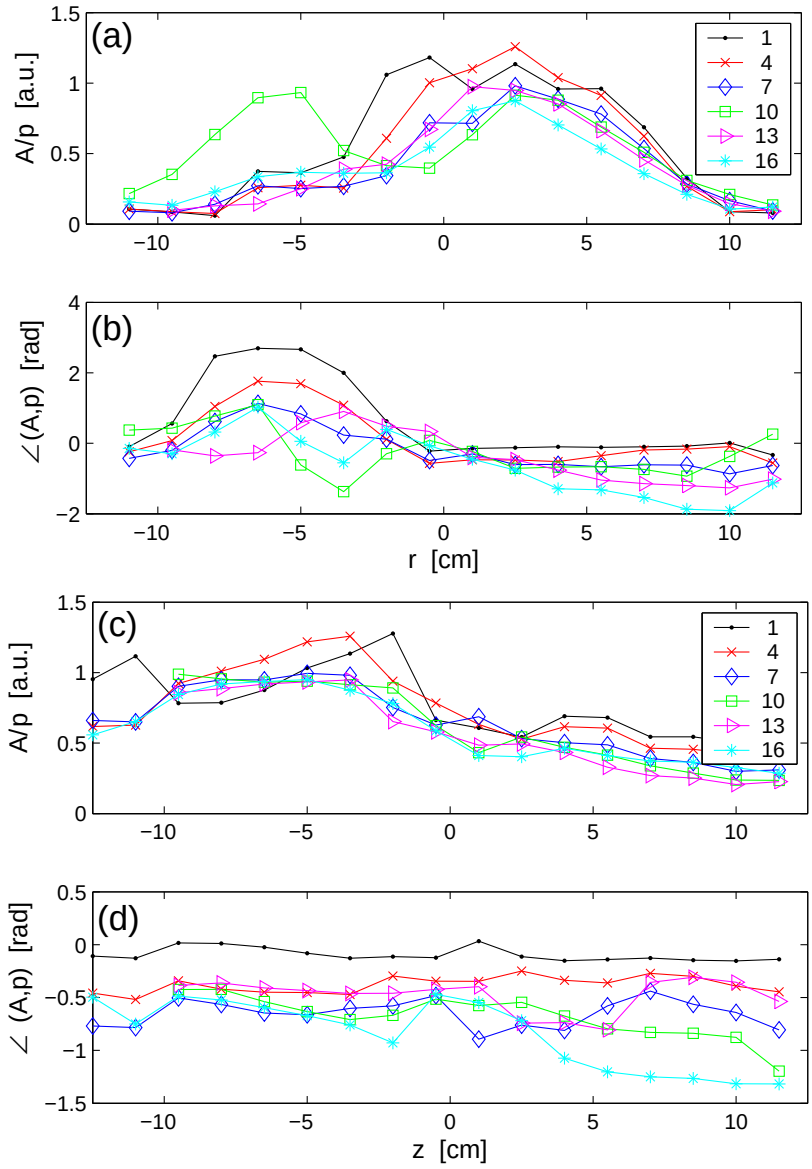

Figure 9.7: Amplitude and phase of the density response to a modulated microwave power for different harmonics of the fundamental frequency. Plots *(a)* and *(b)* refer to a radial cut at the midplane, and plots *(c)* and *(d)* to a vertical cut at $r = 5$cm. The amplitude is normalised to the spectral amplitude of the microwave power signal.

- *Hypothesis no. 3*
  The amplitude of the plasma response is similar for most of the harmonics of the fundamental modulation frequency. Figure 9.7 shows the radial and vertical profiles of amplitude and phase for six harmonics. Strong spatial variations are observed along the radial direction, while the profiles along z are smoother. The maximum amplitude is observed around $r = 3$cm, where the phase is close to zero, consistently with the particle source profile. However, for some of the harmonics a second maximum at $r = -5$cm is measured. Moreover, the phase approaches π for regions $r < 0$, indicating that the decreased injected power leads to an *increase* of the density. This feature is confirmed by traces of n, T_e and V_{pl} obtained with the boxcar-averaging technique (Fig. 9.8). An explanation is suggested on the basis of the plasma production mechanisms. When the injected power is decreased, the UH layer shifts to the high-field side and the density adjusts itself on a new profile. Regions on the low-field side of the UH layer are characterised by a drop of the density. In regions on the high-field side of the UH layer, inside the main plasma, where n is usually slightly higher than n_{uh} (see Sec. 7.1), the density decays until $n \approx n_{uh}$ and the UH resonant condition is satisfied, therefore n increases again. This is in contrast with hypotheses no. 2 and 3.

- *Hypothesis no. 4*
  From Fig. 9.8, we observe that there is a finite perturbation of V_{pl} when negative pulses are applied, which violates the hypothesis no. 4.

In general, there are discrepancies between the results obtained with positive and negative pulses. For the latter, most of the assumptions on which the multi-harmonic analysis is based are clearly not satisfied. For these reasons, only discharges with positive power pulses are used in the next Section to calculate the particle fluxes.

9.3 Measured particle fluxes

The particle flux calculated with the multi-harmonics method is shown in Fig. 9.9, and the components along the three axis, Γ_r, Γ_z and Γ_s, in Fig. 9.10. As discussed in the previous Section, the analysis is restricted to 'positive' power pulse, and only harmonics with $f \leq 1$kHz are included.
The flux removes particles from the region of maximum density, where a radially outward flux is measured. The direction of Γ_r is inverted at $r = 5$cm, in the region of maximum density gradient. Here a strong vertical flux, co-linear with the background $E \times B$ drift, is present. In general, we observe that the sign of Γ_z is consistent with the sign of the $E \times B$ drift, although U_z and $v_{E\times B}$ differ considerably in magnitude. A complicated profile of Γ_s, characterised by a quadrupole-like structure, is observed. Qualitatively, the direction of Γ_s is inverted when the midplane

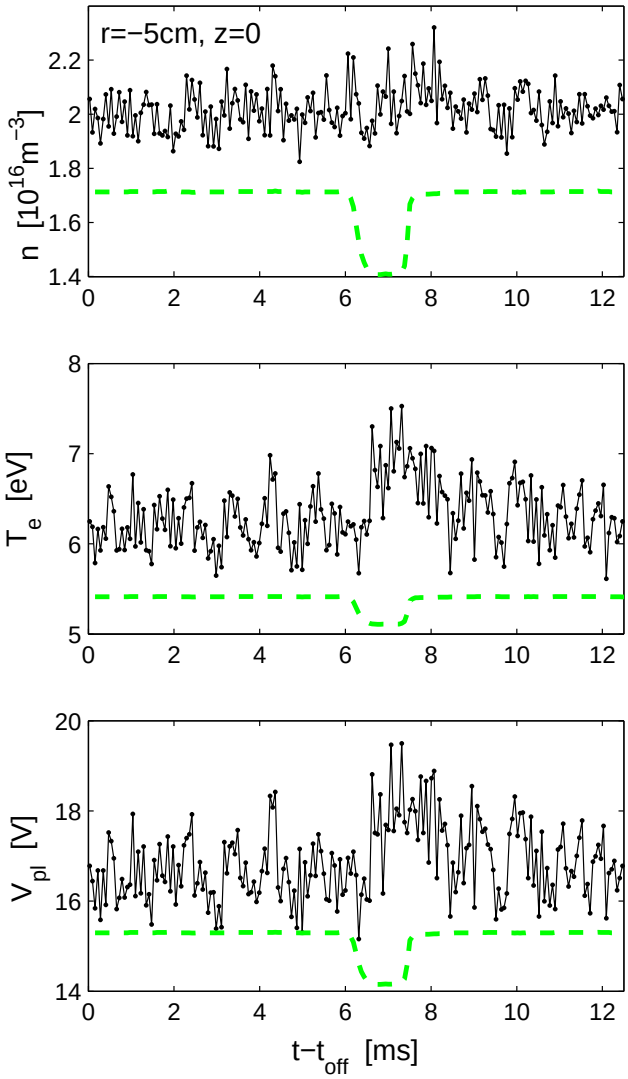

Figure 9.8: Response of n, T_e and V_{pl} to a drop of microwave power, reconstructed by the boxcar-averaging method. Despite the decreased level of injected power, the three parameters show an increase during the pulse.

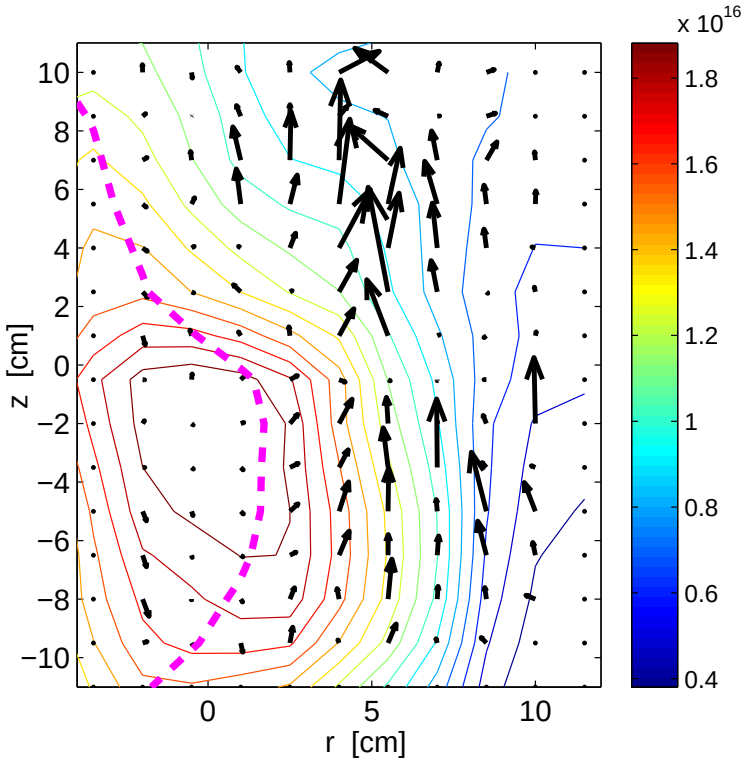

Figure 9.9: Poloidal pattern of the convective velocity calculated by means of the 'multi-harmonics' Fourier analysis. The background density profile (in $[m^{-3}]$) and the position of the UH resonance (thick, dashed line) are shown.

and the UH layer are crossed. It is interesting to note that there are indications of a coupling between the toroidal and vertical flow velocities, with $|U_s|/|U_z| \approx const$ (Fig. 9.11), as expected due to the non-zero tilt angle of the magnetic field.

9.4 Summary and discussion

The total particle flux along the radial, vertical and toroidal directions has been measured by means of techniques based on the modulation of the microwave power. A simplified convective model, assuming negligible perturbations of the convection velocity, is used to interpret the density response to the modulated EC power. The measured fluxes are characterised by complex spatial profiles, which can not be easily interpreted in terms of macroscopic plasma drifts. The ordering of the fluxes, with $\Gamma_r < \Gamma_z < \Gamma_s$, confirms that particle losses mainly occur along the open magnetic field lines. The global loss rate is consistent with that calculated for the density decay time measured in Sec. 7.3.

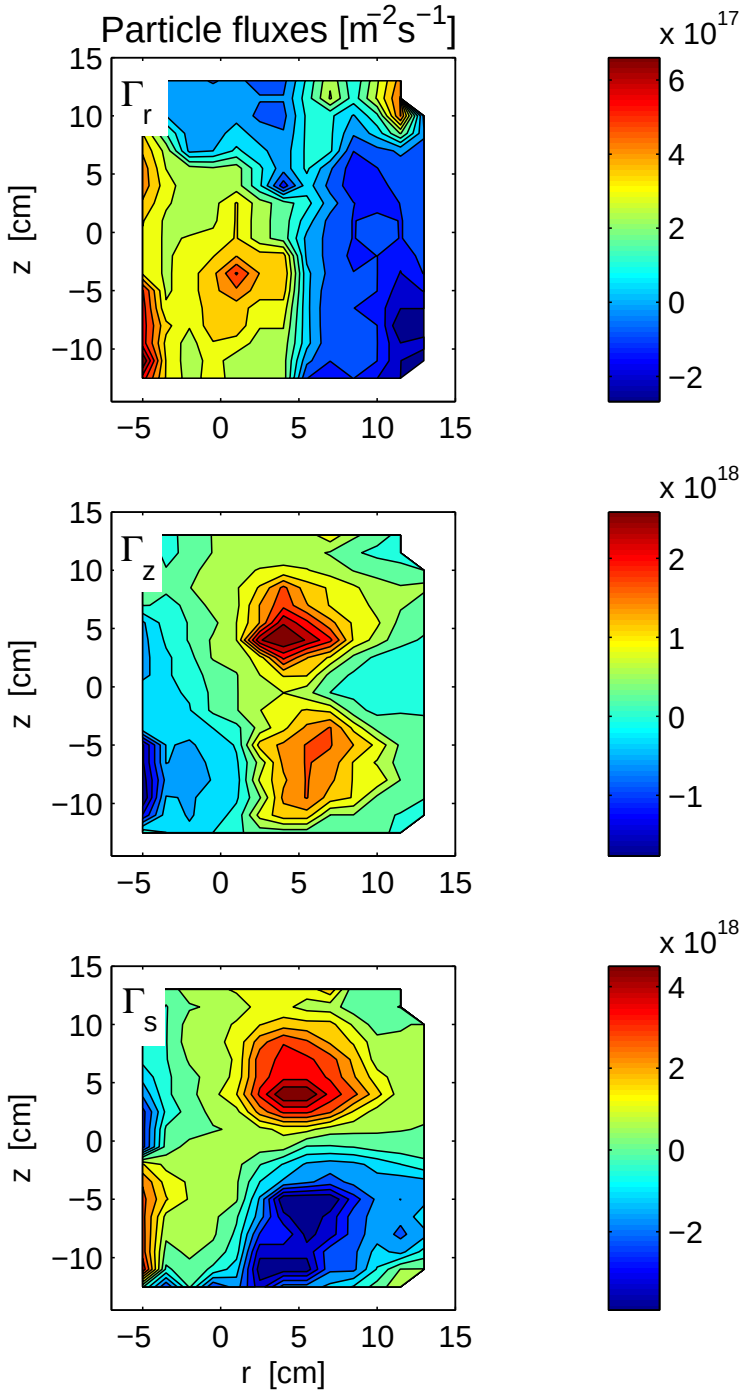

Figure 9.10: Plasma flows along the radial, vertical and toroidal directions calculated via the 'multi-harmonics' Fourier method.

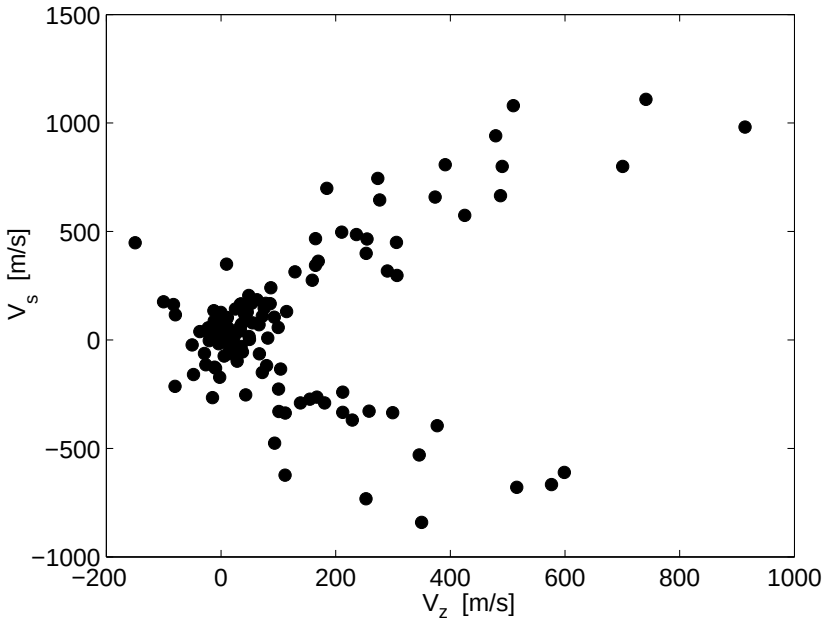

Figure 9.11: Toroidal versus vertical component of the convective velocity, suggesting a possible coupling between the fluxes in the two directions.

It should be noted, however, that the solutions obtained from the system 8.39 are not very stable with respect to particular choices of the analysis parameters, like the range of frequencies from which the input data are taken. For example by restricting the analysis only to frequencies $0.5 \leq f \leq 1$kHz, the convection velocities change by up to 90% for the radial direction and 60% for the vertical and toroidal directions. Nonetheless, the results presented in this Chapter represent a proof-of-principle of the applicability of power modulation techniques to basic laboratory experiments. The technique could be further improved by an optimisation of the modulation parameters, by extending the discharge length and, possibly, by relaxing some of the assumptions for the particle transport model. In particular, the perturbed velocity term, $\underline{U}_1$, could play a considerable role in determining the plasma response also for small modulation amplitudes.
Apart from the information on the total particle fluxes, these results do not allow one to discriminate between the different transport mechanisms which are at play in TORPEX plasmas. In particular, the link between plasma instabilities and the related particle transport can not be established. Other methods must be used, as discussed in the next Chapters.

Chapter 10

Fluctuation-induced flux, spectral analysis

In this Chapter I discuss the main results from measurements of the radial fluctuation-induced particle flux, measured by the TRIP probe (Sec. 3.4) on the midplane. The same probe is used as a triple-probe to the measure electron temperature fluctuations (Sec. 8.1). We can thus calculate the plasma potential from floating potential and electron temperature measurements, as described in Sec. 8.2.
The experimental scenario with $B_z = 1.2$mT, for which a complete characterisation has been given in the previous Chapters in terms of time-averaged profiles and plasma fluctuations, is investigated in detail in Sec. 10.1. In Sec. 10.1.1 the analysis is extended to other values of the vertical magnetic field, for which different features of the plasma instabilities are observed, cfr. Sec. 7.2.
The results are summarised in Sec. 10.2, where the necessity of a having more complete information on the two-dimensional poloidal profiles of the fluctuation-induced flux is discussed.

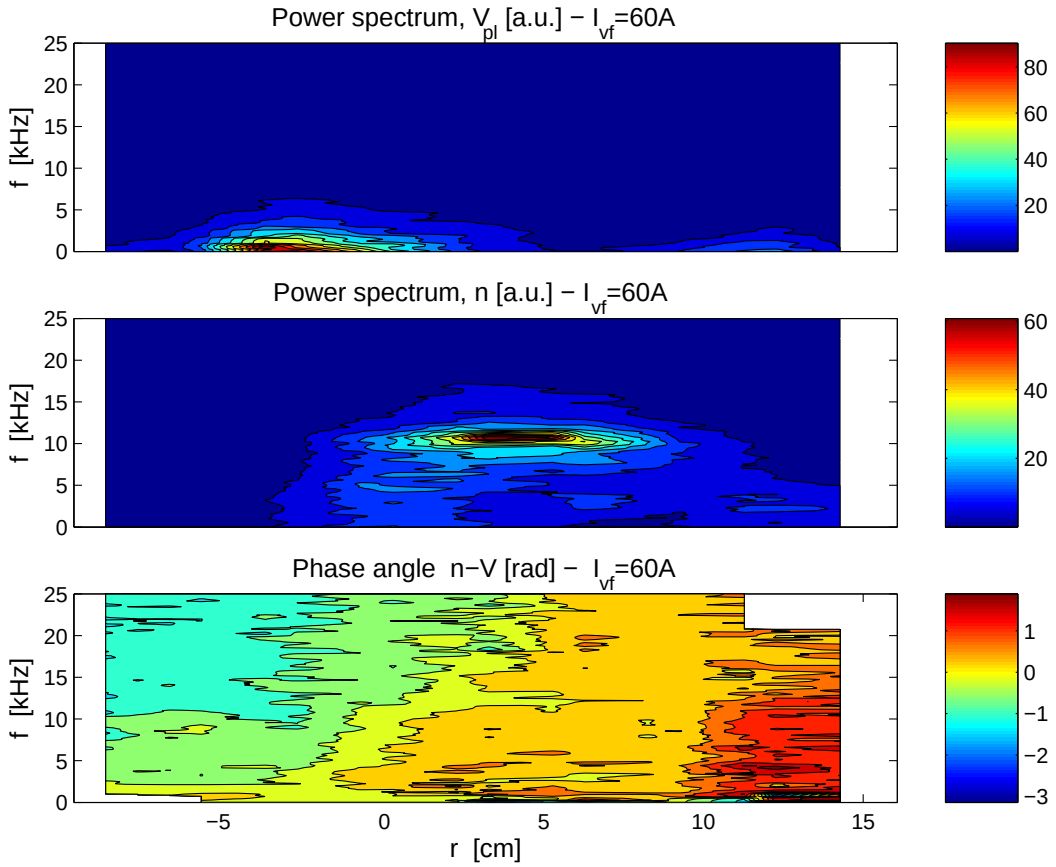

Figure 10.1: Power spectra for plasma potential and density fluctuations, and measured phase between density and plasma potential.

10.1 Measurements of the spectral flux

The target plasma for this Section is obtained from Hydrogen at 6×10^{-5}mbar, with 400W of injected microwave power. The toroidal and vertical magnetic fields are 76mT and 1.2mT. The background profiles of density, electron temperature and plasma potential are shown in Fig. 9.1. Measurements are taken during discharges lasting 300ms, with a spatial resolution of 3cm radially.
Referring to Fig. 7.10, two unstable modes are usually observed for this choice of experimental parameters. A drift mode at $\approx$ 4kHz develops in the density gradient region in the bottom half of the poloidal cross-section. An interchange mode, with frequency $\approx$ 12kHz, forms on the LFS at $z \sim -10$cm. The two modes are convected upward by the $E \times B$ background drift. At the midplane, where measurements are taken, the two modes coexist, although the spectrum is usually dominated by the higher frequency mode. The power spectra of density and plasma potential fluctu-

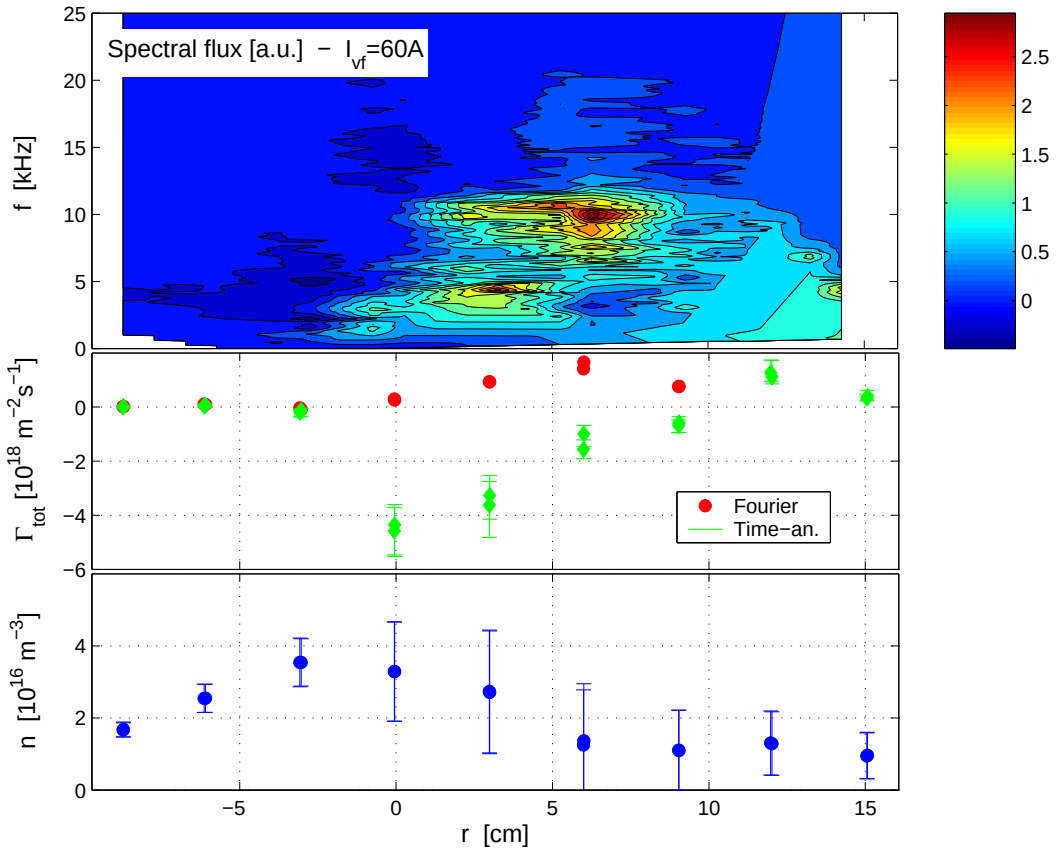

Figure 10.2: Spectral flux (*top*) and total flux (*bottom*) as a function of the radial position. The flux calculated directly from the time-series of n and V_{fl} is shown for comparison. The radial density profile is shown in the bottom figure. The error bars represent the standard deviation of the time series.

ations and their phase angle, $\alpha_{\tilde{n}\tilde{\varphi}}$, are shown in Fig. 10.1 as a function of the radial position. Figure 10.2 illustrates the corresponding radial fluctuation-induced particle flux. The integrated flux is directed radially outward, i.e. it removes particles from the high-density region. It approaches zero at $r \approx 10$cm, where the amplitude of the fluctuations also vanishes. For $r > 10$cm the coherence between n and V_{pl} fluctuations is very low, indicating that here density and plasma potential fluctuations are, in practice, uncorrelated. For comparison, the particle flux calculated directly from the density and floating potential time series is also shown in Fig. 10.2. The discrepancy with the flux calculated through Fourier analysis, including electron temperature fluctuation effects, highlights the importance of a correct measurement of the plasma potential.

From the spectral analysis we observe that the mode at higher frequency accounts

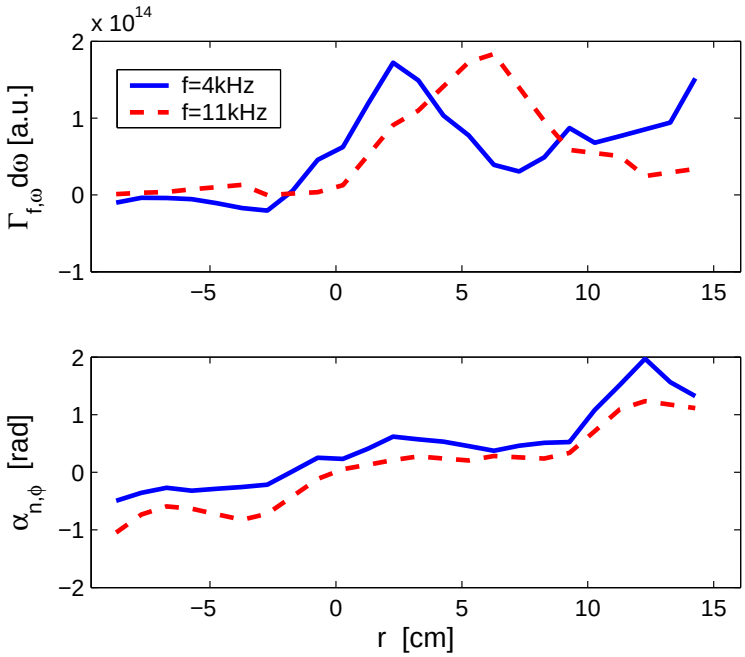

Figure 10.3: *Top:* Radial profile of the spectral flux, $\Gamma_{f,\omega}$, measured at the midplane for the modes at 4kHz and 12kHz. *Bottom:* Corresponding phase angle, $\alpha_{\tilde{n}\tilde{\varphi}}$. For $r > 10$cm the coherence between density and potential approaches zero and the results for $\Gamma_{f,\omega}$ are meaningless.

for almost all the integrated flux for $r \geq 5$cm. Between $r = 0$cm and $r = 5$cm most of the flux is due to the 4kHz mode. The radial profile of the spectral flux for the two modes is detailed in Fig. 10.3, along with the phase angle between density and potential. Note that there is no simple relation between the phase and the flux magnitude, or between the amplitude of the modes and the flux. For example, there is no flux associated with the fluctuations of V_{pl} at frequencies ≤ 1kHz, measured for $-5 \leq r \leq 2$cm (Fig. 10.2). This indicates that all the terms in Eq. 8.23, defining the spectral flux, are in general equally important for a correct estimate of $\Gamma_{f,\omega}$.

10.1.1 Vertical magnetic field scan

To investigate the variations of the fluctuation-induced flux with the characteristics of the naturally occurring unstable modes, the measurements are repeated for different values of the magnetic field, namely $B_z = 0.6$mT and $B_z = 2.3$mT. As discussed in Sec. 7.2, the spectrum at the midplane is dominated by drift modes at low B_z, and by interchange modes for $B_z > 1.5$mT.
The spectra of density and plasma potential fluctuations are presented in Fig. 10.4,

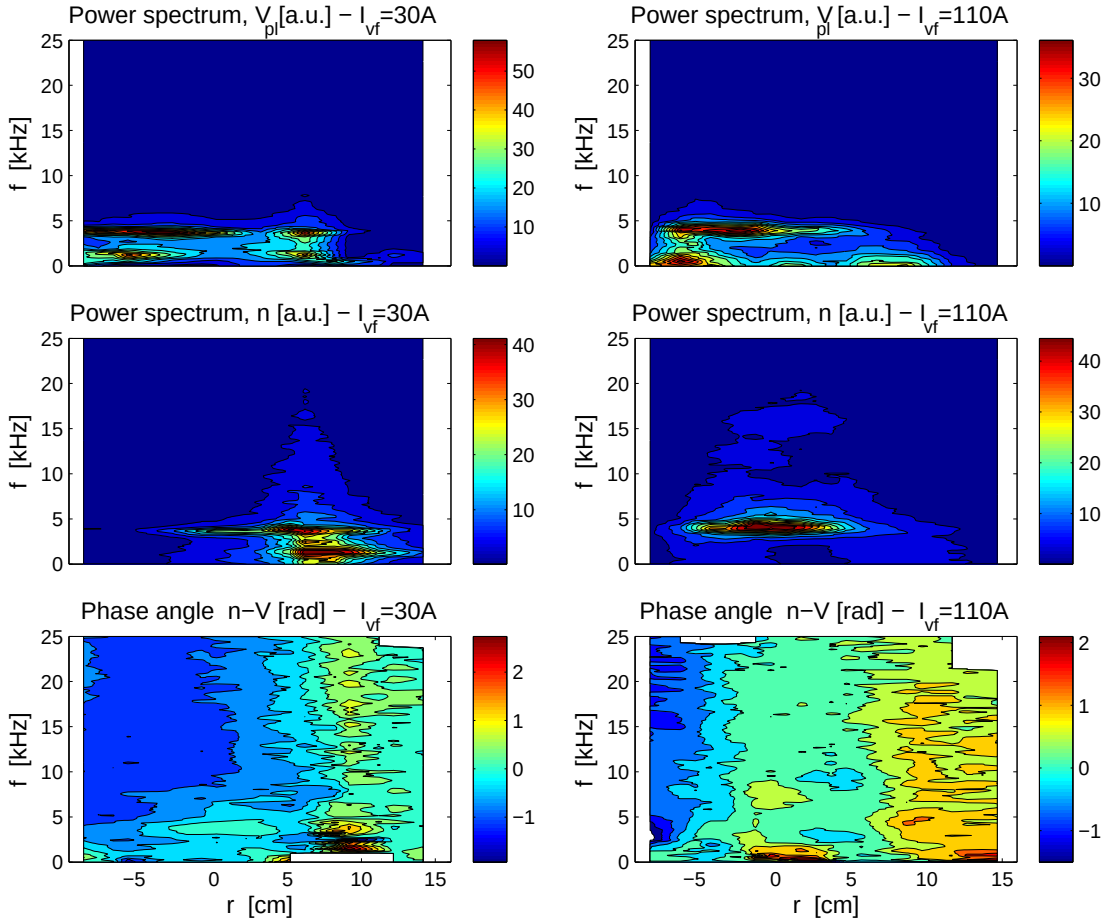

Figure 10.4: Power spectra for V_{pl} and n fluctuations for a vertical magnetic field $B_z = 0.6$mT (*left column*) and $B_z = 2.3$mT (*right column*).

and the calculated radial flux in Fig. 10.5. For $B_z = 0.6$mT two modes are observed. Only the one at 4kHz, which is the same discussed in the previous Section, causes a radial particle flux. Also in this case the relation between flux, phase angle and amplitude of the fluctuations is not trivial. Contrary to the previous example, an inversion in the direction of the flux is observed around $r = 8$cm (Fig. 10.5). Unfortunately, the poor spatial resolution of the measurements does not provide the fine details of this flux reversal.

When the vertical magnetic field is increased to $B_z = 2.3$mT, a single peak is observed in the density and potential spectra between 4kHz and 5kHz, related with an interchange mode (Sec. 7.2). The associated radial flux is positive, and comparable in magnitude with the one measured for the other values of B_z. This particular scenario will be investigated in more details in Chap. 11.

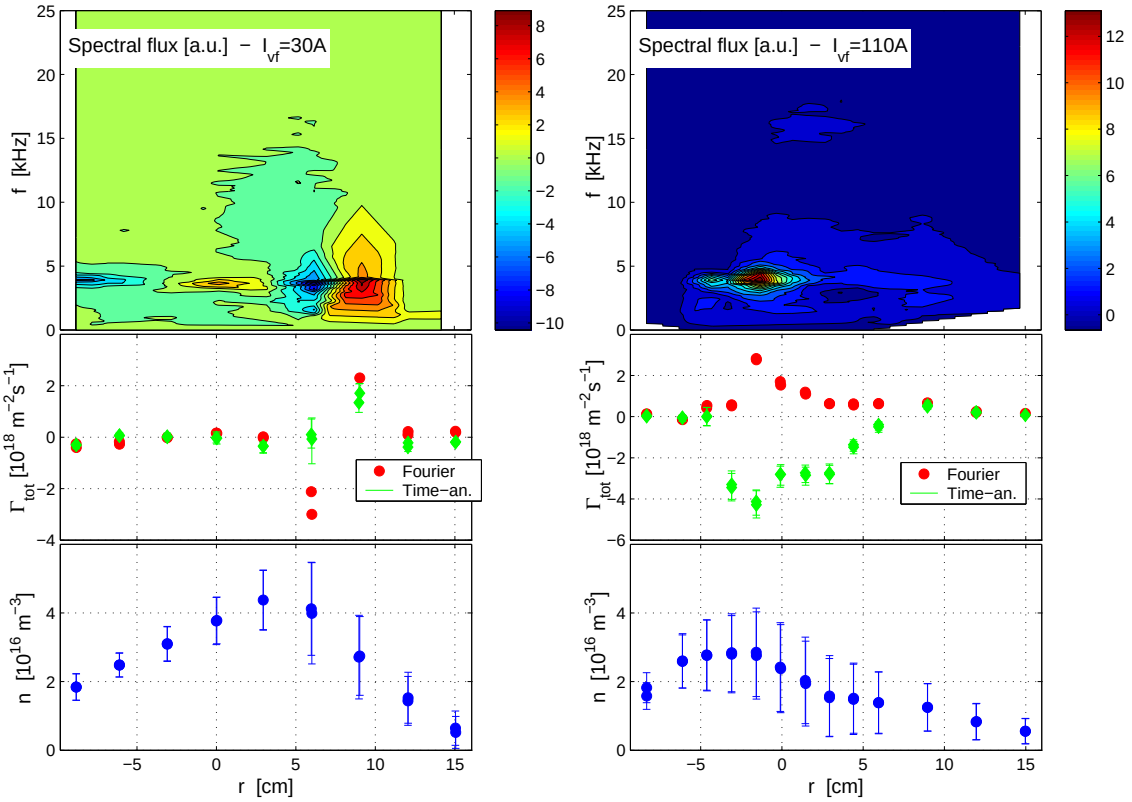

Figure 10.5: Spectral and total radial fluxes for $B_z = 0.6$mT (*left column*) and $B_z = 2.3$mT (*right column*).

10.2 Summary and discussion

In summary, the radial particle flux related to plasma instabilities has been measured for different values of a specific control parameter, the vertical magnetic field. By varying B_z, the spectral features of the observed instabilities changes, thus allowing us to explore the link between the flux and plasma modes with different frequency and wave-number properties.

Qualitatively similar features are observed for all the B_z values, despite the different character of the dominant instability and the different statistical properties of the signals [76] for the different cases. For example, the flux is radially outward from the region of maximum density. Negative values, corresponding to a radially inward flux, are measured for intermediate values of B_z in regions corresponding to the density maximum. The magnitude of the flux is of the order of $10^{18}\mathrm{m}^{-2}\mathrm{s}^{-1}$, comparable with that obtained for the total flux through EC power modulation techniques for $r \leq 5$cm (Fig. 9.10). The fluctuation-induced flux would then be responsible for the transport across B in this region, while the negative total flux measured for $r > 5$cm

remains unexplained.
A critical aspect for the analysis presented herein is the reconstruction of the plasma potential signal from floating potential and electron temperature measurements. The measured flux may even change sign when the floating potential, instead of V_{pl}, is used to evaluate the fluctuating electric field. Particularly important for a quantitative analysis is the measurement of the phase angle, $\alpha_{\tilde{n}\tilde{\varphi}}$. In practice, discharges lasting $>$ 1s, would be required to reduce conveniently the noise in the measurements, especially for the low-frequency components ($f \leq$ 1kHz) of the spectrum. This was not possible for the experiments reported herein, for which, however, the dominant instabilities have $f \geq$ 4kHz and should be well resolved by the measurements.
The results presented in this Chapter are limited to measurements of the radial component of the fluctuation-induced flux. Moreover, only data taken along an horizontal chord at the midplane are available. This represents a limitation for the present analysis, because it can not be excluded *a priori* that the fluctuation-induced flux has a non-negligible contribution also in the vertical direction.
These considerations motivate the investigation of the instabilities properties, and of the related particle flux, over a more extended region. This is the subject of the next Chapter, in which methods based on the analysis of plasma fluctuations and related transport in the time-space domain are used.

Chapter 11

Real-space analysis of fluctuation-induced and structure-related transport

The results presented in the previous Chapters indicate that a complete study of transport phenomena in the toroidal plasmas of TORPEX must be based on measurements covering the entire cross-section. In this Chapter, I present results from two-dimensional measurements of the particle and heat fluxes from two complementary methods, namely the combined CAS-boxcar method and the structure analysis, previously described in Sec. 8.5 and Sec. 8.6, corresponding to two different components (or *orders*) of the total flux.
Two experimental scenarios, achieved by changing the value of the vertical magnetic field from $B_z = 1.2$mT to $B_z = 2.3$mT, are studied. The time-averaged plasma profiles and the properties of the unstable modes are described in Sec. 11.1. Three regions, in which different specific phenomena are at play, are identified in both cases: (i) a 'main plasma' region where unstable modes develop, (ii) a 'source-free' region where isolated plasma structures are intermittently observed, and (iii) a 'transition region' between (i) and (ii), where modes and intermittent events co-exist. This allows us to identify and use a particular experimental scenario for simulating aspects usually observed in the scrape-off layer (SOL) of tokamaks. In particular, the ejection of high-density plasma structures, or *blobs*, from the main plasma into the source-free region is investigated in detail (Sec. 11.2), including the blob origin and propagation characteristics.
The different nature of the flux terms, simply related to fluctuating density and potential, and to macroscopic structures in the fluctuating density, is discussed in Sec. 11.3. A possible ordering, from the zero-th order time-averaged total flux to the second-order fluctuation-induced flux, is proposed as a guideline for the interpretation of the experimental results.
The results from the CAS-boxcar method are presented in Sec. 11.4 for the standard value of the vertical magnetic field, $B_z = 1.2$mT, and for $B_z = 2.3$mT. In general, it is found that the fluctuation-induced particle flux is radially outward over most of the poloidal cross-section, independently of the specific character of the dominant unstable modes. The heat flux is mainly convective. The conduction term is negligible, due to a vanishing phase between electron temperature and plasma potential fluctuations.
For the high-B_z case, isolated high-density structures are clearly observed to originate intermittently from the coherent mode. The transport related to these events is investigated in Sec. 11.5 by means of the structure analysis, and the results are compared with those obtained from the CAS-boxcar method. It is shown that the cross-B particle flux in the source-free region is mainly determined by the radial propagation of the density structures.

11.1 Experimental scenarios: time-averaged profiles, instabilities and definition of the 'SOL-like' configuration

11.1.1 Time-averaged plasma profiles and instabilities

In this Section, I describe the two experimental scenarios in which the particle and heat transport, and the mechanisms behind them, are investigated in detail (Sec. 11.4 and Sec. 11.5). The working gas is Hydrogen for both cases.
The injected microwave power, the neutral gas pressure and the toroidal magnetic field are the same for the two scenarios, with $P_{rf} = 400$W, $p_{gas} = 3.5 \times 10^{-5}$mbar and $B_\varphi = 72$mT. Only the vertical magnetic field is changed, with $B_z = 1.2$mT and $B_z = 2.3$mT for the two cases. By changing B_z, different features in the time-averaged profiles and in the spectral features of the observed unstable modes are present:

- $B_z = 1.2mT$.
  The background plasma profiles for $B_z = 1.2$mT are shown in Fig. 11.1. Density, electron temperature and plasma potential profiles peak around $r = 0$, $z = 0$, then decrease in both the radial and vertical directions.
  Three modes are observed in the density spectrum (Fig. 11.1). Those at $\approx$ 2kHz and 4kHz are identified as drift modes, and the mode at 12.5kHz is an interchange mode (see Sec. 7.2) [80].

- $B_z = 2.3mT$.
  The background plasma profiles for $B_z = 2.3$mT are shown in Fig. 11.2. The plasma profiles are slab-like, with a pronounced vertical elongation.
  In the region $r < 5$cm the fluctuation spectrum is dominated by an interchange mode at 4kHz, which originates at the bottom of the poloidal cross section, then is advected upward by the $E \times B$ drift.

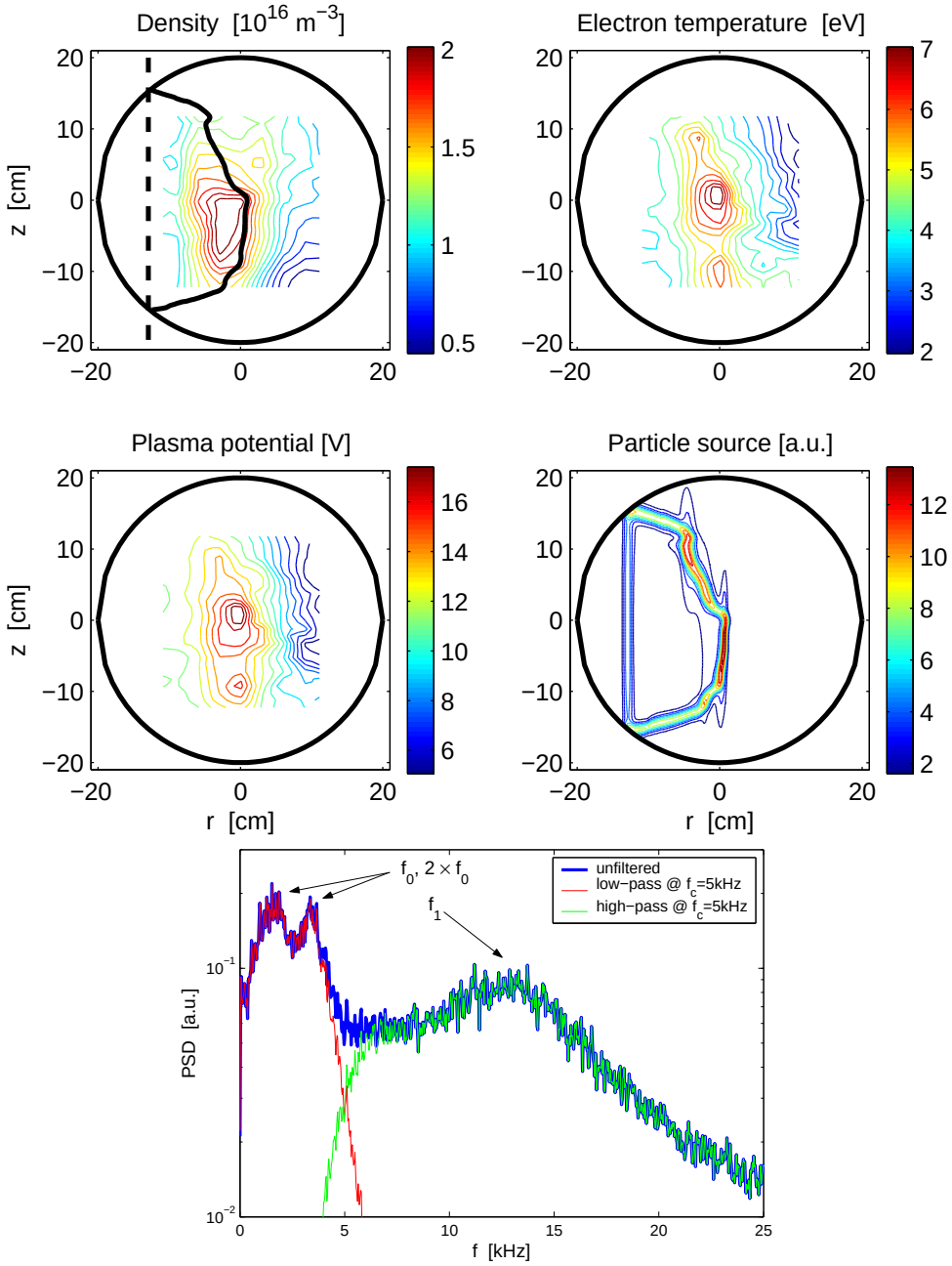

Figure 11.1: Time-averaged profiles of density, electron temperature, plasma potential and particle source for $B_z = 1.2$mT. The bottom figure shows a power spectrum from the reference probe, used in the following for the CAS-boxcar analysis.

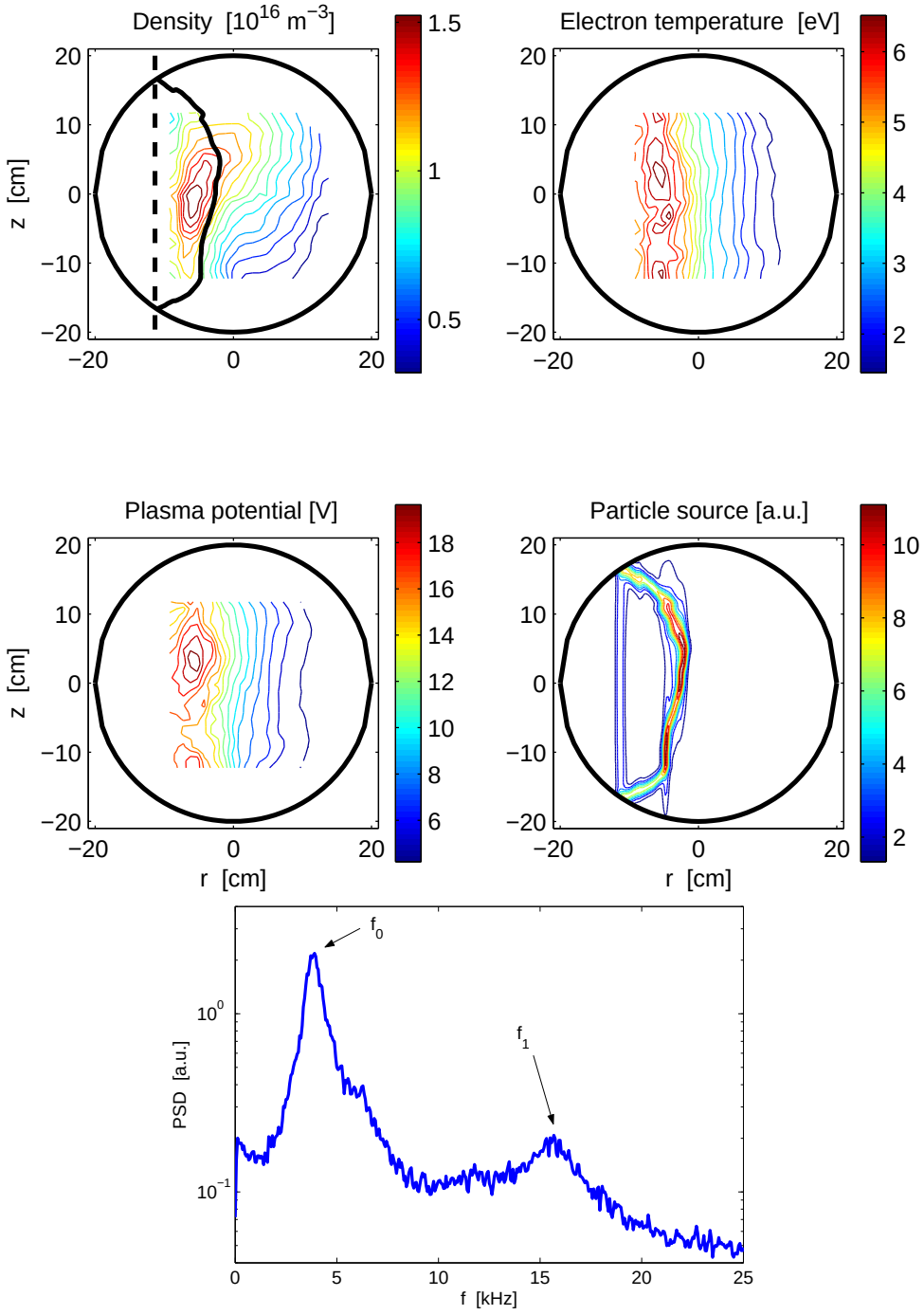

Figure 11.2: Same as in Fig. 11.1 for $B_z = 2.3\text{mT}$.

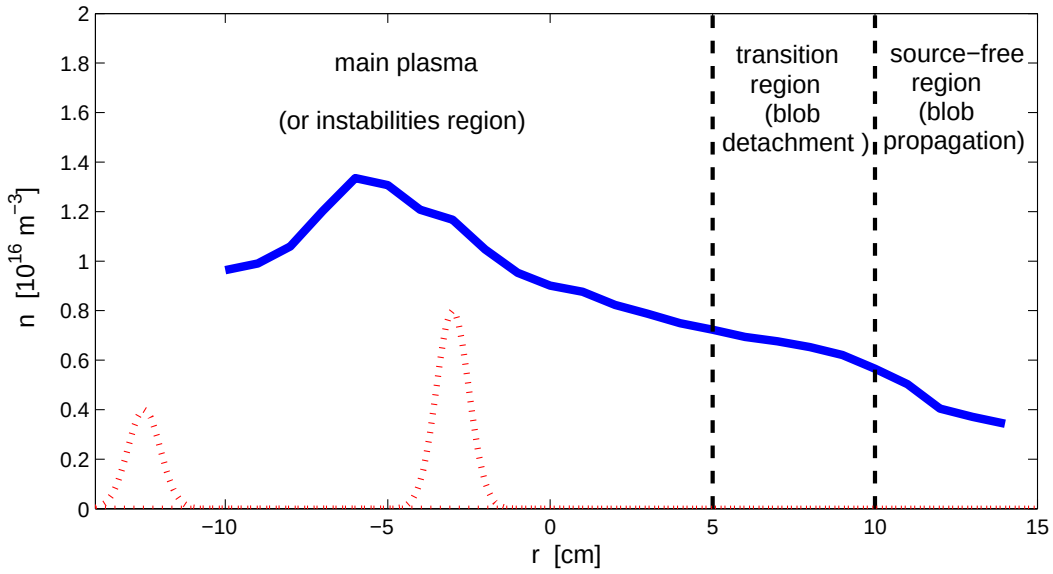

Figure 11.3: Illustration of the three regions in which TORPEX plasmas can be divided. The thick line shows the radial density profile measured at the midplane for $B_z = 2.3$mT. The dotted lines indicate the position of the EC (on the left) and UH (on the right) resonances.

11.1.2 Definition of the *main plasma*, *source-free* and *transition* regions

In general, electrostatic instabilities are observed on TORPEX in regions with strong pressure and plasma potential gradients, extending from the EC resonance out to few centimeters to the low-field side with respect to the UH resonance. They correspond to what can be called the 'main plasma' region (Fig. 11.3). We identify as 'source-free' the region at the low-field side with respect to the UH resonance, separated from the main plasma by a 'transition' region.
Different phenomena are at play in the the main plasma and source-free regions, as results from their characterisation in terms of spatio-temporal and statistical features, discussed below. The case with $B_z = 2.3$mT is used as a reference for the remaining part of this Section.

Spatio-temporal characterisation

The spatio-temporal behaviour of density fluctuations, recovered by means of the combined CAS-boxcar method (Sec. 8.5), is illustrated in Fig. 11.4. The reference probe is located in the source-free region, at $r = 16$cm and $z = 0$. The spatio-temporal evolution of the coherent mode at 4kHz is reconstructed for $r \leq 5$cm. A

different behaviour is observed for $r > 5$cm. Referring to the last frames in Fig. 11.4, the mode is stretched to the low-field side, where an isolated high-density structure, commonly referred to as *blob*, clearly visible in the last frame, forms. The details on the formation of these blobs and their possible impact on transport are discussed in Sec. 11.2.

Statistical characterisation

The skewness and kurtosis[1], S and K, of the density probability distribution function (PDF) are commonly used to characterise the nature of fluctuations [38][56]. In particular, $|S| \gg 0$ is indicative of PDFs with long tails, hence of the occurence of intermittent, large amplitude events, which appears to be a *universal* feature of the edge plasma in a large variety of devices [1]. For the same scenario presented in Fig. 11.4, we calculated S and K from the density time-traces in the poloidal cross-section (Fig. 11.5). We find $K \neq 3$ for the main plasma and the source-free regions, indicating non-gaussian PDFs. The skewness changes from $S \approx -1$ on the high-field side to $S \geq 1$ in the source-free region.
These results can be directly related to the spatio-temporal behaviour of density fluctuations. Across $r = -2.5$cm, where the maximum amplitude of the coherent mode is measured, $S \to 0$ and a double-humped PDF, with $K \sim 2$, is found [56]. The transition from $S < 0$ to $S > 0$, moving toward positive radial positions, suggests the presence of a transport mechanism which pushes particles into the source-free region. For $r > 5$cm a positive skewness and high kurtosis are measured, revealing the presence of high-amplitude, intermittent bursts in the source-free region (Fig. 11.6).

The TORPEX *SOL-like* configuration

The results illustrated above, especially those from the statistical characterisation of density fluctuations, remind closely those obtained from the scrape-off layer (SOL) plasma of tokamaks [12]. For this reason, I will refer in the following to the experimental scenario with $B_z = 2.3$mT as the *SOL-like* configuration, where the main plasma and the source-free regions can be well distinguished in practice. Note that the similarity is restricted to general features, such as the shape and the normalised gradient scale-lengths of the plasma profiles, and to a particular phenomenon, namely the ejection of blobs from the main plasma. Other aspects, specific of the tokamak configuration, can not be addressed in TORPEX. These include, for example, the change in the magnetic field topology, which is possibly relevant for a complete characterisation of turbulence-related transport in fusion-oriented devices [88].

[1] S and K are defined as the third and fourth moments of the probability distribution function.

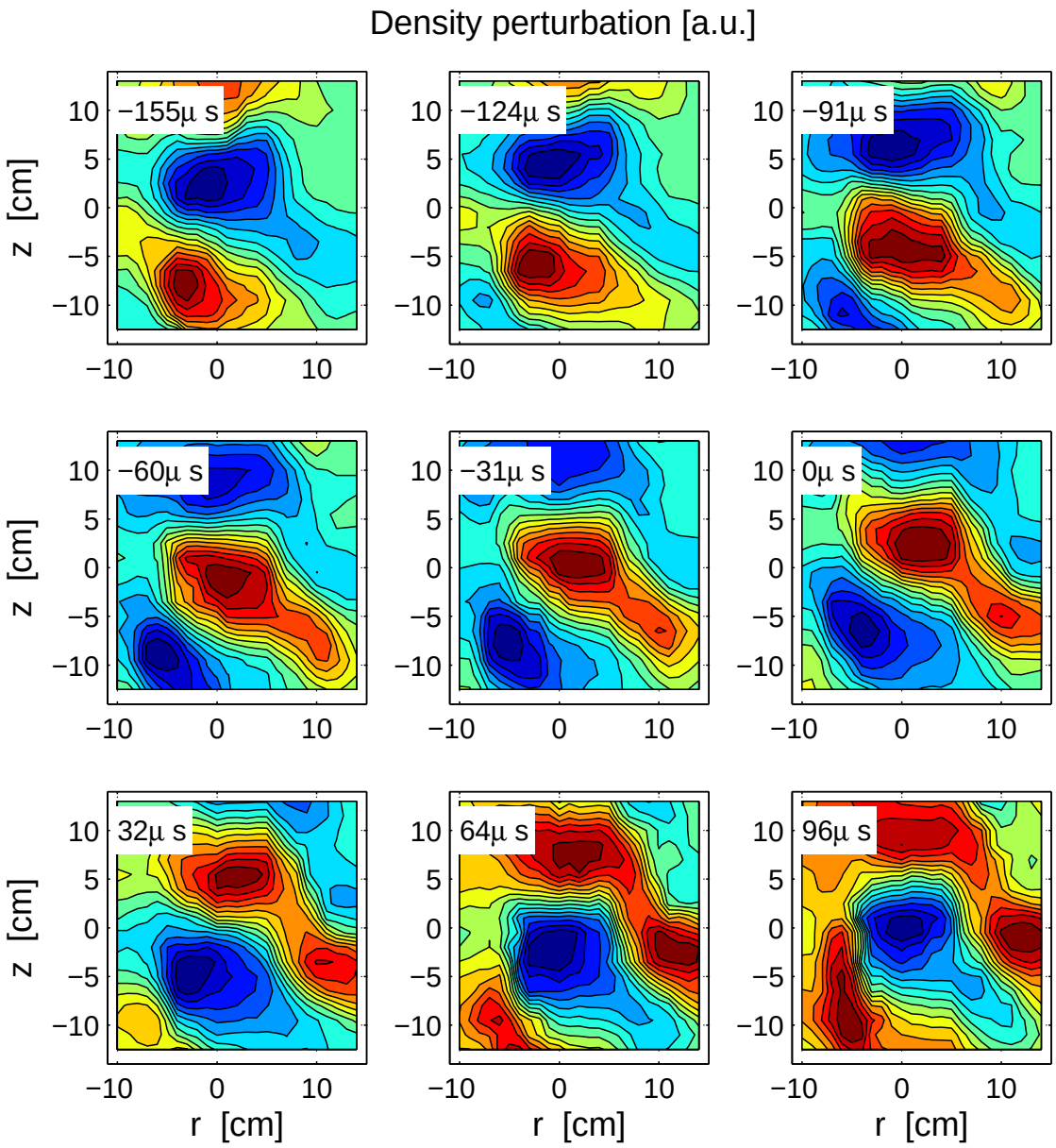

Figure 11.4: Two-dimensional reconstruction of the density evolution by means of the combined CAS-boxcar technique. The spatial resolution of the measurements is 1cm radially and 1.8cm vertically. A coherent mode is clearly visible during the whole sequence. Note the blob which forms from the mode at $t = -91\mu$s and detaches for $t \geq 32\mu$s. A similar behaviour is observed in the plasma potential and electron temperature, see Fig. 11.7.

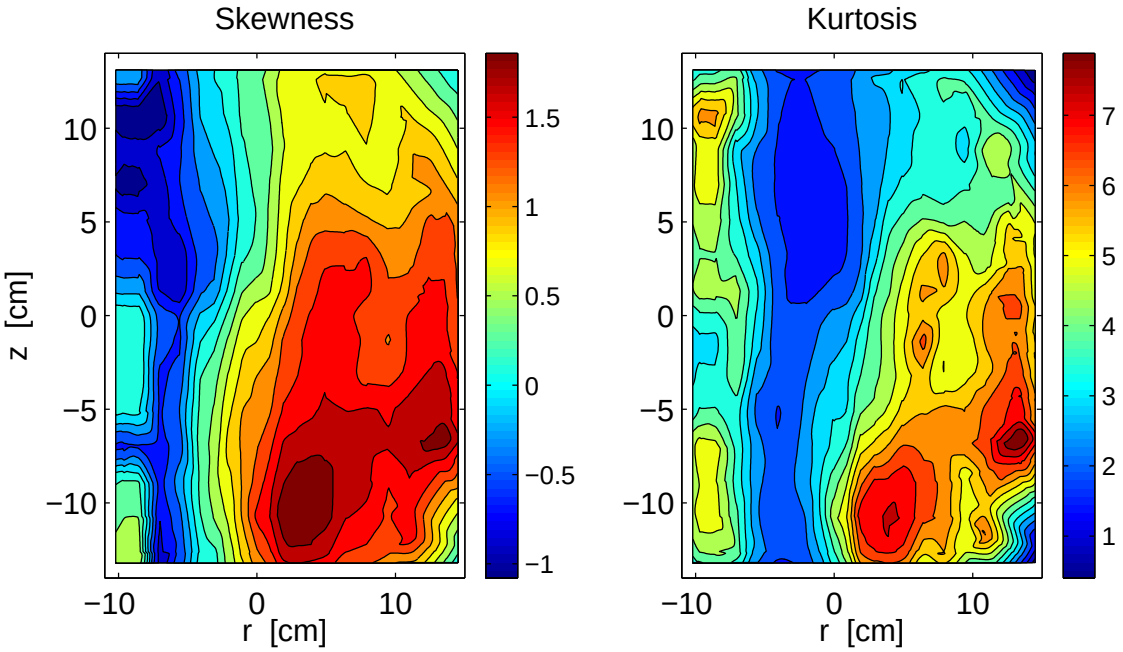

Figure 11.5: Skewness and kurtosis profiles for $B_z = 2.3$mT.

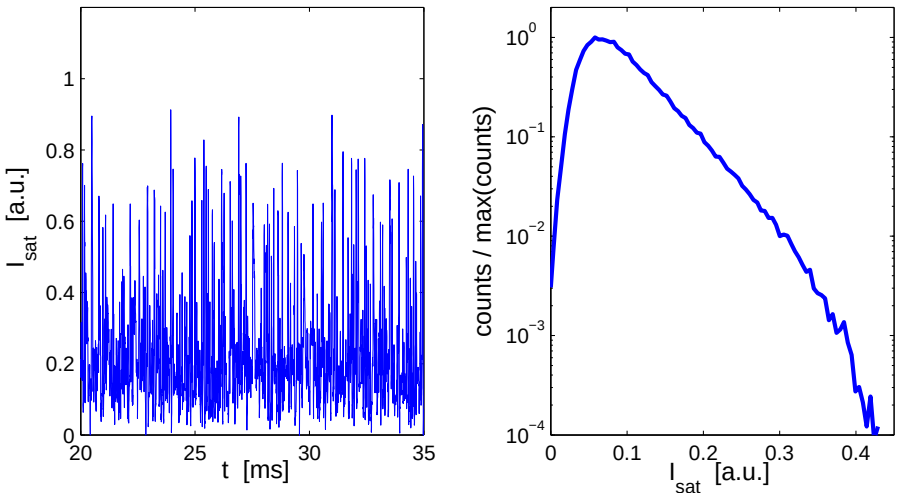

Figure 11.6: Raw ion saturation signal measured at the midplane at $r = 16$cm (*left*). The trace reveals the presence of intermittent spikes, leading to a positively skewed probability distribution function (*right*).

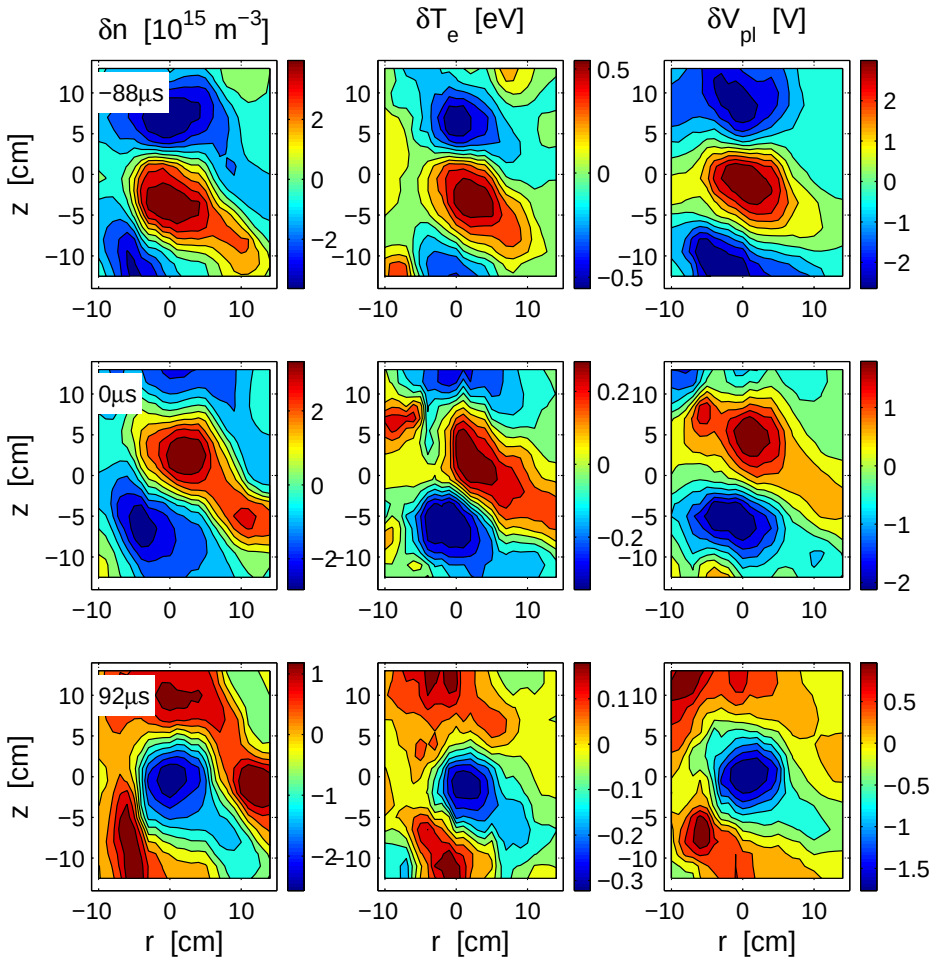

Figure 11.7: Temporal evolution of density, electron temperature and plasma potential related to a trigger event detected at $r = 16$cm for $B_z = 2.3$mT.

11.2 Intermittent *blob* formation

The details of the formation of high-density, isolated structures in the source-free region of TORPEX plasmas are discussed in this Section. To complete the information contained in Fig. 11.4 about the density evolution associated with intermittent events, Fig. 11.7 illustrates the simultaneous temporal behaviour of the perturbed profiles of n, T_e and V_{pl}. We observe that the plasma potential leads the density perturbation, especially for regions $r \geq -5$cm. The details of the perturbed density and plasma potential, n_1 and $V_{pl,1}$, together with the $E \times B$ velocity pattern associated with $V_{pl,1}$, are shown in Fig. 11.8 for the time at which the trigger event occurs, t_{trig}. It is observed that the mode expands radially, and a channel with strong $E \times B$ velocity convects density from the main plasma into the source-free

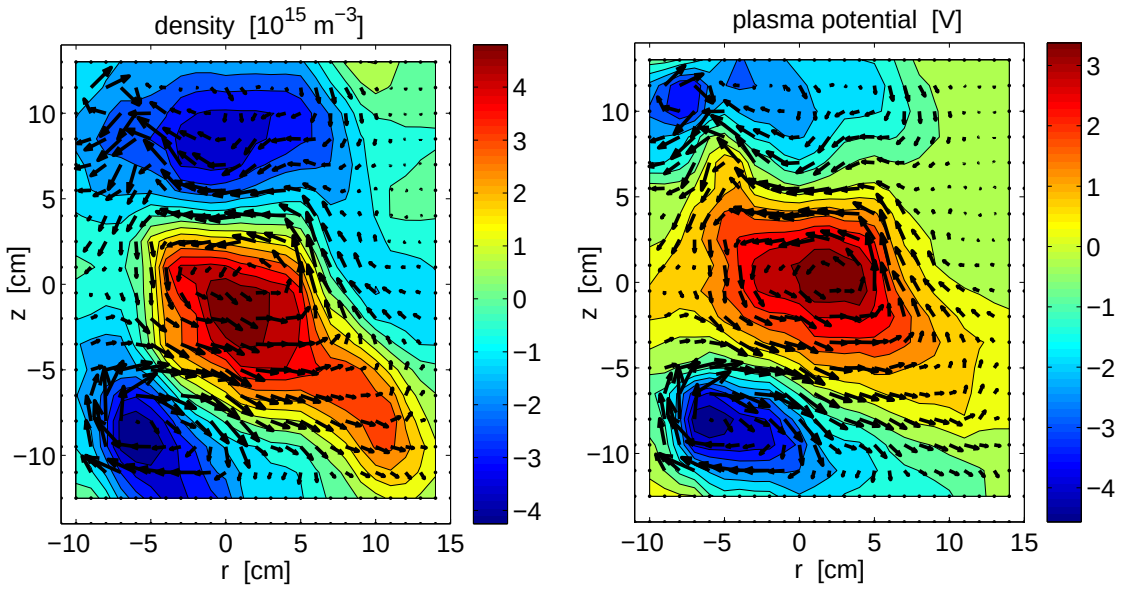

Figure 11.8: Fluctuating density and plasma potential profiles reconstructed for $t = t_{trig}$, when a trigger event is detected at $r = 16$cm, $z = 0$. The arrows represent the $E \times B$ velocity pattern calculated from the instantaneous perturbed plasma potential profile.

region. A clearly defined region, in which the instantaneous density exceeds by almost an order of magnitude the local time-averaged density, forms on the low-field side, where a sheared flow layer is measured (Fig. 11.9). The shear of the $E \times B$ velocity makes this region detach from the mode, forming a bounded structure that can be identified as a blob. The blob exists as a separate entity, characterised by its own dynamics, independent of the mode. The same phenomenon, i.e. the formation of blobs from weakly developed drift-wave turbulence, has been recently observed in a linear magnetised helicon device [115]. It was also observed on TORPEX for Helium plasmas and a similar experimental scenario, with a high B_z value [69], although the analysis was limited to density signals.
Note that for $t = t_{trig}$ the reconstructed structure is located at $z \approx -10$cm (Fig. 11.8), while the reference probe is at $z = 0$. This vertical displacement, roughly equal to $\pi R_0 B_z / B_\varphi$, is due to the toroidal separation of $\approx 180°$ between the reference probe and SLP, used for the boxcar-averaging reconstruction. It indicates that the structures are elongated along $\underline{B}$, as confirmed by measurements done in the toroidal direction by rotating SLP around its axis [104], and similarly to observations in the scrape-off layer of tokamak devices [118].
At present, the cause of the growth and radial expansion of the mode is still under investigation. A dependence upon the instantaneous value of the density (or pressure) gradients in the region in which the instability originates, regulating the

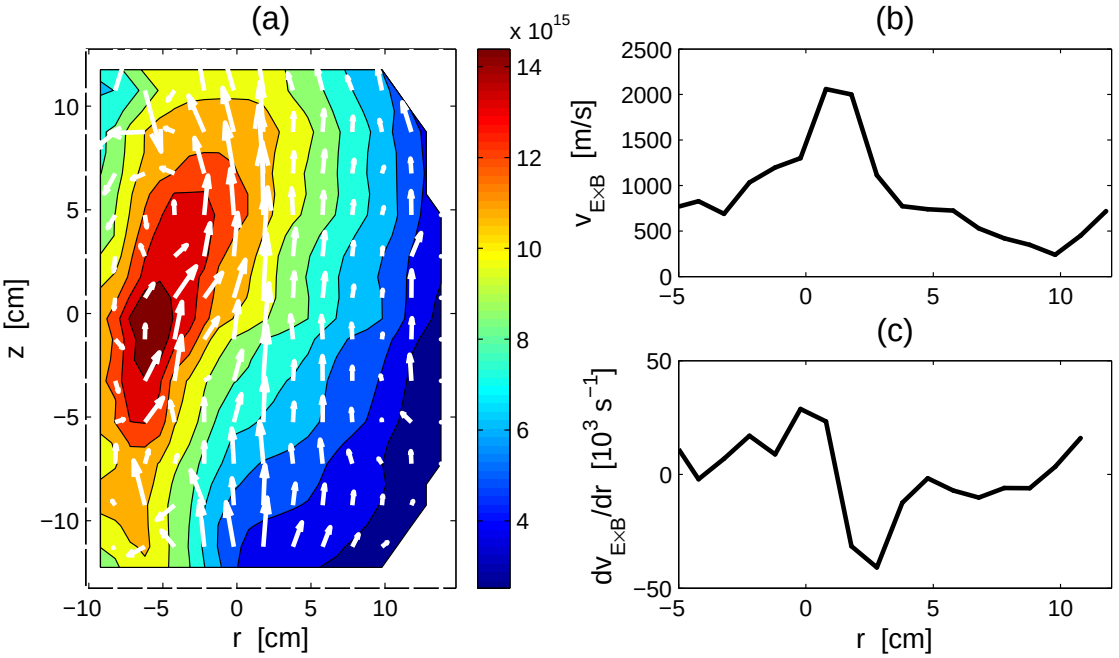

Figure 11.9: *(a)* Density profile for $B_z = 2.3$mT. The arrows represent the time-averaged $E \times B$ velocity pattern. The drift velocity is maximum at $r \approx 1$cm *(b)*, and strongly sheared for $r \approx 2$cm *(c)*.

dynamics of the mode amplitude, has been suggested [31].
In summary, an experimental scenario is identified on TORPEX, for which blobs, originating from a plasma instability, propagate in a source-free region. These structures are detected in the ion saturation current signals of electrostatic probes as intermittent spikes, or bursts (Fig. 11.6). Similar features are commonly observed in the SOL of tokamaks [38][6][14][118][33], stellarators [94], reversed field pinches [99] and linear devices [1][15]. The blobs appear as poloidally localised filaments, elongated in the direction of the magnetic field [119] and propagating radially across the magnetic field. The interest for this type of phenomena resides in the particle and energy carried by the blobs, which may lead to localised power loads for plasma facing components, and in general degrades the confinement properties of the device. In the following Section, I discuss the nature of the flux related to macroscopic plasma structures, with respect to the fluctuation-induced flux (Chap. 10).

11.3 Flux *ordering* and interpretation of the experimental results

In this Section, I identify three terms which contribute to the total particle and heat fluxes along and across the magnetic field, corresponding to different physical mechanisms. I discuss below the possibility of 'ordering' the different contributions to the flux, with the goal of separating terms, that are measured separately, and are associated with specific physical mechanisms. This ordering, which is not based on a rigorous mathematical derivation, provides a general guideline for the discussion in the next Section. In particular, the different quantities are divided into a time-averaged part plus a time-varying part. The latter is assumed to be dominated by linear terms, and the expansion can be truncated at the first order.

11.3.1 Flux ordering

The flux related to macroscopic structures has different origin and properties compared to the fluctuation-induced flux. Starting from the general definition of the particle flux

$$\underline{\Gamma} = \langle\, n\, \underline{v} \,\rangle_t \tag{11.1}$$

the different contributions to $\underline{\Gamma}$ are:

- *Time-averaged total flux:*

$$\underline{\Gamma}_0 = n_0\, \underline{v}_0 \tag{11.2}$$

  By definition, this is the *zero-th* order flux.

- *Fluctuation-induced flux:*
  For electrostatic fluctuations,

$$\underline{\Gamma}_f = \langle\, n_1\, \underline{v}_{E_1\times B} \,\rangle_t \tag{11.3}$$

  Here $\langle \ldots \rangle_t$ denotes a time average over at least one period of the instability. The term $\underline{v}_{E_1\times B}$ is the $E \times B$ velocity calculated from the perturbed electric field, $\underline{E}_1 = -\nabla V_{pl,1}$. Similarly, the fluctuation-induced heat flux is

$$\underline{Q} = \frac{3}{2}\, n_0\, \langle\, T_1\, \underline{v}_{E_1\times B} \,\rangle_t + \frac{3}{2}\, T_0\, \langle\, n_1\, \underline{v}_{E_1\times B} \,\rangle_t \tag{11.4}$$

  where the two terms in the right-hand side represent the *conductive* and *convective* contributions [46].
  Both $\underline{\Gamma}_f$ and $\underline{Q}$ are, formally, *second* order fluxes.

- *Structure-related flux:*

$$\underline{\Gamma}_{str} = \langle n_{str}\, \underline{v}_{str} \rangle_{tr} \tag{11.5}$$

where n_{str} and $\underline{v}_{str}$ are the average density and velocity of structures whose trajectory passes through a specific location, and the brackets $\langle ... \rangle_{tr}$ indicate the average over the ensemble of trajectories (Sec. 8.6).
The order of $\underline{\Gamma}_{str}$ is between that of $\underline{\Gamma}_0$ and that of $\underline{\Gamma}_f$. Based on the fact that n_{str} corresponds to a deviation from the time-averaged value, while no background substraction or other conditions are imposed on $\underline{v}_{str}$, one can refer to $\underline{\Gamma}_{str}$ as a *first* order flux.

11.3.2 Interpretation of the experimentally measured fluxes

Starting from the observations made in the previous Section for the three regions (main plasma, transition region and source-free region), the interpretation of the experimental results in terms of fluxes is discussed below for the two methods that have been introduced before.

Combined CAS-boxcar method

The fluxes are calculated from Eqs. 11.3 and 11.4, with n_1 and $V_{pl,1}$ reconstructed by the CAS-boxcar method. If the perturbations to an equilibrium state are oscillatory, i.e. can be regarded as the superposition of independent Fourier components, they lead to the fluctuation-induced flux. This happens in the main plasma region (Fig. 11.10). In the transition and source-free regions, perturbations are due, at least in part, to isolated macroscopic events, which propagate with a macroscopic velocity. In this case, the measured $\underline{\Gamma}_f$ represents only a fraction of the total flux related to the perturbations.

Structure analysis

Depending on the threshold value used to define a structure, σ_{tot}, different contributions to the total flux can be accounted for by the structure analysis. Referring to the sketch of Fig. 11.11, we identify three possibilities:

1. A single coherent mode, advected by a background velocity $v_{0,z}$, is present[2] (Fig. 11.11a). The density signals measured at different positions, with a skewness $S = 0$, are symmetric with respect to the mean value (Fig. 11.11d),

[2]Here and in the following point we assume that the phase velocity of the mode in the plasma frame is negligible compared to $v_{0,z}$.

and the contributions $\pm n_{str}\, v_{0,z}$ in Eq. 11.5 cancel out. In the limit[3] $\sigma_{tot} \rightarrow 0$, we have that the two different quantities coincide and $\underline{\Gamma}_{str} \rightarrow \underline{\Gamma}_f$. This situation represents the ideal limit in the main plasma region.

2. A superposition of modes, advected by a background velocity $v_{0,z}$, is present (Fig. 11.11b). The density signals measured at different positions have $S \neq 0$, i.e. they are asymmetric with respect to the mean value (Fig. 11.11e). By raising σ_{tot} above the maximum values for signals with $S < 0$, only negative structures are detected. Specular considerations hold for σ_{tot} below the minimum of signals with $S > 0$, when only positive structures are detected. The measured structure-averaged flux is representative of the behaviour of structures with a well defined polarity, advected by $v_{0,z}$. In the limit $\sigma_{tot} \rightarrow 0$ we have, again, that $\underline{\Gamma}_{str} \rightarrow \underline{\Gamma}_f$. This situation represents the real case for the main plasma region, where a number of unstable modes are generally observed.

3. Only isolated blobs, moving with a velocity $\underline{v}_{str}$, are present (Fig. 11.11c). The density signals, with $S \gg 0$, show intermittent spikes (Fig. 11.11e). The measured flux, $\underline{\Gamma}_{str}$, represents the total flux carried by the structures, independently of the value of σ_{tot}. This situation is present in the source-free region, where no unstable modes are observed, and $\underline{\Gamma}_f$ loses its meaning.

[3]The term $\sigma^2_{tot} = 1/MN \sum_{i=1}^{M} \sum_{j=1}^{N} \delta n^2_{ij}$ represents the *total standard deviation*, see pag. 204.

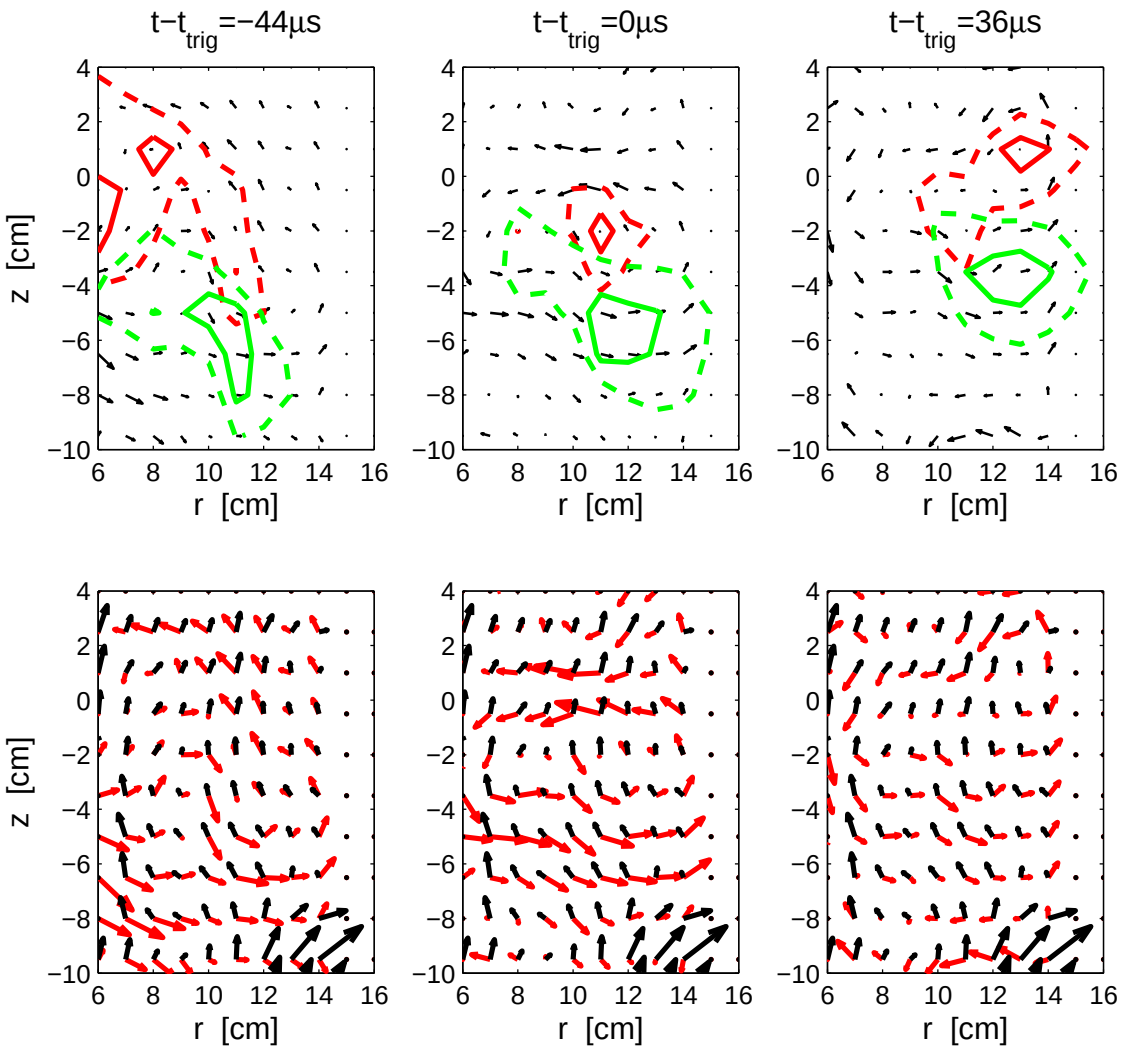

Figure 11.10: *Top:* Density (green) and plasma potential (red) perturbations during and after the detachment of an isolated plasma structure. The solid and dashed lines indicate the iso-contours at 90% and 70% of the local maximum of n and V_{pl}. The arrows represent the instantaneous $E_1 \times B$ velocity. Note the finite phase between n and V_{pl} cells, responsible for the measured $\underline{\Gamma}_f$. *Bottom:* Comparison of the instantaneous patterns of $E_0 \times B$ (black) and $E_1 \times B$ (red) velocities, showing that $|\underline{v}_{E_0 \times B}| \sim |\underline{v}_{E_1 \times B}|$.

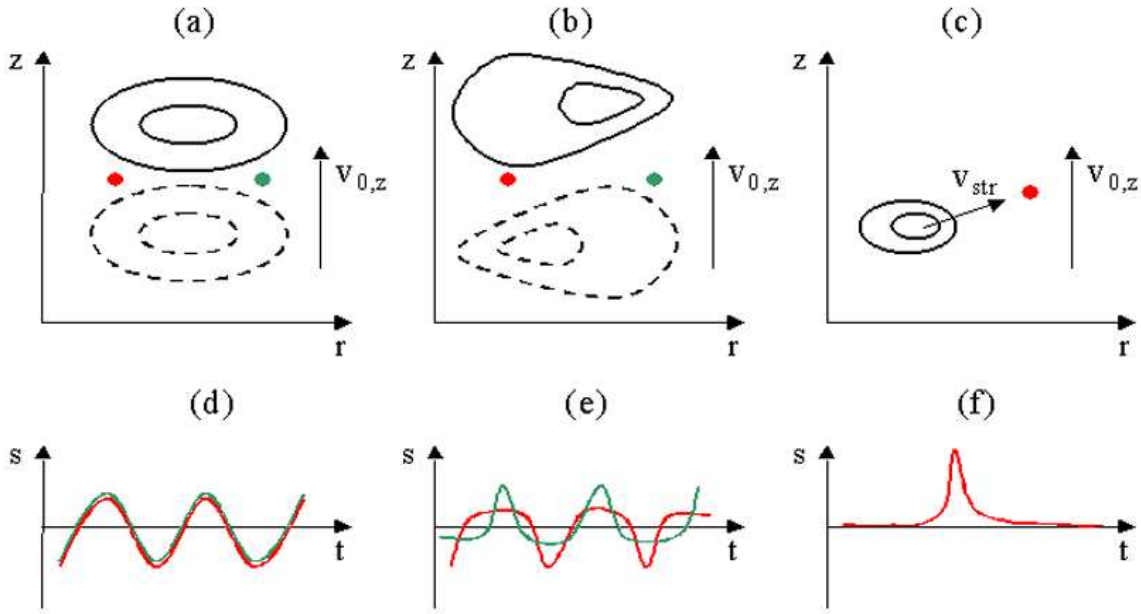

Figure 11.11: Interpretation of the measured structure-related flux for regions where a single mode *(a)*, a superposition of modes *(b)* and an isolated blob *(c)* are present. The scenarios *(b)* and *(c)* correspond to the main plasma and the source-free regions. The density signals (coloured dots in *(a)*,*(b)* and *(c)*) that would be recorded by probes are shown in *(d)*, *(e)* and *(f)*.

11.4 Measurements of the fluctuation-induced flux via the CAS-boxcar method

In this Section, the transport associated with electrostatic fluctuations is investigated by means of the combined CAS-boxcar technique described in Sec. 8.5. The results presented herein refer to the two experimental scenarios discussed in Sec. 11.1.

Case $B_z = 1.2\mathbf{mT}$

The reference probe used for the CAS analysis is at $r = 14$cm on the midplane, measuring the ion saturation current. A simple threshold value is chosen to define a trigger event, namely $n_{th} = 1.5\sigma$ (Eq. 8.30). The reference signal is low-pass filtered at 5kHz to select events related with the low-frequency modes only, and possibly simplify the analysis and the interpretation of the results. The SLP probe is moved shot by shot to span an extended region in the poloidal cross section, with a spatial resolution of 1cm radially and 1.8cm vertically. The voltage applied to SLP is swept at 1kHz from -20V to 5V to collect the $I-V$ probe characteristics, from which the two-dimensional time evolution of the plasma parameters is calculated.
Macroscopic *cells*, representing positive and negative perturbations of the time-averaged profiles, are visible in all the three parameters. On average, the cells propagate upward with a velocity ~ 1km/s, consistent with the time-averaged $E\times B$ flow velocity. The cells are interpreted as the manifestation in the real space of the coherent modes at 2kHz and 4kHz [45]. The modes are excited in the bottom half of the cross section, where the pressure and magnetic field gradients are co-linear, then propagate upward [80], consistently with the results discussed in Sec. 7.2. Plasma potential perturbations lead density perturbations over most of the measurement region, with a finite time delay between the two.
The time delay between potential, density and electron temperature fluctuations, corresponding to a non-zero phase angle in the Fourier representation (Eq. 8.23), may lead to net particle and energy fluxes [45]. A complete reconstruction over most of the cross-section of the two-dimensional fluctuation-induced particle flux, calculated with Eq. 11.3, is presented in Fig. 11.12. The magnitudes of the radial and vertical components of the flux are comparable. The resulting pattern shows an inversion in the radial direction in the region of maximum density gradient. The vertical component, Γ_z, changes sign at $r \approx 10$cm, where a strong shear of the time-averaged $E \times B$ drift is measured. In general, higher fluxes are measured in the bottom regions of the cross-section, where the modes are destabilised and reach their maximum amplitude. As discussed later, the reduction of Γ_f in the upper half is associated with a turbulent spreading of the modes in regions with strong electric field and sheared $E \times B$ flows (see [81] and references therein), leading to a reduction of the mode amplitude and a decorrelation between density and potential

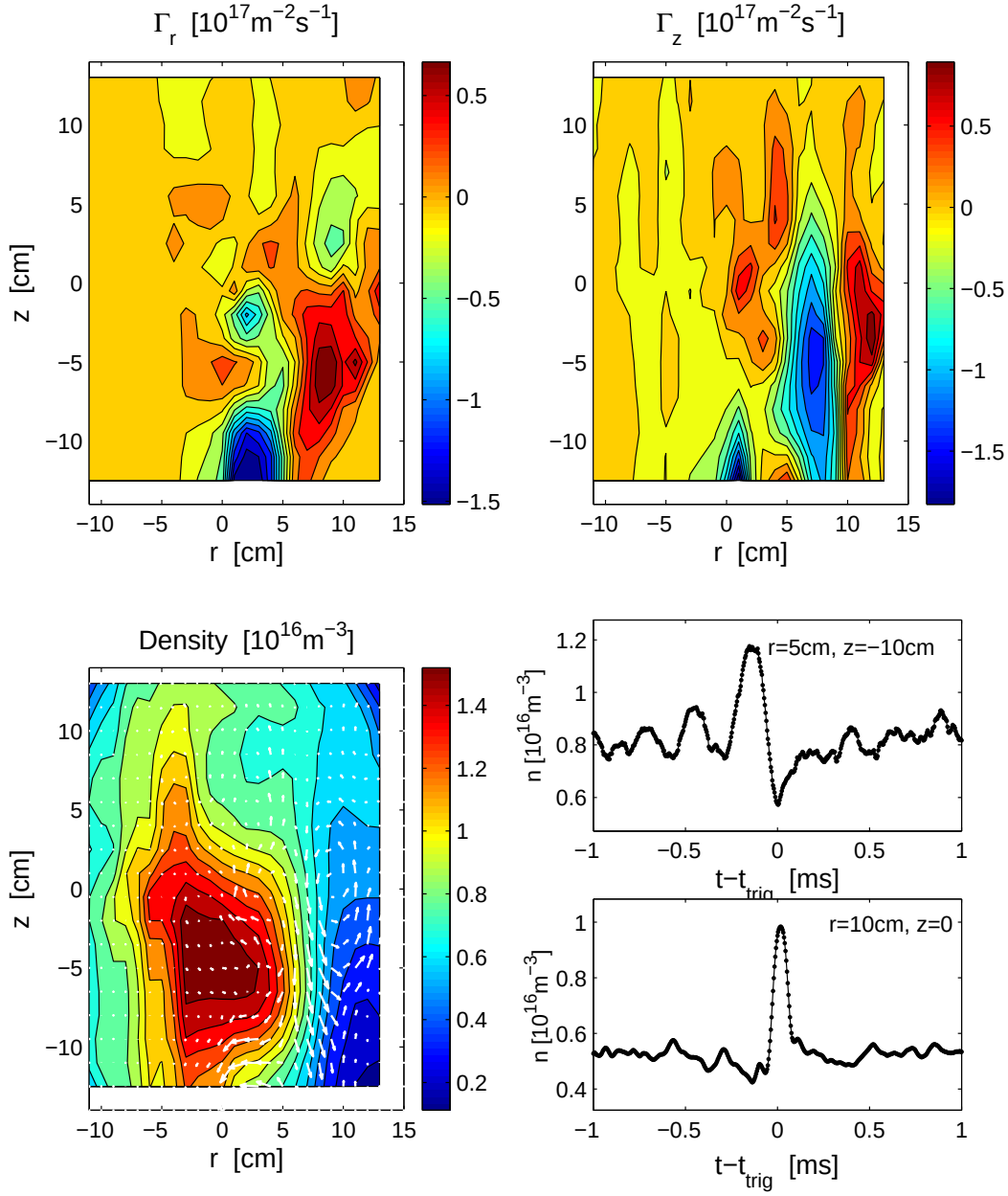

Figure 11.12: Fluctuation-induced particle flux, measured by means of the combined CAS-boxcar techniques, for $B_z = 1.2$mT. The flux pattern is shown on top of the density profile. Two CAS-boxcar reconstructed density traces are also presented for two positions.

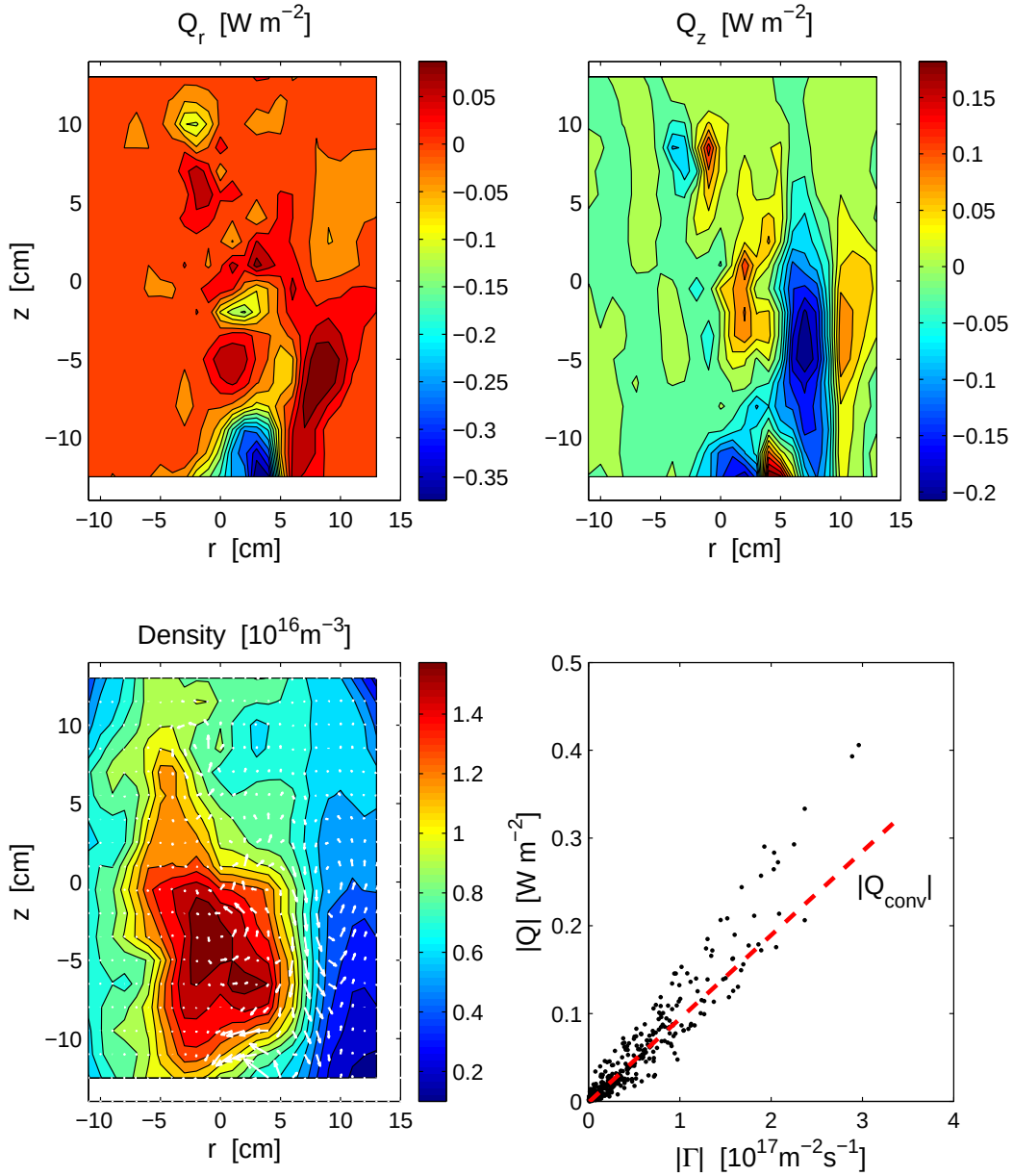

Figure 11.13: Fluctuation-induced heat flux for the same scenario as in Fig. 11.12. The thick, dashed line indicates the average convective heat flux, crf. Eq. 11.4.

fluctuations.
Compared to the fluctuation-induced flux obtained through Fourier decomposition (Chap. 10), the radial component, Γ_r, is ≈ 20 times smaller. The qualitative behaviour at the midplane, for which a direct comparison is possible, is similar, with a flux directed prevalently outward. The discrepancy in the quantitative values can be partially ascribed to the CAS method, which implies an average over multiple realisations and a smoothing effect on the reconstructed $n(t)$ and $V_{pl}(t)$ [5]. Moreover, the finite auto-correlation time of the measured signals, of $\approx 500\mu$s, leads to a gradual decorrelation in time with respect to the trigger event. Assuming that only signals centred in a time window of $\pm 250\mu$s around the trigger event are well reconstructed, a factor ≈ 4 in the flux is recovered, but the discrepancy with the results from the Fourier analysis remains.
The results for the heat flux (Eq. 11.4), presented in Fig. 11.13, indicate that $\underline{Q}$ is dominated by the convective term, i.e. $\underline{Q} \approx 3/2\, T_0\, \underline{\Gamma}_f$. This is due do the fact that $T_1/T_0 \ll n_1/n_0$, with electron temperature fluctuations in phase with potential fluctuations. Therefore, heat is transported by net particle fluxes rather than induced by electron temperature fluctuations themselves.
From this analysis in the real space it is not possible to separate the contributions of the different modes to the flux. Note that, for this specific case, the three modes have frequencies (2kHz, 4kHz and 12kHz) which are roughly multiples of each other. If there exists a coherent phase relation among the modes, as evidenced by recent measurements for TORPEX plasmas [81], their features are reconstructed in the average traces, despite the low-pass filter applied to the reference signal. The scenario discussed in the next Section is more suitable for the interpretation of the results in terms of single spectral components.

Case $B_z = 2.3\mathbf{mT}$

In this case, the reference probe is at $r = 16$cm on the midplane, in the 'source-free' region, which extends from $r \approx 10$cm to the walls. The threshold defining a trigger event is 4σ for the unfiltered reference signal.
Figure 11.14 illustrates the results for the particle flux, which is directed outward, from the region of maximum density to the 'source-free' region on the low-field side, consistently with the analysis in Fourier space (Fig. 10.5). The radial flux is here underestimated by a factor ≈ 5. The reversal of the vertical flux, already observed for the case with $B_z = 1.2$mT, occurs at $r = 0$ in the region of strong electric field and shear of the $E \times B$ drift velocity.
A negligible radial flux is measured in the source-free region. The density decreases, indicating that other mechanisms are responsible for the particle loss. From a qualitative comparison with the results obtained in Chap. 9, e.g. in Fig. 9.10, we conclude that in this region the total flux is dominated by the flow along the magnetic field.

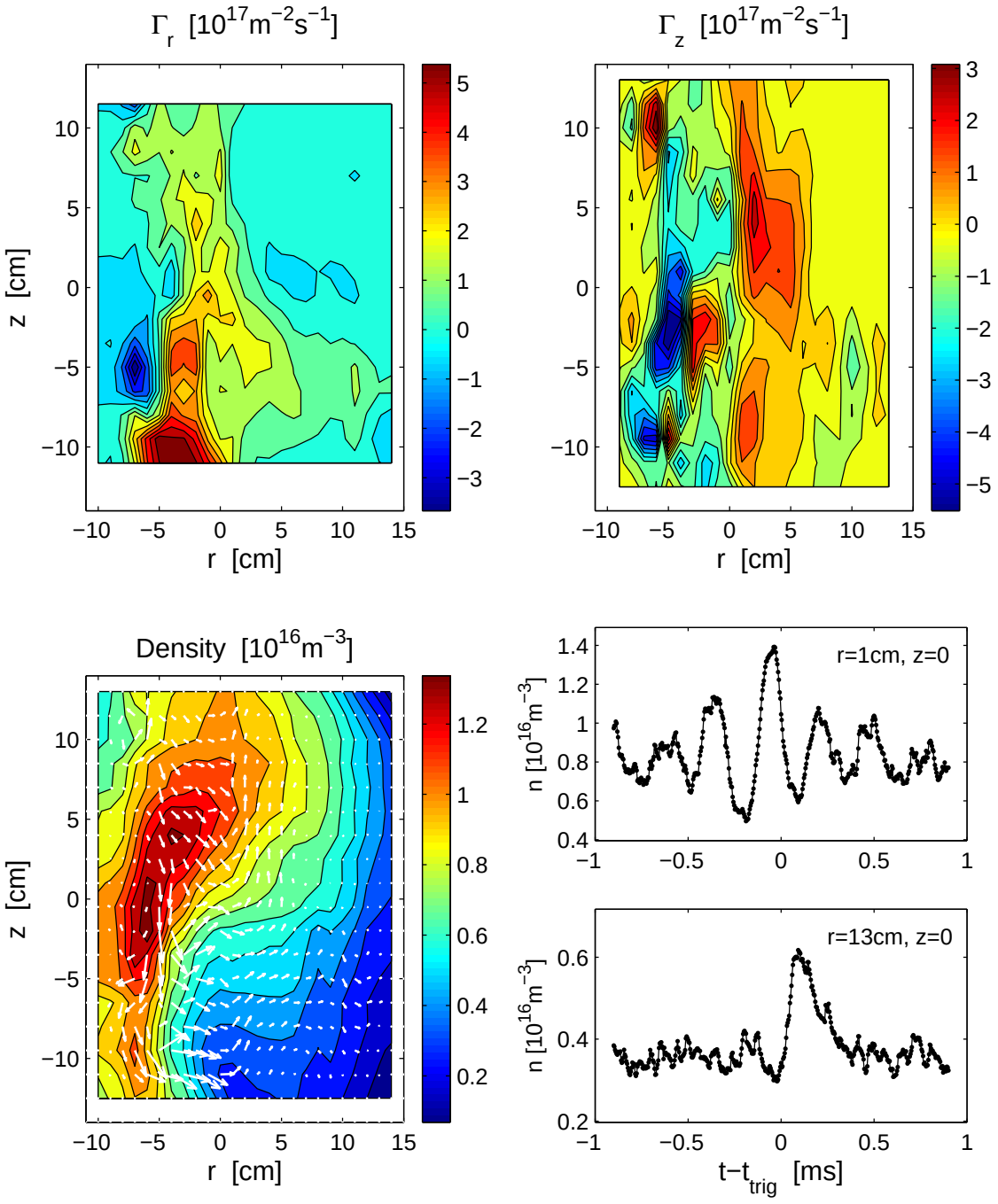

Figure 11.14: Same as in Fig. 11.12 for $B_z = 2.3$mT. The coherent mode at 4kHz is well reconstructed by the CAS-boxcar method.

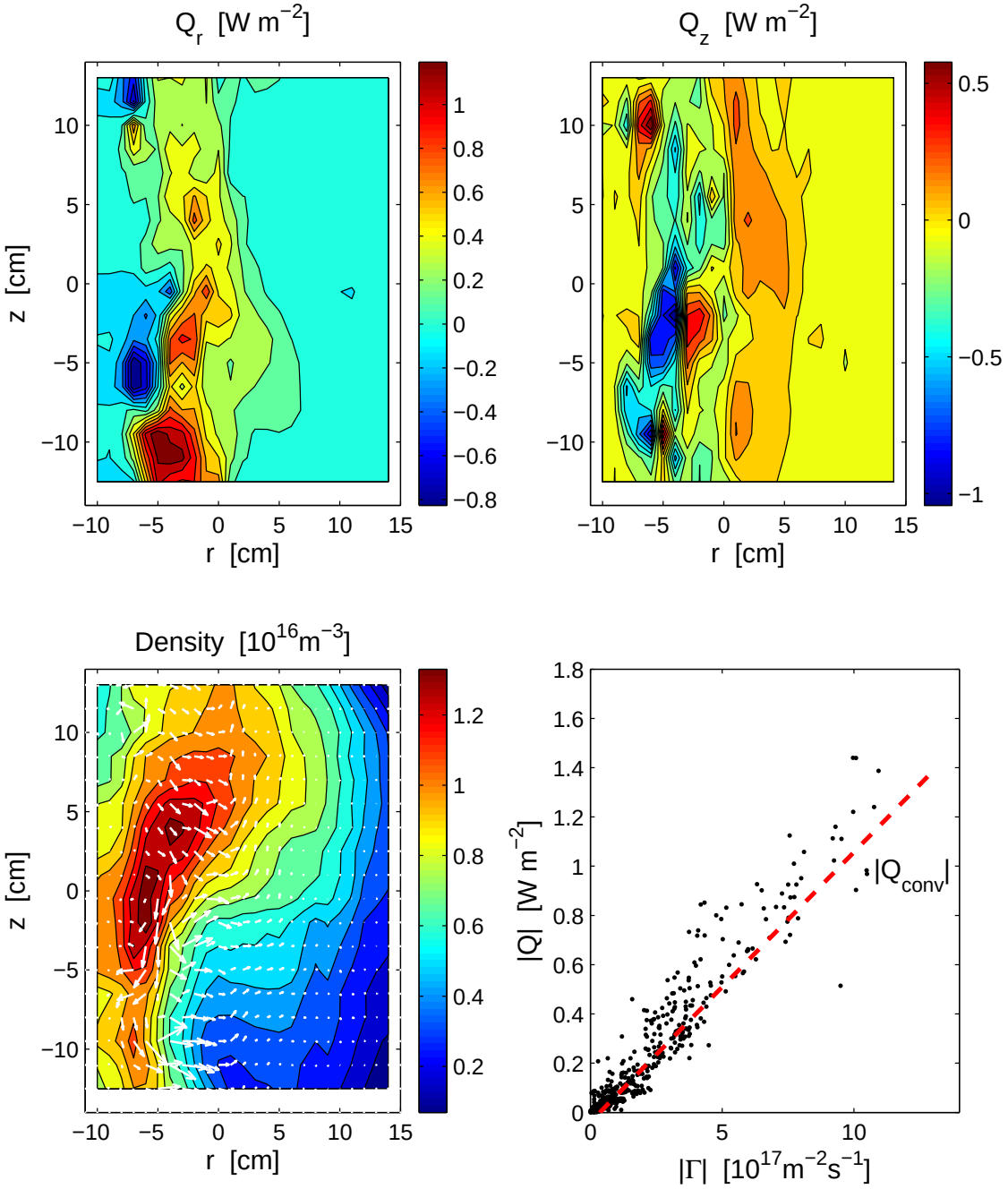

Figure 11.15: Results of the fluctuation-induced heat flux for the same scenario as in Fig. 11.14.

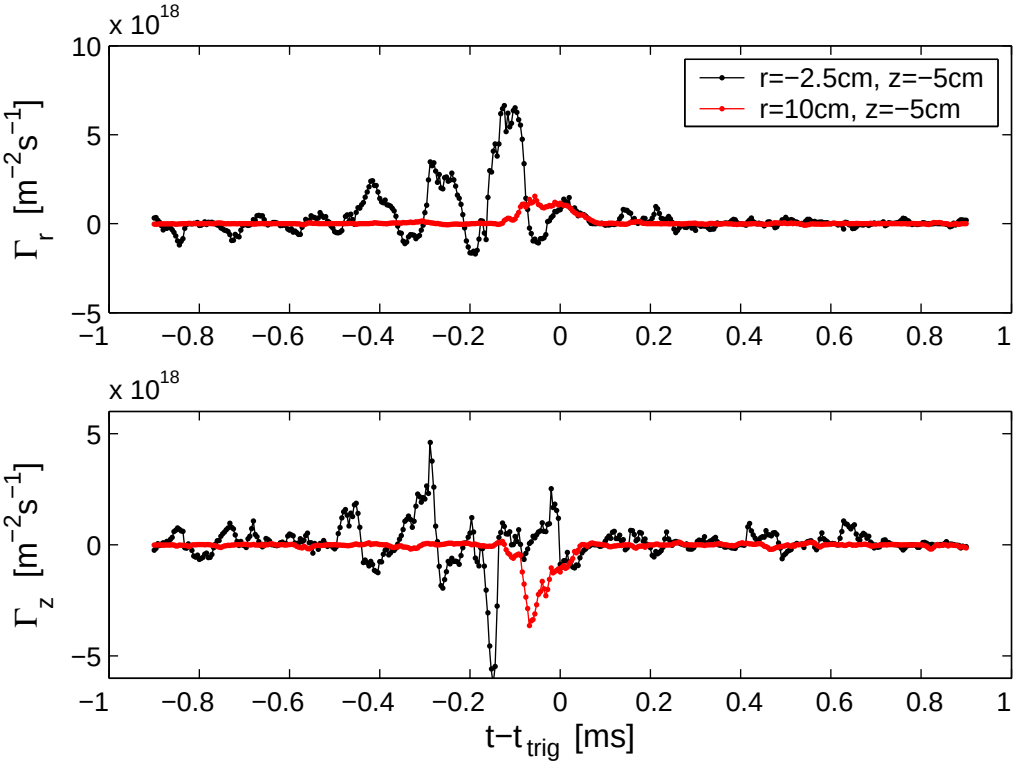

Figure 11.16: Instantaneous radial and vertical fluctuation-induced fluxes measured in the main plasma and in the source-free regions.

The possible contribution to the radial flux from blobs propagating in this region (Sec. 11.2), is investigated in the next Section. The results for the fluctuation-induced heat flux, summarised in Fig. 11.15, confirm that $\underline{Q}$ is mostly due to particle fluxes, similarly to the case with lower B_z discussed previously.

Results very similar to those illustrated in Figs. 11.14 and 11.15 are obtained with a reference probe located in the region $-5 < r < 5$cm at the midplane, where the coherent mode dominates the plasma dynamics. This highlights the tight correlation between the intermittent structure and the coherent mode, from which the structure originates.

Differences are observed for $r \geq 5$cm, where the intermittent events have amplitudes higher than the background profiles. A positive radial particle flux is measured here, as shown in Fig. 11.16. The vanishing flux observed in the upper half of the cross-section for $r > 5$cm is consistent with the advection of blobs, detected by the reference probe at $z = 0$, by the time-averaged $E \times B$. Blobs originating at $z \geq 0$ can not be detected. After the detection of the event, the flux in the 'main plasma' region decreases on time-scales shorter than the decay of the mode amplitude. A possible cause for the flux reduction is a change in the phase between density and

plasma potential. The ejection from the main plasma of structures with average densities comparable with the background plasma would then provoke a relaxation of the instability. The amplitude decays, preceded by a synchronisation between n and V_{pl}.

An apparent contradiction appears when the vertical flux in Fig. 11.16 is compared with the temporal sequence shown in Fig. 11.7. The measured Γ_z is negative, although in that region the density structure moves upward, and a positive vertical flux is expected. In fact, the 'second-order' flux $\underline{\Gamma}_f = \langle n_1 \underline{v}_{E_1 \times B} \rangle_t$ can not account for the 'first-order' flux related to the moving structure, $\underline{\Gamma}_{str}$, as discussed in Sec. 11.3. A description in terms of 'fluctuations' is simply not appropriate for the isolated phenomena at play in the source-free region. In particular, the spectral analysis described in Sec. 8.2 is misleading, and the same analysis performed in the time domain might provide incomplete information, leading to underestimating the flux. Other methods are more appropriate to measure $\underline{\Gamma}_{str}$, as discussed in the next Section.

11.5 Measurements of the structure-related flux via the 'structure analysis'

In the previous Section it has been observed that the fluctuation-induced particle transport can not account for the total effective flux in the presence of blobs, as the two quantities originate from different physical mechanisms. In this Section the statistical analysis of structures dynamics, described in [68][67] and summarised in Sec. 8.6, is applied to the two cases analysed in the previous Chapters. The analysis is based upon data from HEXTIP (Sec. 3.4), with a spatial resolution of 3.5cm. The threshold level to define a structure is set equal to β times the 'total standard deviation'

$$\sigma_{tot}^2 = 1/MN \sum_{i=1}^{M} \sum_{j=1}^{N} \delta n_{ij}^2 \tag{11.6}$$

where δn_{ij} is the matrix of the density signals [68], after the local background (i.e. time-averaged) values have been subtracted. We have chosen the values $\beta = 1$ and $\beta = 0.1$ for the cases $B_z = 1.2$mT and $B_z = 2.3$mT, respectively. Note that a small β is required to capture structures with low density, and to increase the statistics for the far low-field side regions, especially for the case with $B_z = 2.3$mT. Only structures lasting more than 40μs are included in the analysis.

Most structures are found where the amplitude of the coherent modes is maximum (Fig. 11.17). Their typical size is consistent with the measured wavelength of the modes in the poloidal cross-section. This allows one to conclude that where the instabilities are present, the statistical analysis essentially captures their features in the time-space domain (Sec. 11.3). For example, the structure trajectories correspond to the background $E \times B$ drift pattern, compatibly with the convection direction in the laboratory frame. Differences are observed at the far low-field side, where the structures propagate essentially in the radial direction, whereas the time-averaged $\underline{v}_{E\times B}$ is directed upward. It has been shown in the previous Sections that the density dynamics in this region is dominated by isolated intermittent events (blobs), rather than by coherent fluctuations. In practice, this is clearly visible for the case with $B_z = 2.3$mT, where the measurement region in which the blobs can propagate is much broader than for $B_z = 1.2$mT (Fig. 11.17).

The ensemble-averaged flux calculated trough the statistical analysis, $\underline{\Gamma}_{str}$, is

$$\underline{\Gamma}_{str} = \langle\, \overline{n}_{str}\, \underline{v}_{str} \,\rangle \tag{11.7}$$

where the brackets indicate the average over the ensemble of structures detected at each specific location, $\overline{n}_{str}$ is the average density of each structure and $\underline{v}_{str}$ its *total* velocity [68].

The particle flux evaluated via the structure analysis for the two experimental scenarios under investigation are illustrated in Fig. 11.18. For $B_z = 1.2$mT, the flux

reflects the pattern of the trajectories in regions where the instabilities are present. The structures, identified here as the unstable waves, flow upward and the corresponding vertical flux dominates with respect to the flux across the magnetic field. For $B_z = 2.3$mT, the trajectories and the flux pattern are clearly different, because of the lower threshold used to define a structure (Sec. 11.3).

For both experimental scenarios, in the outer region to the low-field side, the structures analysis indicates that the flux is radially outward, with a small vertical component for $r > 12$cm (Fig. 11.19). Note that for the high-B_z case there is a qualitative consistency with the results from the boxcar method, from which $\Gamma_f \sim 10^{17}\mathrm{m}^{-2}\mathrm{s}^{-1}$, although no instabilities are present, as discussed in Sec. 11.3. We find here $\Gamma_{str} \lesssim 10^{18}\mathrm{m}^{-2}\mathrm{s}^{-1}$, i.e. $\Gamma_{str} \gg \Gamma_f$, confirming that in the source-free region the radial transport is ascribed to the propagation of blobs, ejected from the main plasma. For $r > 10$cm, $\underline{\Gamma}_{str}$ is uniform along z, suggesting a uniform probability of blob ejection from the mode during its vertical motion.

The two-dimensional pattern of the structure-related flux provides information on the blob dynamics. Consistently with the observations made in tokamaks [119] and linear devices [15], the blob velocity is dominated by the instantaneous, *total* $\underline{v}_{E\times B}$, to which two terms contribute. The first term, $\underline{v}_{E_0\times B}$, comes from the background electric field, and is essentially vertical for the experiments described herein. The second term, $\underline{v}_{E_p\times B}$, is due to a ∇B-induced polarisation of the blob, producing a vertical electric field, hence an $E \times B$ velocity component in the major radius direction [55][35]. Referring to Fig. 11.19, we find $|\underline{v}_{E_0\times B}| \sim |\underline{v}_{E_p\times B}|$ for $r > 10$cm, where the blobs can be actually considered as entities separated from the coherent mode.

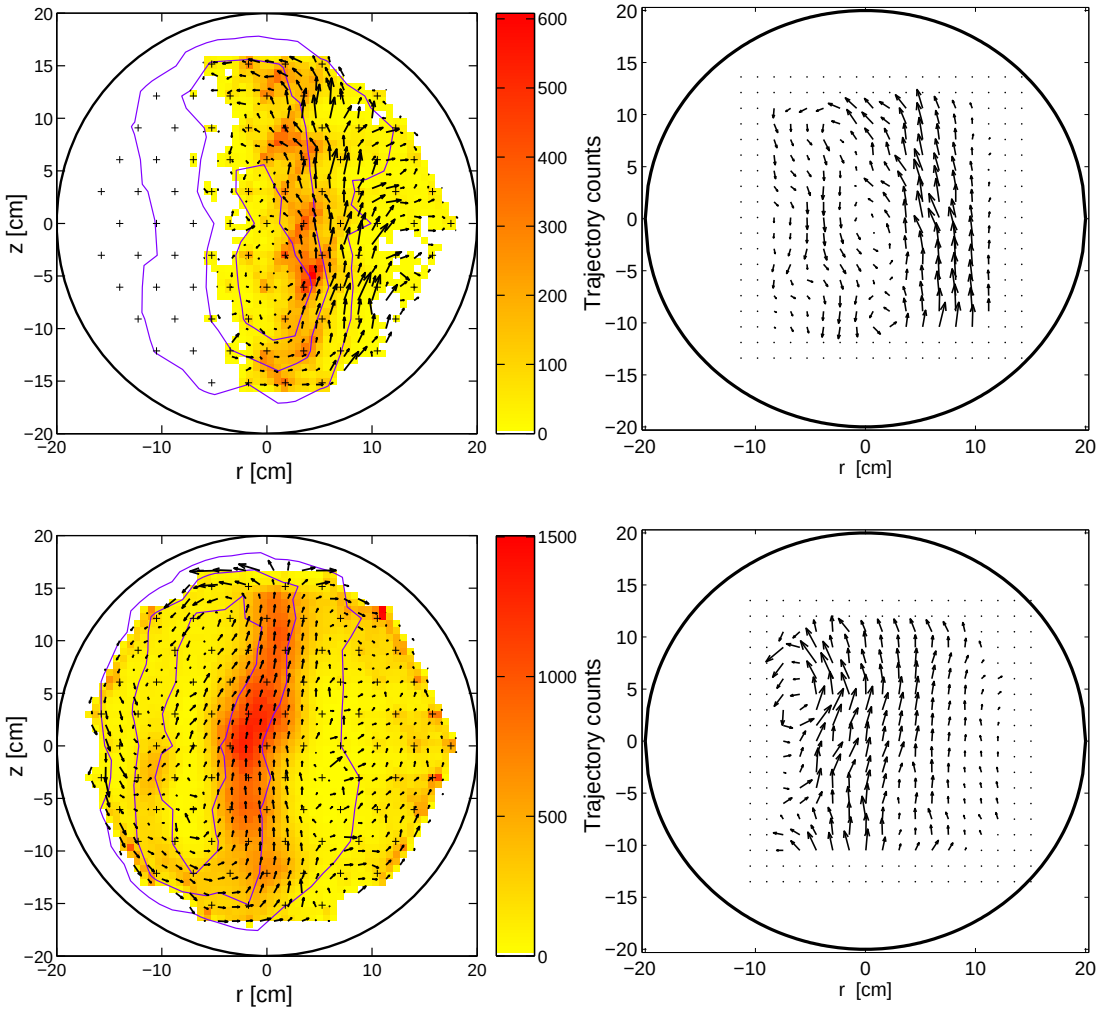

Figure 11.17: *Left column:* Statistical analysis of the trajectory counts for the case $B_z = 1.2\text{mT}$ (*top*) and $B_z = 2.3\text{mT}$ (*bottom*). The arrows represent the trajectory pattern for the detected structures. *Right column:* Time-averaged $E \times B$ velocity pattern for $B_z = 1.2\text{mT}$ (*top*) and $B_z = 2.3\text{mT}$ (*bottom*).

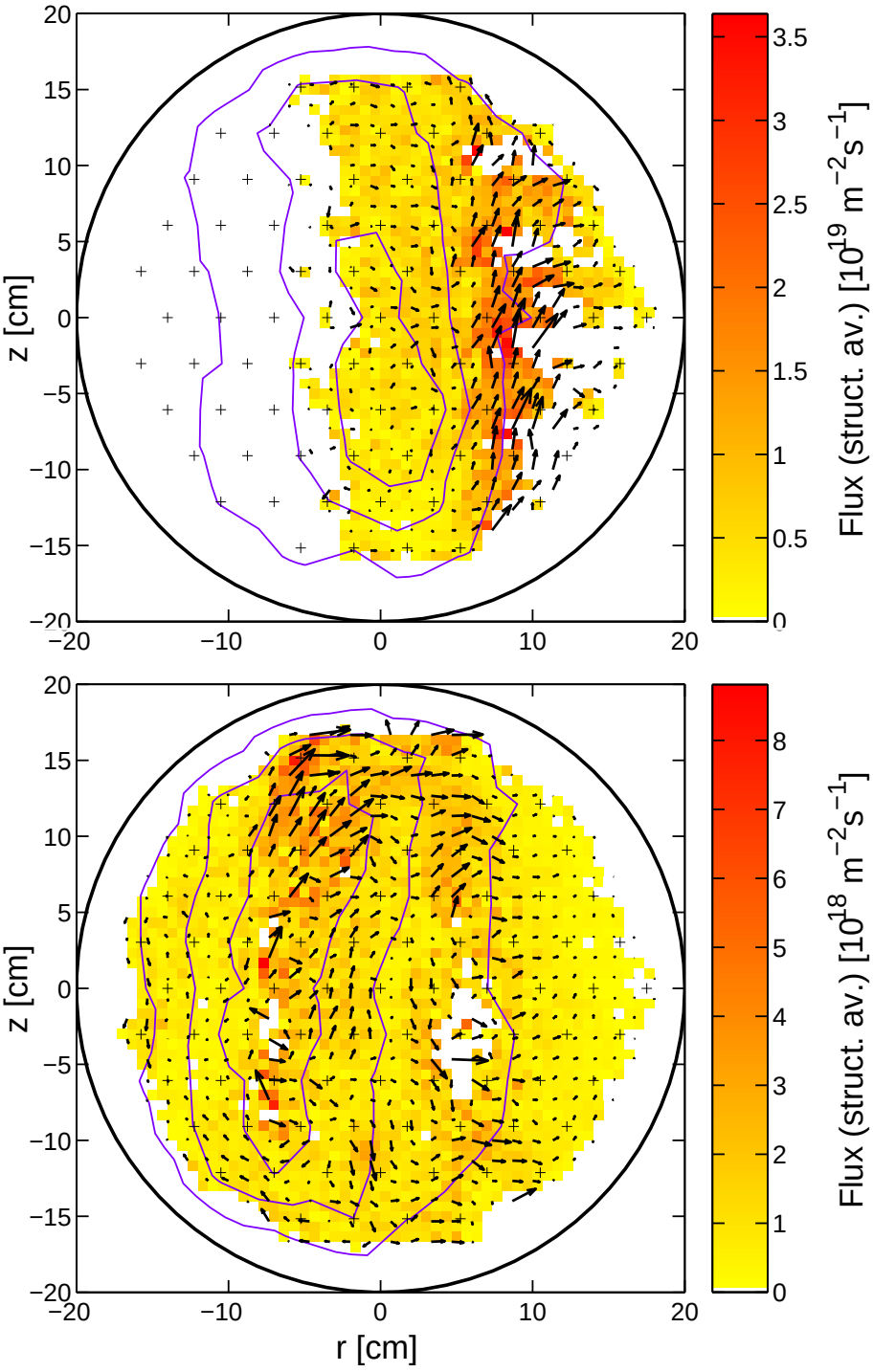

Figure 11.18: Results of the structure-related transport from the structures analysis for the case $B_z = 1.2\text{mT}$ (*top*) and $B_z = 2.3\text{mT}$ (*bottom*).

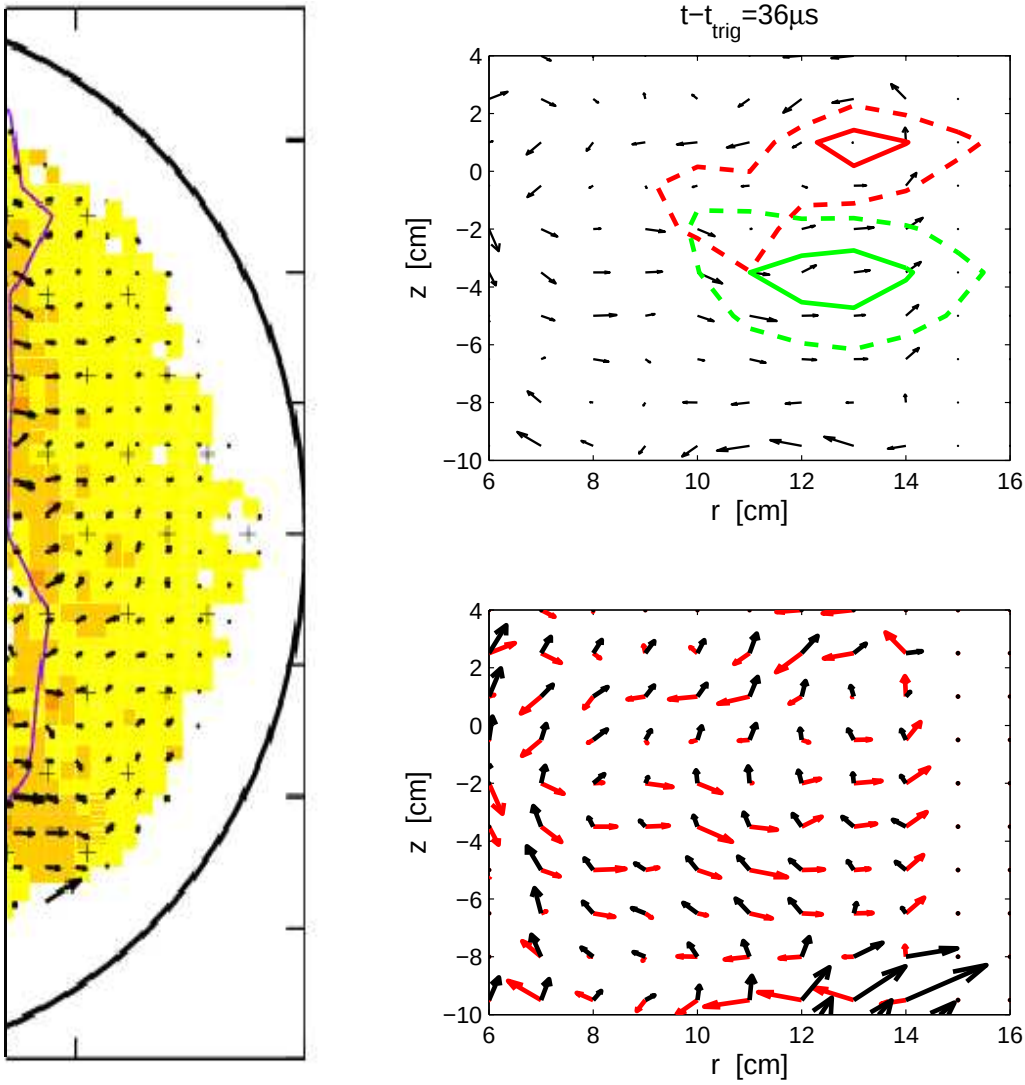

Figure 11.19: *Left:* Detail of Fig. 11.18 for $B_z = 2.3$mT for the region $r > 8$cm. *Top right:* CAS-boxcar reconstruction of the density (green) and plasma potential (red) perturbations associated with a single blob. The solid and dashed lines indicate the iso-contours at 90% and 70% of the local maximum of n and V_{pl}. The arrows represent the instantaneous $E_1 \times B$ velocity. *Bottom right:* Comparison of the instantaneous patterns of $E_0 \times B$ (black) and $E_1 \times B$ (red) velocities, showing that $|\underline{v}_{E_0 \times B}| \sim |\underline{v}_{E_p \times B}|$.

11.6 Summary and discussion

In this Chapter, I have presented results from two-dimensional measurements of the particle and heat fluxes, based on the combined CAS-boxcar method and the structures analysis. Two experimental scenarios were investigated in detail, corresponding to two different values of the vertical magnetic field. Three plasma regions are identified, namely a 'main plasma' region where unstable modes develop, a 'source-free' region where isolated plasma structures, or *blobs*, are intermittently observed, and a 'transition region' between the two, where coherent modes and intermittent events co-exist. The blobs are clearly observed to originate intermittently from the mode. I have identified a 'SOL-like' experimental scenario, in which a phenomenon usually observed in the tokamak SOL, namely the intermittent ejection of high-density plasma structures from the main plasma into the source-free region, has been been investigated.

I have discussed the different nature of the fluxes related to instabilities and to blobs, along with the implications for the interpretation of experimental results. The experimental results show that in the main plasma the fluctuation-induced particle flux is radially outward, independently of the specific character (drift waves or interchange modes) of the dominant unstable modes. The heat flux, with a negligible contribution from conduction, is almost purely convective. It is shown that in the source-free region the cross-B particle flux is mainly determined by the radial motion of blobs ejected from the main plasma, and propagating with the total, instantaneous $E \times B$ velocity. The implications of these results, which are at the core of the subject of this Thesis, are discussed in Part IV.

Part IV

Conclusions

12.1 Summary

This Thesis work addresses two major subjects of research in plasma physics, the plasma production mechanisms by injection of microwaves and the question of the different contributions to the cross-B transport of particles and heat, from fluctuations and related turbulent structures.
The first subject is discussed in detail in Part II, where the basic interaction mechanisms between the injected microwaves and the plasma are identified. In particular, the different role played by the electron-cyclotron and upper-hybrid plasma resonances in the absorption of the microwave power have been highlighted. The effects of the plasma-wave interaction are investigated at a deeper level by measuring the electron distribution function. Two goals have been achieved. First, a semi-empirical model for the plasma particle source term has been developed, to be used in numerical codes for simulating the plasma dynamics in realistic scenarios. Second, it has been possible to relate the properties of the time-averaged plasma profiles to the plasma production mechanisms. By doing so, we have identified a set of 'control parameters', such as the injected microwave power and the vertical magnetic field, to vary in a systematic way the plasma profiles and related quantities, e.g. the gradient scale-lengths, which are relevant for the study of plasma instabilities and associated transport.
The study of particle and heat transport is described in Part III. A number of experimental and analysis techniques have been deployed to identify and quantify different specific contributions to the total fluxes. In particular, a method based on the combination of conditional-average sampling and boxcar-averaging techniques has been developed. Such method allows one to reconstruct the two-dimensional temporal behaviour of density, electron temperature and plasma potential. The results show that, in addition to the time-averaged flows, two distinct mechanisms are responsible for the transport across the magnetic field, associated with low-frequency unstable drift waves and interchange modes and with intermittent, high-density plasma structures - or *blobs*. These findings might contribute significantly to the understanding of similar phenomena, which are thought to be at the origin of the so-called *anomalous* transport, commonly observed in fusion-oriented devices.

12.2 Discussion

As discussed in the Introduction, significant progress in the understanding of the anomalous transport of plasma particles and heat across the magnetic field can be achieved by addressing the following general issues:

1. What is the relative contribution to the cross-B flux from correlated density and potential fluctuations, associated with unstable modes, and from isolated intermittent events (blobs)?

2. Which modes are the most relevant for transport?

3. How do blobs originate, and which mechanisms determine their dynamics?

4. Is there a direct link between unstable modes and blobs?

In this Thesis work, I have provided answers to these questions in a simple magnetised plasma experimental scenario, which retains the ingredients that are relevant for anomalous transport in magnetic fusion devices, i.e. pressure gradients and curvature of the magnetic field lines. In such configuration it is possible to characterise over the whole poloidal cross-section the time-averaged plasma profiles, the unstable modes that develop on top of them, and the basic plasma production and loss mechanisms. The knowledge of these quantities represents a necessary background for transport studies for two main reasons. First, it enables the comparison between the experimental results and the outputs of numerical codes to reach a quantitative level. Second, it facilitates the interpretation of the experimental results, providing information on derived quantities such as $E \times B$ drifts, particle confinement time, space and time scales of fluctuations.
For example, the semi-empirical model for the time-dependent particle source term, developed in Chap. 5, could be included in a two-field fluid code for electrostatic turbulence simulations, such as a specific adaptation to TORPEX [67] of the ESEL code [34]. By doing so, a closer similarity between the real experiment and the simulation can achieved, and *ad hoc* boundary conditions with constant particle fluxes [95] or fixed gradients [34], can be avoided. This would permit one to benchmark extensively the code, which must be able to reproduce basic features, such as the time-averaged profiles. Since for fluid codes long runs are possible, extended time-series of density and potential from 'virtual probes' can be recorded. This permits direct comparisons between experimental and numerical results in terms of:

- Statistical properties, via the probability density function of the signals and its moments, e.g. skewness and kurtosis.

- Spectral features, such as frequency and wave-number spectra, decay index and non-linear interactions between different spectral regions.

- Development of turbulence and macroscopic structures from unstable modes.
- Fluctuation-induced and structure-related fluxes.

In the experiments reported herein, two distinct contributions to the cross-B flux have been identified and quantified, apart from the direct losses along B that are specific to the TORPEX layout (Chap. 9). These contributions are related to density and potential fluctuations, caused by unstable coherent drift and interchange modes, and to blobs, carrying density and heat across the magnetic field. Either mechanism responsible for the cross-B flux dominates in different plasma regions. This has been highlighted in a particular experimental scenario obtained with a high value of the vertical magnetic field, the so-called *SOL-like* configuration, reproducing some of the phenomena of a tokamak scrape-off layer (Sec. 11.1.2). In this case a main plasma region and a source-free region, connected by a transition region, can be clearly separated, for example on the basis of the different statistical properties of density fluctuations. A dominant contribution to the total cross-B flux from the fluctuation-induced and from the blob-related fluxes is characteristic of the main plasma and of the source-free region, respectively.
The fluctuation-induced flux is maximum in the main plasma, where drift and interchange modes are destabilised by the pressure gradients and by the curvature of the magnetic field (Sec. 7.2). Contrary to the predictions of linear theories, a non-vanishing flux is also measured for pure interchange modes. In fact, similar values of the phase between density and plasma potential fluctuations are measured for drift and interchange modes, which are in a saturated state with large amplitudes of density and potential fluctuations. For these conditions, the common approach of classifying the observed instabilities and of predicting their potential effect on transport on the basis of the measured phase between density and potential can be misleading. The generalisation of these results to other devices and other experimental configurations is a question for theory. Note that the role played by collisions, including those with neutrals, and by the finite connection length of the magnetic field lines should also be considered in the theoretical models used for the comparison.
It is observed that the fluctuation-induced flux decreases in regions of strong electric field, also characterised by a strong, sheared $E \times B$ flow. This determines a spreading of the unstable modes, via non-linear interactions in the frequency-wavenumber domain [81], which reduces the correlation and alters the phase between n and V_{pl}. The role of sheared flow layers in reducing the cross-B transport is already known from a number of experimental observations [73][49].
In general, the radial extension of the unstable modes is $\sim 5 - 10$cm, i.e. larger than the characteristic gradient scale-lengths of the time-averaged plasma profiles, which makes the interpretation of the measured fluxes in terms of diffusive processes misleading. This limit case makes TORPEX scenarios a stimulating testbed

for theoretical interpretations, which should be based on non-local, non-diffusive mechanisms. Transport models based upon a generalised probabilistic approach, developed in the past years [107], may be suitable for describing these complex scenarios.
In the source-free region, the cross-B transport is mostly due to blobs propagating radially outward. The average density associated with a blob is comparable with the value measured in the main plasma, indicating that blobs represent an efficient channel for particle losses. The mechanisms behind the blob propagation have been investigated (Sec. 11.5). The 'background' plasma flows seem to affect considerably the final direction of blob propagation. This may have an important impact in transport reduction. For example, a strong poloidal flow in a tokamak SOL would limit the radial blob propagation, hence the heat and particle fluxes to the walls.
In the transition region, unstable modes and blobs coexist. Their tight interlink has been clearly demonstrated in Sec. 11.2. Similar observations have already been made in a number of experiments [115][69], but the experimental information about the blob formation mechanism was incomplete. The results presented in this Thesis provide a direct evidence for these mechanisms, showing that blobs originate in TORPEX plasmas from the radial expansion of unstable modes, which are then sheared off by a strong $E \times B$ flow. The driving mechanism for the growth of the mode has not been unambiguously identified yet, although there are strong indications about the role of the instantaneous density (or pressure) gradients [31].

12.3 Open questions and outlook

The results on basic transport mechanisms discussed in this Thesis open the way to further experimental studies and stimulate more discussions between experiments and theory. The most relevant points are:

- What is the drive for the intermittent growth of a drift or interchange mode and its subsequent radial expansion into the source-free region, originating the blobs on TORPEX?

- Can this be considered a general feature of magnetically-confined plasmas, with different instabilities playing the role of 'blob precursor', represented on TORPEX by drift and interchange modes?

- Can one control the blob generation rate and size, for example by acting on the precurring instabilities and/or on the instantaneous $\underline{v}_{E\times B}$ shear rate? Experiments in this direction have already started on TORPEX, by using a movable antenna [23] and a convenient modulation of the injected microwave power to perturb actively the local plasma dynamics (see below).

- We have shown that the results for the cross-B transport can not be, in general, adequately described in a diffusive/convective framework. Transport models based on a wider class of transport mechanisms [107][93] would be more appropriate. The experimental flexibility of TORPEX may represent an ideal testbed to benchmark numerical codes and theories aimed at relaxing the standard diffusive-convective assumptions.

- The fluctuation-induced and blob-related fluxes originate from substantially different physical mechanisms (Sec. 11.3.2). Particle and heat transport act through different quantities, separated on the basis of the experimental evidence through a tentative 'ordering' (Sec. 11.3). Experimentally, the fluctuation-induced flux can be known from local (ideally, single-point) measurements of the fluctuating density and potential, while the structure-related flux is correctly measured only by knowing its macroscopic dynamics. Techniques providing simultaneous information on both quantities, for example by combining measurements from probes and 2-D imaging devices, are required to improve the experimental characterisation of anomalous transport phenomena.

In conclusion, this Thesis work represents a significative contribution to the understanding of the transport mechanisms at play in magnetised toroidal plasmas. A clear relationship between instabilities and turbulent phenomena (for example, blobs), and their effects in terms of cross-B transport of particles and heat, have been established and investigated in detail. Similar phenomena are at play, under

more complex experimental conditions, in fusion-oriented devices. This confirms the relevance of basic experiments for a better understanding of anomalous transport, to be pursued through a comprehensive comparison of results from theoretical, numerical and experimental plasma physics. For example, progress toward a direct comparison between TORPEX results and a 3D fluid code has been achieved with the ESELTPX project [67], mentioned in the previous Section.
The capabilities of devices like TORPEX in terms of two-dimensional reconstructions of the parameters characterising plasma profiles, instabilities and phenomena like the blob generation, have been extensively demonstrated in this Thesis work. Nonetheless, further improvements are possible by combining and refining different experimental techniques already in use on TORPEX.
The structure analysis (Sec. 8.6) could be extended to the non-perturbative measurements obtained with a recently purchased high-resolution fast camera (Sec. 3.4), shared between TCV and TORPEX. It would be possible, for example, to compare results from TORPEX plasmas in the SOL-like scenario with those from a real tokamak SOL.
The construction of new probes is already planned to extend the measurements of the fluctuation-induced flux, in both radial and vertical directions, over the entire cross-section. This would allow one to compare more extensively the results obtained by the Fourier analysis (Sec. 8.2) and the combined CAS-boxcar method (Sec. 8.5).
The established link between unstable modes, blobs and cross-B transport stimulates experiments aimed at an active control of instabilities and turbulent phenomena. A project has already started to excite, and act on, electrostatic instabilities via a movable antenna [23]. A non-intrusive method for affecting the transport could be based on the fact that the unstable modes extend radially across the upper-hybrid resonance (Sec. 11.1.2). It has been shown, e.g. in Figs. 8.11 and 9.8, that a high-amplitude, fast variation of the injected microwave power can perturb the local plasma parameters, in particular the plasma potential. By modulating the microwave power synchronously to the early phase of the blob formation, it could be possible to induce its premature detachment, thus mitigating the transport associated with the blobs.

Appendix A

TORPEX microwave generator system

TORPEX plasmas are produced by injection of microwaves in the EC range of frequency. The microwave source is then a crucial component, which, after its first commissioning in 2002, has been subject to a number of upgrades and modifications. In this Appendix, I describe the microwave generator system and the modifications implemented during the course of this Thesis.
The different subsystems are described in Sec. A.1, where the main parameters and capabilities of the system are summarised. The main upgrades of the original system are detailed in Sec. A.2

A.1 Hardware layout

The TORPEX microwave generator system can be divided into three main parts:

- Microwave source.
- Timing and control unit, including the measurements of operational parameters such as injected and reflected power, state of the device and faults.
- Transmission line, delivering the microwave power to the vacuum chamber.

Microwave source

The TORPEX microwave generator system is based on a commercial magnetron source, manufactured by Muegge Electronic GmbH (DE). A schematic of the system is shown in Fig. A.1. The power is stored in a capacitor bank connected to the 380V network through a rectifier bridge. The capacitor bank provides a voltage source at 14kV. The current drawn from the capacitors is controlled by the voltage applied to the grid G1 of a tetrode tube[1]. The grid G1 is driven by the 'Endstufe G1' board, which amplifies the low-voltage control signal supplied by the control unit. The tetrode acts as a current source controlled by the voltage applied to G1. A second grid, G2, is used to minimise the spurious capacitance between G1 and the cathode, and is polarised to a constant voltage. The microwaves are produced by a magnetron tube[2], conveniently coupled to the transmission line. The amount of delivered power depends on the current flowing through the tube. Referring to its technical documentation[3], the tetrode tube operating point is:
- Grid G2 voltage : 780V

[1]The tetrode is a EIMAC 8281/4CX15000A tube.
[2]A CTL - 20kW CW S-band magnetron, model CWM-20S.
[3]The notation used in the Microwave System technical manual is adopted throughout this Appendix.

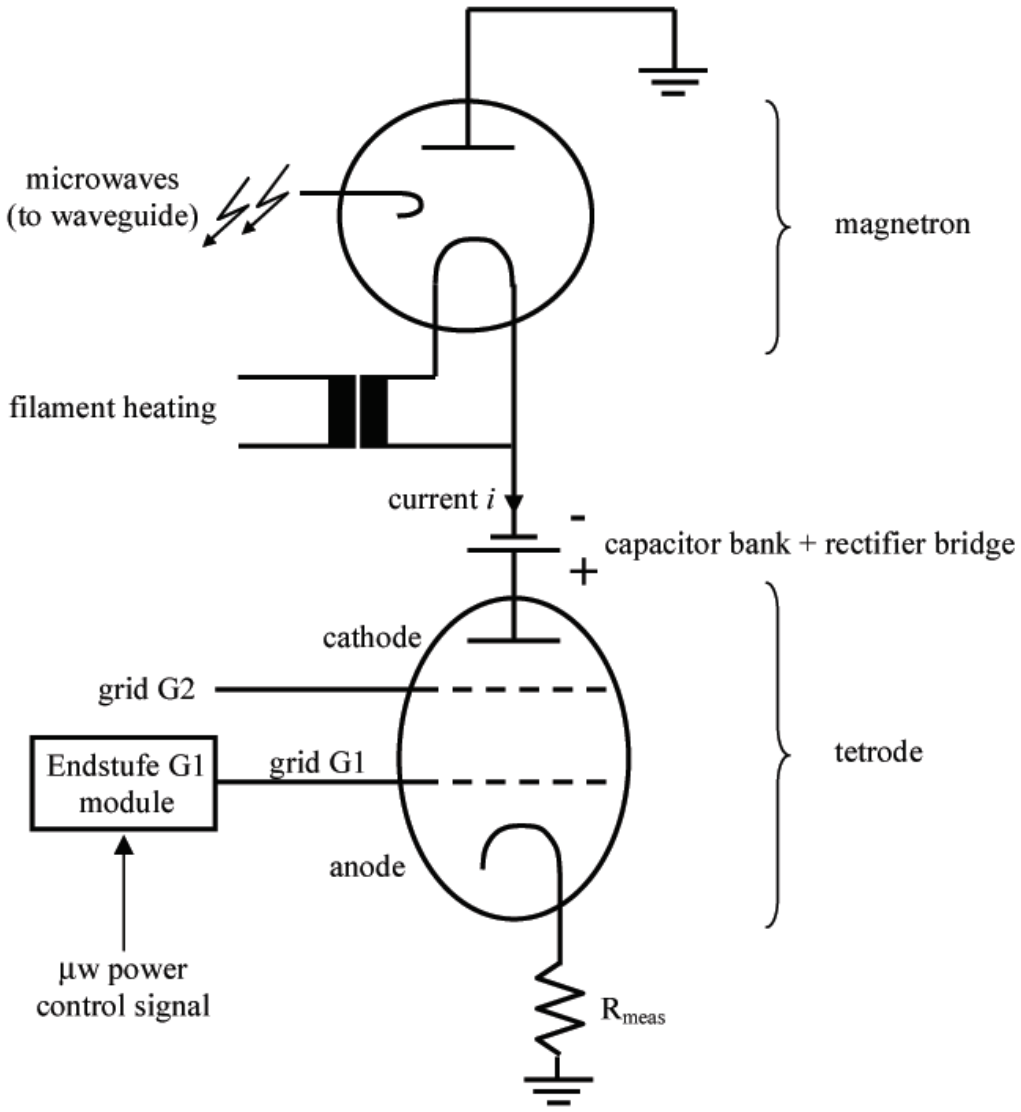

Figure A.1: Layout of the high-power part of the microwave generator system.

- Grid G1 voltage : from -240V to 0V
- Max anode current ca. 7.5A

Parameter	*Nominal value*
max power	50kW (up to 100ms), or
	5kW - CW
typical discharge length	$\leq$ 2s
frequency	2.45GHz $\pm$20MHz
ripple	$< 1\%$
modulation depth	$0 - 100\%$ (min. 200W)
modulation frequency	$<$ 20kHz (square)
	$<$ 100kHz (sinusoidal)
rise/fall time	$10\mu s$ typical
cooling	forced air (power supply)
	demineralized water (magnetron head, circulator)
efficiency	60%

Table A.1: Main parameters of the microwave generator system.

Control unit

The control unit is responsible for the timing, the operation of the microwave source during the discharge and the measurements of the relevant parameters. Most of these components are physically grouped inside the power supply cabinet into a 'magnetron slave unit', developed at CRPP and integrated with the original control [60].
The injected and reflected power are measured on the transmission line by two RF diodes installed on a bi-directional coupler.
A number of signals monitor the state of the system during the operation. Interlocks connected to temperature sensors and flow-meters avoid over/under temperature of the system.

Transmission line

The transmission line (Fig. A.2) is made of two straight sections, a transition from WR430 to WR340 waveguides, a step twist and the pressure window. An adapter DN100-CF $\rightarrow$ DN160-ISO-K (not shown in the figure) is included in the final design to fit the standard flanges installed on TORPEX.
A dual directional coupler is installed on the waveguide to sample the forward and reflected power with an attenuation of -60dB. The signals are measured by RF

diodes, pre-amplified at the output of the diodes and sent to the magnetron slave unit and to the acquisition boards, where they are acquired at 250kSamples/s.

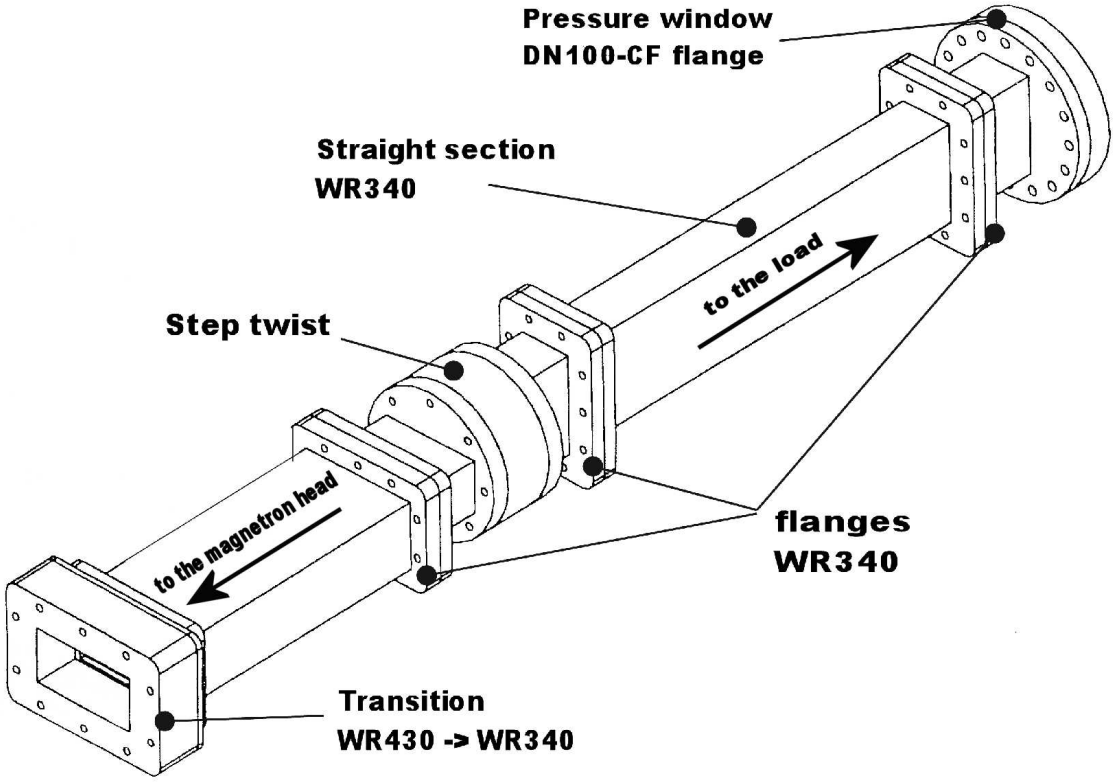

Figure A.2: Transmission line, connecting the microwave source to the TORPEX vacuum chamber.

A.2 System upgrades

During the first few years of operations of TORPEX the microwave system has been subject to a number of modifications and improvements. The modulation capabilities were limited to a $0-100\%$ modulation amplitude, with a modulation frequency up to a $100Hz$ only. To overcome these limitations, a new control circuitry has been developed, partly by-passing the original one.
Technical details are included in the following Sections, intended to provide quick reference on the properties of the microwave generator system. The complete technical documentation is found in the magnetron Manual.

A.2.1 Safety

Microwaves at 2.45GHz may cause severe injuries to the human body[4], therefore a particular care is spent in limiting the possibility of releasing microwaves in the TORPEX laboratory hall. This is mainly achieved by connecting an interlock to the door of the TORPEX experimental zone, so that no microwave pulse can be accidentally launched if the door is open, e.g. if people are working inside the zone. Other interlocks are connected to the doors of the microwave power supply and of the magnetron head cabinets, in which high voltage may be present during operations. An emergency button has been installed at different locations in the laboratory, including the TORPEX control room, by which all the systems can be instantaneously switched off in case of a major problem.
Apart from human safety, the system is protected against major hardware failures. The status of the cooling system is monitored, and an error is produced if the temperature and/or the flow are not within the nominal range. In particular a temperature sensor, installed on the pipes carrying cooling water to and from the magnetron head, is used to stop the operations if the water temperature drops below $\approx 18°$C to avoid condensation inside the magnetron head.

Monitoring of the microwave level in the laboratory

The design of a microwave area monitor has started, in collaboration with J. Rossel and A. Diallo [90]. It is aimed at monitoring the level of microwave power dispersed in the TORPEX hall, and will be connected to an alarm which indicates when the

[4]Information on the risks related to the use of microwaves and the guidelines for limiting the exposure to non-ionising radiation are well documented on the ICNIRP (International Commission on Non-Ionizing Radiation Protection) web-site: <http://www.icnirp.de/>.
The Swiss law which applies to installations exploiting microwave radiation for research purposes is found in the decree 814.710 by the Swiss Federal Council, released on 23 December 1999 (french version only, *Ordonnance sur la protection contre le rayonnement non ionisant - ORNI*)

power exceeds the limits imposed by the law[5].

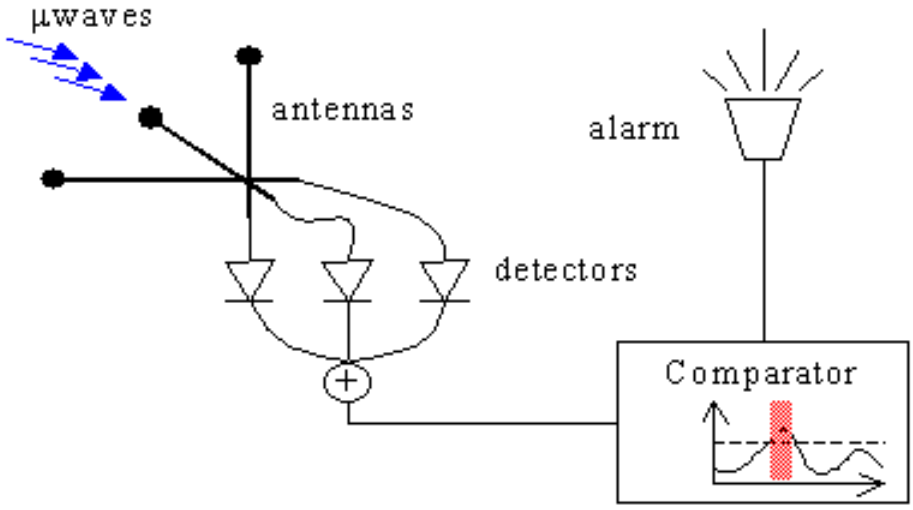

Figure A.3: Schematic of the microwave area monitor.

The device is composed of three antennas, measuring the intensity of the microwave field along the three possible axes of polarisation (Fig. A.3). The signals, detected by microwave diodes, are summed together and sent to a comparator. When the level of the total signal exceed a pre-defined threshold, an alarm is activated, indicating that the maximum allowed level of microwaves is exceeded.

A.2.2 Integration with the TORPEX subsystems

The microwave system was integrated with the TORPEX subsystems (e.g. mechanical structure, cooling system, mother-clock, acquisitions, ...) during the construction of the machine. Because of the low power consumption involved, the microwave generator is directly connected to the standard electrical network. A mechanical support was designed taking into account possible changes in the transmission line layout, implying a variable distance between the magnetron head and the machine. The position of the magnetron with respect to the vacuum chamber can be finely adjusted by means of screws.
The cooling of the magnetron head system is provided by a closed circuit employing demineralised water. The existing infrastructures of the CRPP were adapted to fit the requirements of flow and feeding pressure at the input of the magnetron head. The power supply, where the capacitor bank and the high-voltage tetrode tube are

[5]The limits for radiation between 2 and 300GHz are $50\mathrm{Wm}^{-2}$ for occupational exposure and $10\mathrm{Wm}^{-2}$ for general public exposure (from the *ICNIRP Guidelines*). The latter value should be taken as reference for the maximum intensity in the laboratory.

located, is cooled by forced air flow. The noise generated by the huge fan cooling the tetrode has been considerably reduced by a convenient system of acoustically insulating *chicanes*.
Most of the integration work of the microwave system with TORPEX concerned the timing and the acquisition of the relevant control signals. In general, each subsystem of TORPEX is controlled by a slave unit, connected to the main bus (based on a *Bitbus* protocol) through which commands and instructions are sent from remote [60]. The magnetron slave unit has three main functions, as detailed below: control of the timing, control of the waveform and measurements of the relevant signals from the system. The implementation of the software required to set up the discharge parameters from remote is shortly discussed.

Timing

The timing is imposed by the TORPEX mother-clock by means of two 'on-off' signals. A 'slow' on-off give the start and the stop for the charge-up of the capacitor bank, see Fig. A.4. This phase lasts for about 10s. Once the capacitors are charged, the 'fast' on-off defines precisely the time window of the plasma discharge. Within this time window, a function generator delivers the low voltage signal that controls the power level.
The on-off signals are supplied by two independently adjustable counters, installed inside the magnetron slave. The input values for the counters are loaded from the graphical user interface (GUI) before the discharge. A third signal is used to trigger the waveform generator which provides the waveform for the present discharge (see below).

Waveform

The waveform of the injected power is set before the discharge through the control GUI. Different basic waveforms can be selected, such as constant, sinusoidal, linear ramp, square (Fig. A.5). The relevant parameters (amplitude, frequency, duty cycle) can be arbitrarily adjusted, compatibly with the limitations of the microwave hardware system.
The selected waveform is sent to the magnetron slave unit through the BitBus, and finally loaded into the waveform generator[6] volatile memory via a RS-232 interface connecting the slave to the generator.

Measurements of the magnetron operational signals

The most important and delicate element of the microwave generator is the tetrode tube. A set of measures has been installed to monitor its relevant parameters, which

[6]The model presently used is a *Agilent 33210-A*.

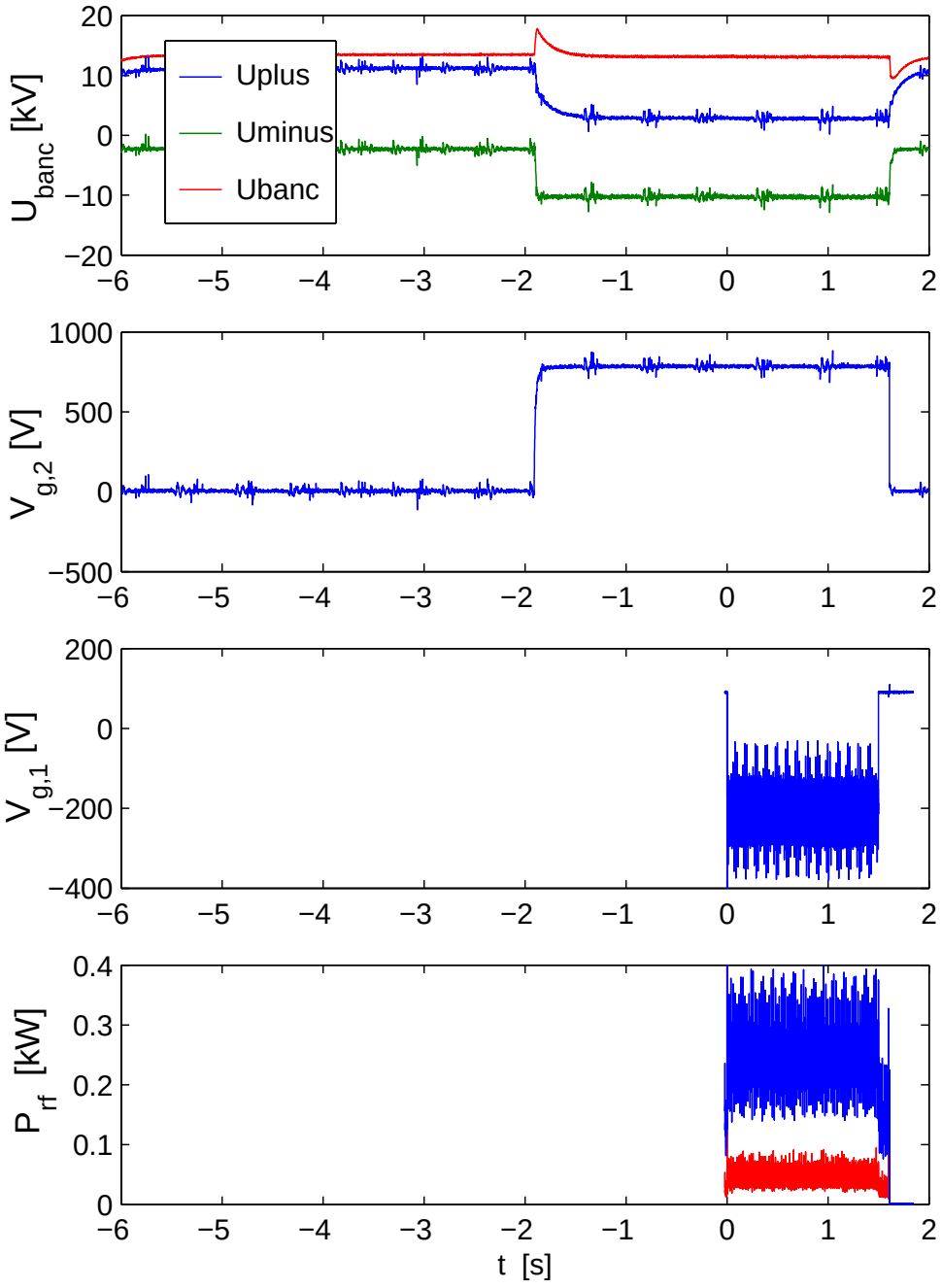

Figure A.4: Example of a typical time sequence for a TORPEX discharge. The main control signals of the microwave generator are shown, the voltages on the capacitor bank (*Uplus, Uminus* and their difference *Ubanc*) and the voltages on the two grids, G1 and G2. The levels of injected and reflected power are shown in the bottom graph.

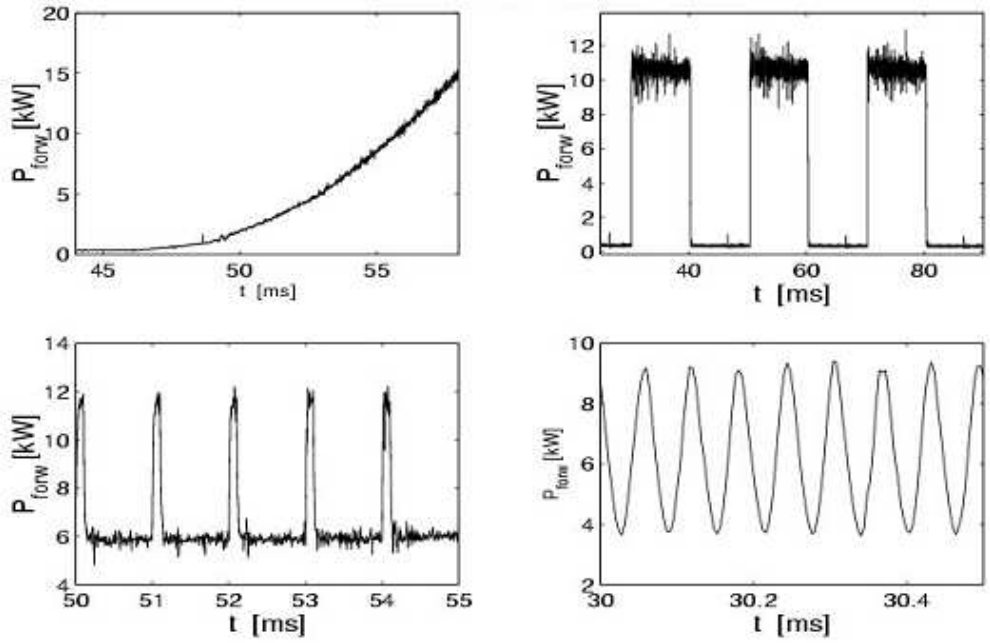

Figure A.5: Examples of waveforms obtainable from the TORPEX microwave system.

are acquired for normal operations on the TRCF acquisition system (sampling frequency 1kHz) and on the DT-200 acquisition system (sampling frequency 250kHz). The following quantities are measured and sent to the acquisition through a 37-pole cable.

- Anode current, from J1:8 pin. Measured on tip5 of 37p/Sub-D
- Capacitor bank, plus voltage, from X10/12 pin. Measured on tip3 of the 37p/Sub-D
- Capacitor bank, minus voltage, from X10/11 pin. Measured on tip4 of the 37p/Sub-D
- Grid G1 voltage, measured on the grid through a 1:240 voltage divider (10kΩ/2.4MΩ). Measured on tip1 of the 37p/Sub-D
- Grid G2 voltage, measured on the grid through a 1:1000 voltage divider (10kΩ/10MΩ). Measured on tip2 of the 37p/Sub-D

To minimise perturbations to the system, the measurements of the anode current and capacitor bank voltages are decoupled from the acquisition through a passive RC circuit (Fig. A.6), with a cutoff frequency of 4.8kHz and a DC gain of 0.0909.

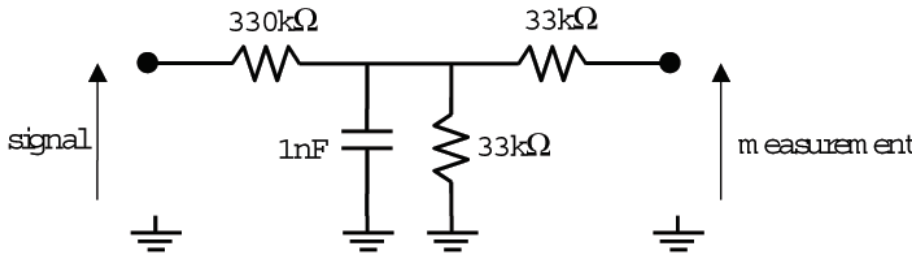

Figure A.6: R-C filter used to limit the perturbations to the system through the measures of anode current and capacitor bank voltages.

Measurements of incident and reflected power

The injected and reflected power is measured by microwave detectors installed on the waveguide through a bi-directional coupler. The coupling factor is -60dB, with a minimum directivity of -125dB. At present, the detectors are of the type DM-211 S-Team. Since the output signals are weak, usually below 100mV, the signals are pre-amplified at the diode output with a gain of 21, then sent to the magnetron slave unit, about 10m far from the measurements. The injected and reflected power signals are used as reference for the feedback loop that controls the injected power level (see below). From the magnetron slave unit they reach the DT-200 acquisition system, where they are sampled at 250kSamples/s.
The typical conversion curve for a DM-211 diode is shown in Fig. A.7. The diode has a non-linear response as a function of the measured power, which complicates the development of a feedback control entirely based on a linear, analog circuitry.

Software developments: control GUI

The GUI[7] used to control most of the TORPEX experimental parameters is shown in Fig. A.8. Concerning the microwave system control, I have provided the necessary information to account for calibration files, and to ensure the full compatibility between software and hardware settings. Referring to Fig. A.8, the waveform is chosen from a scroll-bar menu and the main parameters adjusted in terms of physical quantities such as injected power, modulation amplitude and frequency and duty cycle. The timing is defined by the 'slow' and 'fast' on-offs and the waveform generator trigger time. All the information is then loaded into the magnetron slave unit and the buffer of the waveform generator. The system is thus ready for a discharge.

[7]The interface has been integrated with the TORPEX control system in the past two years by B. Labit, S. H. Müller and I. Furno. The Java GUI has been developed by M. Helletzgruber (Helletzgruber IT Solutions & Consulting).

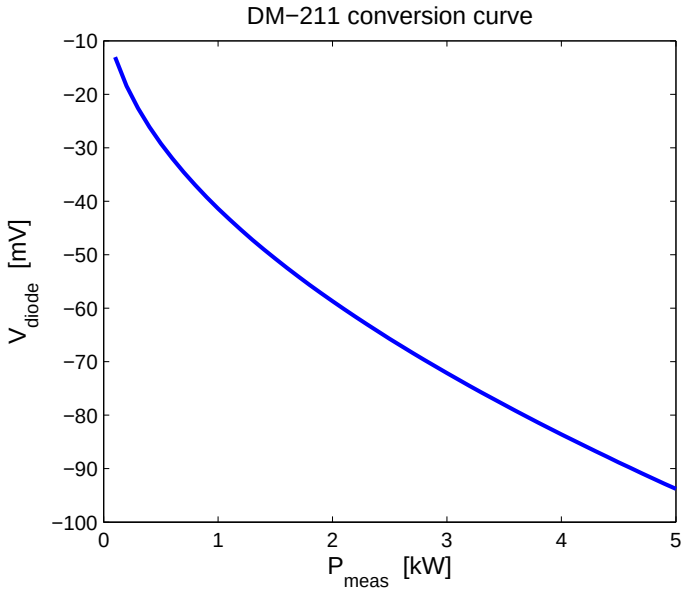

Figure A.7: Calibration curve for the DM-211 diode.

A.2.3 Improved control of the injected power

To improve the performances of the original system, it has been necessary to by-pass the original control unit with a newly developed one, integrated inside the magnetron slave unit. A first version was developed which did not include an accurate control of the injected power, P_{rf}, all along the discharge through a convenient feedback system. This represented a problem, for example, for discharges lasting more than 100ms, where a decrease of the of P_{rf} was observed due to the discharge of the capacitor bank[8].
In any case, the maximum length of the discharges was limited to 100ms by a clamping circuit inside the original control circuit. This circuit had been installed to limit the maximum power to 5kW of equivalent continuous operation, representing the upper limit for the system.
Other minor problems, such as the injection of an unfiltered 50Hz component from the power network, were present. An upgrade of the system was then necessary. The main requirements for the new system were:

1. Stabilise the level of injected power, regardless of the discharge length.

2. Provide a bandwidth for the modulation of the injected power suitable for the exploitation of EC modulation techniques. Increase the pulse length, possibly up to a continuous operation.

[8]The discharge of the capacitor bank during a discharge has a time constant of $\approx$ 300ms.

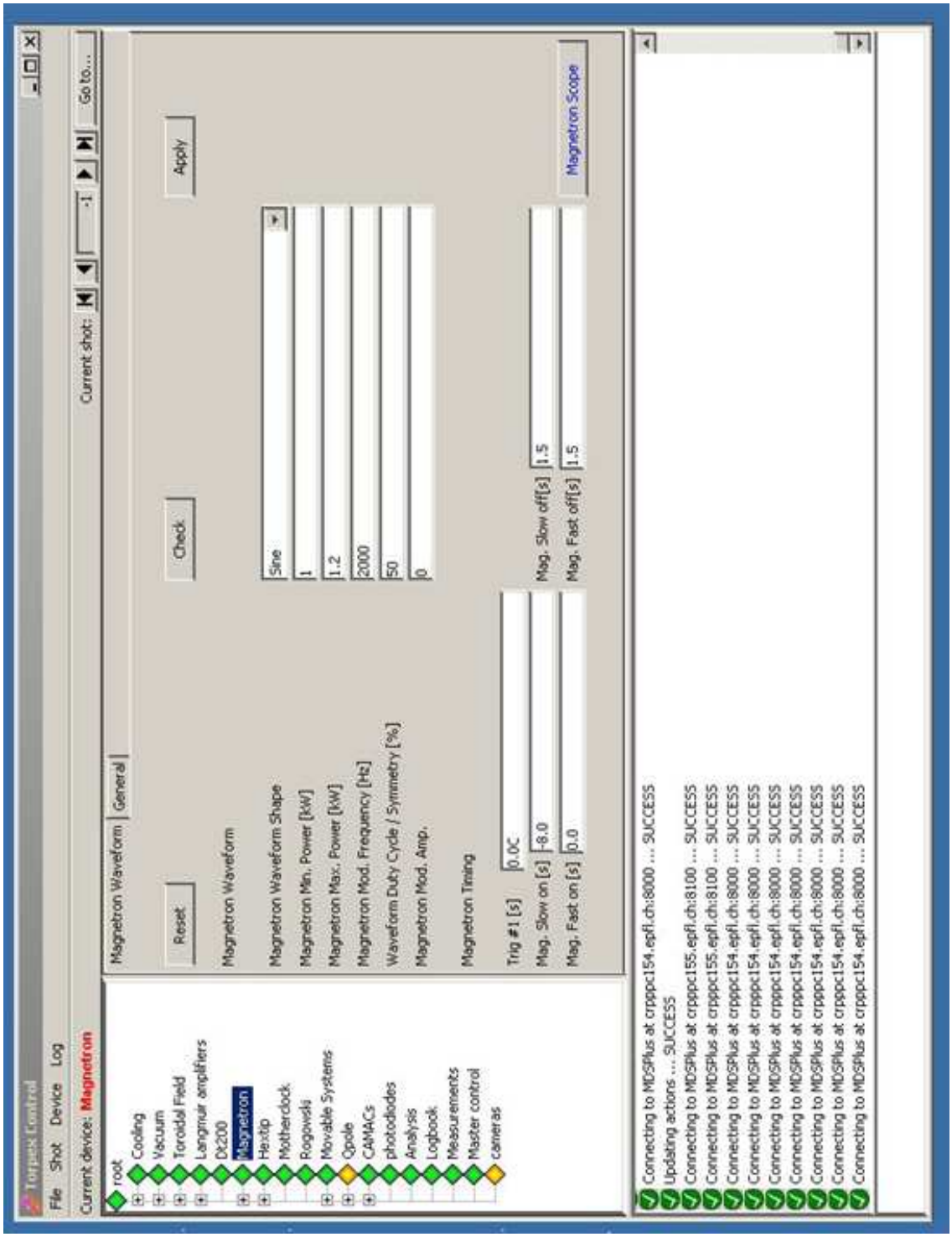

Figure A.8: Configuration of the magnetron parameters through the 'Torpex Control' graphical interface.

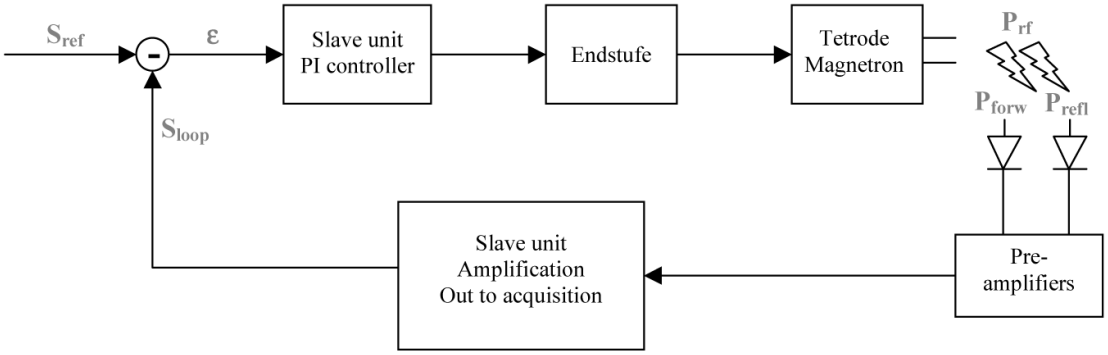

Figure A.9: Schematic of the feedback control system developed to control the level of injected power from the microwave system.

3. Guarantee the safety of the system, independently of possible failures of the control system and/or of the software controlling the machine operation.

4. Guarantee a stable operation of the system for all the possible regimes.

These issues have been satisfactorily addressed and the microwave system operates routinely with the improved control. Nonetheless, it is possible to revert the control back to the original control unit for test purposes or in case of major failures of the new system.

Feedback control of the injected power

The stabilisation of the injected power is achieved via the inclusion of a feedback loop on the measured injected power level, P_{forw}. The layout of the newly developed control system is shown in Fig. A.9. The reference signal, S_{ref}, provided by the waveform generator, is summed with the measured $S_{loop} = S_{loop}(P_{forw})$, to generate the *error signal*, ϵ. A proportional-integral (PI) controller circuit elaborates the signal ϵ and drives the 'Endstufe' stage, providing the control voltage for the tetrode tube, hence of the magnetron tube and of the delivered power, P_{rf}. All the circuitry is encased in the magnetron slave unit, except for the pre-amplifiers providing the P_{forw} and P_{refl} signals to the feedback system.

Bandwidth optimisation and increased pulse length

The bandwidth of the system is optimised in order to keep the response stable for the whole range of control signal amplitudes, $S_{ref} \in (0, 10)$V, and useful modulation frequencies, $f_{mod} \in (0, 100)$kHz. This is achieved by low-pass filtering at ≈ 120kHz the error signal and the measured P_{forw} and P_{refl}. The latter represents the main

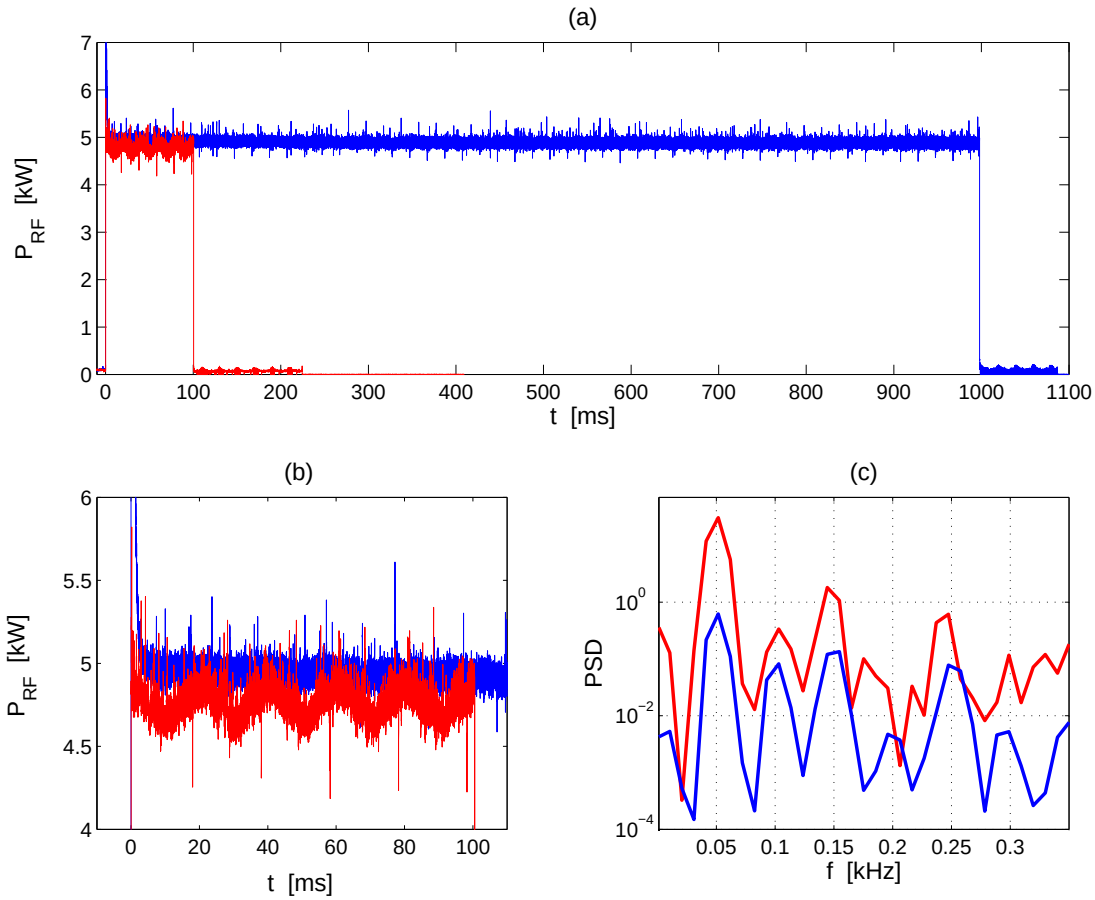

Figure A.10: Comparison between the behaviour of the injected microwave power level before (red traces) and after (blue traces) the implementation of the feedback control system. *(a)* The pulse length is extended, ideally up to a continuous operation for injected power $\leq$ 5kW. *(b)-(c)* The level of the spurious 50Hz oscillation and its spectral harmonics are reduced by one order of magnitude, as results from the power spectral density of the signals.

source of noise, due to pick-up and amplification of electromagnetic disturbances present in the experimental hall, which may interfere with the low-voltage output of the RF diodes.
The present bandwidth is largely sufficient for the type of modulation experiments performed on TORPEX. If necessary, it could be extended by adding a differential part to the PI controller, thus providing a faster response of the feedback loop to variations of ϵ. As a drawback, the possibility of unstable oscillations of the circuit is increased.
The limitation on the maximum discharge length has been removed, by imposing a tighter constraint on the maximum available power (see below). Note that in any case the system stops if the voltage across the capacitor bank decreases below the critical threshold value needed for a correct functioning of the system. An example of the improved performances of the new system is shown in Fig. A.10.

Safety against 'external' failures

To prevent a divergent increase of the power delivered by the magnetron, the control voltage at the input of the 'Endstufe' stage must be kept below 10V, corresponding to 50kW of generated microwave power. Despite a software check of the input parameters is already present in the TORPEX control GUI, an hardware voltage limitation is added in the slave unit circuitry. It is provided by clamping diodes, which finally limit the maximum available power to 10kW.
A potential danger for the water-cooled magnetron head and for the circulator is represented by condensation inside the magnetron head box when the water temperature drops below $\approx 15°$C. Because of the high voltage applied to the magnetron, this could lead to arcs and must be avoided. A thermostat, connected to a safety interlock, has been installed on the cooling water circuit to monitor the temperature and interrupt the operations when the water temperature is outside the allowed range (Fig. A.11). Two LEDs, on the thermostat and on the control unit, indicate the status of the temperature controller.

Stabilisation of the system

After a major failure occurred in December 2005, the microwave system suffered from serious instability problems, which prevented TORPEX from its normal operations. In particular, the following components were repeatedly broken: resistors R22, R7 and fuse F39. The resistors R22 and R7 have been replaced by bigger resistors, which can handle up to 1W and 4W of power. Figure A.12 shows the signals measured on a oscilloscope after repair of the broken elements. The large oscillations visible on the grid voltages led to a crash of the system within a few seconds due to an over-current. From these signals it appeared that the system underwent spontaneous oscillations at 14.5MHz, probably due to the excitation of a resonance. The possibility that

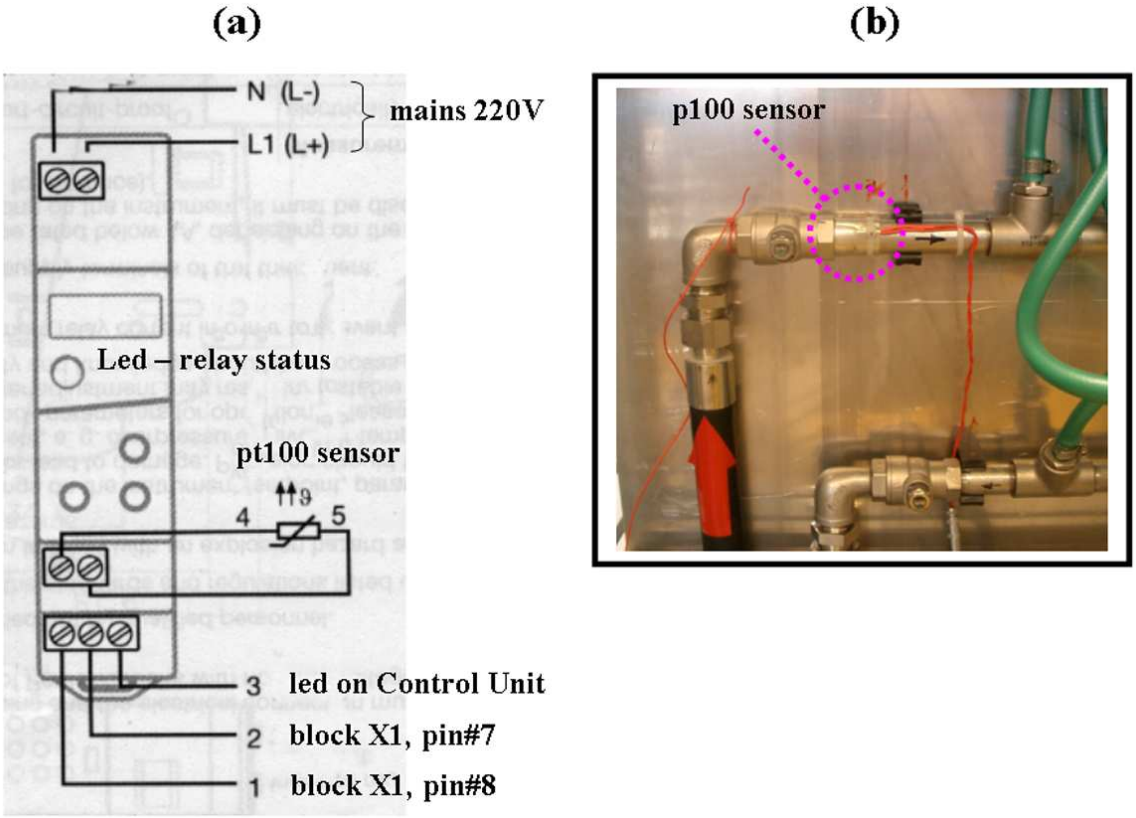

Figure A.11: *(a)* Thermostat controlling the temperature of the water cooling the magnetron head and the circulator. An interlock prevents the system from firing microwaves when the water temperature is too low. *(b)* The water temperature is measured by a Pt100 sensor, installed on the cooling circuit tubes.

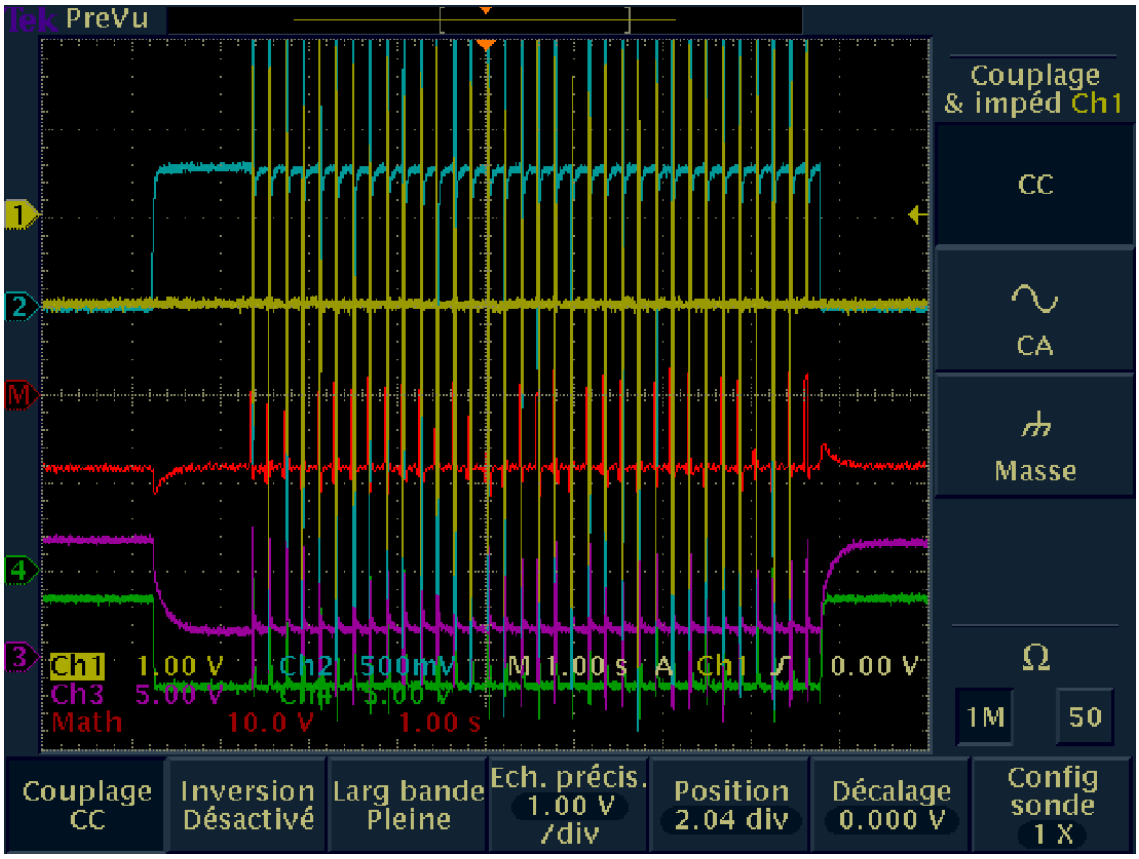

Figure A.12: Traces of the magnetron signals : voltage on grid G1 (yellow) and G2 (cyan), voltage on the capacitor bank (positive: violet, negative: green) and total voltage across the capacitor bank (red). Note the disruptive oscillations of the grid voltages. The system stopped due to the detection of an over-current.

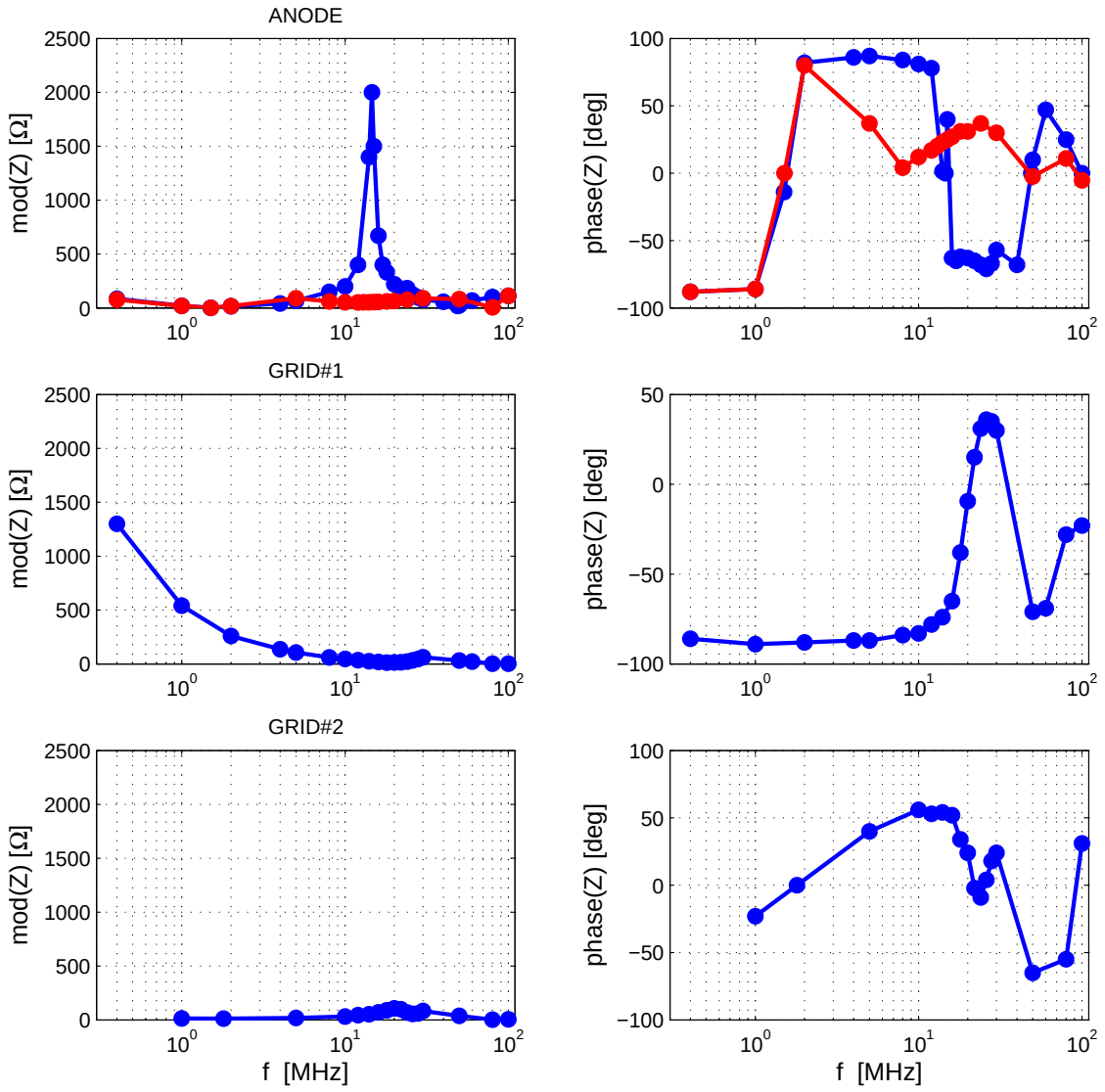

Figure A.13: Blue curves: measured complex impedance seen by the anode and by the two grids (*left column:* module; *right column:* phase). Note the resonance at a frequency of 14.6MHz in the anode curve, responsible for the internal oscillations of the tube. Also shown (red curve) the anode impedance after its compensation, explained in the text.

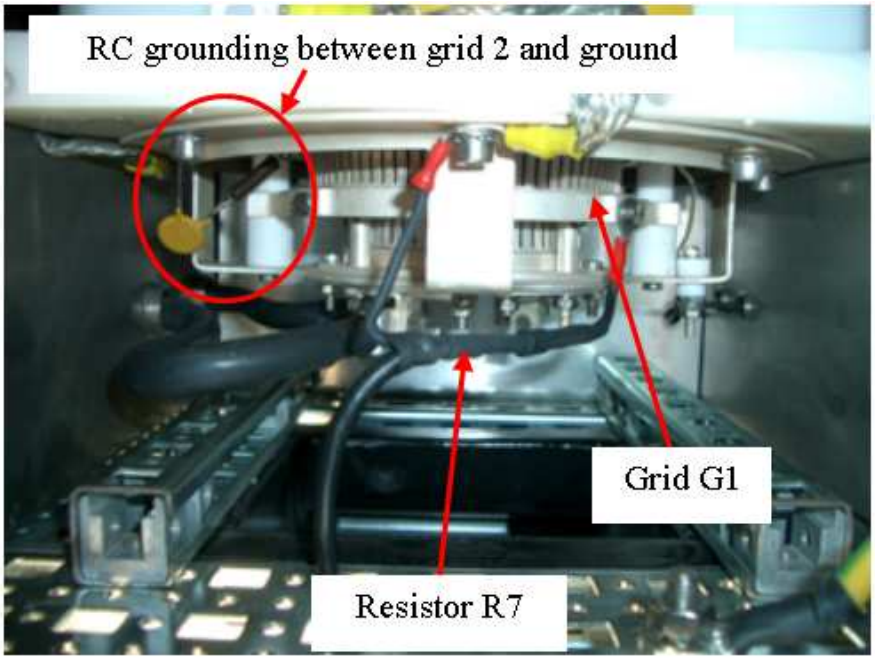

Figure A.14: Picture of the bottom part of the tetrode tube, showing the grid G1 and some of the components that have been modified to stabilise the tube.

these oscillations were caused by the control electronics was ruled out by driving the grid G1 directly through an 'external' signal source, thus opening the feedback loop of the original control system.
To identify the components responsible for the resonance at 14.5MHz the impedance seen by the tetrode grids and anode was measured, see Fig. A.13. A resonance in the anode impedance was identified, while the grids did not show an abnormal behaviour. The series RC high-frequency grounding for the grid G2 (Fig. A.14) has been removed. At present, there is only a high-voltage protection capacitor with $C = 4.7$nF. The anode impedance is compensated by adding a RC grounding between the anode pin and ground, as shown in Fig. A.15. The values $R = 47\Omega$ and $C = 500$pF correspond to a cut-off frequency of 6.8MHz. The results of the compensation in terms of impedance are shown in Fig. A.13. The magnetron control signals after this modification are clean, and no spurious oscillations are observed.

A.2.4 Future developments

An interesting feature for improving the quality of the measurements would be to perform a feedback control on the absorbed power, P_{abs}, instead of the injected power. As explained in Chapter 4 (see, for example, Fig. 4.12), there exists a strong coupling between the plasma density dynamics and the microwave power absorption

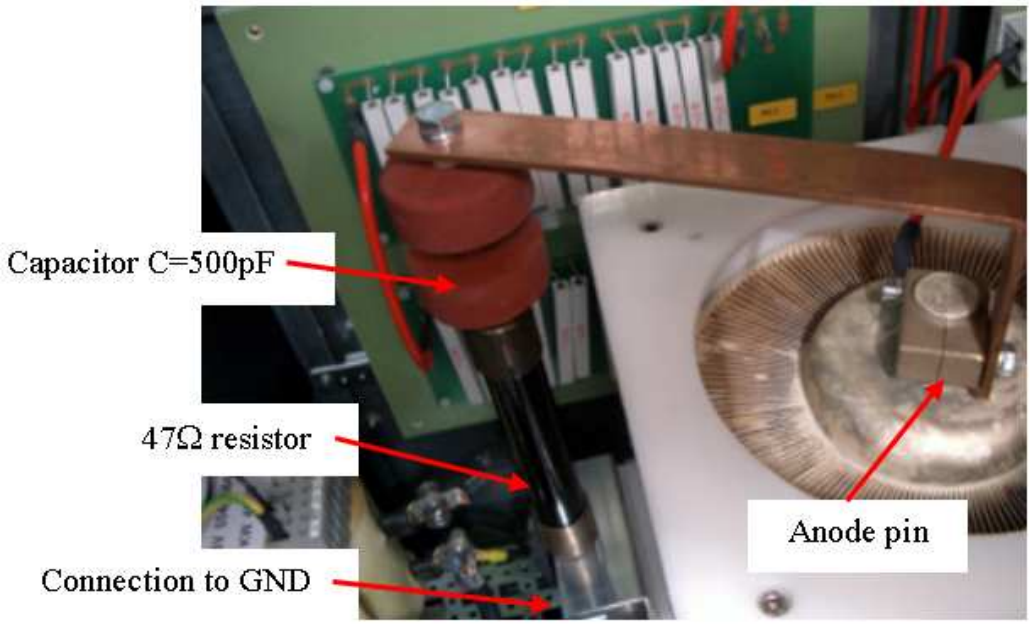

Figure A.15: Picture of the top part of the tetrode, showing the series R-C elements connecting the anode pin to ground for the compensation of the anode impedance.

mechanisms, due to the dependence $f_{uh} = f_{uh}(n)$. By controlling P_{abs}, it would then be possible to reduce the oscillations of the position of the UH resonant layer, where most of the ionisation occurs (cfr. Chapters 4 and 5). The newly developed control system can be already configured to operate with $S_{loop} = S_{loop}(P_{forw} - P_{refl}) \equiv S_{loop}(P_{abs})$. The results from a preliminary test, representing a proof-of-principle of this method, are shown in Fig. A.16. The comparison between similar discharges with the feedback on P_{forw} and on P_{abs} is made by looking at the power spectrum of a probe detecting a coherent mode at $f \approx 2.5$kHz. The signals are much cleaner when the absorbed power is stabilised, and a reduction of the 'turbulent' part of the spectrum, between 5 and 10kHz, is observed. Unfortunately, the operation of the control system becomes unstable as soon as the experimental conditions are slightly changed.
At present, the nonlinearities in the closed loop transfer function do not allow to extend further the bandwidth, and make the optimisation of the feedback circuitry for a large set of experimental conditions difficult. A possible solution would be to base the control circuit on digital signal processing (DSP) technology, which can more easily handle nonlinear operations on the control signals.

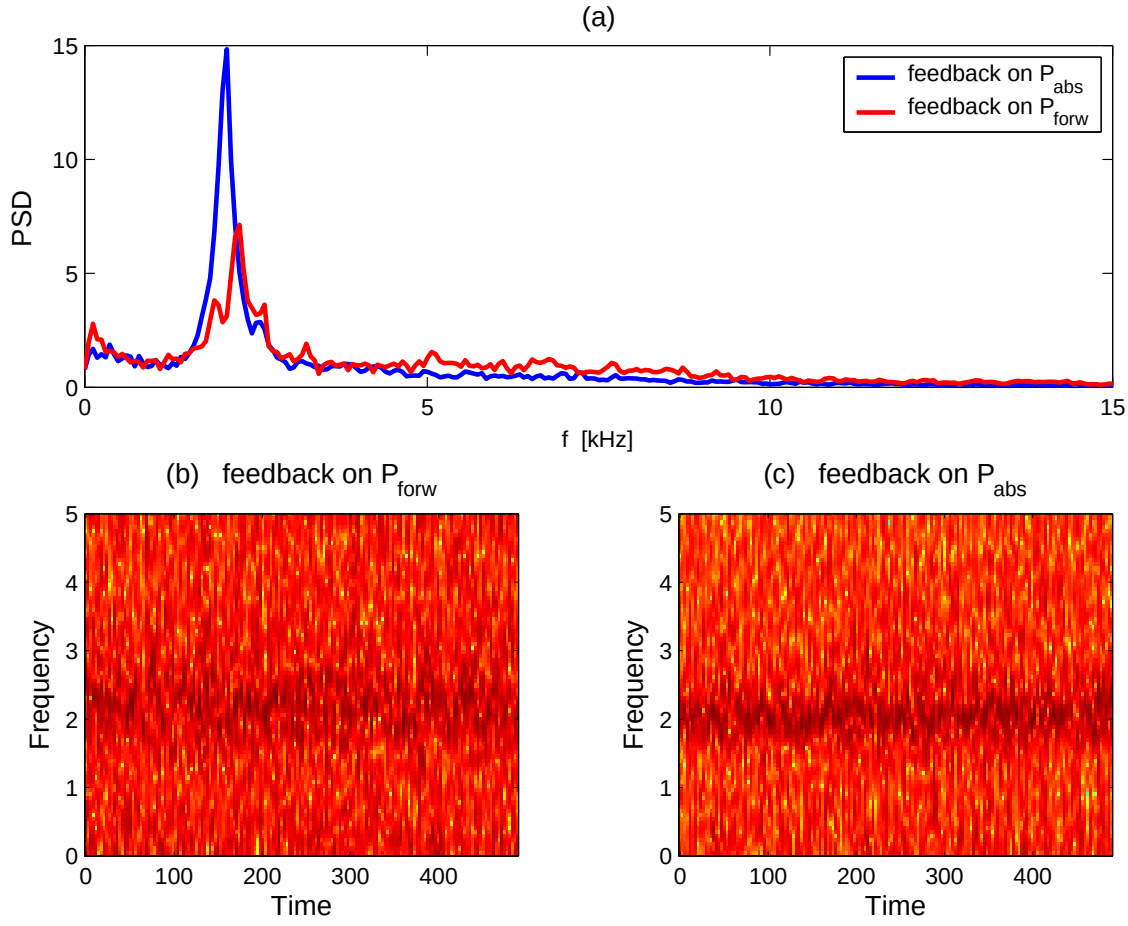

Figure A.16: Proof-of-principle of the stabilisation of the absorbed power through a feedback loop in the magnetron control system. Two similar discharges, with a feedback on the injected and absorbed power, are compared. *(a)* Power spectral density from an ion saturation current signal, detecting a mode at $\approx$ 2.5kHz. The spectrograms measured during 500ms are shown for the case with control on P_{forw} *(b)* and on P_{abs} *(c)*.

A.3 Construction of a simple test dummy load

In this Section, the construction and the use of a simple dummy load are described. It has been used during the first tests of the microwave generator system to check the effective amount of delivered microwave power. No direct measurements of the incident and reflected power were available at that time. The simplicity of the construction and the relatively good accuracy of the power measurements makes it a good alternative to more expensive test loads.
The basic idea is to estimate the amount of microwave power delivered by the system by means of calorimetry. The basic principles of calorimetric measurements and their practical application are described in the following.

Dimensioning of the load

In order to avoid microwave leakage, the load should have closed metallic walls. A cylindrical 'oil tank', easily available at CRPP, was chosen as vessel. The load is enclosed in a shielding box made by a metallic grid to prevent any microwave leakage from the tank.
No detailed calculations have been made to optimise the load impedance as a function of the geometrical dimensions of the tank. Note that the isolator on the transmission line can in principle withstand up to 50kW of reflected power, thus the generator cannot be damaged even in the case of total reflection.
For the frequency of interest, water is an excellent absorber, as evident from the wide use of systems operating at 2.45GHz for heating/drying purposes (cfr. microwave ovens). To optimise the quantity of water that is used to absorb the microwaves, its absorption capabilities must be estimated. By indicating with $\gamma = i2\pi f\sqrt{\mu\epsilon}$ the propagation factor of the microwaves, the absorption length, L_{abs}, can be calculated from the real part of γ:

$$L_{abs} = \frac{1}{Re\{\gamma\}} \tag{A.1}$$

where $\mu \approx \mu_0$ is the magnetic permeability and $\epsilon = \epsilon' + i\epsilon''$ the complex dielectric constant of the medium. The dielectric constants of the water at $T_w = 300$K, $f = 2.45$GHz are $\frac{\epsilon'}{\epsilon_0} = 76.7$ and $\tan\delta = .157$, where $\tan\delta = \frac{\epsilon''}{\epsilon'}$ is the loss tangent and ϵ_0 the dielectric constant in vacuum [108]. Equation A.1 gives $L_{abs} = 28$mm. At this frequency the water cannot be considered a 'surface absorber' as for higher frequencies, and the microwave power is distributed over a larger volume, so that local evaporation is avoided.
Assuming that all the microwave power is absorbed by the water, the increase of the water temperature, T_w, after a discharge[9] as a function of P_{RF} and the amount

[9]It is assumed that the length of the discharge, τ_{RF}, is short enough that during this period the system can be considered adiabatic.

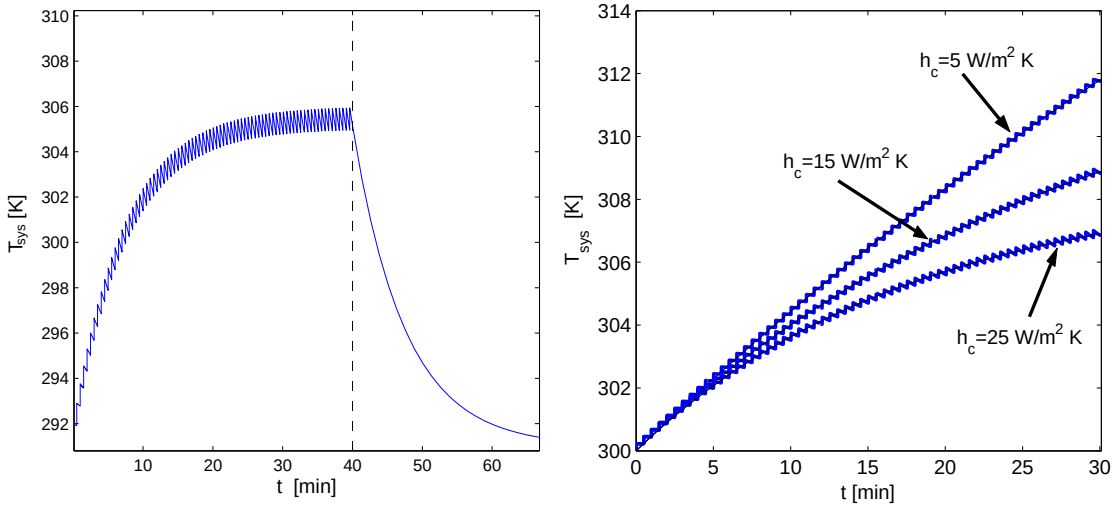

Figure A.17: *Left:* Numerical evaluation of $T_{sys}(t)$ for $P_{RF} = 50\text{kW}$, $\tau_{RF} = 100\text{ms}$, $M_w = 1\text{l}$, $h_c = 15\text{W/m}^2\text{K}$, $T_{room} = 292\text{K}$ and $T_{sys}(t = 0) = T_{room}$. The duty cycle is 1 shot every 30s. The RF generator is 'turned off' at $t = 40\text{min}$ (dashed line on the time axis). *Right:* Results for $T_{sys}(t)$ for different values of h_c.

of water in the tank is

$$\Delta T_w = \frac{P_{RF}\ \tau_{RF}}{M_w c_{p,w}} \tag{A.2}$$

where τ_{RF} is the pulse length, M_w the mass of water and $c_{p,w} = 4.182\text{kJ/kgK}$ the specific heat of water. In Eq. A.2 it is assumed that the heat capacity of the water is much greater than that of the aluminum tank and that the heat conduction from the tank to the waveguide is negligible.
By imposing $\Delta T_w \leq 1\text{K}$ with P_{RF} =50kW and $\tau_{RF} = 100\text{ms}$, we obtain a lower limit for M_w to keep the temperature of the system T_{sys} within a safe range. It is found that 1 liter of water is enough to keep T_w below 1 degree per discharge, with the maximum available power fired into the load[10].
In reality, after each shot the temperature of the system decreases; the heat is dissipated both by natural convection and radiation from the external surface of the cylinder, but also by conduction, and further convective losses, to the transmission

[10] A hollow nylon screw has been used as 'feed-through' to empty the tank and to fix a water level indicator. Depending on its specific chemical composition, nylon has a melting temperature greater than 500K, but a glass transition temperature in the range $315 \rightarrow 330\text{K}$. This is the temperature above which a polymer becomes soft. For this reason, the water temperature T_w should be kept below 315K to keep the vessel watertight.

line. Neglecting the role of the waveguide, the loss rate of heat is

$$\dot{Q}_{conv} = h_c S_{cyl}(T_{Al} - T_{room}) \tag{A.3}$$

$$\dot{Q}_{rad} = \sigma_r (T_{Al} - T_{room})^4 \tag{A.4}$$

where h_c is the convection heat-transfer coefficient, $\sigma_r = 5.6710^{-8}\mathrm{W/m^2K^4}$ the Stefan-Boltzmann constant and T_{room} the room temperature. In the temperature range of our interest the radiation losses can be neglected.
The coefficient h_c in Eq. A.3 is the an average value over the entire vessel surface. It may depend on the spatial temperature distribution on the surface and on the geometry of the tank. To simplify the analysis, we define h_c as an averaged value that can be experimentally measured

$$h_c \doteq \frac{\int_{S_{cyl}} h_c'(\mathbf{x})\,[T_{Al}(\mathbf{x}) - T_{room}]\,d\Sigma}{S_{cyl}(T_{sys} - T_{room})} \tag{A.5}$$

In the following it is assumed that the water and the aluminum tank reach instantaneously the thermal equilibrium, i.e. $T_{Al} = T_w \doteq T_{sys}$, though in practice this assumption could be not well satisfied. This approximation is reasonable when τ_{RF}^{-1} is much greater than the repetition rate of the shots. In conclusion, all the effects of an arbitrary temperature distribution of the system are included in h_c, which can be determined experimentally. Reasonable values for h_c are $h_c = 5 \leftarrow 25\mathrm{W/m^2K}$.
The asymptotic temperature T_{as} reached by the system in the stationary state can be evaluated from a power balance equation:

$$\dot{T}_{sys}(t) = -A\,[T_{sys}(t) - T_{room}] - B\,[T_{sys}(t) - T_{room}]^4 + \frac{P_{RF}(t)}{C} \tag{A.6}$$

where

$$A = \frac{h_c S_{cyl}}{C} \qquad B = \frac{\sigma_r S_{cyl}}{C} \tag{A.7}$$

and $C = c_{p,w}M_w + c_{p,Al}M_{Al}$ is the heat capacity of the system; again, the contribution of the aluminum vessel to C can be neglected. Some typical results of the analysis described above are presented in Fig. A.17.

Construction details

A commercial, cylindrical aluminum tank, with a volume of 30l, is used. The radius is 180mm and the length 485mm. A schematic of the front- and rear-ends of the tank is shown in Fig. A.18. The aperture is approximately 150 × 110mm, which allows one to introduce a WR340-type flange. A metallic shield closes the remaining slits to avoid RF leakage. For safety reasons, the tank is enclosed into a shielding box during the tests. On one side of the tank, the original plastic cap is used to introduce

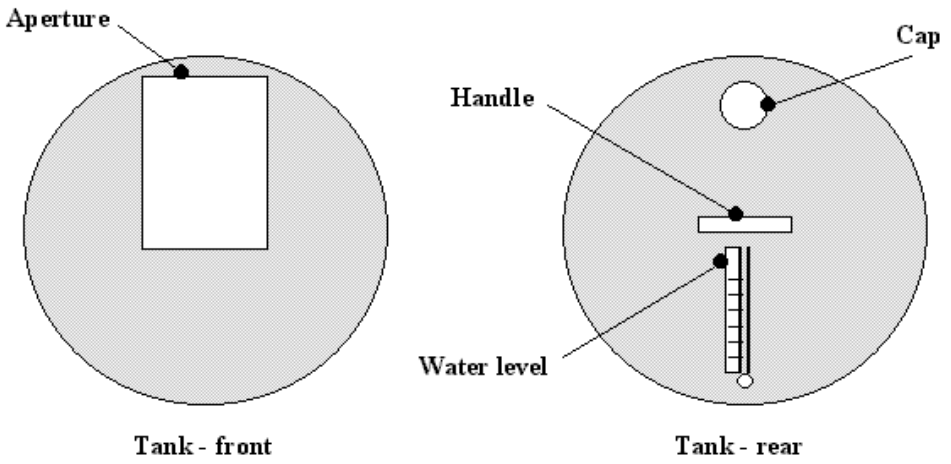

Figure A.18: Front and rear view of the tank.

water. A second aperture on the bottom of the cylinder is used to install a water level indicator and to empty the tank. Since the plastic cap is just in front of the RF input, it has been screened with a copper foil ('deflector') and a metallic grill to avoid RF leakage and damages of the cap (Fig. A.19).

A.3.1 Calorimetric measurements

The same principles introduced to dimension the dummy load apply to the calorimetric measurements. The fraction $\eta_{pow} = P_{refl}/(P_{refl} + P_{forw})$ of reflected power, is introduced. The power injected to and reflected from the load is indicated with P_{forw}, P_{refl}. η_{pow} would allow to determine the value of the power injected in the system, P_{inj}. Assuming that all the forward power is absorbed by the load (no transmission losses), is

$$P_{inj} = P_{abs} \frac{1}{1 - \eta_{pow}} \tag{A.8}$$

where P_{abs} is the absorbed power measured experimentally.
Assuming that convection is the dominant loss channel, i.e. $\dot{Q}_{rad} \ll \dot{Q}_{conv}$, in the stationary case the dependence of T_{as} on P_{RF} can be deduced from Eq. A.6:

$$P_{RF} = \delta AC(T_{as} - T_{room}) \tag{A.9}$$

where T_{as} is the asymptotic temperature reached in the stationary regime, and $\delta = (\tau_{dc} + \tau_{RF})/\tau_{RF}$ is a factor that takes into account the pulsed behaviour of the source. τ_{dc} is the length of the 'off' period during a shot. The temperature T_{as} can be extrapolated by fitting $T_{sys}(t)$ with

$$T_{sys}(t) = T_{as}(1 - e^{-\alpha t}) \tag{A.10}$$

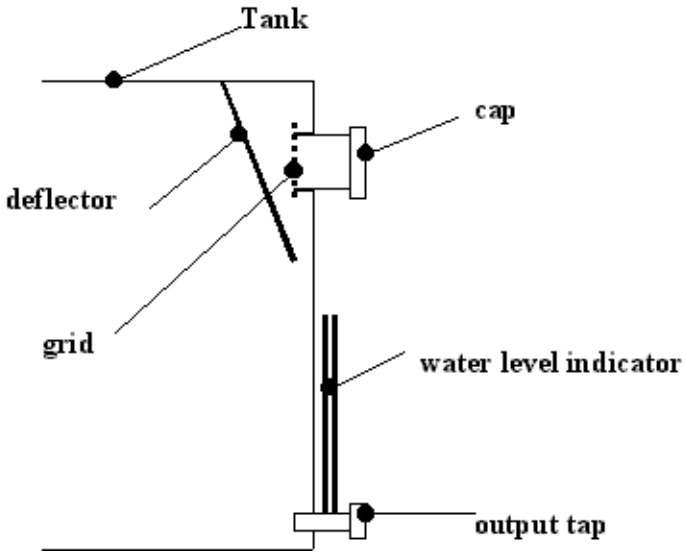

Figure A.19: Side view of the tank, rear-end.

The parameter α depends on load geometry, convective heat-transfer coefficient, amount of water, etc. . In practice, it should be equal to the coefficient A in Eqs. A.6 and A.9. The coefficient A can be deduced more accurately from the decaying part of the curve in Fig. A.17, where

$$\dot{T}_{sys}(t) = -A(T_{sys} - T_{room}) \tag{A.11}$$

so that the curve $T_{sys}(t)$ is fitted by

$$T_{sys}(t) \sim e^{-\gamma t} \tag{A.12}$$

By setting $A = \gamma$ in Eq. A.9, $P_{RF} = P_{abs}$ and then P_{inj} is obtained from Eq. A.8. This method is preferable, since there are no sources of errors due to the presence of the pulsed RF source. Note that the value of P_{RF} could also be inferred from the slope of $T_{sys}(t)$ in the initial phase of the discharge. In this case the assumptions made to derive Eq. A.6 may break, and a high precision in the measurements is required. Therefore, this latter method could be of practical interest only if h_c is so low that $T_{as} \gg T_{cr}$ when $P_{RF} \simeq P_{RF}^{max}$.
It should be noted that the fraction η of power coupled into the load from the transmission line should not change significantly to make the procedure presented above valid. Since all the parameters that influence the impedance of the load are constant during the experiment, this requirement should be fulfilled without particular problems. Nevertheless, it is better to check that the stationarity of η, i.e. $\eta \approx \eta_{aver}$, before accepting and storing the measured values.
A flow-chart of the procedure used to measure P_{inj} is presented in Fig. A.20.

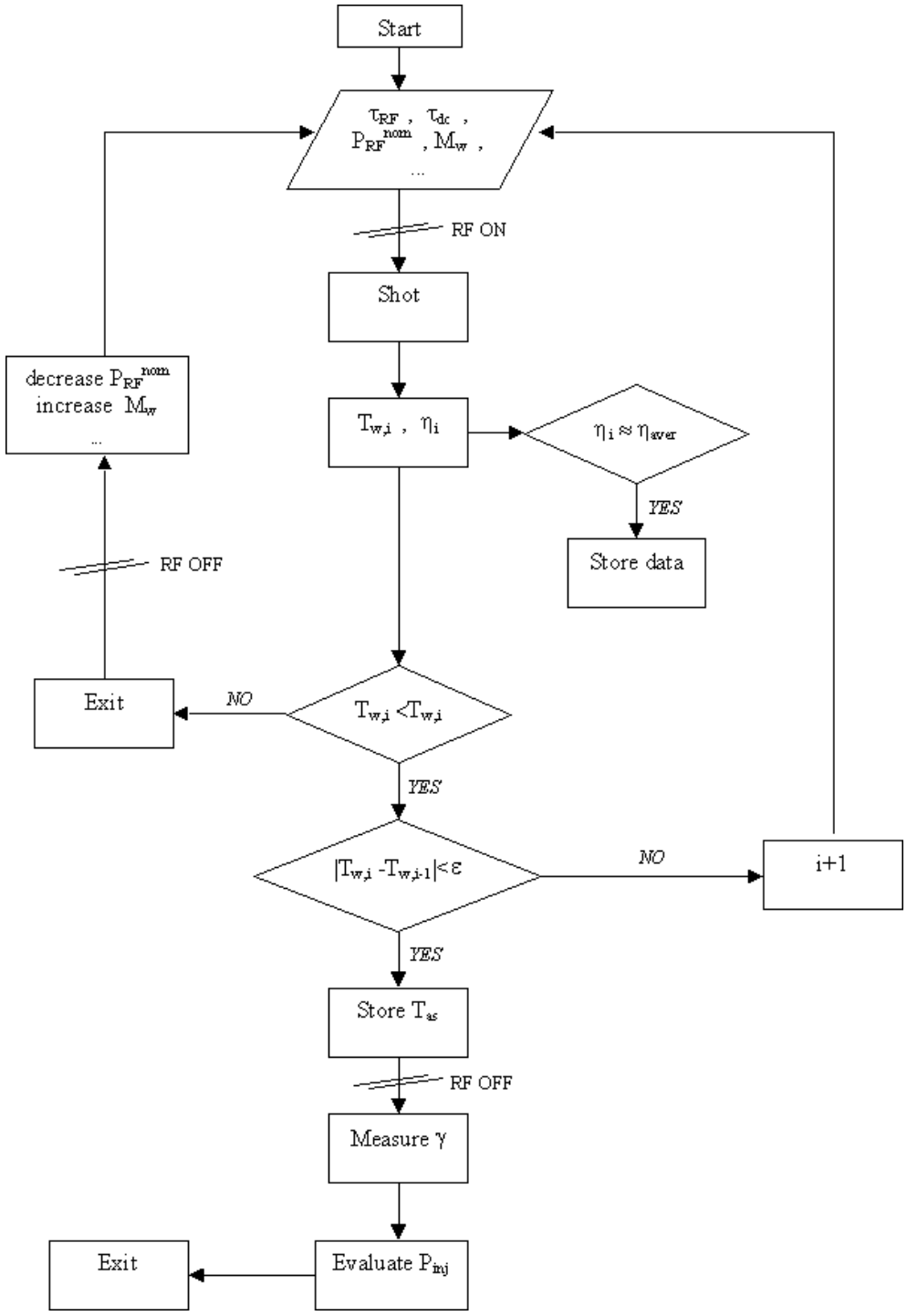

Figure A.20: Procedure proposed to measure the injected power P_{inj}.

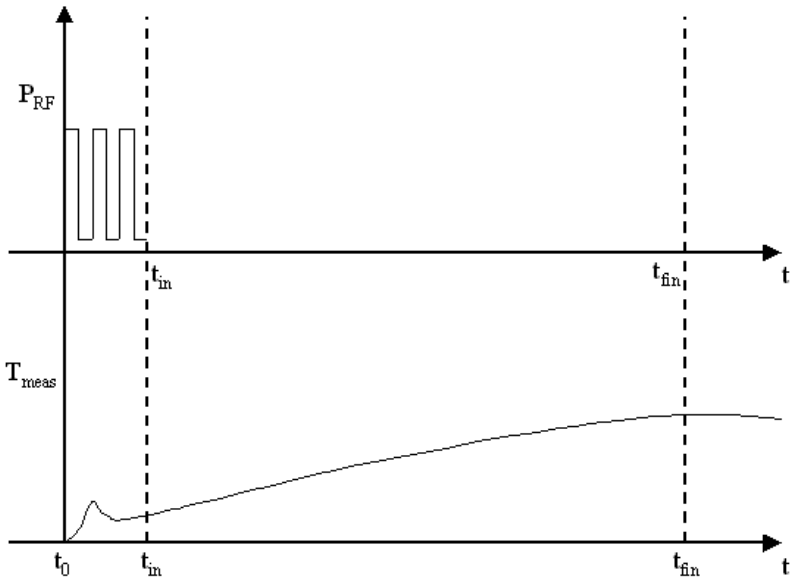

Figure A.21: Typical sequence observed during the tests. The RF power is on from t_0 to t_{in}. The temperature continues to grow also after P_{RF} is turned off.

In practice, an alternative method for estimating the power absorbed by the load might be preferable. A typical sequence observed during the tests is shown in Fig. A.21. It is observed that, during the injection of the microwave power, the measurements are affected by a high noise level. Therefore, it would be preferable to infer P_{abs} from the behaviour of T_{sys} after the discharge. From Eq. A.6, neglecting the effects of radiative losses, is

$$\dot{T}_{sys}(t) = -A[T_{sys}(t) - T_{room}] + \frac{P_{abs}(t)}{C} \tag{A.13}$$

The losses during the discharge are assumed to be negligible. The power P_{abs} absorbed by the system determines an increase from $T_{sys}(t_{in})$ to $T_{sys}(t_{fin})$. At the same time, power is dissipated by convection. An upper limit, t_{fin}, can be chosen as the time where T_{sys} is equal to its maximum. The energy balance equation reads

$$\int_{t_0}^{t_{in}} P_{abs}(t) k_{dc} dt = \int_{t_{in}}^{t_{fin}} C[\dot{\xi(t)} - A\xi(t)]dt \tag{A.14}$$

where a new variable $\xi \doteq T_{sys}(t) - T_{room}$ is introduced. The coefficient $k_{dc} = \delta^{-1} = \tau_{RF}/(\tau_{RF} + \tau_{dc})$ accounts for the pulsed behaviour of the source. To solve Eq. A.14 the time-steps are discretised

$$\int_{t_{in}}^{t_{fin}} \xi(t)dt \approx \sum_{i}^{N} \xi_i \Delta t_i \tag{A.15}$$

where ξ_i are the measured values of ξ, N is the number of samples and Δt_i is the inverse of the sampling frequency ($\Delta t_i \equiv 1$s for the measurements reported herein). Equation A.14 can be integrated and solved for P_{RF}.

$$P_{abs} = \frac{1}{k_{dc}\,\Delta t_0}\{c_{p,w}\,M_w[T(t_{fin}) - T(t_{in})] + h_c\,S_{cyl}\,\Delta t_{meas}\sum_i^N \xi_i\} \tag{A.16}$$

where $\Delta t_0 = t_{in} - t_0$, $\Delta t_{meas} = 1$s and all the relevant physical quantities are written explicitly. Once the values ξ_i are known, the average value of P_{RF} absorbed during the discharge can be estimated. Note that the result does not depend explicitly on the particular form of $T_{sys}(t)$, but only on its initial and final value.

Sensor and data acquisition

The range of temperature of interest, $0 \leftarrow 100$°C, is covered by the PT100 family of sensors. The PT100 is a resistor whose resistance, R_{sens}, has a linear dependence on the temperature[11]:

$$R_{sens}[\Omega] = .385T[^\circ C] + 100.09 \tag{A.17}$$

The offset due to a finite resistance of the wires connecting the sensor to an instrument (ohm-meter, multimeter, ...) must be also taken into account during the tests. A constant-current source allows to measure the value of R_{sens} with a digital multimeter, connected to a PC via a RS232 interface for data acquisition. A Matlab routine has been developed to acquire, store and analyse the data following the procedure illustrated in Fig. A.20.
The current flowing through the PT100 must be limited to $5mA$. A voltage of a few hundreds of millivolts develops across the sensor. The resolution of the multimeter used in the tests (model METEX M-3660D) is $\pm 0.1mV$, corresponding to $\pm.1\Omega$ and, finally, $\pm.19^\circ C$ of accuracy on the measured temperature. A simple solution is to measure directly the value of R_{sens} with a ohm-meter, so that the current source is no more necessary and the apparatus is simplified.
The RS232 interface has been successfully tested for a cable length of 10m. Its low baud-rate allows a maximum sampling rate of approximately 3Samples/s. During the measurements a sampling rate of 1Sample/s, which gives a sufficiently high temporal accuracy. The reacting time of the PT100 sensor, τ_{reac}, should be lower than the maximum possible sampling period. This requirement is fulfilled by the model used herein, for which $\tau_{reac} = 120$ms.

Measurements of h_c

The results of the measurements of h_c without RF power are presented in Fig. A.22. The tank is filled with 5l of water at ≈ 30°C and the time evolution of T is measured.

[11]Standard IEC/DIN/EN 60 751-2 RTD

The shielding metallic grid is removed during these measures. The room temperature is $T_{room} = 18°C$.
The PT100 sensor is encased in a small aluminum holder glued on the bottom of the tank. A thin layer of thermo-conducting grease between the sensor and the aluminum walls ensures an 'ideal' contact and an efficient heat transfer. The sensor is connected to a multimeter, which acquires the values of R_{sens}. The data is acquired via a RS232 interface on a PC and stored for the analysis.
From Fig. A.22 it can be seen that during the initial phase, when the tank is still at room temperature, the heat conduction along the aluminum walls plays an important role. The slope of the curve is higher than in the second part, from $t = 1500$s to the end, where the shape is well fitted by a simple exponential, cfr. Eq. A.12. Two fits are shown, spanning over the entire time range and from $t = 1500$s to the end. The values of h_c extrapolated from the two curves are $6\text{W/m}^2\text{K}$ and $5.4\text{W/m}^2\text{K}$. These measurements suggest that neglecting the role of conduction could lead to errors, but the practical effects are not dramatic until the power is absorbed almost completely by the water, rather than by the aluminum walls.

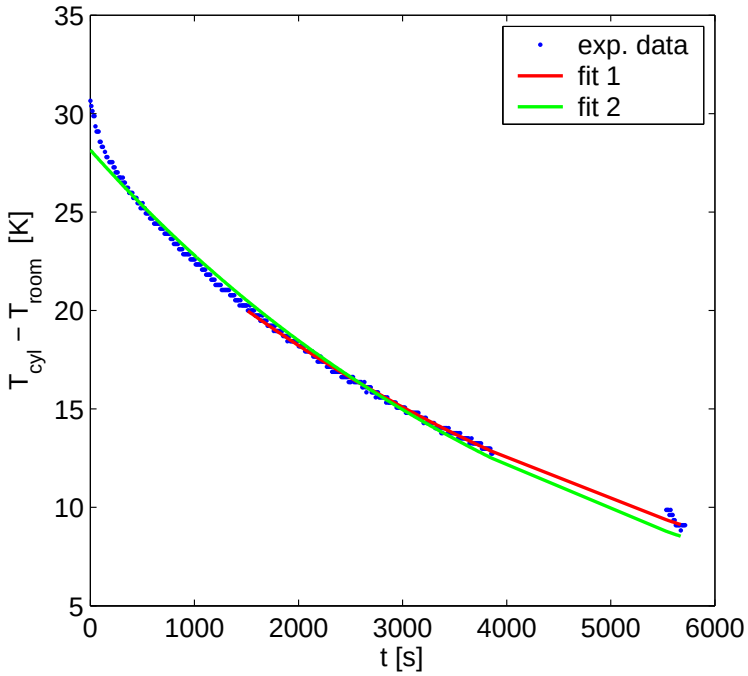

Figure A.22: Measurements of the convective coefficient, h_c. The dots represent the experimental data, and the two lines are two different fits. The parameters can be found in the text.

Results of the tests

A first series of tests are carried out to estimate the RF power delivered by the source and, possibly, optimise the construction of the dummy load. A small RF antenna, connected to a spectrum analyser and to an oscilloscope, is mounted inside the tank. The attenuation of the signals is $-20dB$ and $-10dB$, respectively, to reduced the power at the input of the electronics. The amount of injected power, read on the Control Panel of the microwave generator, is taken as a reference for the instantaneous power fired into the load, which has to be compared with the results of the calorimetric analysis. The measure of the reflected power is not available.
Several observations emerge from these tests. First, it is necessary to ensure a common ground for RF perturbations for all the components (transmission line, tank, shielding box). When the grid and the tank are electrically floating, e.g. due to 'bad' electrical connections or ground not present[12], the noise on the measured signals makes the measurements meaningless. The effects of RF fields on the accuracy of the PT-100 are also not clear.
Second, it is observed from the tests that the simple method explained in Section A.3.1 is hardly applicable. In fact, the coupling between the waveguide and the tank changes considerably during the discharge. Moreover, the thermal inertia of the load makes the temperature increase after the discharge, probably because of the heat redistribution inside the water takes place on a long time scale. This can be due to a localised power deposition, and subsequent redistribution via heat diffusion and convection inside the volume of water. Finally, the heat is transmitted to the aluminum walls and from there to the PT-100 sensor, which is mounted on the outer surface of the tank.
For all these reasons, the second method illustrated in Section A.3.1 is used for the analysis. An example is shown in Fig. A.23. The nominal value of injected power is $P_{RF} = 10\text{kW}$, with $t_{on} = 10\text{ms}$ and $t_{off} = 40\text{ms}$. The length of the discharge is approximately 60s. In this case, the estimated value of RF absorbed power is $P_{abs} \approx 4\text{kW}$. Note that the experimental curve does not reach its saturation value, thus the power could be underestimated. The order of magnitude agrees well with the nominal injected power, considering that $\approx 40\%$ of power matched from the transmission line to the load is a realistic assumption.

[12]Note that a simple, thin cable connecting the metallic structures to ground may not provide a sufficiently low impedance to ground for the high frequency microwaves.

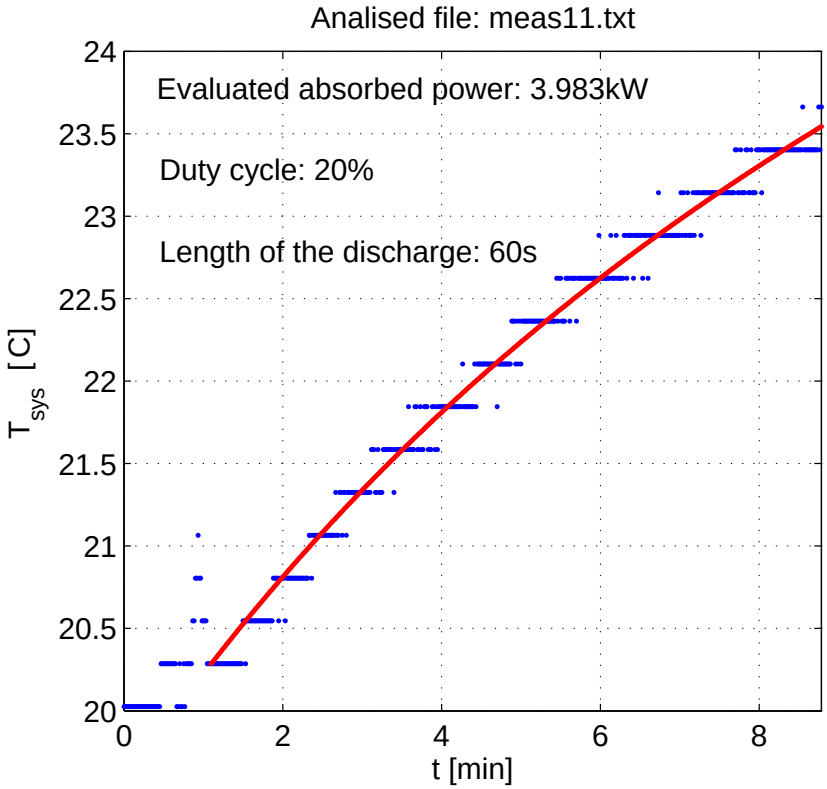

Figure A.23: Result of the calorimetric analysis based on Eq. A.16. The nominal injected microwave power is 10kW, in agreement with estimated absorbed power of $\approx$ 4kW if a coupling efficiency of 40% between the transmission line and the tank is assumed.

Appendix B

Analysis of Langmuir probe data

B.1 Semi-automatic analysis of Langmuir probes data

Typically a Langmuir probe (LP) provides two signals, the voltage applied and the current drawn by an electrode (tip) inserted into the plasma [47][97][17]. There are three possible modes of operation:

- *Saturation current mode.* The tip is biased to a sufficiently negative (positive) voltage compared to the plasma potential. The ion (electron) saturation current, I_{sat}, is measured, with $I_{sat} \propto nT_e^{1/2}$, where T_e is the electron temperature. For electron temperature fluctuations negligible with respect to density fluctuations, the ion saturation signal is simply assumed to be $\propto n$, and provides information on the density. The time resolution depends on the acquisition frequency. No information on the electron temperature and the plasma potential can be deduced.

- *Floating mode.* The tip is electrically insulated from the ground, or in practice connected to it only through a very large resistor, so that the measured tip potential, V_{fl}, depends only on the local values of plasma potential and electron temperature. V_{fl} is ideally given by $V_{fl} = V_{pl} - \mu\, T_e/e$, where the coefficient μ depends on gas type, magnetic field and tip geometry (see Sec. B.2). The time resolution depends on the acquisition frequency.

- *I-V characteristic mode.* The tip voltage, V_{pr}, is swept at a frequency f_{sw} over an appropriate range and the resulting current I is measured. The relation

$$I(V_{pr}) \approx I_0 \left[1 - e^{\frac{V_{pr}-V_{fl}}{T_e/e}}\right] \tag{B.1}$$

  with

$$I_0 \approx \frac{1}{2}\, q\, n \sqrt{\frac{T_e}{m_i}}\, A_{eff} \tag{B.2}$$

  is called the 'characteristic' of the probe, and depends on the values of plasma density, plasma potential and electron temperature. Here q is the elementary charge, m_i the ion mass and A_{eff} the effective tip surface [47]. The three parameters can be determined at the same time, with a maximum time resolution corresponding to half-period of the sweeping frequency. On TORPEX, f_{sw} is usually $\leq$ 1kHz, which gives a maximum time resolution of 500μs.

The mode of operation is chosen before the shot, depending on the quantities of interest and the required time resolution.
The raw data is stored in a MDS-plus structure after each discharge. To *analyse* it, a number of operations must be carried out, such as conversion into physical

units, correction for offsets and noise introduced by the electronic modules. A semi-automatic analysis procedure has been developed to process the data from Langmuir probe[1].
The procedure followed to perform the analysis is summarised in Fig. B.1. The main inputs are the lists of shots and channels to analyse. Other parameters, such as the probe tip surface, the gas type and the time interval of interest can be introduced. For each shot, the injected microwave power signal is loaded to determine the time window at the end of the discharge from which the electronic noise and offset is evaluated. The current and voltage signals are loaded for each channel, and corrected for noise and offset. Their general features, e.g. the presence of a sweeping voltage, are analysed to determine the specific type of analysis that must be performed. Depending on the analysis type, different subroutines are called and the signals analysed. The output can be directly passed to other routine for further analysis or stored into the MDS database. In the latter case, the results are compressed and stored into the tree structure as analysed data under the branch 'ANALYSIS.TCPIP.dt003'. They can be accessed by using the *tdi* command with tags $\backslash dt\_03\_chn$: followed by ne, Te, $Vfloat$, $tdecay$. A 'log' file, containing the analysis parameters and the eventual comments and warnings, is stored into the field $config$. The different steps of the analysis can be visualised during the analysis with specific debugging tools, as shown in Fig. B.2 for the case of a probe operating in the I-V mode.

A practical example

The easiest way to analyse a set of data is to call the main routine with the shot and channel numbers as input, for example:
Res=LP_analysis(1240, 23);
where 1240 is the shot number and 23 is the channel where the current signal from the first tip of the movable probe SLP was acquired. The results of the analysis are stored as *data* entries in the structure *Res*, with fields *n*, *Te*, *Vfl* and *time*:
Res.n.data
Res.Te.data
Res.Vfl.data
Res.time.data
If the probe is in the ion saturation mode of operation, an additional field, *Res.tdecay*, contains the estimation of the density decay time (see Sec. 7.3). The routine determines τ_{dec} for each on/off cycle of the injected power. If there is a modulation of the power, a value of τ_{dec} for each value of t_{off} is computed. The average τ_{dec} is also stored, conventionally referred to $t = -111$ms. A value $\tau_{dec} = -1$ is stored when the estimation of τ_{dec} fails.

[1]The routine package can be found under *crpppc154/home/torpex/matlab/LP_analysis*.

The routine can be called with vectors as input for both the shot and the channel numbers. In this case, the resulting structure has the form (e.g. for the temperature): *Res(j).Te(k).data*, where the index j runs over the shot list and k over the channel list.

Options

It is possible to control different options of the routine. All the options are passed as (*Opt, Val*) pairs[2]:
Res=LP_analysis(shotno, channo, Opt1, Val1, Opt2, Val2, ...)
Most of the options can only assume the values 0 (disabled) or 1 (enabled). The available options are:

- *tmin, tmax*, allows you to define the time window chosen for the analysis. Default: $(-5ms, 120ms)$
- *time_select*, if =1 overwrites the selected time window if it doesn't include any portion of the plasma phase. This option is normally active
- *nper*, define the number of half-periods taken to average the I-V curve. Default is $nper = 3$
- *overlap*, if =1 the I-V curve analysis is performed every half-period, otherwise the time step is defined by *nper*. Default is $overlap = 0$ (disabled)
- *aver*, if =1 the data are smoothed before the analysis
- *shunt*, value of the shunt (sensitivity of the current measurement). Usually its value is automatically loaded from the MDS tree
- *tip_area*, collecting area of the tip. The default is a cylindrical tip with radius $r = .45mm$ and length $l_{tip} = 5mm$
- *an_type*, if =-1 the type of analysis is automatically determined, otherwise the routine can be forced to perform a chosen analysis. Possible values are -1 (automatic, default value), 1 (I-V curve), 2 (I_{sat}) and 3 (V_{fl})
- *rem_noise*, if =1 removes from the current signal the 'deterministic' components of the noise due to the sweeping voltage. Is active by default
- *gas*, type of gas injected during the shot (Ar or H). Default is Ar
- *min_t_res*, minimum time resolution for the results of I_{sat} and V_{fl} analysis. Default is $min\_t\_res = .5ms$

[2] *Opt* is a string, *Val* can be either a string or a number

- *sm_numb*, number of points used to smooth the output. The default value is $sm\_numb = 5$
- *shotno_rem*, number of the shot taken as reference to remove the noise. If empty, the actual shot is taken as reference
- *Te_ext*, value of the electron temperature used for the I_{sat} analysis. The default value $T_e = 5eV$.
- *tau_range*, time window used for the estimation of τ_{dec}. Default value is $3ms$
- *showfit*, if =1 shows the result of each fit (debug mode)
- *showres*, if =1 shows the final result of the analysis (debug mode)
- *write_to_tree*, if =1 write the output data to the MDS tree
- *overwrite_tree*, if =1 force the routine to overwrite the data already stored in the MDS tree
- *log_file*, if =1 all the information from the data analysis process are stored into a text file 'LP_fit.txt' in the current directory. It can be a useful tool to verify the success of the analysis

For each tip the analysis is performed on both the current and the voltage signals. The results of the analysis are stored in the MDS tree under the node that corresponds to the channel signal for that particular probe.

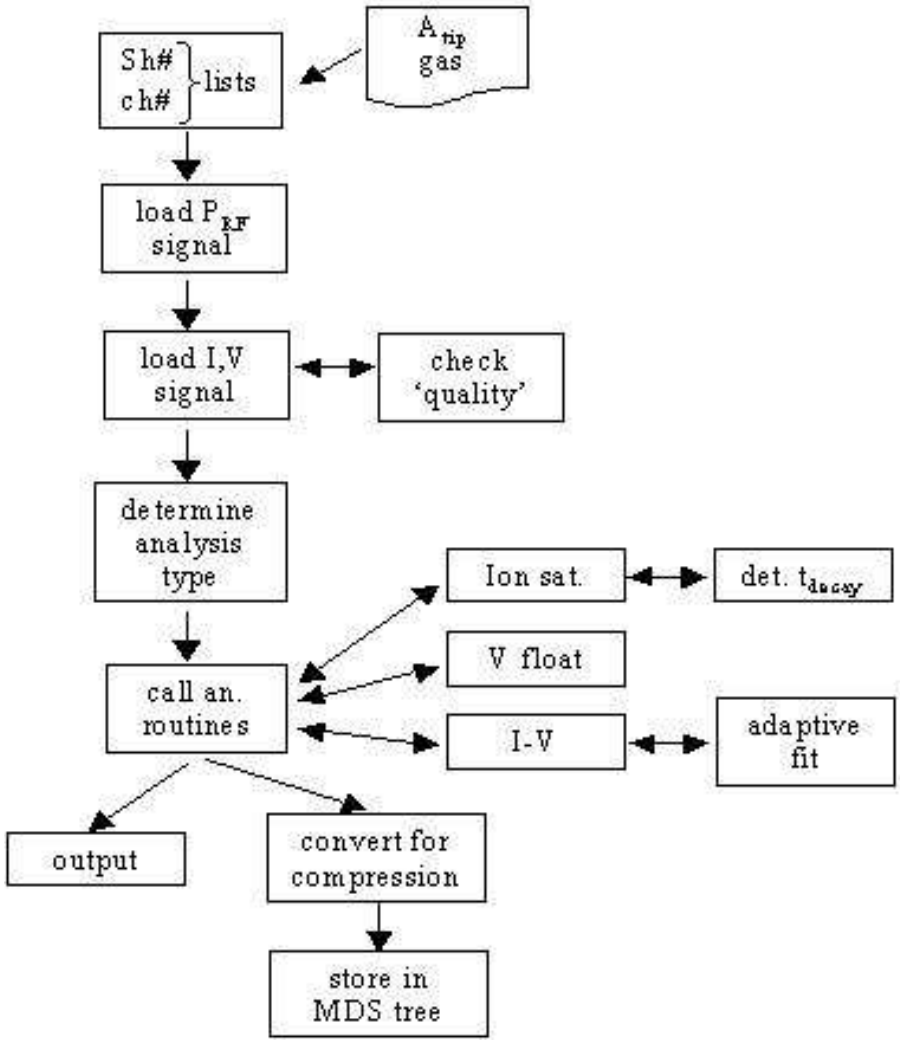

Figure B.1: Procedure used for the semi-automatic analysis of LP data.

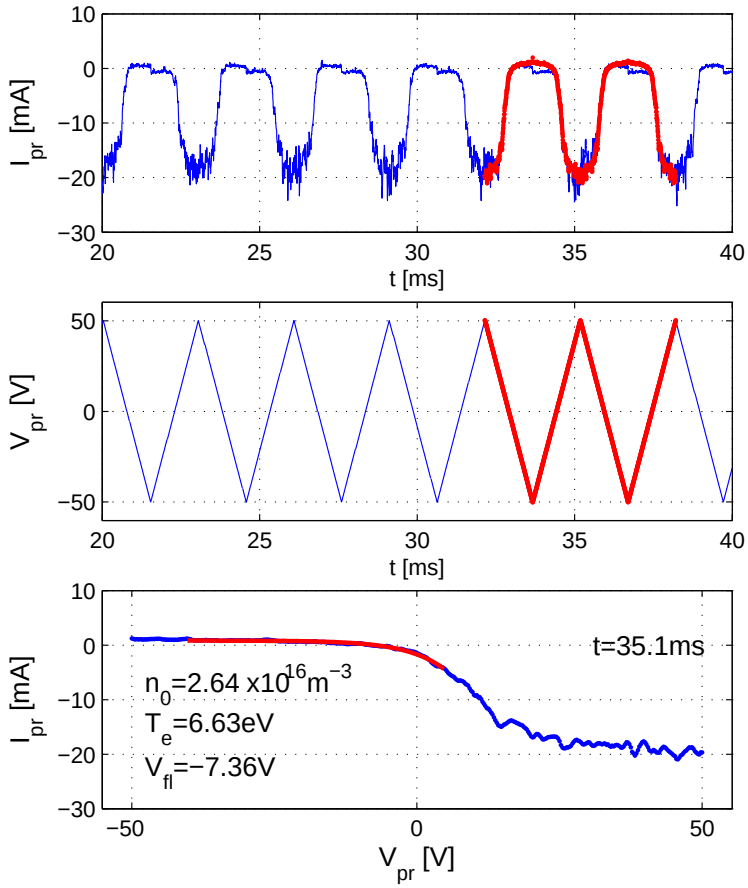

Figure B.2: Example of fit of I-V curves.

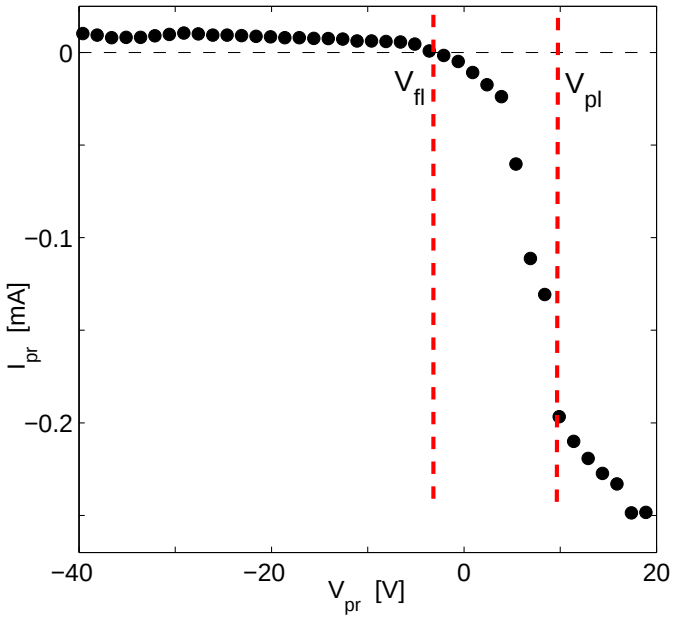

Figure B.3: Example of a current-voltage characteristic from a Langmuir probe. The floating and plasma potential are highlighted by the red dashed lines.

B.2 Measurements of the plasma potential

The plasma potential, V_{pl}, is an important quantity for a complete experimental description of plasmas. When electron and ion temperatures are low, V_{pl} is usually measured by means of Langmuir probes. However, a direct measurement of V_{pl} is not trivial. The use of dedicated techniques, such as the use of emissive probes, is well documented (see, for example, Ref. [22] and references therein). However, the proposed methods imply considerable complications in the probe and/or electronics design, and are rarely applied in practice.

This Section describes the method used on TORPEX to calculate V_{pl}. Since data from swept Langmuir probes are needed, the maximum temporal resolution is $\leq 500\mu$s (see Appendix B.1) and the method can not be used for studying fluctuations in V_{pl}.

In principle, V_{pl} can be identified as the value for which the current-voltage (I-V) curve shows an inflection point before the electron current, I_e, saturates (Fig. B.3). In practice, the increased range of the sweeping voltage required to reach V_{pl} implies a more complex electronics and slow sweep frequencies, in order to preserve a sufficient number of experimental points for each I-V curve. Moreover, I_e does rarely show a clear saturation and probes drawing a large electron current can burn. Thus the probe voltage, V_{pr}, is usually kept well below V_{pl}.

However, the plasma and floating potentials are related by [47][17]

$$V_{pl} = V_{fl} + \mu \frac{T_e}{e} \tag{B.3}$$

where

$$\mu = log\left(\frac{A_e}{A_i} \sqrt{\frac{2m_i T_e}{\pi m_e \left(T_e + \gamma T_i\right)}} \right) \tag{B.4}$$

Here A_e, A_i are the *effective* collection surfaces for electrons and ions, $m_{e,i}$ and $T_{e,i}$ electron and ion mass and temperature and γ the adiabatic index. The problem of evaluating V_{pl} reduces to the determination of μ, which depends on the gas type, the magnetic field and the probe geometry. From Eq. B.4, the terms containing probe geometry can be separated from those depending on plasma parameters:

$$\mu_G = log\frac{A_e}{A_i} \qquad ; \qquad \mu_T = log\sqrt{\frac{2m_i T_e}{\pi m_e \left(T_e + \gamma T_i\right)}} \tag{B.5}$$

In the limit $T_i \ll T_e$, and for small spatial variations of the magnetic field, μ reduces to a constant for each specific probe.
The coefficient μ could be directly estimated from Eq. B.4, but important errors might be introduced by a inaccurate evaluation of A_e, A_i and γ. Instead, if the plasma and the floating potential can be measured for different values of T_e, then μ can be estimated experimentally:

$$\mu = \frac{d\widetilde{V}(T_e)}{dT_e} \tag{B.6}$$

where $\widetilde{V}(T_e) = V_{pl} - V_{fl}$. This evaluation of μ may give inaccurate results if additional terms have to be added to the right hand side of Eq. B.3. This is the case, for example, if suprathermal electrons are present. Fast electrons can introduce an effective offset voltage ΔV, independent of T_e [100], and Eq. B.3 becomes

$$V_{pl} = V_{fl} + \mu \frac{T_e}{e} + \Delta V \tag{B.7}$$

Note that $V_{fl} \neq V_{pl}$ for $T_e \to 0$, therefore the value of μ from Eq. B.6 would be overestimated by an additional term $e\Delta V/T_e$. To reduce the error, the histogram of the experimental values, μ_i, is fitted with a gaussian. μ is set equal to the mean value, $\mu =< \mu_i > \pm\sigma(\mu_i)$, where σ is the full-width at half maximum. The μ obtained in this way is less sensitive to errors due to a fast electron component, which mostly contribute to the tail of the gaussian and do not affect the fit of the bulk. As a drawback, the possible dependence of μ on T_e is lost.

The method described above is used to characterise TORPEX probes[3]. Examples for the SLP and GLP probes are shown in Fig. B.4 for the two gases commonly in use, viz. Argon and Hydrogen. The results for the probes used to estimate V_{pl} are summarised in Tab. B.1.

probe	*Hydrogen*	*Argon*
SLP	3.1 ± 0.6	4.4 ± 0.3
HEXTIP	2.5 ± 0.4	2.5 ± 1
GLP	2.1 ± 0.5	3 ± 0.9
Tweedy	$1.6 \pm .6$	3.6 ± 0.6

Table B.1: Summary of the results of the experimental determination of μ for different probes installed on TORPEX. The coefficient μ is given in the form $\mu =< \mu_i > \pm\sigma(\mu_i)$. Values for HEXTIP are also given, although no measurements of V_{pl} are not routinely available from that probe.

[3]Another possibility would be to fit the data with Eq. B.7 and estimate both μ and ΔV. However, the increased number of parameters makes this approach slower and less practical, especially if the term ΔV varies in space.

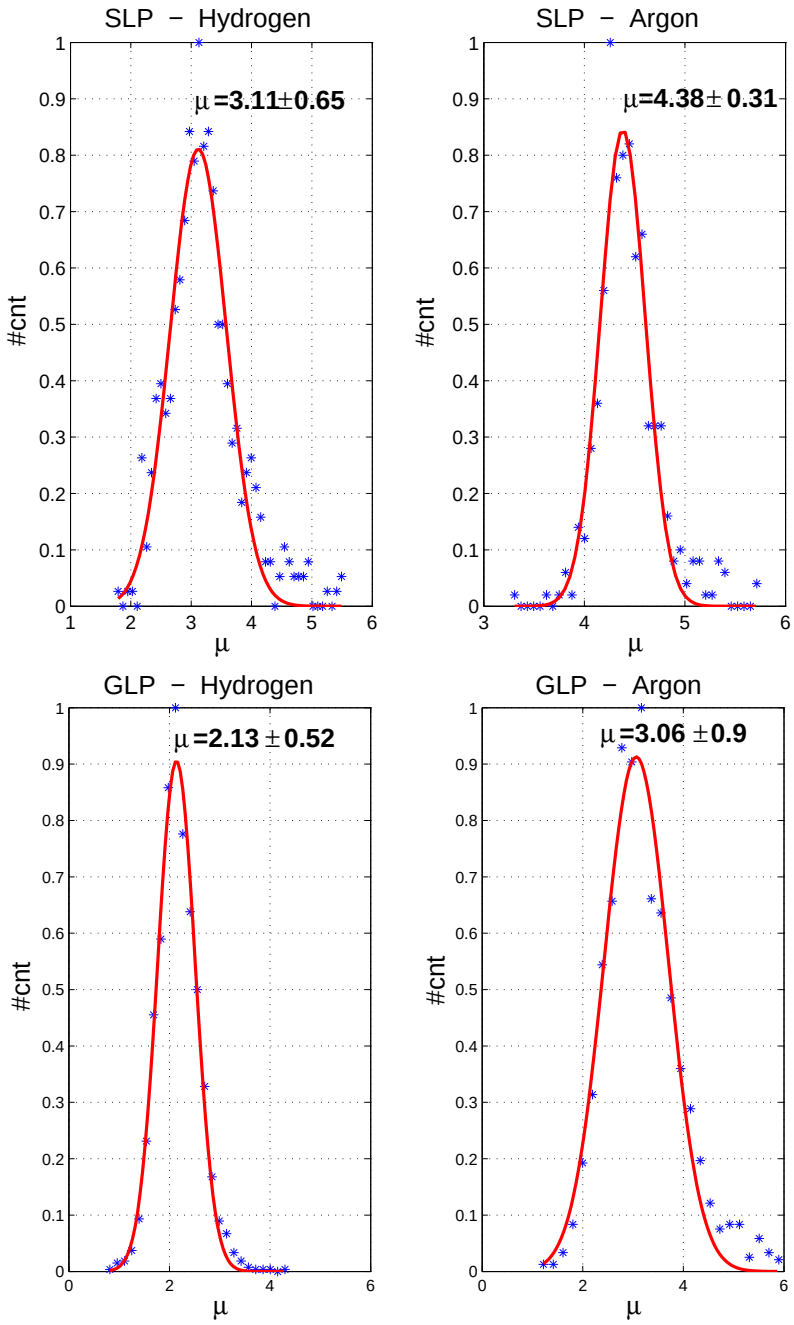

Figure B.4: Histograms of the measured values of μ for the probes SLP and GLP. The number of counts, $\#cnt$, is normalised to unity. Note the asymmetry of the distributions and the high tails for $\mu \gg < \mu >$, due to fast electrons.

Appendix C

Particle source, a simple Monte Carlo code

A simple numerical code, based on a Monte Carlo (MC) approach, has been developed with the goal of providing information that could not be easily verified experimentally, cfr. Chap. 5. The main questions to answer are:

- What is the ionisation profile, as a function of the density profile and of other parameters, such as the vertical magnetic field amplitude and the neutral gas pressure?
- How does the ionisation profile depend on the particular shape of the electron distribution function?
- Can we evaluate the ionisation efficiency?
- Can we derive a semi-empirical expression for the spatial profile of the particle source, based upon the experimental results and the results of the code?

C.1 Survey of physical processes and their implementation in the code

- From the plasma density profile we can evaluate the positions of the EC and UH resonances, where $f_{ec} = f_{rf}$ and $f_{uh} = f_{rf}$. These positions are the starting points for the N_{tr} primary electrons.
- The initial energy, E_{fast}, is randomly extracted from distributions such as maxwellian or constant.
- The initial directions with respect to the magnetic field, γ_i $(i = 1, 2, ..., N_{tr})$, are randomly extracted from an isotropic distribution.
- The particles are supposed to travel mainly along the field lines. The effects of the single-particle ∇B and curvature drifts are included by introducing an additional vertical displacement during the motion of the electron along $\mathbf{B}$. No other drifts are taken into account.
- The perpendicular and parallel energies of the test electrons change due to Coulomb collisions at the rate $\nu_{\parallel,\perp}$. This process is not treated with MC rules. The evolution of parallel and perpendicular energies is calculated along the possible vertical path. If there is possible change in the direction γ, the electron path is restricted to the values of y for which the parallel velocity does not change its sign. The values of $E_{\parallel,\perp} = E_{\parallel,\perp}(y)$ are then used to evaluate the ionisation and scattering cross sections.

Note that in a MC code a correct treatment of scattering processes from ions and electrons should start from the kinetic theory, with a Focker-Planck expression for the collisional term. This treatment is not implemented in the code.

- The energy lost by the primary electrons during their motion inside the chamber is negligible compared to the initial energy.

- Three types of interaction are considered: ionisation, scattering from neutrals, scattering from ions and electrons.

C.2 Scheme of the code

First, the main parameters of the system are set, including B_φ, B_z, N_{tr}, the energy of the primary electrons E_f and the background plasma profiles. Second, each primary electron of the initial population evolves iteratively, according to the following scheme:

1. The set of parameters $\{y_i, E_i, \gamma_i\}$ are used to determine the 'possible' path of the electron, from y_i to the wall (at y_{max}), upstream or downstream with respect to $\mathbf{B}$ depending on the sign of γ_i. A new variable s is introduced, to take into account the effective length of the path, equal to the projection of the vertical displacement along the field lines.

2. The evolution of $E_{\parallel,\perp}(y)$ is evaluated, for each reachable y. If there is a change in the sign of γ_i, this point is taken as y_{max}.

3. The cross sections σ_{iz}, σ_{sc}^{gas} are evaluated for $y \in (y_i, y_{max})$.

4. The interaction location and the type of event are chosen.

5. Depending on the interaction, the parameters $\{y_i, E_i, \gamma_i\}$ are updated to $\{y_i', E_i', \gamma_i'\}$.

6. If the event is the ionisation of a neutral, a new particle with parameters $\{y_k, E_k, \gamma_k\}$ is added to the population. The position and the time-of-flight of the ionising particle are stored in a record as a 'ionisation location' and 'time'. They will be used to evaluate the average ionisation rate as a function of y.

7. If $y_i' > a$ (a is the minor radius of the vessel) the particle is lost.

8. If E_i' (or E_k) are smaller than W_i, the history of this particle ends. Its actual position, energy and total time of flight are stored in a record as a 'thermalisation location'.

9. If $y_i' < a$ and $E_i' < W_i$, the procedure starts again from point 2.

Since most of the particles are lost in a few steps, a refinement, known as *biased sampling*, of the 'brute-force' MC method proposed here could be introduced to force them to collide inside the chamber. Their relative weight w_i in the final score is then conveniently reduced. The 'life' of a particle ends when w_i is lower than a given value (ex. $w_i^{min} = 10^{-4}$, the initial value being $w_{i,0} = 1$).

C.3 Examples of the results of the code: ionisation profile

The most urgent question related to the plasma production processes is the identification of the particle source profile. The subject has been treated in Chap. 5, where a combined analysis of the experimental results and of the results of the simple code is attempted. Further examples of the results of the code on this subject are shown below, in Figs. C.1 to C.4.

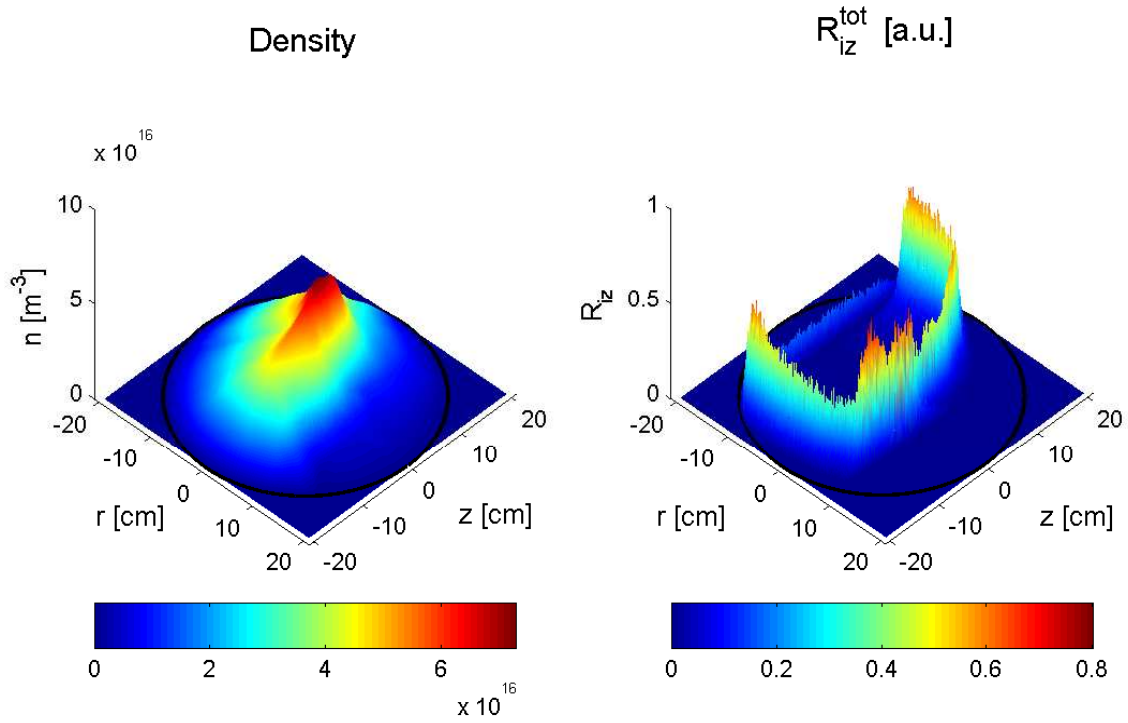

Figure C.1: Density profile for Hydrogen plasma (*left*) and reconstructed two-dimensional spatial profile of the particle source in a poloidal cross-section (*right*). The injected microwave power is 400W. The currents in the toroidal and vertical magnetic field coils are $I_{tf} = 380$A and $I_{vf} = 60$A, corresponding to $B_\varphi = 76$mT on the axis and $B_z = 1.2$mT.

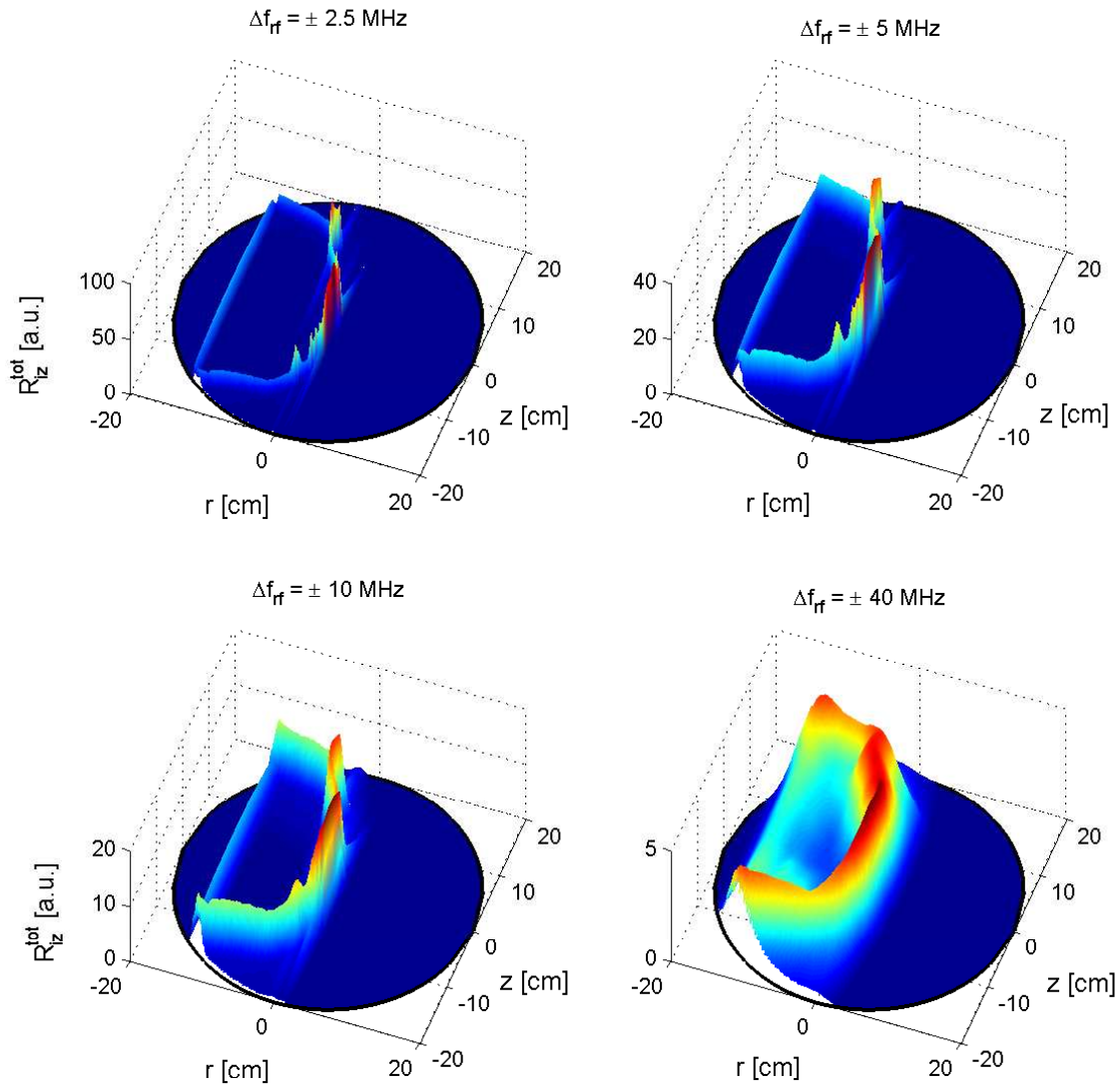

Figure C.2: Reconstructed spatial profile of the particle source for different values of the bandwidth of the injected microwaves, Δf_{rf}. Note the broadening of the source profile, due to the mechanisms explained in Chapters 4 and 5. The plasma parameters are the same as in Fig. C.1.

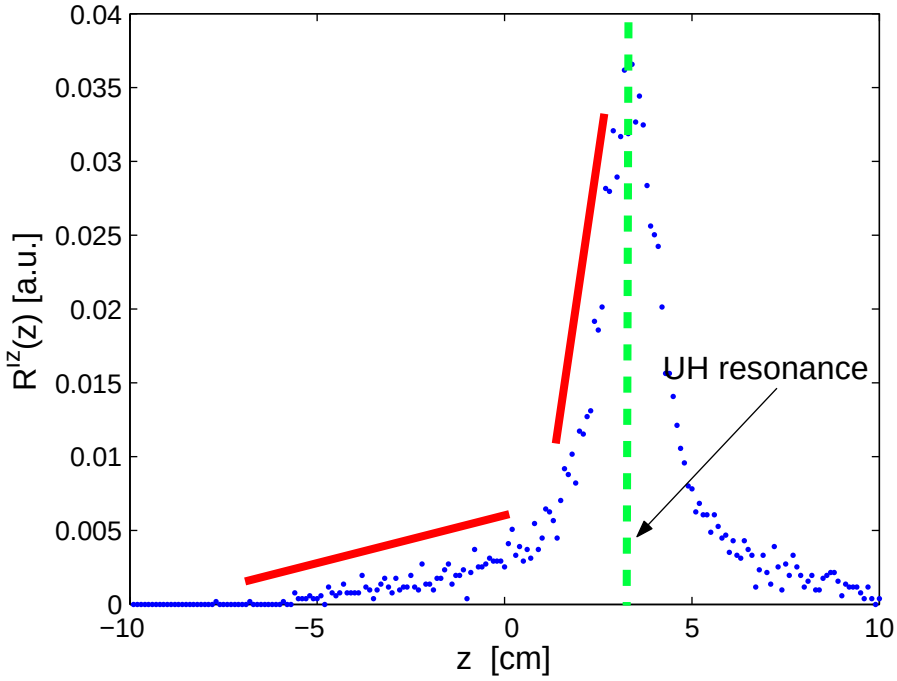

Figure C.3: Vertical profile of the particle source at the UH resonant layer (thick, dashed line), as estimated from the simple code. Note the two slopes of the profile, which are finally included in the semi-empirical analytical expression, Eq. 5.8.

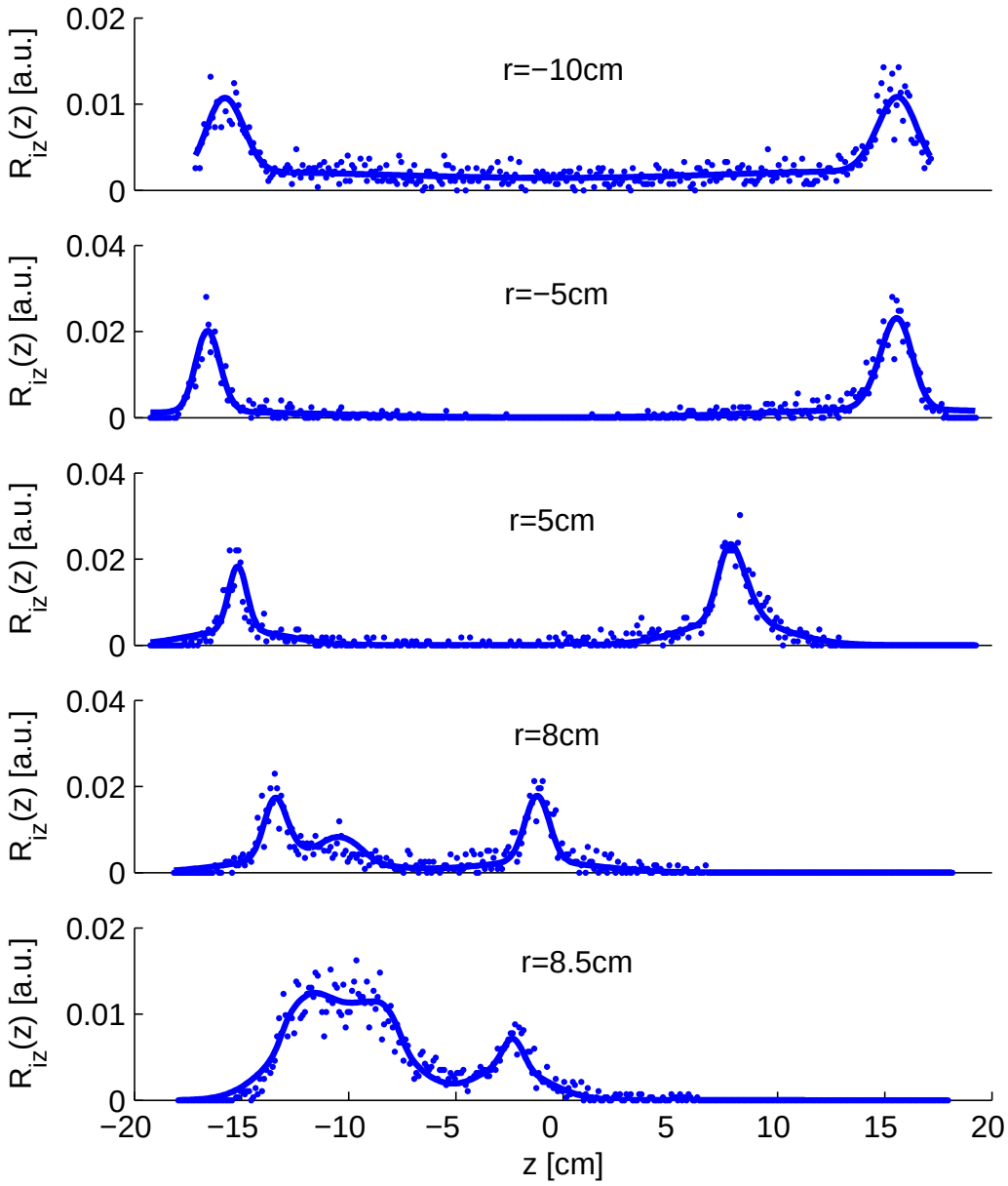

Figure C.4: A detail of the output of the simple code in terms of local particle source (blue points) for the profile shown in Fig. C.1. The continuous line shows the result of a least-square fit based on Eq. 5.9.

Bibliography

[1] G. Y. Antar, G. Counsell, Y. Yu, B. Labombard, and P. Devynck, Phys. Plasmas **10** (2003), 419.

[2] C. A. Balanis, *Anthenna theory: analysis and design*, John Wiley and Sons Inc, New York, 1997.

[3] J. M. Beall, Y. C. Kim, and E. J. Powers, J. Appl. Phys. **53** (1982), 3933.

[4] R. J. Bickerton, Nucl. Fusion **13** (1973), 290.

[5] D. Block, Phys. Scr. **T122** (2006), 25.

[6] J. A. Boedo, D. Rudakov, and R. Moyer et al., Phys. Plasmas **8** (2001), 4826.

[7] M. Bornatici, R. Cano, O. De Barbieri, and F. Engelmann, Nucl. Fusion **23** (1983), no. 9, 1153.

[8] M. Brunmayr, EPFL/CRPP, internal report, 2006.

[9] R. A. Cairns, *Radiofrequency heating of plasmas*, The Adam Hilger series on plasma physics, Bristol, Philadelphia and New York, 1991.

[10] E. Canobbio, Nucl. Fusion **9** (1969), 27.

[11] N. J. L. Cardozo, Plasma Phys. Control. Fusion **37** (1995), 799.

[12] B. A. Carreras, J. Nucl. Mater, **337-339** (2004), 315.

[13] B. A. Carreras, C. Hidalgo, E. Sanchez, and M. A. Pedrosa et al, Phys. Plasmas **3** (1996), 2664.

[14] B. A. Carreras, V. E. Lynch, and B. Labombard, Phys. Plasmas **8** (2001), 3702.

[15] T. Carter, Phys. Plasmas **13** (2006), 10701.

[16] R. Chavan and A. Fasoli, *Bidding documents of the contract for the TORPEX vacuum vessel*, CRPP/EPFL 2002, Ref. TPX - VV.

[17] F. F. Chen, *Plasma diagnostic techniques*, Academic Press, New York, 1965.

[18] S. L. Chen and T. Sekiguchi, J. Appl. Phys. **36** (1965), no. 8, 2363–2375.

[19] S. Coda, M. Porkolab, and K. H. Burrell, Phys. Rev. Lett. **86** (2001), no. 21, 4835.

[20] J. W. Connor and O. P. Pogutse, Plasma Phys. Control. Fusion **43** (2001), 155.

[21] G. D. Conway, B. Scott, J. Schirmer, M. Reich, A. Kendl, and ASDEX Upgrade Team, Plasma Phys. Control. Fusion **47** (2005), 1165.

[22] V. I. Demidov, S. V. Ratynskaia, and K. Rypdal, Rev. Sci. Inst. **73** (2002), no. 10.

[23] A. Diallo, P. Ricci, A. Fasoli, I. Furno, B. Labit, S. H. Müller, M. Podestà, F. M. Poli, and F. Skiff, submitted to Phys. Plasmas (2007).

[24] P. H. Diamond, S-I. Itoh, K. Itoh, and T. S. Hahm, Plasma Phys. Control. Fusion **47** (2005), R35.

[25] J. Egedal, A. Fasoli, D. Tarkowski, and A. Scarabosio, Phys. Plasmas **8** (2001), 1935.

[26] V. Erckmann and U. Gasparino, Plasma Phys. Control. Fusion **36** (1994), no. 12, 1869.

[27] A. Fasoli, *Proposal to the Fonds National Suisse pour la Recherche Scientifique*, 2001.

[28] A. Fasoli, B. Labit, M. McGrath, S. H. Müller, G. Plyushchev, M. Podestà, and F. M. Poli, Phys. Plasmas **13** (2006), 055902.

[29] T. Fujimoto and S. A. Kazantsev, Plasma Phys. Control. Fusion **39** (1997), no. 9, 1267.

[30] I. Furno, A. Diallo, A. Fasoli, B. Labit, S. H. Müller, G. Plyushchev, M. Podestà, and F. M. Poli, 11th EU-US Transport Task Force meeting, 2006.

[31] I. Furno, A. Diallo, A. Fasoli, B. Labit, S. H. Müller, M. Podestà, F. M. Poli, and P. Ricci, submitted to Phys. Rev. Lett. (2007).

[32] O. E. Garcia, Eur. J. Phys. **24** (2003), 331.

[33] O. E. Garcia, J. Horacek, and R. A. Pitts et al., Plasma Phys. Control. Fusion **48** (2006), L1.

[34] O. E. Garcia, V. Naulin, A. H. Nielsen, and J. Juul Rasmussen, Phys. Rev. Lett. **92** (2004), no. 16, 165003.

[35] O. E. Garcia, V. Naulin, A. H. Nielsen, and J Juul Rasmussen, Physica Scripta **T122** (2006), 89.

[36] R. Geller, *Electron cyclotron resonance ion sources and ECR plasmas*, Institute of Physics Publishing, Bristol and Philadelphia, 1996.

[37] V. A. Godyak, R. B. Piejak, and B. M. Alexandrovich, Plasma Sources Sci. Technol. **1** (1995), 36.

[38] J. P. Graves, J. Horacek, R. A. Pitts, and K. I. Hopcraft, Plasma Phys. Control. Fusion **47** (2005), L1.

[39] B. Grek and M. Porkolab, Phys. Rev. Lett. **30** (1973), no. 18, 836.

[40] Y. Hamada, A. Nishizawa, T. Ido, and T. Watari et al, Nucl. Fusion **45** (2005), 81.

[41] G. W. Hammett, M. A. Beer, W. Dorland, S. C. Cowley, and S. A. Smith, Plasma Phys. Control. Fusion **35** (1993), 973.

[42] W. W. Heidbrink, K. H. Burrell, Y. Luo, N. A. Pablant, and E. Ruskov, Plasma Phys. Control. Fusion **46** (2004), 1855.

[43] C. Hidalgo, Plasma Phys. Control. Fusion **37** (1995), A53.

[44] C. Hidalgo, M. A. Pedrosa, E. Sanchez, and B. Gonçalves et al., Plasma Phys. Control. Fusion **48** (2006), S169.

[45] W. Horton, Rev. Mod. Phys. **71** (1999), no. 3, 735.

[46] J. Hugill, Nucl. Fusion **23** (1983), 331.

[47] I. H. Hutchinson, *Principles of plasma diagnostics*, Cambridge University Press, New York, 1987.

[48] I.H. Hutchinson, Plasma Phys. Control. Fusion **44** (2002), 1953.

[49] K. Ida, Plasma Phys. Control. Fusion **40** (1998), 1429.

[50] ITER Physics Expert Group, Nucl. Fusion **39** (1999), no. 12, 2175.

[51] C. Jan, EPFL/CRPP, TP-IV, 2005.

[52] F. Jenko, W. Dorland, M. Kotschenreuther, and B. N. Rogers, Phys. Plasmas **7** (2000), 1904.

[53] H. Johnsen, H. L. Pécseli, and J. Trulsen, Phys. Fluids **30** (1987), 2239.

[54] A. N. Karpushov, B. P. Duval, T. P. Goodman, and C. Schlatter, *in 47th EPS meeting of the European Physical Society*, 2006.

[55] S. I. Krasheninnikov, Phys. Lett. A **283** (2001), 368.

[56] B. Labit, A. Diallo, A. Fasoli, I. Furno, S. H. Müller, M. Podestà, and F. M. Poli, submitted to Phys. Rev. Lett. (2006).

[57] B. Labit, A. Fasoli, M. McGrath, S. H. Müller, M. Podestà, and F. M. Poli, 10th EU-US Transport Task Force meeting, 2004.

[58] M. A. Lieberman and A. J. Lichtenberg, *Principles of plasma discharges and material processing*, John Wiley and Sons, New York, 1994.

[59] Z. Lin, T. S. Hahm, W. W. Lee, W. M. Tang, and R. B. White, Science **281** (1998), 1835.

[60] J. B. Lister, Ph. Marmillod, P. F. Isoz, I. E. Piacentini, and B. Marletaz, *in 16th Symp. On Fusion Technology (SOFT)*, 1990, p. 1268.

[61] L. Ljung, *System identification, theory for users*, Prentice-Hall, Inc, New Jersey, 1987.

[62] S. Longo, Plasma Sources Sci. Technol. **15** (2006), S181.

[63] P. Mantica and F. Ryter, C. R. Physique **7** (2006), 634.

[64] A. Marinoni, P. Mantica, and D. VanEster et al., Plasma Phys. Control. Fusion **48** (2006), 1469.

[65] M. McGrath, A. Fasoli, B. Labit, S. H. Müller, M. Podestà, F. M. Poli, and K. Schombourg, *in 31st EPS Conference on Controlled Fusion and Plasma Physics*, 2004, pp. P–5.077.

[66] G. R. McKee, R. J. Fonck, M. Jakubowski, and K. H. Burrell et al, Plasma Phys. Control. Fusion **45** (2003), A477.

[67] S. H. Müller, Ph.D. thesis, Ecole Polytechnique Fédérale de Lausanne, 2006.

[68] S. H. Müller, A. Diallo, A. Fasoli, I. Furno, B. Labit, G. Plyushchev, M. Podestà, and F. M. Poli, Phys. Plasmas **13** (2006), 100701.

[69] S. H. Müller, A. Diallo, A. Fasoli, I. Furno, B. Labit, M. Podestà, F. M. Poli, and P. Ricci, submitted to Phys. Rev. Lett. (2007).

[70] S. H. Müller, A. Fasoli, B. Labit, M. McGrath, M. Podestà, and F. M. Poli, Phys. Rev. Lett. **93** (2004), no. 16, 165003.

[71] J-M. Moret and Equipe TORE SUPRA, Nucl. Fusion **32** (1992), 1241.

[72] S. Nakao, K. Ogura, Y. Terumichi, and S. Tanaka, Phys. Rev. **96A** (1983), 405.

[73] G. Van Oost, J. Adámek, V. Antoni, and P. Balan et al., Plasma Phys. Control. Fusion **45** (2003), 621.

[74] P. J. Paris and N. Rynn, Rev. Sci. Instrum. **61** (1990), 1095.

[75] Th. Pierre, A. Escarguel, and D. Guyonmarc'h et al., Phys. Rev. Lett. **92** (2004), no. 6, 065004.

[76] O. Pisaturo, Master's thesis, Ecole Polytechnique Fédérale de Lausanne, 2005.

[77] M. Podestà, A. Fasoli, B. Labit, M. McGrath, S. H. Müller, and F. M. Poli, Plasma Phys. Control. Fusion **48** (2006), 1053.

[78] M. Podestà, A. Fasoli, B. Labit, M. McGrath, S.H. Müller, and F. M. Poli, Plasma Phys. Control. Fusion **47** (2005), 1989.

[79] F. M. Poli, Ph.D. thesis, Ecole Polytechnique Fédérale de Lausanne, 2007.

[80] F. M. Poli, S. Brunner, A. Diallo, A. Fasoli, I. Furno, B. Labit, S. H. Müller, G. Plyushchev, and M. Podestà, Phys. Plasmas **13** (2006), 102104.

[81] F. M. Poli, M. Podestà, and A. Fasoli, submitted to Phys. Plasmas (2007).

[82] M. Porkolab, Nucl. Fusion **18** (1978), 367.

[83] E. J. Powers, Nucl. Fusion **14** (1974), 749.

[84] R. Prater, Phys. Plasmas **11** (2004), no. 5, 2349.

[85] M. Pyton, EPFL/CRPP, TP-IV, 2005.

[86] G. L. Ragan (ed.), *Microwave transmission circuits*, MacGraw Hill Book Company Inc, New York, 1948.

[87] S. V. Ratynskaia, V. I. Demidov, and K. Rypdal, Phys. Rev E **65** (2002), 066403.

[88] T. T. Ribeiro and B. Scott, Plasma Phys. Control. Fusion **47** (2005), 1657.

[89] B. Richards, M. E. Austin, R. V. Bravenec, and D. L. Brower et al., Nucl. Fusion **32** (1992), 567.

[90] J. Rossel, Tech. report, Ecole Polytechnique Fédérale de Lausanne, 2005.

[91] K. Rypdal, A. Fredriksen, O. M. Olsen, and K. G. Hellblom, Phys. Plasmas **4** (1997), no. 5, 1468.

[92] K. Rypdal, E. Gronvoll, F. Oynes, and A. Fredriksen et al, Plasma Phys. Control. Fusion **36** (1994), 1099.

[93] R. Sanchez, B. VanMilligen, and B. A. Carreras, Phys. Plasmas **12** (2005), 056105.

[94] R. Sanchez, B. VanMilligen, D. Newman, and B. A. Carreras, Phys. Rev. Lett **90** (2003), 185005.

[95] Y. Sarazin and Ph. Ghendrih, Phys. Plasmas **5** (1998), 4214.

[96] K. Schombourg, Master's thesis, Ecole Polytechnique Fédérale de Lausanne, 2004.

[97] L. Schott, *Plasma diagnostics*, North-Holland publishing company, Amsterdam, 1968.

[98] P. K. Sharma, J. P. Singh, and D. Bora, Plasma Phys. Control. Fusion **39** (1997), no. 10, 1669.

[99] M. Spolaore, V. Antoni, and E. Spada et al., Phys. Rev. Lett **93** (2004), 215003.

[100] P. C. Stangeby, Plasma Phys. Control. Fusion **37** (1995), 1031.

[101] T. H. Stix, *Waves in Plasmas*, Springer, New York, 1992.

[102] U. Stroth, F. Greiner, C. Lechte, K. Rahbarnia N. Mahdizadeh, and M. Ramish, Phys. Plasmas **11** (2004), no. 5, 2558.

[103] J. L. Terry, S. J. Zweben, K. Hallatschek, and B. LaBombard et al, Phys. Plasmas **10** (2003), 1739.

[104] C. Theiler, Master's thesis, Ecole Polytechnique Fédérale de Lausanne, 2007.

[105] M. Q. Tran, P. Kohler, P. J. Paris, and M. L. Sawley, *The Linear Magnetised Plasma device (LMP)*, LRP 205/82, CRPP/EPFL, 1982.

[106] I. Uzun, *in 48th DPP meeting of the American Physical Society*, 2006, p. 360.

[107] B. VanMilligen, R. Sanchez, and B. A. Carreras, Phys. Plasmas **11** (2004), 2272.

[108] A. von Hippel et al., *Dielectric materials and applications*, John Wiley and Sons, New York, 1954.

[109] F. Wagner and U. Stroth, Plasma Phys. Control. Fusion **35** (1993), 1321.

[110] P. Weber, Master's thesis, Ecole Polytechnique Fédérale de Lausanne, 2003.

[111] H. Weisen, I. Furno, and TCV team, Nucl. Fusion **41** (2001), 1227.

[112] J. Wesson, *Tokamaks*, Oxford University Press, Oxford, 2004.

[113] R. C. Wetzel, F. A. Baiocchi, T. R. Hayes, and R. S. Freund, Phys. Rev. A **35** (1987), no. 2, 559.

[114] D. R. Whaley, T. P. Goodman, A. Pochelon, and R. Behn et al., Nucl. Fusion **32** (1992), 757.

[115] T. Windisch, O. Grulke, and T. Klinger, Phys. Plasmas **13** (2006), 122303.

[116] K. L. Wong, R. Nazikian, R. J. Jayakumar, R. Prater, and C. C. Petty, Bull. Amer. Phys. Soc. (Savannah, Georgia, USA), vol. 49, 2004, p. 1088.

[117] A. J. Wootton, B. A. Carreras, and H. Matsumoto et al, Phys. Fluids B **2** (1990), 2879.

[118] S. J. Zweben, Phys. Fluids **28** (1985), 974.

[119] S. J. Zweben, R. J. Maqueda, and D. P. Stotler et al., Nucl. Fusion **44** (2006), 134.

Curriculum Vitae

MARIO PODESTÀ
CRPP-EPFL, Station 13
CH-1015 Lausanne, Switzerland

Tel. +41 21 693 19 28
Fax: +41 21 693 37 51
e-mail: mario.podesta@epfl.ch

Areas of interest

Basic plasma physics, magnetic fusion, diagnostic techniques, plasma-wave interactions.

Languages

· Italian, native
· English, fluent
· French, fluent

Education

· EPFL, Lausanne, Switzerland
Ph.D., Physics (expected Feb. 2007):
"Plasma production and transport in a simple magnetised toroidal plasma" (Director: Prof. A. Fasoli).

· Politecnico di Milano, Italy
Diploma degree (US equiv. M.S.) in Nuclear Engineering, June 2001:
"Experimental study and modeling of plasma parameters in front of the Lower-Hybrid grill of the CASTOR tokamak" (Directors: Dr. G. Piazza, Prof. M. Lontano, Dr. F. Zacek).

Post-graduate research experience

CRPP-EPFL, Lausanne Switzerland. PhD student (11/2001-present)
Participation to the conception and design of the TORPEX device at CRPP/EPFL, Lausanne. Development of the 2.45GHz EC system currently used to produce the plasma in TORPEX. Conception, design and construction of various electrostatic probes (Langmuir probes, Mach probes, gridded energy analysers). Experimental activity on TORPEX: characterisation of the plasma production mechanisms by EC waves, measurements of the resulting electron distribution function, characterisation and modelling of the particle source, investigation of the mechanisms leading to particle transport (plasma instabilities, fluid drifts), application of EC modulation techniques for transport studies. Specific competences acquired: advanced analysis of electrostatic probes data, physics of RF waves in plasmas, analysis techniques based on Fourier and Laplace methods, two-points correlation techniques (Conditional Average Sampling), software-implemented boxcar averaging technique. Technical competences: electronics for diagnostics and control of RF systems, vacuum techniques.

Undergraduate research experience

Politecnico di Milano, Italy.
Investigation of the modification of the plasma parameters during the injection of Lower-Hybrid waves into a tokamak plasma. Study of the interactions of LH waves with the edge plasma, due to spurious components in the injected wave-number spectrum, leading to generation of suprathermal particles. Measurements of the plasma parameters with electrostatic Langmuir probes. Experimental activity conducted on the CASTOR tokamak at IFP, Prague, Czech Republic.

Teaching experience

CRPP-EPFL Lausanne, Switzerland (11/2001-present). Teaching assistant: General physics, Plasma physics.
External expert: exam of Particle Detectors (EPFL).

Refereed publications

· M. Podestà, A.Diallo, A.Fasoli, I.Furno, B.Labit, S.H.Müller, G.Plyushchev and F.M.Poli, *Plasma Phys. Control. Fusion* **49**, 175 (2007)
· F.M.Poli, S.Brunner, A.Diallo, A.Fasoli, I.Furno, B.Labit, M.McGrath, S.H.Müller, G.Plyushchev and M.Podestà, *Phys. Plasmas* **13**, 102104 (2006)
· S.H.Müller, A.Diallo, A.Fasoli, I.Furno, B.Labit, M.McGrath, G.Plyushchev, M.Podestà and F.M.Poli, *Phys. Plasmas* **13**, 100701 (2006)

· G. Plyushchev, H. Boehmer, A. Diallo, A.Fasoli, B.Labit, S.H.Müller, M.Podestà and F.M.Poli, *Rev. Sci. Instrum* **77**, 10F503 (2006) (2006)
· A.Fasoli, B.Labit, M.McGrath, S.H.Müller, G.Plyushchev, M.Podestà and F.M.Poli, *Phys. Plasmas* **13**, 055902 (2006)
· M.Podestà, A.Fasoli, B.Labit, M.McGrath, S.H.Müller and F.M.Poli, *Plasma Phys. Control. Fusion* **48**, 1053 (2006)
· S.H.Müller, A.Fasoli, B.Labit, M.McGrath, S.H.Müller and F.M.Poli, *Phys. Plasmas* **12**, 090906 (2005)
· M.Podestà, A.Fasoli, B.Labit, M.McGrath, S.H.Müller and F.M.Poli, *Plasma Phys. Control. Fusion* **47**, 1989 (2005)
· S.H.Müller, A.Fasoli, B.Labit, M.McGrath, M.Podestà and F.M.Poli, *Phys. Rev. Lett.* **93**, 165003 (2004)
· F. Zacek, V. Petrzilka, K. Jakubka, J. Stockel, J. Gunn, M. Goniche, P. Devynck, M. Podestà, S. Nanobashvili, *Czech. Journal of Physics* **51**, 10 (2001)

Acknowledgements

First of all, I would like to thank the CRPP Direction for the opportunity of doing my thesis at CRPP, and especially my thesis director, prof. A. Fasoli.
Among the many people who have contributed to this work, I kindly acknowledge the friendly support from the technical staff of CRPP during all these years. Being this an experimental work and, moreover, conducted on a newly built device, it would never have been possible without their help. In particular, I wish to thank P. Marmillod, B. Marletaz, X. Llobet, D. Fasel, U. Siravo, A. Perez, J-F. Mion, P. Conti, O. Bartolomeoli and C. Moura for their continuous effort in maintaining TORPEX operational. I also have to mention the profitable help from P. Pagnoni and E. Bader, who retired in the course of my thesis. And I can not forget the discussions and the valuable contributions coming from the *atelier de dessins* for the development of most of the TORPEX diagnostics. A special thank is due to the *atelier méchanique* (and to the Big Boss, R. Chavan) for their competence, for their sympathy, and for the regenerating smell coming out from their "mezzanine" each and every friday at launch time. However, they have never revealed me the right places to find mushrooms in the neighbourhoods of Lausanne, so that I had to import them (legally?) from Italy from time to time... I hope this lack of information between technicians and scientific staff will be solved in the future, for the great benefit of the CRPP (just check out the good quality of the mushrooms). Anyway, I am indebted with all of them for the knowledge I have acquired on electronics, microwaves, mechanics and vacuum techniques, to which they contributed by letting me exploit almost freely, but always safely, my nature of *bricoleur*.
I must mention the great work done daily by all the CRPP secretary staff in taking care of (most of) the bureaucratic issues, thus allowing a young physicist to concentrate on physics, and not on incomprehensible papers/bills/travel plans/etc.. Guest star in the list is E. Grüter, the prototype of the Efficient Swiss Secretary and, more important, a good friend and a very nice person.
The list of acknowledgements would get too long if I had to thank separately all the physicists who contributed through discussions, suggestions and criticisms to this work. A special mention for few of them: S. Coda and S. Brunner, members of my "thesis committee" in the last years, along with S. Alberti, who introduced me to the funny world of microwaves (actually, it is funny until you destroy a 2000-CHF

microwave diode. After that, it just becomes "amazing"); A. Pochelon, O. Sauter, R. Pitts and A. Fasoli for the discussions we had during these years.
Being the ubiquitous A. Fasoli the head of the TORPEX group, he deserves a third mention, along with all the other members of the team with which I had the pleasure to work: Francesca, Stefan, Mark, Benoit, Gennady, Ahmed, Ivo, Paolo, Davoud and, of course, Ambrogio himself. I would also acknowledge the contributions to the TORPEX group activities from all the undergraduate students who joined us in these years: Pierre, Karin, Olivier, Jacques, Cristoph, Martin, Nicolas, Jonathan, Michael and Christian. For those of them who have been students of mine (i.e. I was asked by the EPFL to give a note, along with Ambrogio, at the end of their TP or diploma) let me just apologize for having been, sometimes at least, too hard/strict: you know how it works, Ambrogio and I have to share the roles of the "good" and "bad" cop, and he always wanted to be the good one... and he's the chief, no way to invert the roles... so, if you are not satisfied by the note you received, that's entirely my responsibility.
Thanks also to all the PhD students, who greatly contributes in making the CRPP a nice place to do a PhD, with free-wheelin' discussions on any subject and regardless of the specific area of interest (TORPEX, TCV or Industrial Plasmas). Moreover, the definition of the CRPP as the "Club Med of the plasma physics research" is, perhaps, not totally appropriate, but the opportunities of having fun, from time to time, are ensured by the huge community of PhD students.
Finally, I thank my family - to which this thesis is dedicated - and all my 'italian friends', for the constant support during the past years, and for the restoring ambience I experienced each time I came back home.